ABSTRACT

Title of Document: **IGNITION, COMBUSTION AND TUNING OF NANOCOMPOSITE THERMITES**

Kyle Sullivan, Doctor of Philosophy, 2010

Directed By: Full Professor, Michael Zachariah, Department of Mechanical Engineering and Chemistry

Nanocomposite thermites, or Metastable Intermolecular Composites (MICs), are energetic systems involving the reaction between nanoparticles of a metal fuel and another metal or metal oxide. When nanoparticles are used, the interfacial contact area and homogeneity of mixing are greatly improved, dramatically decreasing the characteristic mass diffusion length between the fuel and the oxidizer. Nano-sized aluminum is commonly used as a fuel, due to a combination of its abundance, good reactivity, and its ability to produce environmentally benign reaction products. A variety of oxidizers have been studied depending on the particular application. Nanocomposite thermites are currently being investigated for uses in propellants, pyrotechnics, and explosives, as well as some more exotic applications such as micro-propulsion and joining applications. Despite the research efforts and potential applications, the reaction mechanism remains poorly understood. As the particle size transitions into the nanometer regime, properties such as the melting temperature, surface energy, drag force, along with the characteristic time scales of thermo-chemical processes can change. In an exothermically reacting system, all of

these considerations must be taken into account simultaneously, a rather daunting task. However, if we design parametric experiments to look at relative trends, we can develop scaling laws and determine which parameters are perhaps the most important in the reaction mechanism. This work largely involves combusting thermite materials in a pressure cell, and also uses new techniques such as inducing a reaction inside an electron microscope with a specially designed heating holder. The results suggest that the pressurization and optical emission can arise from fundamentally different phenomena. A reactive sintering mechanism occurs which rapidly decomposes the oxidizer and pressurizes the system. This is followed by the remainder of the fuel burning in a gaseous, pressurized environment, where the burning rate is controlled by the fuel. Also in this work, we combust new fuels and oxidizers such as nano-sized boron, $AgIO_3$, and Ag_2O. Boron can be used as an additive to increase the energy density in thermites. The silver-based oxidizers are currently being investigated in nanocomposite thermites for their ability to generate a product which can effectively destroy harmful biological spores, such as Anthrax.

IGNITION, COMBUSTION AND TUNING OF NANOCOMPOSITE THERMITES

By

Kyle Sullivan

Dissertation submitted to the Faculty of the Graduate School of the
University of Maryland, College Park, in partial fulfillment
of the requirements for the degree of
Doctor of Philosophy
2010

Advisory Committee:
Professor Michael Zachariah, Chair
Dr. Sheryl Ehrman
Dr. Gregory Jackson
Dr. Christopher Cadou
Dr. Bao Yang

Dedication

This work is dedicated to my friends and family who have always believed in me getting my PhD, even when I had my doubts myself. To my parents, thank you for everything you have done for me growing up. I would not be where I am today without your competence and love in raising me. To Kat, it's no surprise to me that my productivity increased when we met. I became a much more confident person, and you have served to bring out the best in me. Thank you for your patience, love, and support through this process.

Acknowledgements

I would first like to thank my advisor, Dr. Michael Zachariah. He has taught me much more than how to collect and interpret data, he has taught me how to succeed as a professional researcher, and has supported me in every step along the way. I'd like to acknowledge the Army Research Office and the Defense Threat Reduction Agency for financial support in my project. Thanks to Wen-An Chiou and Rich Fiore for all your help with the microscopy studies, along with the Maryland Nanocenter and Protochips, Inc. for providing the equipment needed to make the microscopy studies possible. Curtis Johnson and Greg Young, it was a pleasure working with you both, and I hope to collaborate in the future. To all by lab mates and roommates, thank you for all your invaluable support in this work, and for making my time here a memorable experience.

Table of Contents

Contents

List of Tables

List of Figures

lifted off the wire. Overall, the material is removed from the wire much slower than was observed for the thermite.

Figure 7.10 Series of snapshots of nano-Al/Fe_2O_3 thermite reacted on the wire. Note the formation of micron-sized spherical particles, in this case much larger than was observed for the nano-Al/CuO thermite (see Figure 7.8). Some particles appear to be hollow in this case. The formation of spherical particles occurs well before the onset of optical emission was measured.

Figure 7.11 Model predictions of the total time to sinter CuO nanoparticles in air at 1700 K relative to a characteristic reaction timescale. The total sintering time is assumed to be the sum of two components depicted in the figure; the heating (sensible and latent) time of nanoparticles to the melting temperature, along with the time to fuse the particles calculated by a viscous flow mechanism. The timescale of fusion is found to be much faster than the heating time, therefore, the calculation of the total sintering time can be reduced simply to a calculation of the time it takes to heat and melt nanoparticles. The results show the sintering and reaction timescales are comparable, indicative of a reactive sintering mechanism.

Figure 8.1.1 Thermal analysis by DSC-TGA of $AgIO_3$ heated under nitrogen at 5 K/min. The $AgIO_3$ was commercial micron sized $AgIO_3$ ball milled down to a particle size of around 900 nm.

Figure 8.1.2 Transient gas release profile as determined by rapidly heating $AgIO_3$ in the mass spectrometer. The material is the synthesized 270 nm $AgIO_3$.

Figure 8.1.3 Sequential snapshots of Al/$AgIO_3$ burning in air. The wire can only faintly be seen, and remains stationary throughout the burning. The thermite is Al (ALEX) and $AgIO_3$ (270nm), with an equivalence ratio of 1.0.

Figure 8.1.4 Video images of the combustion of three thermite samples in air. The images at the top show the samples prior to combustion, with a 45 mg line of powder placed on an aluminum support. A grid directly behind the sample has a spacing of 10.8 mm between lines. Samples were ignited by a spark from a wire attached to a tesla coil (tip of wire visible in the upper left corner of the top images). Images were recorded at 10 μs intervals, using a 2 μs exposure. The Al in this study is 80nm from NanoTechnologies. The CuO in this study is 45 nm from Technanogy. Each sample was fuel-rich in this study with equivalency ratios of 1.12 for the nano $AgIO_3$ material, 1.06 for the micron $AgIO_3$ material, and 1.27 for the CuO material.

Figure 8.1.5 Representative TEM image and 2D elemental maps (using EDX) of Ag, Al, I, and O after reaction inside the combustion cell. Higher resolution images could not be achieved due to beam interactions and morphological changes in the sample with prolonged beam exposure. The thermite was Al (ALEX) and synthesized $AgIO_3$ (270 nm) with an equivalence ratio of 1.0.

Figure 8.1.6 TEM image and 1D elemental linescan (using EDX) across two adjacent particles of Al/$AgIO_3$ reacted in the pressure cell. Note the presence of an Al/O core surrounded by AgI in each particle. The extra (green) line shown in the image was Carbon from the film. The thermite was Al (ALEX) and synthesized $AgIO_3$ (270 nm) with an equivalence ratio of 1.0.

Figure 8.1.7 XRD patterns (Intensity vs 2θ) for pure $AgIO_3$, along with the thermite before and after reaction in the pressure cell. The major detectable reaction product is AgI. Unless otherwise noted, the AgI peaks are γ-AgI. The thermite was Al (ALEX) and synthesized $AgIO_3$ (270 nm) with an equivalence ratio of 1.0.

Figure 8.1.8 Scanning electron micrographs of reaction products from spark initiated nano Al/$AgIO_3$ (20 mg) deposited on a copper plate. Micrographs a, b, and d (taken at different magnifications) show the region of the copper plate that was positioned 10 mm directly above the sample. Micrograph c shows a region of the copper plate that was 10 mm distant from the spot of the top micrograph. Micrograph c was taken in the quantum backscatter mode, where the light elements (Al, O) appear as dark spots in the image, while the heavy elements (Ag, I) appear as light spots. Small islands of elemental Ag (essentially free of iodine) are marked in micrograph c. The nearly horizontal lines result from abrasive polishing of the copper plate. The Al was from Nanotechnologies, and the $AgIO_3$ was synthesized (270 nm).

Chapter 1: Introduction

Nanotechnology has been an exciting topic in the recent literature, and a vast research effort has been put forth to discover new applications in virtually every engineering field. While the use of nanoparticles can actually be dated to a very long time ago, recent improvements in manipulation and characterization at the nanoscale has taken the excitement to new levels. As the particle sizes become smaller, materials display very different properties than bulk materials, and a "bottom-up" construction of new and improved materials has been envisioned since Richard Feynman gave his famous talk at the American Physical Society Meeting in 1959, entitled "There's Plenty of Room at the Bottom."

1.1 Energetic Materials

Of the seemingly endless applications of nanoparticles, the one that will be discussed in this particular work will be their use in energetic materials. Energetic materials, in the most basic sense, are materials with large amounts of stored chemical energy which is meant to be released with a controlled rate upon ignition. While things like gasoline and batteries are technically energetic systems, the conventional use of the term generally applies to propellants, explosives and pyrotechnics. Metals, in particular, are interesting fuel choices, largely attributed to their high energy density and low cost. Metals are relatively stable species, and react to form products which are chemically inert and thus generally nontoxic to humans or the environment. When a metal is mixed with another metal/metal oxide, the reaction between the two is referred to as a thermite reaction. The most well known example of a thermite system is aluminum mixed with iron oxide. As the two materials react, a very high temperature (>3000 K) is achieved and this is useful to fuse dissimilar materials together. This technique has historical significance, as it has been used to weld rail tracks together.

1.1.1 Nanocomposite Thermites, Metastable Intermolecular Composites (MICs), Superthermites

When a thermite system is prepared with the constituent particles having dimensions on the nanoscale, the reactivity can increase by several orders of magnitude. This discovery can be traced back to 1995 when Aumann[1] used thermogravimetric analysis, Rutherford backscattering spectrometry and transmission electron microscopy to conclude that Al/MoO_3 exhibited almost three orders of magnitude higher reactivity when nanoparticles were used in place of larger particles. Since then, research efforts have increased to understand the reactivity of these systems, so that improvements in their safety and performance could be made. There currently is not a consensus on what to call these materials. We have preferred to use "Nanocomposite Thermites," but Metastable Intermolecular (or Interstitial) Composites (MICs), and Superthermites have also been coined for these systems. All of these terms can and have been used interchangeably, and generally refer to lose powder mixtures of fuel/oxidizer nanoparticles.

A schematic of a nanocomposite thermite system is shown in Figure 1.1. The overall idea of nanocomposite thermites is simple; pack an oxidizer in as close proximity to the fuel as possible. This will increase the interfacial contact, homogeneity of mixing, and will dramatically decrease the characteristic mass diffusion length. All of these considerations enhance the combustion performance, and will result in systems that behave more like conventional explosives, where the fuel and oxidizer are intermixed on the atomic scale, and thus react on very fast timescales.

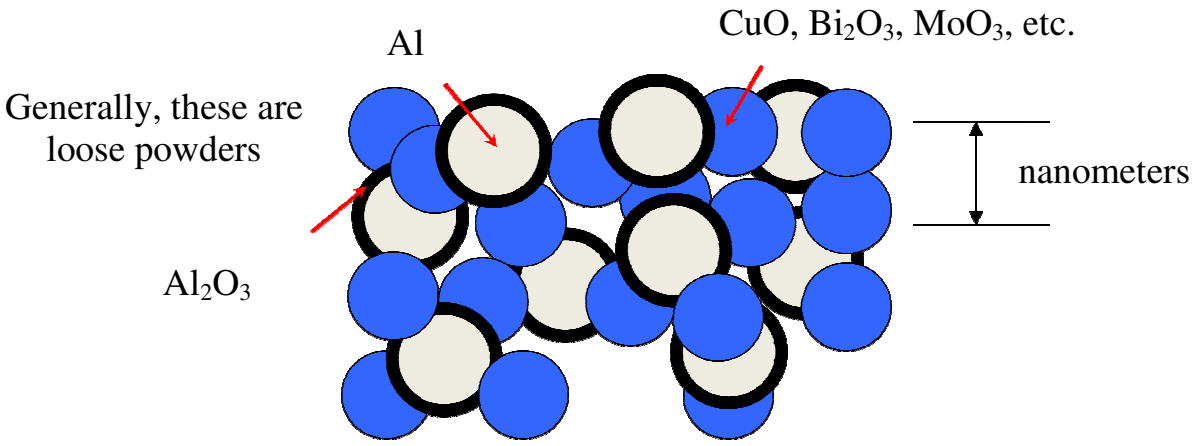

Figure 1.1 Simplified schematic of a nanocomposite thermite. As prepared, these are generally loose-powder mixtures and most often use nano-sized aluminum as the fuel.

Aluminum has traditionally been used as the fuel, due to a combination of its high energy density, good reactivity, and abundance/low cost. There are a wide variety of oxidizers which can be reduced when reacted with aluminum, and the particular oxidizer will be based on the desired application. In an article written in 2005, Wilson et al.[2] presented a schematic which showed where MICs stood in comparison to both propellants and explosives, and this is included here as Figure 1.2. What can be seen is that MICs exhibit faster burning velocities than propellants, but cannot achieve the high overpressures characteristic of explosives. The energy density of aluminum-based thermites is shown in Figure 1.3, and this is another large motivating factor of studying these systems. It can be seen that certain mixtures have a higher mass and volumetric energy density than explosives, and this fact makes them attractive systems to study either as a stand-alone energetic or as additives to other energetic systems. The real engineering challenge involves controlling the rate at which the available energy can be extracted during a chemical reaction.

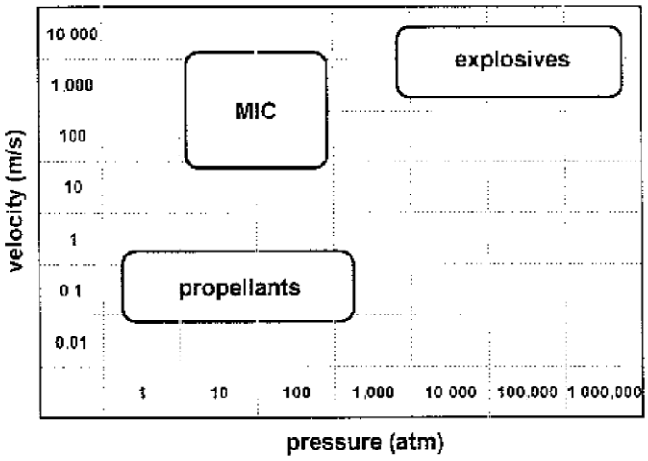

Figure 1.2 A comparison of the velocity (reactivity) and pressures achieved in various energetic systems. This figure was reproduced from a work by Wilson and Kim.[2]

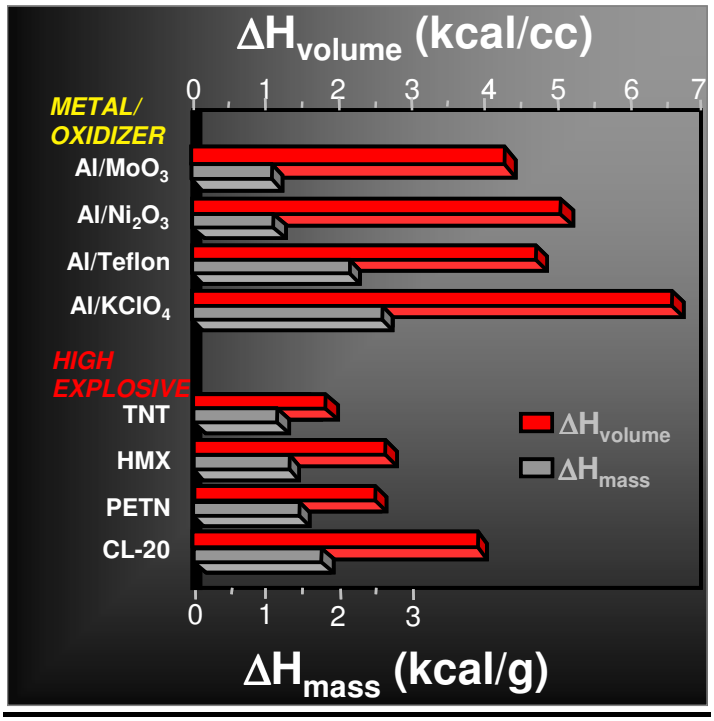

Figure 1.3 Mass and volumetric energy density of thermite mixtures along with some common explosives. This figure is taken from Fisher and Grubelich.[3]

1.2 Motivation of this Work

This work is primarily an investigation to understand how a mixture of metal fuel and metal oxide nanoparticles ignite and combust. One big issue which will become apparent early

is the need to perform measurements either in-situ, or to use experimental techniques which can simulate a rapidly heated high temperature environment. In a real combusting environment, the particles will be heated at a rate of approximately 10^6 K/s, and this is considered a good ballpark value for what experiments should try and reproduce. If the heating rate is too slow, then relatively slow processes such as solid state diffusion might appear to be important, when in fact some of these processes may be insignificant in a real combusting environment.

A mixture of fuel and oxidizer nanoparticles may seem like a simplistic system to start with, however, there are a large number of variables involved. Some variables which have been experimentally shown to impact the combustion characteristics are; type of fuel and oxidizer, particle size and morphology, stoichiometry, heating rate, degree and uniformity of mixing, characteristic heating and sintering timescales, gas production, packing density, and oxidizer decomposition mechanism. There are many other variables not listed here which may, in time, also prove to be important in the mechanism.

1.3 Experimental Strategy

With so many variables involved, it's difficult to study a particular parameter without simultaneously affecting several others. Therefore, the experimental strategy which has been employed throughout this work is to devise experiments which can probe certain variables while keeping as many other parameters constant as possible. For example, if the goal of a study is to determine the effect of equivalence ratio on the reactivity, then the same exact fuel, oxidizer, and preparation technique should be used so that the results can confidently be attributed to changing the equivalence ratio. There will always be other variables which we cannot control, for example as the equivalence ratio changes so does the adiabatic flame temperature and amount of available enthalpy. Also, the interfacial contact area may be affected by changing the

stoichiometry. These considerations must always be kept in mind when analyzing experimental results or interpreting other researchers' results.

1.4 Chapter Guide

The goal of Chapter 2 is to provide a general overview of several key differences between large and small particles. All of the topics presented were at some point used in this work, either directly or indirectly, and are all fundamental nanoparticle topics which should be well understood by any new researcher intending to take on a similar project. In addition to the thermophysical properties, several relevant timescales are also included, which must always be considered in the context of this work. Several practical examples and calculations are included to emphasize how different things are when the particle diameter becomes small. Chapter 3 is a review of the relevant literature, and breaks down nanocomposite thermites into several pertinent "sub" problems. For example, in order to know how nano-sized aluminum will ignite in a composite and at a high heating rate, an important prerequisite is to understand how nanoaluminum ignites in a simpler environment such as in air at 1 atm. All experimental techniques that were used in the context of this work are then discussed in Chapter 4. A new researcher to this field should find this chapter to be quite useful in that it is a condensed version of the available experimental techniques at your disposal. Chapter 5 is an investigation of using nano-sized boron to enhance the reactivity of thermites. Chapter 6 is an investigation of the reaction mechanism of thermites by simultaneously measuring the pressure and optical emission during the combustion. In Chapter 7, we utilize several high-heating experimental techniques to investigate the reaction mechanism, in particular the role of condensed phase reactions and a reactive sintering mechanism. Chapter 8 is both practical and mechanistic in nature, and is an investigation of the burning of two new silver-based oxidizers, $AgIO_3$ and Ag_2O. Both of these

are of interest because of their ability to produce silver-species upon reaction, and important for anti-microbial energetic systems. A summary of the major findings, along with recommendations for future work is given in Chapter 9.

Chapter 2: Nano vs Micro

At what point can we actually call something a "nanoparticle?" This topic is only the beginning of a long and continuing debate about what exactly is the appropriate way to describe the physical and chemical properties of nanoparticles. A variety of nanoparticles with various sizes, shapes and morphologies are shown in Figure 2.1. Describing the particle size in terms of a common physical dimension is not exactly straightforward, due to the various morphologies present. In fact, anything that has at least one characteristic length scale that can be measured using nanometers can be classified as a nanoparticle, and this is currently the most widely accepted definition. The appropriate classification beyond this point will depend on the particular application.

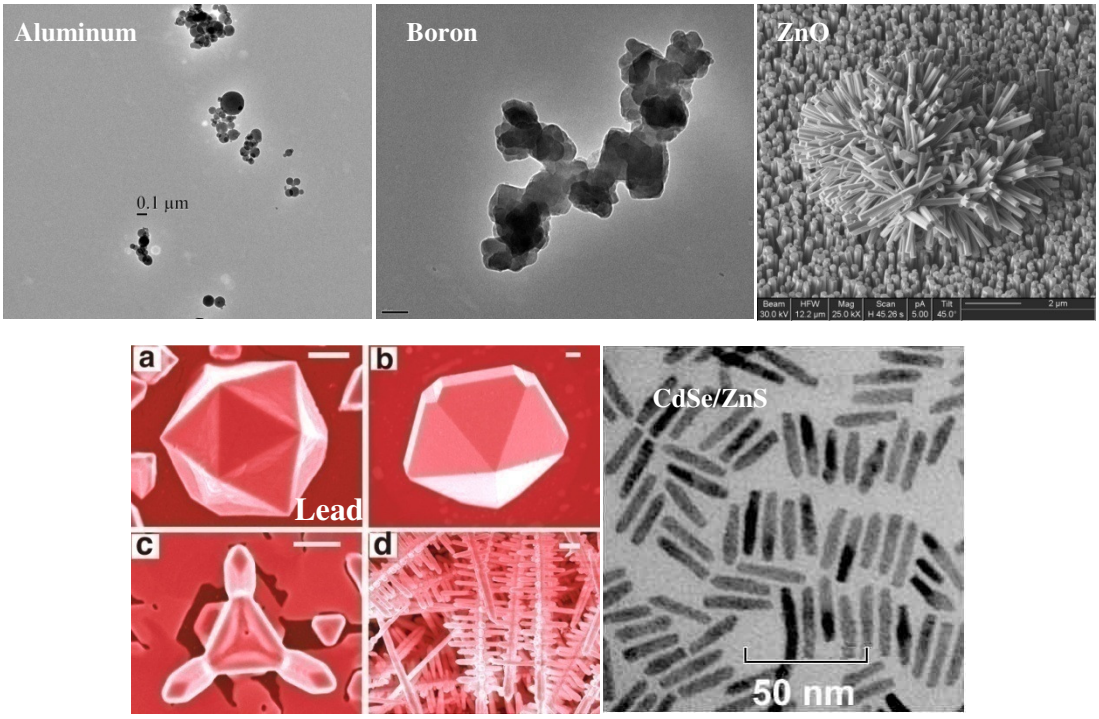

Figure 2.1 Various nanoparticles. Aluminum and Boron images were taken by our group.
ZnO image: www.phy.bris.ac.uk/groups/electron_microscopy/index.html
Lead images: www.anl.gov/Media_Center/ArgonneNow/Fall_2007/user-friendly.html
CdSe/ZnS images: www.nanofm.com/hnanorods.html

2.1 Thermophysical Properties

As the particle size transitions into the nanometer regime, multiple thermophysical and chemical properties become different. While on one hand this has been a driving force for the excitement surrounding nanotechnology, it has also created the need to re-evaluate our thinking about things at the nanoscale to determine whether materials will behave the same way as they do in the bulk. In many cases, this is far from true. Several material properties are very different at the nanoscale than the microscale. Our idea of a "surface" becomes somewhat obscure, and the high number of atoms near the surface relative to the bulk is one of the key artifacts as to why other properties deviate from their bulk values. This chapter discusses the surface to volume ratio, and continues to describe how that can change properties such as the melting temperature and vapor pressure over the highly curved surface. Various characteristic timescales, which will be important in the context of this research effort, will then be discussed.

2.1.1 Surface to Volume Ratio

In chemical reactions, surface area is an important consideration, as the reaction rate generally scales proportionally to it. In particle burning, the instantaneous reaction rate is proportional to the available surface area, while the overall burn time depends on the volume of the particle. For these reasons, the surface to volume ratio is also accepted as an appropriate metric for combustion applications. An inherent assumption in using surface to volume ratio is that there are two types of atoms present within the particle; surface atoms and bulk atoms. However, as the particle size becomes smaller, the designation becomes a bit unclear.

As the particle size becomes smaller, the percentage of particles which constitute the "surface" increases. As an example, for an idealized spherical particle where the atoms are

arranged in a perfect lattice everywhere, the percentage of atoms occupying the outermost shell of the particle relative to the total number of atoms in the particle can be estimated. For this calculation, I assume the "surface" involves a monolayer of atoms. The thickness of this layer can be estimated to be 4.1 Å (the lattice constant of aluminum). Based on the geometry and assuming bulk density, the percentage of atoms in the shell relative to the bulk is calculated as a function of diameter, and the results are shown in Table 2.1.

Table 2.1 The percentage of atoms occupying the outermost shell relative to the bulk. This calculation assumes a perfectly spherical particle with the outermost layer have a thickness of 4.1 Angstroms, based on a typical lattice parameter distance for Aluminum.

Particle Diameter (nm)	% of Atoms Occupying the Outermost Shell
10,000	0.025
1,000	0.25
100	2.4
10	23
5	42
2	79
1	99

What can be seen is that below ~100 nm, the ratio of atoms near the surface starts to become a significant amount. It can also be seen that for 1 nm Al, 99% of the atoms are near the surface. In fact, at some critical diameter, all atoms within the particle may behave as if they were located on the surface, and this may lead to dramatic changes in material properties. At such small sizes, these are more commonly referred to as "clusters" of aluminum, and an entire field is dedicated to this research. Most nanoparticles are 10's to 100's of nanometers in size, and many of the enhancements and changes to materials properties can fundamentally be traced back to this idea of a higher number of atoms constituting the surface relative to the bulk.

2.1.2 Curvature and Surface Tension

A phenomenon which changes as the surface to volume ratio increases is the surface tension. The concept of surface tension can be envisioned when one thinks about neighboring atoms and the inter-atomic forces between them. Atoms which are located in the bulk of a material are generally in a low energy state because they have neighboring atoms completely surrounding them, and thus there is minimal net force acting on them. Atoms near the surface, however, do not have neighboring atoms on all sides, and thus are in an undesirable position. In a material which has a perfectly flat surface, the atoms near the surface have approximately half the number of neighboring atoms than the atoms in the bulk of the material. The free energy and surface tension can be calculated using the inter-atomic potentials of the atoms in a particular material.

As the particle size becomes smaller, the curvature of the surface becomes higher. As this happens, the atoms near the surface are surrounded by even fewer neighbors than a flat surface, rendering an even more undesirable situation. A schematic of this is shown in Figure 2.2. The free energy of the surface which results from this curvature and the surface tension becomes increasingly important for small particles, and can lead to very different behavior in other thermo-physical properties such as evaporation and melting. The governing thermodynamic equations often have to be modified for nanoparticles by inclusion of a surface free energy term, which becomes significant as the surface to volume ratio increases.

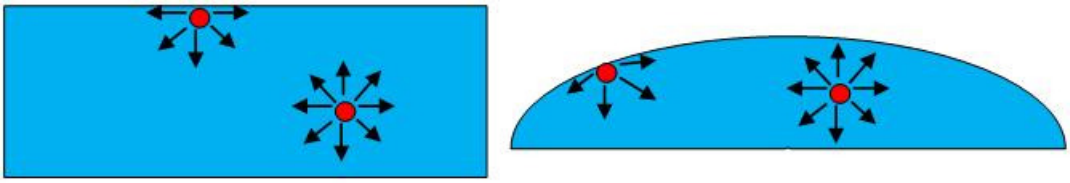

Figure 2.2 Schematic of the forces acting on atoms near the surface and in the bulk. As the surface is curved, atoms near the surface are in an increasingly undesired state due to the imbalance in forces.

2.1.3 Melting Point Depression

The melting temperature of a material is defined at the point where the liquid phase is in thermodynamic equilibrium with the solid phase. When the particle size becomes small and the curvature and surface energy increase, it has been observed that particles can melt at lower temperatures than the corresponding bulk material. The depression of the melting temperature is most dramatic for very small <10 nm particles, but does still occur to a lesser extent for larger particles. Buffat and Borel[4] developed a generalized empirical correlation for predicting the melting temperature of nanoparticles based on measurements of the melting point depression of gold nanoparticles. This correlation is given as:

$$T_{mp}(d_p) = T_m \left[1 - \frac{4}{L\rho_p d_p}\left(\sigma_s - \sigma_l \left(\frac{\rho_p}{\rho_l}\right)^{2/3}\right)\right] \tag{2.1}$$

In this formula, T_m is the bulk melting temperature, L is the latent heat of fusion, d_p is the particle diameter, and ρ_p, ρ_l, σ_s, and σ_l are the density and surface energy of the solid and liquid phases, respectively. The calculated melting temperature is shown as a function of particle size for aluminum in Table 2.2. For this calculation, some approximate values are:

L = 400 kJ/kg, T_m = 933 K, ρ_p = 2702 kg/m^3, ρ_l = 2380 kg/m^3, σ_s = 1.3 J/m^2, σ_l = 1.01 J/m^2

Table 2.2 Melting point depression as a function of particle size for aluminum, and using the empirical correlation developed in Buffat and Borel.[4]

Particle Diameter (nm)	Melting Temperature (K)
Bulk Value	933.0
10,000	932.9
1,000	933.3
100	925.9
10	862.5
5	791.9
2	580.3
1	228.0

As can be seen, it's not until the particle size becomes <10 nm very small that the melting temperature decreases dramatically. It is important to mention because many of the nanoparticle systems which will be later discussed have very polydisperse size distributions, and thus likely have a wide range of melting temperatures within the sample. If the melting of the particles is somehow important in the reaction mechanism, then modeling it accurately will require the use of such correlations.

2.1.4 Equilibrium Vapor Pressure Over a Curved Surface

If we think of a nanoparticle in equilibrium with its surroundings, then the solid/liquid phase must be in equilibrium with the gaseous phase. Predicting the criteria for this equilibrium again goes back to the fundamental idea of free energy. The total free energy must be decreased in order for, say, a particle to condense from its vapor. As discussed, the surface energy becomes an important part of this calculation, especially as the particle size becomes small. Frenkel (1946) expressed the Gibbs free energy of this system as follows:

$$G = n_A\mu_A(p,T) + n_B\mu_B(p,T) + 4\pi r^2\sigma \qquad (2.2)$$

In this equation n_A and n_B are the number of moles in the vapor and particle phases, and μ_A and μ_B are the chemical potentials of those phases. The final term represents the surface free energy of the particle, and r is the particle radius while σ is the surface tension corresponding to the bulk material with a planar surface. The condition for equilibrium is that the $\delta G = 0$, and after some derivation (see Friedlander,[5] chapter 9 for more details), the equation can be expressed as the well known Kelvin relation:

$$Ln\ \frac{p}{p_s} = \frac{4\sigma v_B}{d_p RT} \tag{2.3}$$

The terms p and p_s correspond to the vapor pressure and the vapor pressure over a planar surface, and v_B is the molar volume in the liquid. This result is very important in the thermodynamics of aerosols, and states that the equilibrium vapor pressure increases exponentially as the particle size becomes smaller. The surface tension for aluminum was considered to be 1 J/m^2, and the equilibrium vapor pressure is shown as a function of particle size in Table 2.3. The Kelvin effect can useful in predicting if and at what sizes particles will condense out of the vapor based on the saturation ratio ($S = p/p_s$). This analysis is essentially related to the reduced melting point described above, however, it is another common way of looking at the implications of the thermodynamics.

Table 2.3 The Kelvin effect showing the increase in equilibrium vapor pressure as the particle size decreases and the curvature of the surface increases. The calculations are for Aluminum at 300 K.

Particle Diameter (nm)	p / p_s (Saturation Ratio)
10,000	1.00
1,000	1.01
100	1.1
10	2.20
5	4.97
2	55.1
1	3040

Another way to think about the formation of a particle in equilibrium with its vapor is that the evaporation rate of molecules leaving a particle has to be equal to the arrival rate of molecules to the surface, otherwise the particle would either grow or shrink. Since small particles have very high equilibrium vapor pressures, they will nearly instantaneously evaporate as they form unless the arrival rate is sufficiently high. Therefore, very high saturation ratios are required to induce homogeneous nucleation. The flux at which particles come and go from the surface can generally be expressed in the free molecular regime via the following form:

$$Flux = \frac{P}{\sqrt{2\pi m k_B T}} \tag{2.4}$$

Here m is the molecular mass, k_B is Boltzmann's constant, T is the temperature and P is the pressure. To calculate the arrival rate, the P used is related to the concentration of molecules in the gas phase. In order to calculate the evaporation rate, the appropriate P to use is the equilibrium vapor pressure for the particular size particle at that temperature, and this rate is independent of the concentration of molecules in the gas phase. The size of a particle which condenses out of the gas phase is governed by these considerations, and it follows that smaller particles can form for higher saturation ratios.

These ideas can also be extended to describe the differences between homogenous and heterogeneous condensation. The aforementioned discussion simply describes thermodynamic equilibrium, and thus does not include the kinetics of a nucleation event. For example, let's say that for a given saturation ratio the critical particle diameter which can form is 10 nm. The atoms would have to nucleate and grow into that size at a rate faster than the evaporation, and this is somewhat daunting when one considers the 30,000+ atoms which must arrange to form a stable 10 nm particle. If, however, a site for condensation already exists, it's much easier for

individual atoms to condense onto that material than form an entirely new particle. Hence, heterogeneous condensation is greatly favored over homogeneous, and requires much smaller saturation ratios to occur for a given particle size. (This phenomenon is one reason why the idea of adding particles to clouds can actually work to make it rain.)

2.1.5 Presence of an Oxide Shell

Everyone knows that iron will eventually "rust," and this process is generally accelerated in the presence of water. Rusting is nothing more than the reaction of iron to form iron oxide (orange-ish in color). In fact, every single metal will oxidize in air if given enough time because the metal oxide is more thermodynamically stable than the metal. Some metals, such as gold, are much more resistant to this oxidation than others, but it will inevitably happen with enough time. In a particle, what this means is that a certain amount of metal oxide is always present, and manifests itself as an oxide shell surrounding a core of the unoxidized fuel. The thickness of the shell will really depend on its permeability to oxidizing species, and after a certain thickness is achieved the rate of further oxidation becomes slow enough that a metastable nanoparticle is formed. In spherical aluminum particles, the thickness of the oxide shell is typically on the order of 2-5 nm in thickness. If we assume that the average value of the shell thickness is exactly 2 nm, we can calculate the Wt% of the oxide shell in the total mass of the particle, and this is shown in Table 2.4.

Table 2.4 Calculation of the Wt% of a 2 nm thick Al_2O_3 shell in an aluminum particle with given diameter. For large particles, the oxide shell represents an insignificant amount of the total volume, whereas the amount becomes quite large as the particle size is decreased.

Particle Diameter (nm)	Wt% Oxide Shell
10,000	0.18
1,000	1.7
100	16
50	29
25	50
10	84
5	99

In energetics, the presence of the oxide shell ends up being a critical issue for small particles because the shell is essentially dead weight. Metals are not only chosen because they are very reactive, but also because they exhibit excellent mass and volumetric density relative to other materials. If, however, the fuel is 50% inert, this presents a problem in that it greatly reduces the energy density. Research efforts are currently underway to develop methods of coating nanoparticles with materials which will participate in the reaction, so as not to waste any material. From a mechanistic standpoint, the presence of an oxide shell in nanoaluminum combustion and its implications is a very important topic, and more will be presented on this in the literature review of Chapter 3.

2.2 Timescales

This section is designed to discuss some important timescales which are relevant to the current work. With large surface to volume ratios, the timescales associated with heat transfer and flow relaxation are quite important. Also, sintering and coalescence times become increasingly faster as the particle size decreases, and especially when phase transitions occur and the particles become liquid-like. The relevant timescales are dependent on the thermophysical and material properties, and vary greatly depending from system to system.

2.2.1 Flow Relaxation

When one first learns about the motion of objects using Newton's Laws, there is no mention of a drag force. The reason for this is that it makes little difference when describing the motion of large, dense materials through a not-dense medium like air. The truth is, if an object is moving through any fluid medium, a drag force always exists and opposes the motion of an object. As the particle size becomes smaller, this is an increasingly significant force, and always needs to be considered when describing the motion of nanoparticles. The drag force felt by an object is the product of its velocity and some friction coefficient. The friction coefficient for spherical particles is given by Stoke's Law:

$$f = 3\pi\mu d_p \tag{2.5}$$

where μ is the viscosity of the medium and d_p is the diameter of the particle. For nanoparticles, as the particle size becomes comparable to the mean free path of the fluid, Stoke's Law over predicts the drag force. Thus a slip correction factor is introduced, C:

$$f = \frac{3\pi\mu d_p}{C} \tag{2.6}$$

For spherical particles in air, the values of C are near unity until about 1 micrometer, and then increase as the size shrinks. For a 1 nm, the correction factor is 216.

The drag force at a given time is proportional to the friction coefficient and the instantaneous velocity. Using these ideas, we can calculate how long a spherical aluminum particle will take to hit the floor if dropped from a height of 1 m, and as a function of diameter. Secondly, we assume an aluminum particle is given an initial velocity of 1000 m/s, and calculate

the approximate time for the particle to come to a stop in air at atmospheric conditions. The results of both calculations are shown in Table 2.5.

Table 2.5 Calculations of the gravitational settling time and the stopping distance of different sizes of aluminum particles thrown with an initial velocity of 1000 m/s in air. The correction factor is given in Friedlander.[5]

Particle Diameter (nm)	Slip Correction Factor	Time to fall 1 m by gravity	Stopping Distance if Initial velocity = 1000 m/s
10,000	1.016	117 seconds	87.6 cm
1,000	1.164	169 minutes	1.00 cm
100	2.85	115 hours	0.246 mm
10	22.2	61.7 days	19.1 μm
5	43.6	18.0 weeks	9.40 μm
2	108	45.3 weeks	3.72 μm
1	216	1.75 years	1.86 μm

What can be seen from these calculations is that nanoparticles are virtually unaffected by gravity, and also cannot travel very far in a fluid before the drag force brings them to a stop. One implication of Stoke's Law is that nanoparticles will essentially be swept up and carried by a gas, due their ability to rapidly "relax" to the momentum of the flow. This is an important consideration in energetic systems involving nanoparticles, especially when gases are produced during the reaction. As intermediate gases are generated during a chemical reaction, the gas can sweep up unreacted or partially reacted particles, and this will be an important consideration when discussing self-propagating reactions in loose nanoparticle samples. The characteristic timescale for a particle to adjust to a change in momentum of a fluid is given as a function of the density and diameter of the particle, ρ_p and d_p, and the viscosity of the fluid μ as:

$$\tau_{flow} = \frac{\rho_p d_p^2}{18\mu} \tag{2.7}$$

This calculation is an approximation of flow relaxation time. If this value is very low, it implies that the particle will follow the gas flow, and if it is high, a particle will be unaffected by the gas flow and continue on its path via its own momentum.

2.2.2 Heat Transfer

As the surface to volume ratio increases, heat transfer timescales become increasingly fast. A nanoparticle itself is a very small thermal load with a high rate of heat transfer, making it very difficult to heat a nanoparticle above the ambient temperature. For solid/fluid systems, if the heat transfer rate within the solid is much faster than the rate at which heat is exchanged at the surface, then a lump capacitance method is valid. The lump capacitance method essentially assumes the object is at an instantaneously uniform temperature. The transient temperature of the object is governed by the rate of heat exchange between the surface and the surrounding fluid. In this case, the characteristic heat transfer time scale is:

$$\tau_{heat} = \frac{\rho V c_p}{hA} \tag{2.8}$$

where ρ and c_p are the density and heat capacity of the solid, h is the heat transfer coefficient, and A and V are the surface area and volume of the solid, respectively. This calculation is a good first order approximation for the time it takes for a solid to heat/cool to the temperature of the ambient fluid.

While this calculation itself is a rather simplistic one, there is a whole field of research devoted to measure and predict the heat transfer coefficient. For spherical particles, h can be expressed in terms of the dimensionless Nusselt number, Nu as:

$$h = \frac{Nuk_G}{d_p} \tag{2.9}$$

In this equation, k_G is the thermal conductivity of the fluid and d_p is the particle diameter. The Nusselt number is something that is dependent on the actual material and gas, and also varies with the lengthscale of the particle versus the mean free path of the gas, i.e. the Knudsen number. A detailed analysis of the values of Nu is given by Filippov and Rosner.[6] In the limit that the particle size is much greater than the mean free path, the Nu number converges to a constant value of 2. As the size is decreased and approaches the free molecular regime, the value can drop by almost two orders of magnitude, and thus will greatly affect the heating rate.

As an example, at one point there was interest in heating 100 nm particles of aluminum in air using a CO_2 laser. The goal was to see whether the particle could rapidly be heated in air from room temperature up to its ignition point, ~1000 K. This problem is easily modeled using an energy balance.

$$\rho V c_p \frac{dT}{dt} = \dot{q}_{in} - \dot{q}_{out} \tag{2.10}$$

where the energy input comes from absorption of the laser:

$$\dot{q}_{in} = \alpha P \frac{A_c}{A_{beam}} \tag{2.11}$$

and the rate of energy loss is through collisions with the gas:

$$\dot{q}_{out} = \left(\frac{Nuk_G}{d_p}\right) A_p (T_{(t)} - T_{amb}) \tag{2.12}$$

In these equations, ρ, V, c_p, A_c, A_p, d_p and T are all properties of the particle, and correspond to the density, volume, heat capacity, cross-sectional are, surface area, diameter, and transient temperature of the particle. P and A_{beam} correspond to the power and cross-sectional area of the laser beam, and α is the material-dependent absorption coefficient at the wavelength of the laser

light. This value is not very well known for nanoparticles, and is likely in the range of 0.02-0.1 for aluminum.[7] T_{amb} and k_G are the temperature and thermal conductivity of air at 300 K, and assumed to be constant. The Nusselt number was assumed to be 0.15, estimated using the predictions in Filippov.[6] The radiation term in this case was ignored for simplicity, as its contribution was found to be relatively insignificant at low temperatures. These equations are solved numerically in MATLAB using a time step of 1 ns. The iterations stop when a steady state value of temperature is reached, reported as T_{max}. This temperature is listed in Table 2.6 as a function of various parameters, including laser power, absorption coefficient, and pressure.

Table 2.6 Parametric study of the maximum temperature achieved by a 100 nm Al particle continuously heated by a CO_2 laser. The absorption coefficient is not well known for Al, but is likely in the range of 0.02-0.1.

Laser Power (W)	α	Beam Diameter (mm)	Tmax @ 1 atm (K)	Tmax @ 0.1 atm (K)
100	1	3	392	555
100	1	1	1123	2451
100	1	0.5	3405	5565
100	0.1	3	309	326
100	0.1	1	383	530
100	0.1	0.5	630	1211
100	0.01	3	301	303
100	0.01	1	308	323
100	0.01	0.5	333	392
1000	1	3	1214	2651
1000	1	1	6276	7837
1000	1	0.5	>10000	>10000
1000	0.1	3	392	580
1000	0.1	1	1123	2632
1000	0.1	0.5	3405	5565
1000	0.01	3	309	326
1000	0.01	1	383	530
1000	0.01	0.5	630	1211

The results indicate that a very high powered and focused laser must be used in order to heat the aluminum up to 1000 K. While a 1000 W laser focused down to a millimeter is not an

unrealistic scenario, the temperature achieved would be highly dependent on the unknown absorption coefficient, and thus it was unclear whether this setup could achieve ignition.

Laser heating is just one example of how the heat transfer timescale can be useful in making research decisions. In the context of this work, the discussion of heat transfer often occurs when talking about the burning mechanism of aluminum. If the energy liberated during the reaction occurs at a rate faster than the energy dissipated by heat losses, then the particle can heat up to its boiling point, something that is seen for large aluminum particles. However, if this is not the case, then the particle will have difficulty rising in temperature above the ambient temperature, and thus lead to a very different mechanism, speculated to involve heterogeneous surface reactions. The transition in burning mechanisms is seen to occur somewhere around 10 μm for aluminum.[8]

In the context of superheating particles above the ambient temperature during combustion, having fast heat transfer timescales is a disadvantage for nanoparticles. However, there are other scenarios where fast heat transfer is beneficial. Two examples where this is the case are self-propagating reactions, and nanoparticles added to explosives. In both cases, rapid heating serves to ignite particles on fast timescales, thus minimizing any ignition delay associated with heating. Later in this work (Chapter 5), we discuss the addition of nano-sized boron to an Al/CuO nanocomposite. In this study, we modeled the heating time and argued that rapid heating of the boron to its ignition point was allowing the boron to participate in the combustion.

2.2.2.1 Radiation Contribution

In the example of laser heating presented earlier, it was suggested that radiation can generally be ignored. It should be noted that this assumption will ultimately be system-

dependent, and is something which should always be considered before justifying ignoring radiation heat losses. Several times in this work, we use heating models to calculate the time it takes to heat a particle from room temperature to some maximum temperature. The calculation is always checked with and without the radiation term to determine whether its contribution is significant. The radiation term is expressed as:

$$\dot{q}_{rad} = \varepsilon\sigma_B A_p({T_p}^4 - {T_{inf}}^4) \tag{2.13}$$

where ε is the material-dependent emissivity, σ_B is the Stefan-Boltzmann constant, A_P is the surface area of the particle, T_p is the particle temperature, and T_{inf} is the temperature far from the particle.

The radiation term can become quite significant if the temperature is high. However, for all the heating calculations in this work, the radiation term was insignificant. As an example, and as will be discussed in more details in Chapter 5, we modeled the time it takes to heat nano-sized boron from room temperature to the ambient temperature. For this calculation, we assumed the particle was a blackbody with an emissivity of 1. At an ambient temperature of 2400 K, a 100 nm particle of boron heats to the surrounding temperature in 18.5 μs, whereas it takes 16.6 μs without the radiation term, approximately a 10 % difference in time. In most of the calculations, the uncertainty is even smaller than this, and 10 % can be taken as an approximate value for the maximum uncertainty of the heating calculations presented in this work if radiation has been ignored.

One case where caution must particularly be made in ignoring radiation is if the temperature gradient between the particle and the surrounding is small. If this is true, then the relative contribution of the convective term is lowered, and radiation becomes increasingly important. It has been mentioned that nanoparticles have difficulty superheating above the

ambient during combustion. In this example, there may be only a small temperature difference between the particle and the surroundings, and thus radiation heat losses may far exceed convective heat losses. Throughout most of this work, however, calculations were made to estimate the time to heat particles up to a particular temperature. In all of our calculations, there exists a relatively strong thermal gradient ($\Delta T > 100$ K), and thus the convective term generally contributes much more than the radiation term.

2.2.3 Sintering/Coalescence

Another important process which can occur at fast timescales is the sintering/coalescence of particles. Predicting if, how, and to what extent particles will do this requires detailed knowledge of the material properties within the system. The fundamental reason any particle sinters or coalesces is to minimize its free energy. The kinetic timescale of the sintering event is of particular relevance in the current work (see Chapter 7). In predicting the timescale of two particles fusing into a single particle, two different mechanisms are considered;

1) Solid grain boundary diffusion
2) Viscous diffusion if the particles melt

The equations for both of these timescales were taken from Mukherjee,[9] and more details of the calculations along with the original references can be found in that work.

Below the melting temperature, the timescale can be expressed in terms of thermodynamic properties and the grain boundary diffusion coefficient:

$$\tau_f = \frac{3k_B T_p N}{64\pi\sigma_s D_{eff}} \quad \text{, where } D_{eff} = D_{GB}\left(\frac{\delta}{d_{P(small)}}\right) \tag{2.14}$$

where D_{GB} has the Arrhenius form:

$$D_{GB} = A\exp(-B/T_p) \tag{2.15}$$

In these equations, k_B is Boltzmann's constant, T_P is the particle temperature, N is the number of atoms in the particle, σ_s is the surface tension of the solid, D_{eff} is the effective diffusion coefficient. D_{eff} is a function of the grain boundary width δ, smallest particle which can undergo the process, $d_{p(small)}$, and the grain boundary diffusion coefficient, D_{GB}, which has an Arrhenius pre-exponential factor A and activation energy B.

Above the melting temperature, the characteristic fusion time is predicted using a viscous flow mechanism as:

$$\tau_f = \frac{\mu d_{eff}}{2\sigma_l} \tag{2.16}$$

In this case, μ is the viscosity of the liquid, and can be calculated as a function of temperature through empirical relationships. σ_l is the surface tension of the liquid. Values for pure aluminum were looked up, and the characteristic fusion time was calculated for various sizes of aluminum, below and above the melting temperature (933 K). The results are shown on a log/log plot as Figure 2.3. Also included is a generous range of burning times measured for aluminum particles as a comparison.

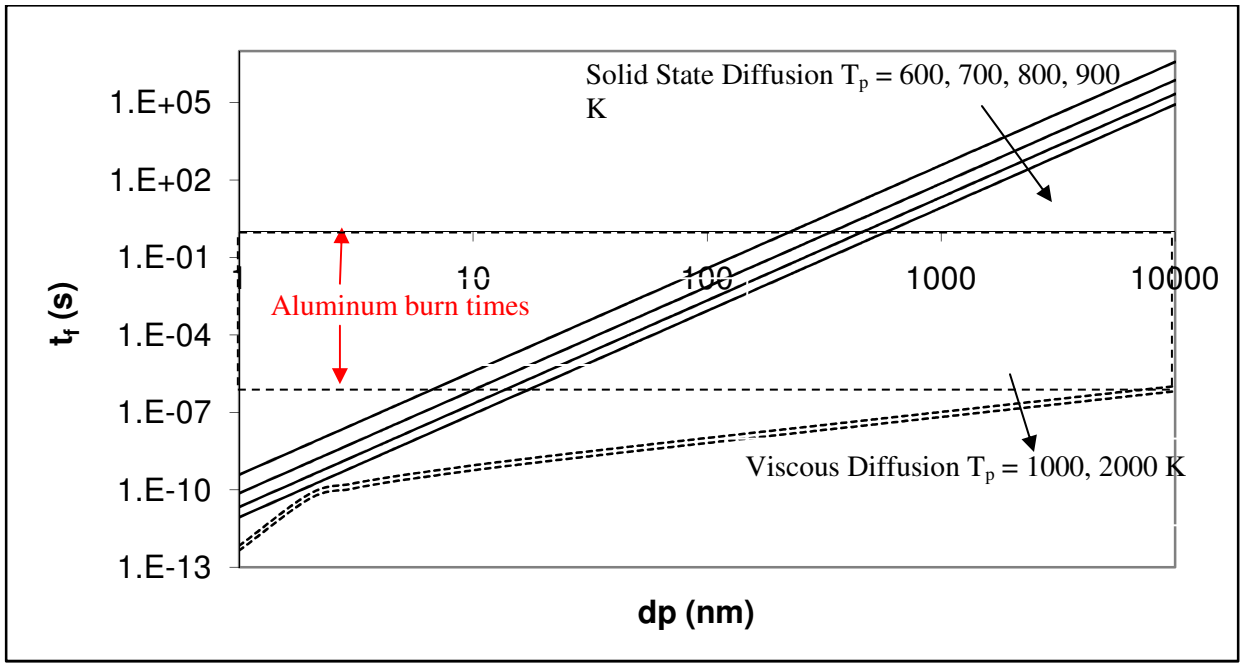

Figure 2.3 Characteristic fusion time of spherical aluminum particles as a function of the diameter and temperature. Below the melting temperature (933 K), a solid state diffusion mechanism is assumed, while above a viscous flow mechanism is used. A wide range of burning times is included as a reference.

What can be seen from these calculations is that above the melting temperature, sintering times become very fast. Even below the melting temperature the solid state diffusion processes can occur on comparable, and maybe faster, timescales as combustion. This result may prove to be particularly important in combusting aggregated nanoparticles. If the timescale of combustion is much faster than the characteristic fusion time, the particles should maintain their initial morphology during the burning. However, if the fusion time is much faster, then large aggregated shapes could very quickly fuse into a single spherical particle early in the burning, and thus the initial morphology is completely changed. These ideas will be one of the major conclusions in Chapter 7, where a large amount of sintering was observed to occur early during the reaction.

Chapter 3: Review of Relevant Literature

This chapter reviews the relevant literature on the ignition and combustion of nanocomposite thermites, and also discusses some other practical systems relevant to the current work. First, some key considerations for nanoaluminum are presented, along with some of the challenges associated with understanding its mechanism in section 3.1. Next, the problem is built up in terms of complexity. The ignition and combustion of nanoaluminum in a gaseous environment is first outlined in section 3.2, followed by the ignition and combustion of nanocomposites in 3.3. In a truly self-propagating reaction, the heating rate is system dependent, but is speculated to be anywhere from 10^4 K/s[10] to greater than 10^8 K/s (an ad-hoc calculation assuming the particles reach a temperature of ~1000 K within 10 μs, a typical value for the rise time of the pressure signal measured during the burning). One issue which will be discussed is that various experimental techniques employ dramatically different heating rates and/or uniformities in heating. This has been a significant problem in trying to sort through and interpret the results between authors. For this reason, each section is broken down into more specific subsections based on the type of experimental technique (and thus heating rate) used. In section 3.4, a diffusion vs a melt-dispersion mechanism is discussed, for it is currently an ongoing debate which will be referred to in the context of the current work.

After the review on mechanistic considerations is complete, section 3.5 describes the motivation for using nanoboron, and provides some key differences in its mechanism compared to aluminum. Section 3.6 discusses the motivation and design of anti-microbial energetic, or biocides. These systems are a relatively new concept, and present a new application for MICs; a system designed to exhibit explosive characteristics while generating species which can continue

antimicrobial activity long after the reaction is over. Finally, some review on particle sintering is presented in section 3.7.

3.1 Nanoaluminum

This section outlines some of the more general ideas surrounding the use of nanoaluminum for energetic applications. Direct comparisons to micron-sized aluminum are made to address some of the key concepts relevant to this work. This section starts by describing the physical core-shell structure formed naturally by aluminum, followed by some works on coating aluminum with different passivation layers. The idea of nanoaluminum being a small thermal load with fast heat transfer is introduced, along with the implications in terms of the combustion mechanism. Finally, some methods on mixing and characterizing nanoparticles and nanocomposites are discussed.

3.1.1 The Oxide Shell

Metal particles always partially oxidize when exposed to air and form an oxide shell. In aluminum, the shell is amorphous[11, 12] with a thickness between 0.5 nm[13] and 4 nm,[14] but most commonly accepted as being 2-3nm.[15] If the particle sizes are micrometers, this represents an insignificant amount of the total particle mass. However, as the particle size becomes smaller, this oxide shell can become very significant, sometimes being over 60% of the total mass[16] if the particle size is small enough. One thing which is generally agreed upon in the literature is that understanding the interaction of the core and shell during thermal heating is critical to understanding the ignition mechanism of nano-sized aluminum. Since aluminum has a much lower melting temperature (933 K) than its oxide shell (2327 K), it will melt first upon being heated. The melting leads to a volumetric expansion (~6%), and as a result can induce stresses

on the solid oxide shell. The Al_2O_3 shell is often considered "dead weight" in that it is inert and reduces the amount of available metal in the fuel.

3.1.2 Alternate Coatings

A few works have emerged which investigate the coating of aluminum with other materials in place of the oxide shell. Transition metals such as nickel,[17, 18] gold, silver and palladium[17] have been successfully coated on the surface of aluminum, along with carbon.[19] Jouet et al.[20, 21] investigate the use of perfluoroalkyl carboxylic acids with the idea that the aluminum can react with the fluorine in the shell's coating, thereby leaving no dead weight. Though the coatings have been shown to prevent the formation of Al_2O_3, most experimental works use aluminum particles which contain the oxide shell, since the production of sizable quantities of coated particles is in a rudimentary stage of development.

3.1.3 Heat Transfer and Deviation From D^2 Law

Another major difference between nano and micron particles is that a nanoparticle is a significantly smaller thermal load than a large particle, and the surface to volume ratio greatly enhances the heat transfer to and from the particles. This means that a nanoparticle can very rapidly be heated to the gas temperature, but it also implies that heat losses may prevent it from superheating above the gas temperature, unless the pressure is low enough. Therefore, nanoparticles burning in a gas will essentially burn at the gas temperature. This has led to the need for a new conceptual model for nanoparticle combustion, and it is generally accepted that heterogeneous surface reactions are important.

The combustion of large particles (>10 μm) can be described quite nicely by a droplet burning model, and a "D^n" law can be used to predict the droplet burning time based on the

diameter. If the particle behaves exactly like a liquid droplet, the value of the exponent is 2,[22] while experiments have shown it to be range of 1.5-1.8 for aluminum.[23] (The reduction is explained by the formation of an "oxide cap" which slightly lowers the value of the exponent).[24] A D^2 burning mechanism involves a lifted diffusion flame where the fuel evaporates from the particle surface and is met by incoming oxidizer at some distance away from the particle surface. The flame is therefore separated from the particle, and is a very thin region of intense chemical reaction which conducts heat back to the particle and further drives the evaporation until the mass is consumed. In order to burn by this mechanism, the flame temperature must exceed the fuel's boiling point, and thus conducts heat back to the particle and drives the evaporation. According to Glassman's criterion,[25] aluminum will combust by this mechanism because its flame temperature is near the boiling point of Al_2O_3 (~4073 K), higher than the boiling point of aluminum (2740 K). A material such as boron will behave differently, and this will be discussed in section 3.5.

Nanoparticles, on the other hand, are small thermal loads with much faster heat transfer, and are inherently difficult to heat above the ambient temperature. The current speculation is that the mechanism for nanoparticle combustion involves heterogeneous surface reactions with the flame sitting much closer to, or on, the particle surface. The burning lifetime in this case would follow a "D^1" law at best, indicative of a reaction mechanism limited by surface kinetics instead of diffusion of oxidizers. A recent experiment by Bayzn et al.[26] examines this in more detail, and suggests the transition begins at 10 μm at a pressure of 8.5 atm for aluminum. Furthermore, the authors measure the flame temperature by three-color pyrometry and report it to be very close to the boiling point of aluminum. This is a much lower temperature than what is

measured in the lifted off diffusion flame for large particles burning, and supports the speculation that heterogeneous surface reactions control the burning for nanoparticles.

3.1.4 Synthesis and Characterization

There currently is really no consensus on the proper way to report the physical dimensions of nanoparticles, and this can complicate how to analyze and report experimental results. Nanoparticles have been successfully synthesized by various techniques, including the electro-explosion of a heated wire,[27-33] flame synthesis,[34-39] thermal decomposition of a precursor,[17, 21, 36] and evaporation/condensation[19, 40-49] of bulk materials. Evaporation by a pulsed laser or arc discharge[19, 44, 48] are techniques used by our research group for small-scale production of pristine metal particles. In all of these techniques, nanoparticles are often agglomerates of finer "primary" particles, and have a distribution of sizes making it unclear as to what is the best way to measure the particle dimensions. If the morphologies are such that the particles are not spherical, then a further complication to measure an appropriate size is introduced.

High resolution microscopy (TEM or SEM) is perhaps the best technique to characterize particles, but is a costly and time-consuming method that requires a large number of samples in order to make an appropriate determination of the average properties of the particles. Therefore, other characterization methods are used to measure average particle properties. A common method to do this is Brauner-Emmett-Teller[50-52] (BET), a technique which utilizes gas adsorption to measure the average surface area, an important parameter in reactivity studies. The other advantage of reporting the surface area is that morphology isn't so much an issue, for example if the synthesized particles are rods or wires[53, 54] instead of spheres. Recent progress has been

made to measure size information by small angle neutron or x-ray scattering[55-57] (SANS/SAXS). Borchert et al.[55] show a comparison between particle sizes measured by TEM, XRD, and SAXS. Another recent technique[58] measures the size distributions using Thermogravimetric Analysis (TGA) by assuming a model of uniform oxidation from the exterior to the interior of the particle. The authors claim this technique to be useful for powders with a broad size distribution, and to measure traces of very large particles (500-5000 nm) within the mixture of fine nanoparticles.

A technique used by our group is to use a differential mobility analyzer (DMA) coupled with a condensation particle counter (CPC) in a system called a scanning mobility particle sizer (SMPS). This technique works by electrically charging an aerosol, (i.e. Al nanoparticles carried by Argon) and then passing the particles into a region with an applied voltage which creates an electric field. The electric force drags the particles inwards, and their motion is balanced by a drag force. There is a one-to-one correlation between the voltage and the size of a particle which can successfully make it into a small exit slit. If the outlet is connected to an instrument designed to measure the concentration (a CPC), the concentration can be recorded for a given voltage/particle size, and the measurement can then be repeated with a different voltage to construct a size distribution. The "size" reported in this technique is the same as the diameter of a spherical particle which experiences an equal drag force, and so it essentially separates particles by their surface area. This technique has been used in a few works[19, 44, 48] by our group to select and study the oxidation of aerosolized aluminum particles with known sizes.

3.2 Ignition and Reactivity Experiments of Nanoaluminum

This section describes the ignition and combustion of nanoaluminum in an oxidizing gas. As mentioned previously, in "real" combusting systems involving metals or composites, the particles will be subject to environments where the heating rates are on the order of 10^6 K/s.

Designing a controlled experiment which can uniformly heat the sample with such a high heating rate is a critical challenge in the research community. Many experimental techniques have been employed to study the ignition and combustion of metals and metal composites using a wide range of heating rates. Each of the following sections is subdivided based on the experimental technique used.

3.2.1 Ignition of Nanoaluminum in a Gaseous Oxidizing Environment

Ignition is described as the temperature where the chemical reaction generates enough heat to overcome losses, and thus the particle combustion becomes self-sustaining. The ignition delay is the time it takes the particle to ignite after exposure to heating. For metals, long ignition delays are due to relatively slow heterogeneous reactions leading up to the self-sustained combustion.[15, 59-61] Trunov et al.[62] offer a brief review of experimental studies on aluminum ignition. A compilation of the results from their paper is included here as Figure 3.1, and does not include the various heating rates used. An important feature to note is that the ignition temperature for aluminum is very different as a function of particle size; i.e. it's near the melting point of Al_2O_3 (2327 K) for large particles and much closer to the melting point of aluminum (933 K) for small particles. Very few studies examine the ignition temperature of nanoaluminum at high heating rates. Those that do generally report the temperature of the environment in which signs of ignition, i.e. optical emission, are seen to occur.[63] That being said, it's generally accepted and experimentally verified that ignition in aluminum can occur near the melting point of Al below a critical size.

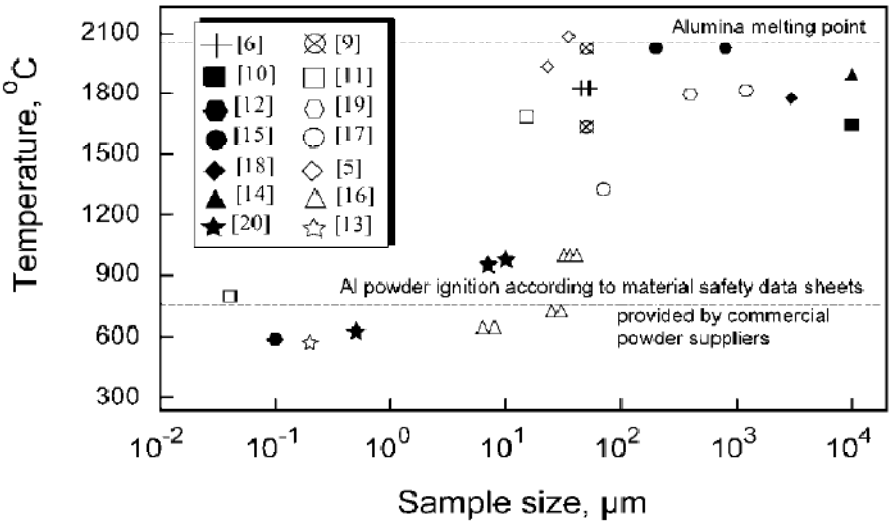

Figure 3.1 Figure 5 from Trunov et al.[62] compiling measured ignition temperatures for nanoaluminum in air, and as a function of particle size.

3.2.2 Reactivity of Nanoaluminum in a Gaseous Oxidizing Environment

3.2.2.1 Thermal Analysis

The most commonly used technique which has been used to study nanoparticle oxidation in a gaseous environment is thermal analysis, which uses a combination of Thermogravimetric Analysis (TGA), Differential Scanning Calorimetry (DSC), and Dynamic Thermal Analysis (DTA). In some cases, X-Ray Diffraction (XRD) can be used to investigate phase changes leading up to ignition. Thermal analysis subjects the particles to a very slow temperature ramp and examines kinetic behavior by monitoring the mass gain/loss (TGA) and heat flow to and from the sample (DSC/DTA). Diffraction patterns (XRD) can be used along the way to monitor the formation and disappearance of crystalline phases within the sample, and speculate on the reaction mechanism. This technique has been used by several authors[15, 57, 58, 64-66] and allows for uniform sample heating and a detailed understanding of phase transformations within the

material. Trunov et al.[15, 57, 61] use their results to write the ignition and oxidation of both micron and nano aluminum as a mechanism which occurs in four distinct stages.

During Stage I, the natural amorphous oxide shell grows in thickness to a critical value of about 5 nm, where the oxide-metal interface stabilizes the amorphous oxide at low temperatures.[11, 12] Stage II is then initiated, where the shell is transformed into γ-Al_2O_3, which has a higher density than the amorphous Al_2O_3.[67] The smallest crystallites of γ-Al_2O_3 are around 5 nm,[68] and so the transformation to a denser material can perturb the continuous shell and expose some of the core aluminum. During Stage III, the γ-Al_2O_3 grows in thickness and can form other crystalline phases, such as δ and θ Al_2O_3. Stage IV is achieved when all of the oxide has transformed into α-Al_2O_3 and the shell grows in thickness. The oxidation with such a mechanism is described as a diffusion mechanism through the grain boundaries, and the authors suggest that one difference between nano and micron aluminum is that the healing of the oxide shell can occur in micron aluminum but not in nanoaluminum, hence the very different ignition temperatures and combustion mechanisms between the two. A schematic of the authors' mechanism is provided below as Figure 3.2.

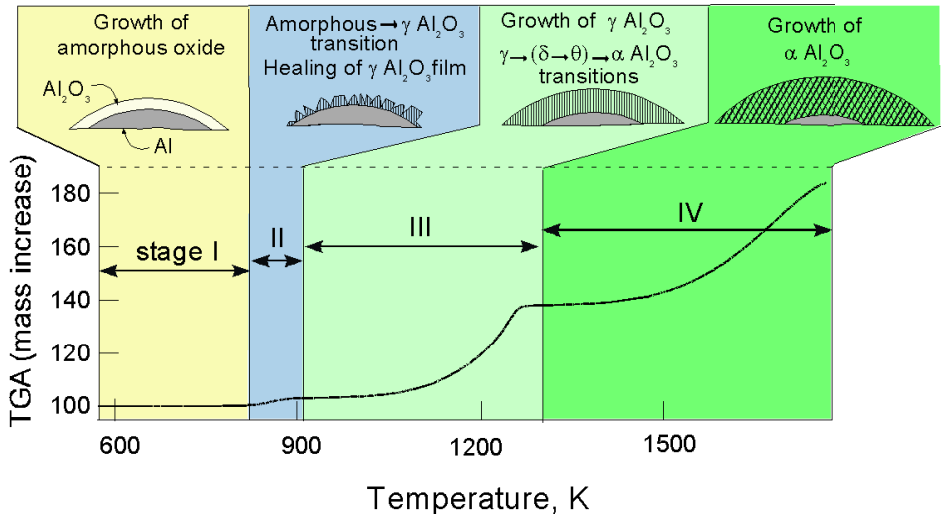

Figure 3.2 Ignition and combustion model for aluminum suggested by Trunov et al.[15, 57, 61]

3.2.2.2 Oxidation in a Furnace

One major drawback of using thermal analysis to study ignition and combustion of nanoparticles is that the heating rate is only a few degrees per minute. The particles are given time to equilibrate and change phases, processes which may happen on long timescales relative to reaction and heat transfer times. It's unclear whether nanoaluminum would behave the same if heated with a much faster heating rate. Therefore, nanoaluminum oxidation in a gaseous environment was addressed in recent efforts by our group.[44, 48, 69] Aerosolized particles of aluminum were passed into a furnace with air and heated to different temperatures. The particles were analyzed online by a single particle mass spectrometer capable of determining the atomic ratio of aluminum and oxygen.[70] The size and density changes of the particles were also monitored using aerosol mobility classifiers, and the particles were collected and viewed in a TEM to examine the morphology.

These experiments led to some very interesting observations. First, below 1273 K, the oxidation could be described by a "shrinking core" model, where gaseous oxidizer diffuses

through the solid Al_2O_3 shell and reacts with aluminum at the Al/Al_2O_3 interface. Second, TEM showed that the aluminum leaked out above 1273 K, verified by the existence of a hollow Al_2O_3 shell in the product, and indicating that the outward diffusion of aluminum was occurring above this temperature.[48] The authors proposed that aluminum nanoparticle oxidation occurs in two regimes; a slow regime below the melting temperature of aluminum and dominated by inward diffusion of oxygen, and a fast regime above the melting of aluminum and dominated by the outward diffusion of aluminum. The only real drawback of this experiment is that the particles are still subject to a relatively slow heating ramp, on the order of 10^3 K/s. Although the heating is orders of magnitude faster than thermal analysis, it is still not in the range of practical applications (10^6-10^7 K/s). Despite this drawback, this work provided valuable evidence to bridge the gap between slow and fast eating rates, and also showed that the results can be very different depending on the heating rate used.

3.2.2.2 Oxidation Using a Shock Tube

A shock tube is one of the few experimental techniques which achieves high heating rates (~10^6 K/s). Combustion experiments of nanoaluminum in a gaseous environment were performed behind reflected shock waves in a shock tube.[71, 72] In this work, the authors used optical broadband emission to monitor the burning time. Different oxidizing environments were used to study the combustion in oxygen and carbon dioxide at variable pressures and temperatures. The particle temperature was measured using 3-color pyrometry, and the highest temperatures achieved were, not surprisingly, for the highest temperature (2000 K), highest pressure (32 atm) and highest O_2 mole fractions (50%). In this case, the particle temperature was measured to be 3500 K. (It's interesting to note that this temperature is still several hundred degrees lower than the flame temperature of micron aluminum.) This experiment offers the

ability to heat the particles with very high heating rates, and also with a well-controlled environment and time, calculated using shock theory. However, there are a couple of limitations to this work. First, the particles are dispersed by the incoming shockwave, and this can perhaps lead to the partial damaging of the oxide shell. The second drawback is that the only measurement of combustion is an optical measurement. This will be biased to the more massive particles in the system, as the emission intensity scales with mass. Despite these drawbacks, this experimental technique offers an excellent way to measure the combustion of a dispersed cloud of particles in a gaseous environment and subject to practical heating rates.

3.3 Ignition and Reactivity Experiments for Nanoaluminum Composites

Studying the ignition and combustion of composite materials is a much more daunting task. As mentioned in the introduction, the underlying idea of composite materials is to closely pack the fuel and oxidizer particles to decrease their characteristic mass diffusion lengths and increase the reactivity. Upon ignition, the flame becomes self-propagating and thus the mode of energy propagation through the powder also becomes important. Therefore, in order to understand the intrinsic ignition and reaction in the composite, it's most appropriate to use experimental techniques which can reproduce the self-heating environment achieved in a propagating reaction. A rough estimate of this heating rate is system-dependent and has been speculated to be anywhere from 10^4-10^8 K/s. Recreating an environment which uniformly heats the particles at such a high heating rate is a critical challenge. To make this even more difficult, the flame velocity and gas production can vary by orders of magnitude from system to system, along with the fact that particles have a distribution of sizes and shapes and batch to batch variations can occur. The following section outlines the relevant work on nanocomposite thermites, and again is subdivided based on heating rate.

3.3.1 Ignition Experiments for Nanocomposite Materials

3.3.1.1 Thermal Analysis

The key advantage of thermal analysis is that it is able to heat the sample uniformly, and the onset of oxidation can be clearly seen by very sensitive heat flow measurements (DSC/DTA). However, a very slow heating rate is used and one must use caution in reporting appropriate ignition temperatures. Differential scanning calorimetry (DSC) was used to study Al/CuO composites by Umbrajkar et al.[73] and Al/MoO_3 composites by Schoenitz et al.[74] The authors report the ignition temperature to range between 600 and 900 K. The authors also vary the heating rate, and use a model to extrapolate to high heating rates and compare with heated filament data. In the heated filament data (discussed later) for Al/MoO_3, the authors report the ignition to occur at higher temperatures, ~950 K at a heating rate of 282 K/s, and around 1025 K using a higher heating rate of 4024 K/s. The authors conclude that the ignition is primarily controlled by oxygen diffusion into Al_2O_3.

3.3.1.2 Laser Ignition

Lasers offer the advantage of high and easily-adjustable heating rates. Lasers have been used to study the ignition of condensed materials with heating rates on the order of 10^6-10^7 K/s by several authors.[75-80] In other works,[81-84] heating rates in excess of 10^9 K/s were used. Analyzing the results at such high heating rates must be done with caution, for it may not necessarily mimic the ignition of a particle at a lower heating rate. One relevant work to the current topic is that Granier et al.[16] investigate the ignition of pressed pellet of aluminum with molybdenum trioxide (Al/MoO_3) as a function of particle size and stoichiometry. The authors heat the sample with a 50 W CO_2 laser, and use a high speed camera and thermocouples to

record the ignition behavior of the sample. One problem with laser heating a pressed sample is that various particles will absorb the laser light differently, causing them to heat at very different rates. Also, a pressed pellet is a relatively large mass, and therefore will be subject to conductive heat transfer which is nearly impossible to quantify without careful thermal diffusivity measurements of a packed bed of various particle sizes with voids. The authors report ignition temperatures of around 400 K, well below that measured by any other experiment and perhaps a result of the experimental methods employed in this work.

3.3.1.3 Shock Tube

In a study by Bazyn et al.,[63] the ignition of nanocomposites of Al/Fe_2O_3 and Al/MoO_3 in the region behind a reflected shock in a shock tube was investigated. The sample is placed near the end of the tube, where an incoming shock wave lifts and disperses it. The shock wave then reflects off the wall and rapidly heats the particles to ignite and combust them. The ignition is said to occur when the onset of optical emission can be measured. The authors performed the study in both an inert and oxidizing environment. Both materials showed extremely rapid ignition compared to large particles, and the ignition temperature was found to be 1400 and 1800 K for the Fe_2O_3 and MoO_3, respectively. This temperature is significantly higher than what is observed from thermal analysis, and is well above the aluminum melting point (933 K).

3.3.1.4 Heated Filament

A relatively new technique to study the ignition of nanocomposite materials is to place the sample on an ultra-thin platinum filament or wire. A tunable voltage pulse is then used to heat the wire through resistive heating, and between 10^2 and 10^5 K/s. The ignition can also be measured, and is typically quantified as the point when a rise in optical emission is observed.

This sort of analysis is excellent in that a relatively small amount of sample is needed, thus minimizing interparticle or bulk effects. Also, it heats the sample uniformly and with a range of known heating rates. This technique has been used by a few authors,[73, 85-88] and we have developed one of these setups within our group. The ignition temperature generally increases with heating rate, and is typically in the ballpark or slightly above the melting temperature of aluminum. Typical ignition temperatures of nanoaluminum in gas, both published and unpublished, are in the range of 900-1200 K as measured by this technique, and results generally show an increase in the ignition temperature with increasing heating rates.

3.3.2 Reactivity of Nanocomposite Materials

3.3.2.1 Thermal Analysis

A combination of differential scanning calorimetry (DSC) and x-ray diffraction (XRD) can be used to study composite systems. A DSC measurement reports at what temperature endotherms and exotherms occur, and therefore monitors phase changes and reactions. Furthermore, the area under an exotherm can show the heat release, another important piece of information when analyzing the results. XRD gives information about crystalline phase changes, and can be used with the DSC measurement to speculate on the reaction mechanism. This technique has been used to study Al/CuO reactions by Umbrajkar et al.,[73] and Al/MoO_3 reactions by Schoenitz et al.[74] One must be careful in using low heating techniques, due to the rapid heat transfer characteristic in nanoparticles. Even if the reaction is initiated, it can rapidly be quenched, thus making interpretation of the results challenging when trying to predict a mechanism which predominantly occurs at high-heating rates.

3.3.2.2 Shock Tube

Bazyn et al.[63] studied the combustion of Al/Fe_2O_3 and Al/MoO_3 in a reflected shock region in a shock tube. The authors used optical signals to measure burn time, and also used 3-color high speed pyrometry to track the flame temperature. The measured flame temperature was between 2700 and 3350 K in an inert environment, with MoO_3 having a higher temperature than Fe_2O_3. When oxygen was introduced, the flame temperature rose to 3350-3800 K, indicating that heterogeneous reactions can play a role if the particles are combusted in an oxidizing environment. It's interesting to point out that the combustion temperatures in an inert environment are very close to the adiabatic flame temperature of the samples. It's also important to point out that they are well below the ~4000 K temperature that large aluminum particles burn at with a lifted off diffusion flame (Except when gaseous O_2 was added).

3.3.2.3 Flame Velocity and Pressurization Rate

Perhaps the most common method to study the reaction of nanocomposites is to ignite the powder and measure the flame velocity and/or the pressurization rate. Both are a relative measurements, and have been found to correlate with each other.[89] The flame velocity has been measured by unique techniques such as the electric conductivity,[90] but the most common technique is to image the flame with a high speed camera or photodiodes spaced a known distance apart. This has been performed for various configurations of the sample, including burning in an open channel,[51, 91-96] burning in microchannels,[97] and burning in a cylindrical tube.[98-100] Time-resolved optical emission can be monitored to determine the kinetics of the reaction[92, 93], and pressure sensors can be used to collect simultaneous pressure data as the reaction propagates past a transducer.[98, 100] Knowledge of the emission and pressure rise, along

with burning velocities can provide some valuable insight as to the reaction mechanism during the self-propagating reaction.

The other experimental technique used to study the reactions of composite materials is to combust a fixed mass in a constant-volume chamber and record the dynamic pressurization. Many different vessels have been used, including large vessels,[96] small vessels,[52, 101, 102] and standard vessels for oxygen bomb calorimetry.[50, 103] In these experiments, the flame temperature is speculated to be nearly adiabatic as a result of the very slow heat transfer time to the walls relative to the reaction time scale. Therefore, the pressure increase can in some way be correlated to the energy produced during the combustion.[103]

As mentioned before, the reaction in MICs is a self-propagating process. That is, the energy generated during the combustion is being transferred to the subsequent layer to ignite it. There are four possible mechanisms for energy propagation; conduction, convection, radiation, and acoustic/compaction. Acoustic/compaction is generally only important for detonations, and is speculated to not be important in MIC formulations where detonations are not achieved.[104] Radiation heat transfer has been shown to be possible (and will strongly depend on the conditions and temperatures achieved), but is a relatively small contribution compared to convection,[105] and thus is often not considered to be significant. Asay et al.[104] investigated the remaining modes of energy transfer, and found convection to be the dominant mechanism. This was further corroborated by Bockmon et al.[99] One implication of convection being important is that, unlike conventional explosives, increasing the packing density can actually slow down the flame velocity.[98] The current speculation is that increasing the density hinders convective heat transfer by packing the particles closer together.

Asay et al.[104] combusted an Al/MoO_3 sample in a burn tube at atmospheric pressure and under vacuum, but report no measurable difference in flame velocity. Therefore, the interstitial air does not appear to play a role in the energy propagation. The current speculation is that hot gaseous species form during the reaction which can transfer energy and ignite the unreacted fuel, and this mode of energy propagation can be compared with convective detonation,[98] which has been modeled in a porous media by Ershov et al.[106, 107] The importance of gas production has been observed by several authors. First, the optimum reactivity often occurs at off-stoichiometric conditions.[16, 99, 108] Sanders et al.[98] investigated this for four metal oxides, and used thermodynamic equilibrium calculations to show that the optimum reactivity does not typically correspond to the stoichiometry which predicts the highest temperature, but instead to the mixture which produces the most product gas. The hot gaseous species transfer energy via convection, and species such as Bi, Mo, and Cu may even condense on the unreacted particles and greatly enhance the energy transfer.[97]

3.4 Diffusion vs Melt Dispersion Mechanism

In a self-propagating flame, the particles will be self-heated with high heating rates, but there are several other processes occurring which make it difficult to isolate the intrinsic ignition and combustion behavior of the constituent particles during the burning. This problem is currently being addressed as experimental techniques such as a heated filament and shock tube are being modified and improved. In the meantime, there is some speculation of how a nano-aluminum particle will mechanically respond when rapidly heated. As discussed, aluminum has a thin oxide shell which melts at a much higher temperature than the core. Two schools of thought have prevailed in the literature. The first is termed the "Melt Dispersion Mechanism,"[109-111] and claims that upon rapid melting, the volumetric expansion of the core induces significant stresses

on the oxide shell, causing it to rupture. The rupturing creates a tensile stress on the molten core which unloads the aluminum as small molten clusters, and with high velocities.

The second school of thought is generally referred to as a "Diffusion Mechanism."[15, 48, 112, 113] In this case, the aluminum melts and expands, causing some stress the shell and the diffusion of Al outwards. Just how the aluminum migrates through the shell is not specifically known; it could either diffuse through a permeable polymorph of Al_2O_3, or the shell could crack/break down via thermal tresses, producing some conduits for the aluminum to escape. Also, an electric field can arise near the Al/Al_2O_3 interface due to local Al^+ concentrations through the shell, and this could play an important role in facilitating the outwards diffusion of aluminum.[112] This debate can only be resolved through the further development of experimental techniques capable of rapid and uniform heating. Understanding this ignition step in the mechanism is of critical importance, as it affects both nanoaluminum and nanocomposites, and will determine the subsequent combustion mechanism.

3.5 Combustion of Alternate Fuels - Nanoboron

An alternate fuel that has been studied in this work is boron, and thus a brief review should be given. Boron contains more energy than aluminum on both a mass and volumetric basis, however, kinetic limitations explain why it rarely achieves its full potential and thus has not replaced aluminum. Like aluminum, boron contains an oxide shell which forms around the elemental core. However, there is a critical difference between aluminum and boron: in aluminum, the core melts at a lower temperature than the shell, while in boron the shell melts at a lower temperature than the core.

The presence of the oxide shell is speculated to slow down the kinetics of boron combustion, for it acts as a liquid barrier to oxidation if it is not removed efficiently. In fact, if oxidation occurs faster than the shell can be removed, the shell can grow in thickness and severely retard the kinetics. In the pioneering work of Macek and Semple,[114] the authors proposed that the combustion of boron always happen in two steps. The first step involves the removal of the oxide shell, and is a slow kinetic/diffusion controlled process which comprises a large amount of the overall time. The second step involves the combustion of bare boron. The appearance of this "two-step" burning has been corroborated by other authors, such as Ulas et al.[115] Recent work[115] has rejuvenated the hope for boron combustion by using fluorine-containing oxidizers. The authors reported the disappearance of the "two-step" combustion by using fluorine. Other than that, the only practical way to use boron is to combust it at temperatures above the boiling point of B_2O_3, so that the shell gets removed efficiently through the convective heat transfer from the high-temperature surroundings. However, combustion at such high temperatures would result in the formation of gaseous boron oxide products, and thus the latent heat of condensation is not released. These limitations make boron relatively impractical when compared with aluminum, however, we will discuss a practical use of nanoboron later in the results section.

3.6 Anti-Microbial Energetic Systems

Interest in neutralizing biological-based weapons has posed a challenge to the use of traditional energetic materials which produce a very short lived thermal event. It has recently been proposed that a new class of energetic material, which offers both a thermal event coupled with a long lasting biocidal character, could be useful in mitigating biological materials. What really matters then is how much biocidal agent can be produced by the energetic, along with

what chemical form it presents itself in the final product. The latter point is particularly relevant, since it is quite possible to have a biocidal product which either ends up to have a low surface area and thus minimal efficiency, or worse yet, be wrapped up within the matrix of one of the products of reaction and thus not exposed to the environment.

An ideal energetic system designed for neutralization of biological agents should possess the following characteristics.

1. High thermal release with minimal overpressure.
2. Produces a species which is effective against the biological agent, is non-toxic to humans, and also is chemically and thermally stable to keep it active for sustained periods of time.

For the thermal release component, nanocomposite thermites produce a very high energy release per unit volume or mass. Furthermore, since the products of combustion tend to be primarily in the condensed phase, some of the issues associated with high blast overpressures are minimized. For the biocidal component, a variety of materials could potentially be used. The goal in this case would be to generate a product during the reaction which would stay around and continue to destroy harmful spores at room temperature.

The highly insoluble salt, silver iodate ($AgIO_3$), has been considered recently for its potential use in thermite-based biocidal applications.[116] Silver exhibits biocidal properties in many forms.[117] Morones et al.[118] have investigated nano-sized silver, and showed it to be effective at killing bacteria, especially when the particle size was very small (<10 nm). Smetana et al.[119] also investigated the biocidal activity of several silver/silver-based samples with and without coatings and concluded that small, irregular surfaces are necessary for high biocidal activity. The authors claim that silver ions are the actual biocidal species, and having silver

oxide surfaces on the nanoparticles can serve to facilitate the transport of silver ions, and thus improve the effectiveness. Silver bromide nanoparticle/polymer composites have been reported to exhibit potent, long lasting antibacterial activity,[120] and silver iodide is used as an antiseptic.[121] Iodine is also a widely known and used biocide.[122]

3.7 Sintering of Nanoparticles and Aggregates

One other phenomenon which has received little attention in nanoparticle combustion studies and will be a topic of discussion in this work is the sintering of adjacent particles. This directly impacts the question of size dependence to reactivity, and what is the "effective" particle size of the reacting material. Commercially available nanoparticles are almost always highly agglomerated, and the size specified by a supplier oftentimes is the average size of the primary particles within these aggregates. Surface tension forces will of course drive the particles to coalesce if the temperature is sufficiently high to make the particles liquid-like.[123, 124] In a reacting thermite, nanoparticles can be heated and sintered by heat transfer from the surroundings, as well as from the energy liberated during an exothermic chemical reaction. The latter is referred to as reactive sintering, and is a phenomenon which, for example, has been shown to be important in Al/Ni reacting systems.[125, 126]

Sintering is a phenomenon which must be considered when predicting the growth dynamics of aerosols.[9] Although sintering can occur below the melting temperature, the kinetics are generally thought to be slow since they are controlled by solid-state diffusion processes. Once the particles melt, the kinetics are greatly accelerated, and the particles can sinter according to a viscous flow mechanism.[127] The particle melting temperature and viscosity must be well known, and empirical correlations have been developed for both as a function of particle size.[4, 128] In addition, sintering itself is an exothermic process, and can raise the temperature by as much

as several hundred degrees for very small particles.[124] Hawa et al.[123] used molecular dynamics simulations to predict scaling laws for aggregates of nanoparticles with various fractal natures, and found that low fractal dimension agglomerates (i.e. straight chains) took characteristically longer times to sinter than high fractal structures. All of these considerations will be important in accurately predicting particle sintering times.

Chapter 4: Experimental Techniques

This chapter outlines several experimental techniques which were used in the context of this work. When trying to fully describe a system, it is important to both physically and chemically characterize the individual components along with the mixed composite systems. The reactivity can then be measured by various experimental techniques within our research group, and particular graduate students are generally responsible for the different experimental techniques. Most of my original work was done using the constant-volume pressure cell, along with the high resolution microscopy work. However, since many other experimental techniques are useful to draw conclusions about the mechanism, all techniques relevant to this work will be presented so the reader has a broad idea of what instrumentation was used. A table at the end of this chapter (Table 4.1) summarizes all of the experimental techniques, along with the sample mass/size and what can be learned from these techniques.

4.1 Physical Characterization

4.1.1 X-Ray Diffraction (XRD)

This technique is a common method used to determine crystalline information about a sample. It works based on the fundamentals of Bragg's Law:

$$n\lambda=2d\sin(\theta) \tag{4.1}$$

where λ is the wavelength of the x-rays, d is the spacing between adjacent atoms, n is any integer, and θ is the angle that light is bent. As an oscillating electromagnetic wave passes through a small slit, the wave can be bent in certain ways. While most waves cancel out, certain directions can constructively interfere, and thus will create a pattern of bright/dark spots as a

function of angle. In the case of atomic crystals, two adjacent atoms are nothing more than a small "slit" that light must pass through. A requirement of the Bragg's Law approach is that the electromagnetic wave has a wavelength comparable to the distance of the spacing of the slit. An electron oscillates with a wavelength between 1 and 100 Angstroms depending on the energy, and thus is an ideal source for looking at atomic spacing.

The Department of Chemistry at the University of Maryland has a user shared facility with two different X-Ray Diffraction instruments. The one used in this work is a Bruker C2 Discover Diffractometer. This uses a CuKα source with a HiStarr (GADDS) detector capable of real time analysis. All samples we looked at were loose powders. After the data is collected, background subtraction is done and the resultant plot shows the intensity as a function of scattering angle (2θ). A typical plot using XRD is shown in Figure 4.1, and is Ag_2O nanopowder that was synthesized here via a wet chemical method by Dr. Chunwei Wu, and which will be discussed later.

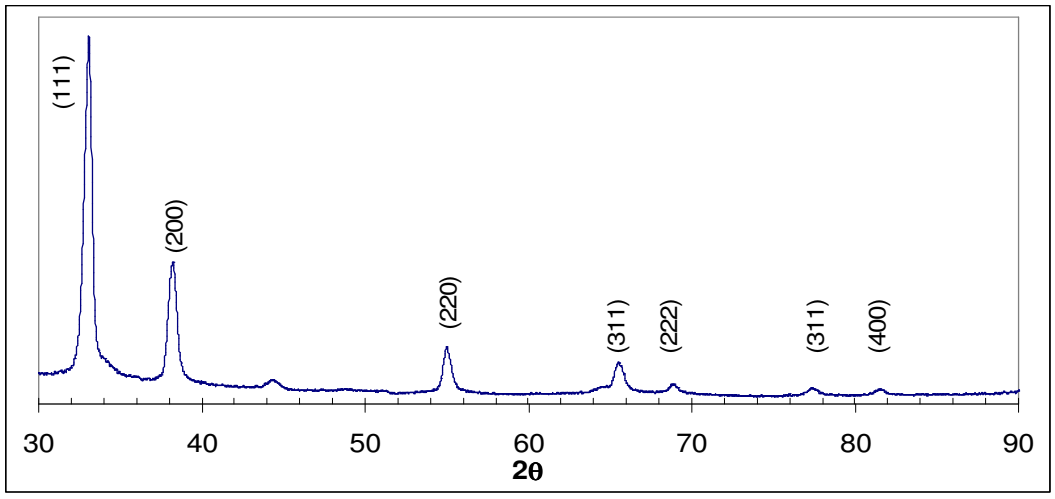

Figure 4.1 Typical XRD data showing intensity as a function of angle (2θ).

The labels in parenthesis in Figure 4.1 correspond to the various crystalline configurations possible. It is typical to have many peaks for a given species, due to the different orientations of the crystalline planes relative to the incident x-rays. It is important to note that the position of the peaks alone cannot tell the difference between species which have identical crystalline behavior. For example, if two species have a face centered cubic (FCC) structure, the peaks will be in identical positions. Further processing must be done in order to do species identification based on the peak widths.

4.1.2 X-Ray Photoelectron Spectroscopy (XPS)

This is another instrument located in the shared user facility of the Department of Chemistry at the University of Maryland. XPS is a technique useful for determining the chemical composition of a surface. It works by illuminating a sample with soft x-rays, and upon absorption of the x-rays, atoms can ionize and emit an electron with a particular kinetic energy equal to the difference in energy between the incident x-rays and the binding energy of the core electrons. Two x-ray sources are used, monochromatic Al and dual anode Al/Mg, and this particular instrument is equipped with a high sensitivity Kratos AXIS 165 spectrometer.

Due to the physics of the process, it should be noted that the beam can penetrate several nanometers into the sample. For this work, we were looking at loose powders, and these commonly can have core-shell structures with shells that are several nanometers thick. Due to simple geometric and probability considerations, the strongest signal will naturally come from the first 1-2 nm, followed by a weaker signal from the next 1-2 nm layer, and so forth. The exact dimensions and behavior will depend on the species and wavelength of the x-rays, but this concept should be kept in mind in the context of this work. This technique was used later in this

work (Section 8.2) in for investigating the reacted product of Al/Ag_2O to determine whether elemental silver was present on the surface, and an example of the data can be seen in that section.

4.1.3 Electron Microscopy

4.1.3.1 Scanning Electron Microscopy (SEM)

This technique is very useful for imaging of very small particles. SEM works by raster scanning a highly focused electron beam onto a sample, and the electron beam interacts with the surface species to emit several forms of electromagnetic waves. The sample must be conductive, or sputter coated with a thin layer of conductive material (i.e. Carbon, Palladium) if it is not. The instrument used in this work was a Hitachi Su-70 Ultra High Resolution Field Emission SEM. A ZrO/W Shottky field emission source is used, and can produce electrons with energies from 0.5 to 30 kV. The magnification can be changed from 20 to 800,000 x, and the best possible resolution reported in the instrument specifications is ~1.0 nm. This instrument can be used to image a very wide range of particle sizes, but the information only comes from the first few nanometers near the surface, again depending on how much the beam penetrates and how much volumetric interaction occurs. These considerations would ultimately determine the actual resolution, and may be sample-dependent.

The most common electrons captured in an SEM are secondary electrons (SE) and backscattered electrons (BSE). The highest resolution images come from SE and thus it is most commonly employed. However, BSE images have situational use, especially when there are high disparities of atomic weight within a sample. BSE works essentially by reflecting electrons, and thus atoms with a higher atomic weight can more easily do this. In a BSE image, higher

atomic weight atoms will appear as bright, while low atomic number species appear as dark. Figure 4.2 shows a secondary and a backscattered image of a mixture of aluminum and Bi_2O_3. The SE image gives a high resolution picture while the BSE image shows elemental contrast, and thus can show where the species are if the constituents have much different atomic weights.

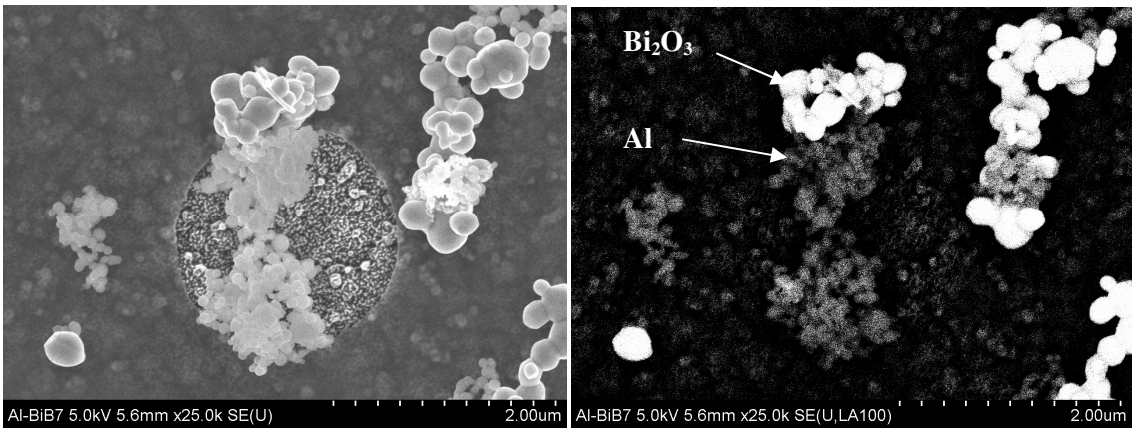

Figure 4.2 Secondary electron image (left) and backscattered electron image (BSE, right) showing an Al/Bi_2O_3 thermite. In the BSE, heavier species appear as brighter, and thus this is a quick way to essentially do elemental mapping.

4.1.3.2 Transmission Electron Microscopy (TEM)

Conceptually, a transmission electron microscope is similar in appearance and operation as an SEM, however, the difference is that the electrons collected are the ones that transmit through the sample. The detector in this case is situated below the sample, and in line with the electron beam. This technique can produce a very high resolution image, but is limited to particles generally smaller than ~1 micron so that the beam can penetrate through the material. The sample must also be placed on an ultra thin substrate, so that the beam can easily pass through the sample and substrate. There are several TEM grids available combining a slew of mesh materials with various coatings. Ideally, no coating material would be used to give the best picture, and this can possibly be achieved if the particles can be cantilevered off the edge of a

film. More commonly, however, a low molecular weight carbon or carbon-based polymer film is used.

The NISPLAB at the University of Maryland has two nearly identical TEMs for users; the only real difference is the electron source. The JEOL JEM 2100 Lab6 TEM uses a thermionic emission electron source, and can produce electrons from 80 to 200 kV, in roughly steps of 20 kV. The maximum resolution is 0.23 nm, and the beam can be focused down to approximately 1 nm in size in analytic mode. The JEOL JEM 2100 FE-TEM uses a ZrO/W Shottky field emission electron source, and can produce electrons with either 160 or 200 kV energy. This source gives a higher spatial resolution, down to 0.19 nm and the beam can be focused down to ~0.5 nm in size. What really sets this system apart, however, is that a JEOL SIOD digital scanning system is installed on this device. This allows the beam to be operated as a so-called scanning tunneling electron microscope (STEM). What this allows the user to do is to scan the beam over a certain line or area, and this coupled with a point by point elemental map becomes a strong analytic tool. Figure 4.3 shows a typical image of a single aluminum nanoparticle with its amorphous oxide shell. Note how the lattice planes of individual atoms can be resolved within the particle, and the atomic spacing can even be measured.

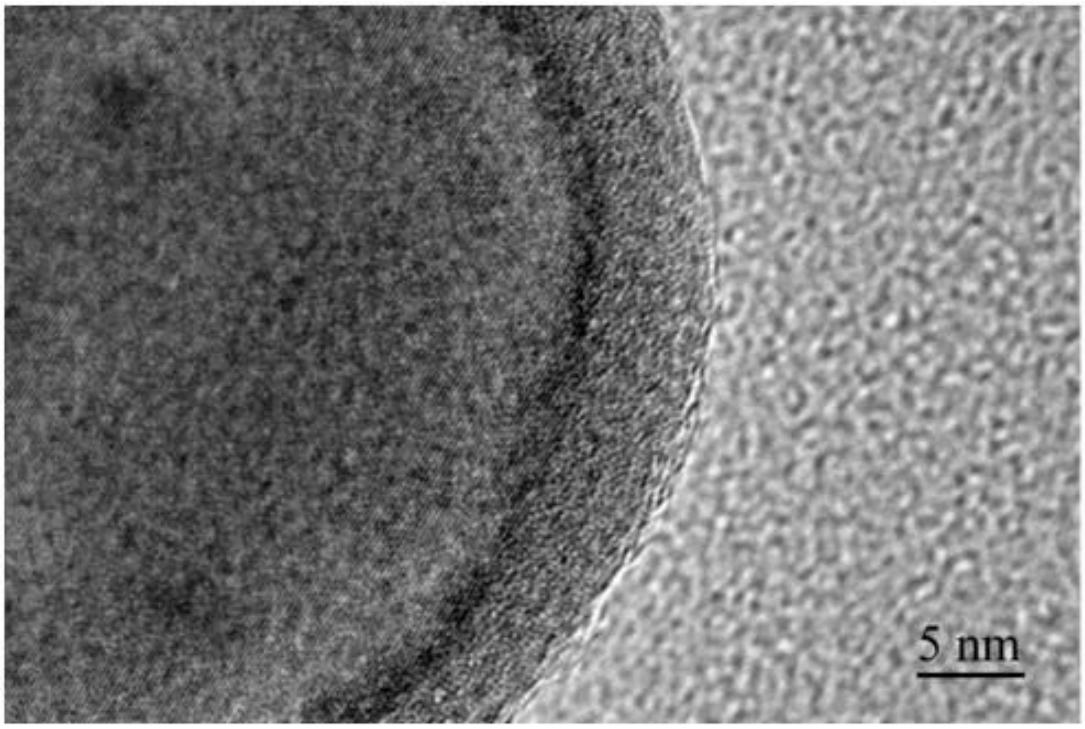

Figure 4.3 Transmission electron microscope image of nano-aluminum and its oxide shell. Note that lattice fringes can be seen using a TEM.

4.1.3.3 Energy Dispersive X-Ray Spectrometry (EDX/EDS)

One very powerful technique relevant to this study is the coupling of microscopy and elemental analysis. When atoms are excited by a high energy electron beam, the excited states can relax and emit characteristic electrons with well defined energies corresponding to orbital transitions. The energy spectrum emitted is unique to a given species, and by collecting the emitted electrons, one can perform high resolution elemental analysis for a sample. Both the Hitachi Su-70 SEM and JEM 2100 FE-TEM have an attached EDS units (SEM: Bruker Silicon Drift Detector, TEM: Oxford Inca 250). If the beam can be raster scanned across a certain line or area, then a point-by-point elemental map can be constructed to determine the elemental distribution. EDS can also give elemental ratios through the strength of the signal, with some corrections based on the probability of emitting an x-ray for a specific beam condition.

The EDS detectors are often situated above the sample, and slightly off to the side. What this implies is that it can only detect the x-rays which geometrically can travel to the detector, and this includes some unwanted x-rays which reflect off the walls inside the chamber. In addition, the beam penetrates some distance into the sample, depending on the beam energy. The x-rays may therefore be emitted from inside the particle, and can interact with neighboring elements to cause additional excitation. Thus, there is inherently some spatial resolution loss associated with EDS. The actual resolution will be determined by a combination of the beam energy, the geometric shape factor of the detector, and also the thickness and type of species itself. Nonetheless, unless ultra-high spatial resolution is required, this technique gives an excellent representation of the atomic distribution. Figure 4.4 shows a few experimental results relevant to this work.

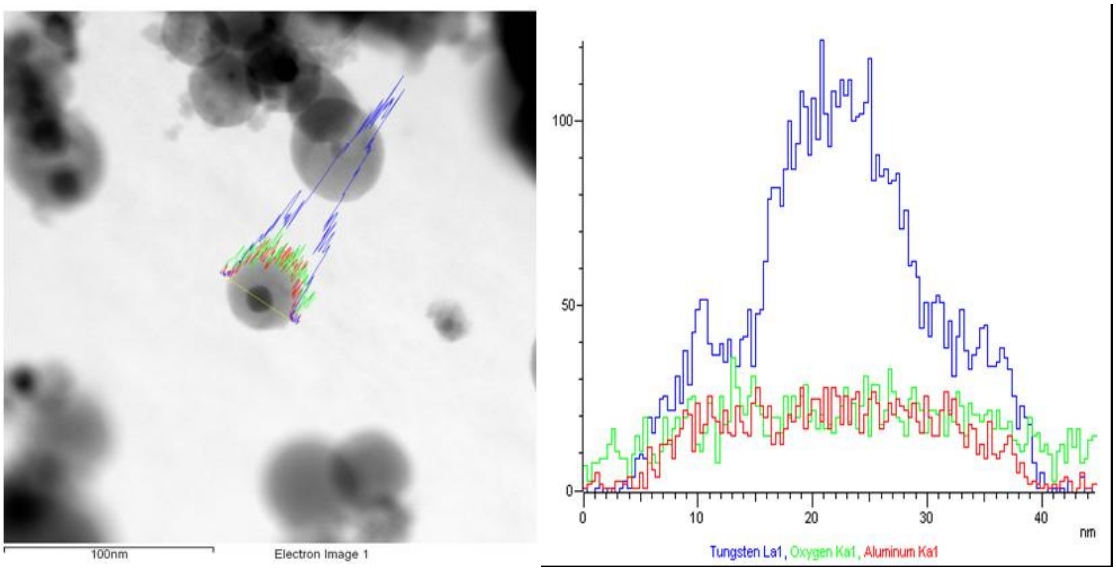

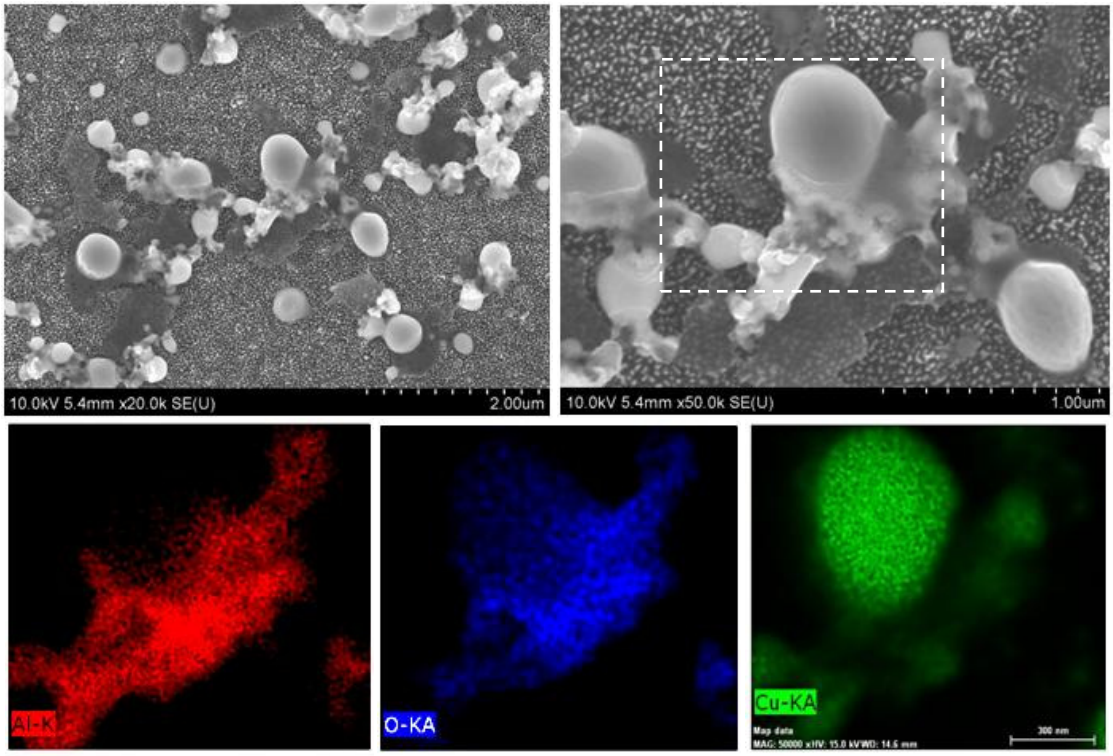

Figure 4.4 Examples of energy dispersive x-ray spectroscopy (EDS) measurements. A TEM image of reacted Al/WO_3 is shown in a) along with a linescan analysis verifying the existence of a tungsten core. An SEM image of reacted Al/CuO is shown in b) along with an area mapping of the elements.

4.1.3.4 Electron Energy Loss Spectroscopy (EELS)

Though it was not specifically used in this work, it should be noted that the JEOL 2100 FE-TEM is equipped to perform EELS measurements. The system is equipped with a Gatan 863 GIF Tridiem system, and the detector in this case is located underneath the sample. EELS works based on the principal that electrons passed through a material can be inelastically scattered or absorbed by the species. In particular, this technique probes the inner core electrons. The detector measures the energy of the transmitted electron beam, and the difference in energy between the incident and measured electron (energy loss) corresponds to what was absorbed by the species. The absorption energy can give species identification based on the electronic orbital structure, and thus is another way to construct an elemental map by raster scanning the beam

across a line or area, and looking at the point-by-point absorption spectrum. What sets EELS apart from EDS is that this technique does not suffer as much from volumetric effects, and thus is a higher resolution technique. The detector is underneath the sample, and the transmitted beam is probed, giving a very strong signal with a spatial resolution roughly equal to the beam diameter.

4.2 Thermal Analysis

4.2.1 Thermogravimetric Analysis (TGA)

TGA is nothing more than an ultra-sensitive scale with a programmable heating furnace. A flow gas can often be introduced, if the goal for example is to study the adsorption or oxidation behavior of a species. This technique can also be useful to measure the decomposition of a material as a function of temperature. If coupled to a mass spectrometer or other gas analyzer, species identification allows for an excellent analysis of the thermal decomposition mechanism. The TGA used in this work was a Thermo Cahn instrument, with a mass sensitivity of 1 microgram. In the context of this work, the TGA was only used to measure the active content of aluminum. As mentioned previously, aluminum forms an oxide when exposed to air. Knowing the weight percentage this shell occupies is an important consideration when weighing out the mixture with a precise stoichiometry.

An example of the TGA performed is shown in Figure 4.5. In this example, approximately 100 mg of a loose powder sample of ALEX nanoaluminum was placed into a ceramic crucible, and heated in a flow of air from room temperature to 1000 C at a rate of 10 C/min, then was held for an hour before being returned to room temperature. Both the weight and the temperature are plotted as a function of time. The elemental content of aluminum can

easily be calculated, if one assumes that the weight gained is only from oxidation of aluminum with oxygen, and only if the reaction proceeds entirely to completion via the mechanism:

$$2Al + 3/2\ O_2 \rightarrow Al_2O_3$$

These are valid assumptions for aluminum, though ideally the N_2 would be replaced with an inert such as Argon to prevent the possible formation of aluminum nitride. In this case from the TGA results we found the ALEX to be 70% elemental by mass, and always assume this number when weighing out samples.

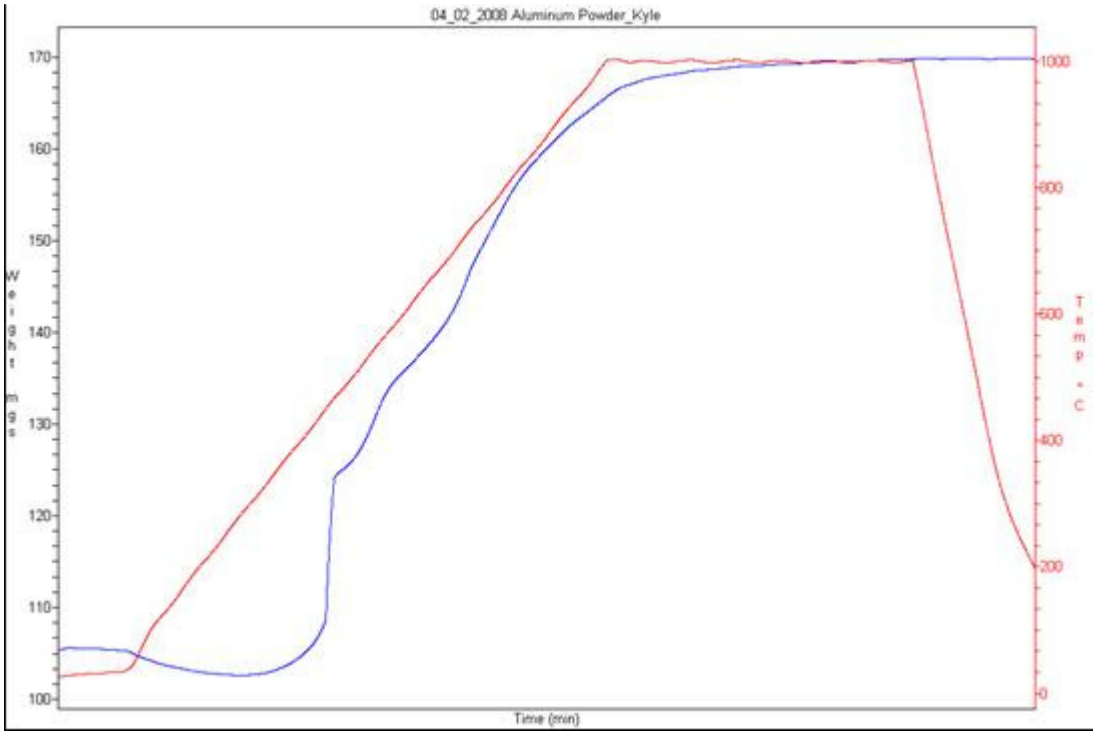

Figure 4.5 An example thermogravimetric analysis (TGA) of nanoaluminum. The corresponding weight gain along with the initial weight can be used to determine the elemental aluminum content, if one assumes complete conversion to Al_2O_3.

4.2.2 Differential Scanning Calorimetry (DSC)

This technique is useful in determining the heat flow in and out of a sample, and thus can generate quantitative data such as the latent heat of fusion or activation energy for thermodynamic processes. It works by supplying heat to an unknown sample and a reference sample. A feedback system monitors the temperature, and the heating source either needs to supply more or less energy to maintain a constant temperature. Oftentimes the heat flow is plotted as a negative value, so that the profile qualitatively is intuitive. An endothermic process, in this case, would show as a decrease in the heat flow signal, whereas an exothermic process would show as an increase. Coupled with a TGA, the data can also distinguish between processes involving mass changes versus simple phase changes such as melting. Some DSC results will be presented later in Chapter 8 (see Figure 8.1.1), where the thermal decomposition of $AgIO_3$ was investigated using this technique.

4.3 Ignition and Combustion Characterization

Measuring the ignition and combustion of condensed phase materials is not at all a straightforward and trivial process. One complication is that the most appropriate measurements are performed in-situ, and thus we are largely limited by measureable quantities, i.e. optical emission. While optical emission is used by several authors, attributing it to chemical reaction processes is the subject of a long and difficult debate. As an example, let's assume that a researcher wants to add spherical aluminum particles to an explosive as a means to boost the energy density and temperature of the energetic system. One experiment which is relevant to this example is to measure the reactivity of aluminum particles in CO_2.

First of all, the reaction rate will likely follow an Arrhenius behavior, and thus will be exponentially sensitive to the temperature. Also, the particle will be heated with an intense heating rate (~10^6 K/s) as the explosive goes off. The local pressure around the particle may be many hundreds of atmospheres. For this example, the most appropriate way to make the measurement is to reproduce a rapidly heated and pressurized CO_2 gaseous environment to ignite the particle. One technique which does accomplish this is a shock tube, which heats particles with controllable heating rates and pressures, while also varying the gas composition through the generation of a tunable shock wave.

Now that the environment can be experimentally simulated, the first question is; how does one make the measurement of the particle/flame temperature and burning time? One way which is typically used is to collect the light emitted from the particles during the process. If one assumes the particles to be blackbody radiators, then the filtered emission can be collected at different wavelengths of light. To extract temperature data, the intensities are fitted using Planck's formula which correlates emission intensity with wavelength, yielding the temperature of the solid particle. Measuring the actual flame temperature may require a slightly altered technique, in particular if the flame region is detached from the surface and is at a higher temperature than the particles (this is the case for aluminum). To do this, scientists have started looking at the molecular emission from AlO. AlO is an intermediate gaseous species which emits light around 486 nm when excited. By looking at the strength of the molecular peaks, an estimation of the flame temperature can be made. The duration of the AlO signal has also been used to quantify the particle "burn time."

These techniques are generally accepted as a valid means to make the measurements, however, and as is the case across the board, experimental techniques always have limitations.

Particles are not perfect blackbody radiators, and during a chemical reaction the surface may constantly be changing. Spectroscopy measurements are inferred based on statistical thermodynamics and radiation parameters, which are generally very hard to experimentally verify. The flame temperature is based on some statistical assumption of distribution of excited states, and the burn time is taken to be the duration of this trace. While we cannot argue that the analysis is necessarily wrong, we cannot prove that it is right either, and thus some skepticism must always be employed. It may be, in fact, that the luminous period corresponds to only a fraction of the total burning time, and this is an important thing to keep in mind when measurements are attributed to "real" phenomena such as particle burning.

That being said, these points are not a unique concept in science. The truth is, researchers must start with some measureable quantity, else no progress will ever be made. The techniques can be refined as the technology improves, and as calibration standards are developed. A good way to perform measurements such as this is to look at generalized trends and develop scaling laws. For example, more pertinent questions to ask if one is limited to using optical emissions are: what happens to the measured temperatures and duration of the AlO signal as the particle size is decreased? What happens when O_2 is used in place of CO_2? What is the function of pressure and mole fraction of the oxidizer on these measureable quantities? The trends in the measurements often yield more useful information than any individual measurement, and this fact allows us to experimentally validate the use of other techniques which have not been accurately calibrated. Several of the experimental measurements made in this work are treated as relative measurements, and the reader should keep this in mind through the remainder of this section. As specific parameters are perturbed, the resultant trends in the data have been used to interpret the results and draw conclusions about the mechanisms.

4.3.1 Combustion Cell

The bulk of the experimental work was done using a constant volume combustion cell to light off a fixed mass of sample of thermite powders. The cell originally was only equipped with a piezoelectric pressure transducer, capable of recording the transient pressure signal during the combustion, and was later modified with an optical port to simultaneously collect the optical emission. While each measurement itself is a relative measurement, the coupling of both of these signals was a powerful step to allow us to draw some conclusions about the mechanism of burning. Figure 4.6 shows a schematic of the modified pressure cell. The cell consists of three separate parts; the stainless steel base with the diagnostic pressure/optical ports drilled into the walls, the top "T" shaped stainless steel piece which has an electrical feed through of a thick copper wire, and the sample holder which is removable for cleaning and loading new samples.

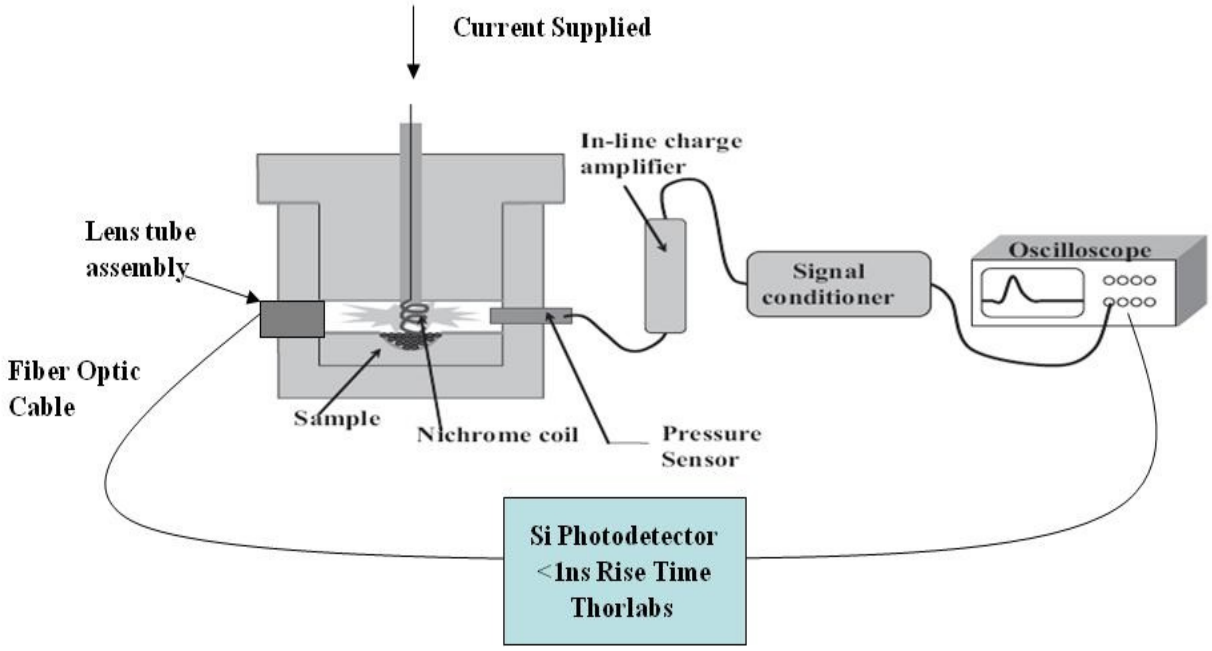

Figure 4.6 Schematic of the combustion cell used in this work. A fixed mass of sample sits in a bowl-shaped holder and is ignited by resistive heating of a nichrome wire. The pressure and optical emission are captured simultaneously, and the pressurization rate is a relative measurement of reactivity while the full-width half-max of the optical emission is taken to be the burning time.

The electrical feed through is a copper wire, and a small (~3 mm) length sticks out from the "T" piece and into the cell. In order to create an ignition source, approximately 8-10 cm of a thin Nichrome wire is wound onto the copper, and a coil is made with a straight tail (~2-3 cm) of the wire sticking out. As the "T" piece is lowered down into the base of the cell, the tail makes contact with the inner cell wall and a circuit is complete. Once closed, the purpose of the coil is simply to make contact only with the top of the sample. A current is then passed through the wire using a standard power source, and the nichrome resistively heats until the sample ignites.

The pressure port contains a piezoelectric pressure transducer attached in series to an in-line amplifier and conditioner before being recorded by an oscilloscope. The conversion specified by the supplier is that 1 mV read the scope corresponds to 0.237 psi of pressure. The optical port contains a lens tube assembly which collects and filters the light and then focuses onto a fiber optic head using a series of lenses. The signal is carried through the fiber to a Si photodetector (Thorlabs, DET10A), which converts the signal to a digital format to be read by the oscilloscope. The current is ramped up by hand until the sample ignites. Upon ignition and after a low threshold of optical intensity is achieved, the data collection triggers from the rising optical signal and the optical and pressure signals are captured simultaneously.

An example of the raw data collected by this system is shown as Figure 4.7a. In this case the voltage has been converted into a pressure using the equipment conversion 1 mV = 0.237 psi. As can be seen, there is a delay between the onset of the optical signal and the pressure signal. This delay is due to the ~3 cm distance between the sample and the pressure transducer, and can be expected due to the slow speed of sound compared to light. Also, the data is quite noisy as is. In order to have some reproducibility in the measurements, several processing steps are performed using Excel.

1) Smooth the data by averaging 5-10 adjacent points.
2) Use the MAX function to calculate Pmax and Vmax.
3) Calculate 5% of Pmax and Vmax, and also 50% of Vmax.
4) Remove the delay between signals by shifting the time of the pressure data.
    a. Caveat 1: Assumes the delay is solely due to the travel time of the pressure signal.
    b. Caveat 2: Assumes the onsets of pressure and optical emission occur concurrently.
5) Shift the data so that t=0 corresponds to 5% of the maximum values.
    a. 5% is an arbitrary assignment, and is only done for consistency.

An example of the processed data is shown in Figure 4.7b.

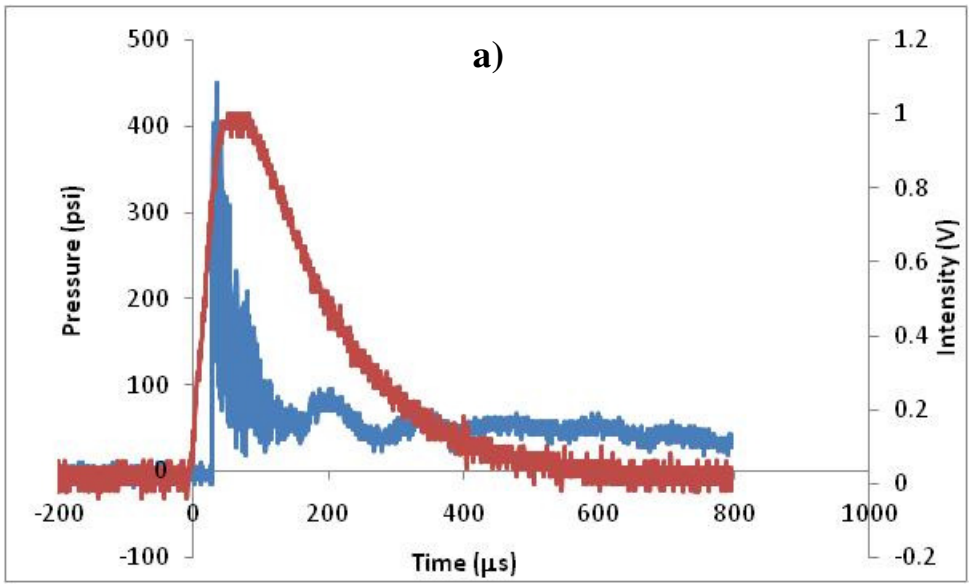

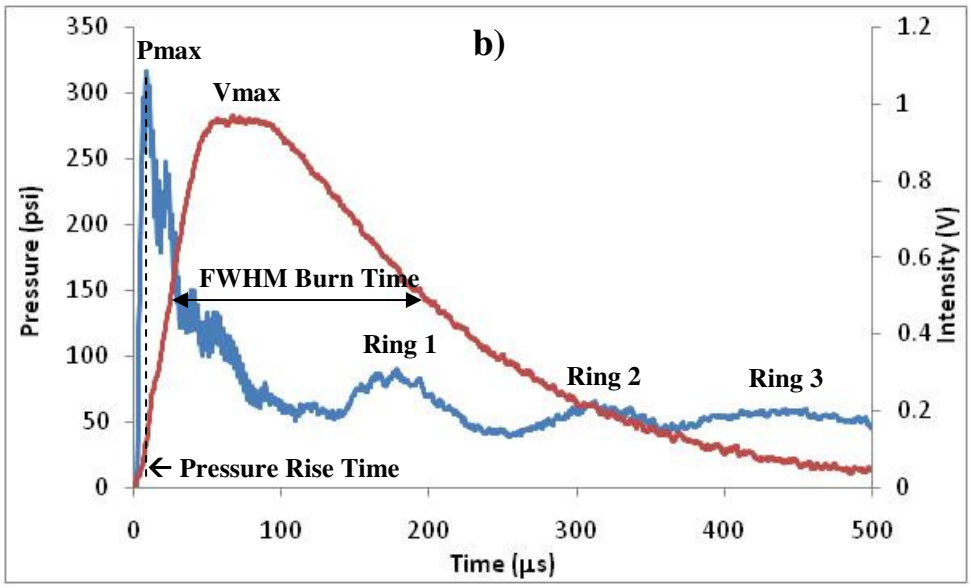

Figure 4.7 An example of raw (a) and processed (b) data recorded by the pressure cell. The pressurization rate is calculated as the maximum pressure divided by the pressure rise time (5% Pmax to peak) and the burn time is measured as the difference in time between the when the optical emission reaches 50% of Vmax. The rings correspond to reflections off the wall opposite the pressure transducer.

Now that the data is processed, the pressurization rate and burn time can be read in a repeatable way. The maximum pressure is calculated from the MAX function, and the pressure rise time is the time it takes to reach this value, and is read in the from the plotted data. The pressurization rate is taken as the peak pressure (psi) divided by the pressure rise time (µs), and is the typical way we report the data. The burn time of the thermite is taken to be the full-width at half max (FWHM) of the optical signal. It should be noted that this assignment is a somewhat arbitrary one, and we have not verified whether this measurement is a good quantification of the burning times. The peaks labeled "ring" in Figure 4.7b are attributed to the pressure wave travelling across the cell, reflecting off the wall, and returning to the transducer, and the time between rings is comparable to the travel distance divided by an estimate of the speed of sound.

A full description of how to operate the pressure cell is located in the Appendix.

4.3.2 Burn Tube

This technique is used to measure the burning velocity of thermites self-propagating in an enclosed tube. The tubes used were acrylic and 10 cm in length, with an inner diameter of 3 mm and a thickness of 2 mm. Approximately 250 mg of thermite was prepared and packed loosely into the tube. Two fiber optic heads are situated externally and perpendicularly to the propagation direction, and a known distance apart. The first fiber is located approximately 3 cm from the ignition point so that the thermite can reach a steady-state velocity by the time the flame reaches the first photodiode. The thermite is lit off with the same nichrome wire as used in the combustion cell, and the data collection triggers via the onset of the optical emission on the first photodetector. Both photodiodes output the transient emission onto an oscilloscope. The flame velocity is calculated from the difference in time between the onsets of optical emission on the two photodiodes, along with the known separation distance between the two. Further details are not provided, since this system was only used briefly in this work. As mentioned previously, the pressurization rate and flame velocities are in some way correlated, but we find that this correlation is only qualitative. A doubling of the pressurization rate does imply a doubling of the linear burning rate, however, a higher pressurization rate does imply a faster burning velocity.

4.3.3 Fast Heated Wire

This system was developed by other members of the group, and the goal is to have an experimental system which can rapidly heat a small amount of sample with a practical (~10^6 K/s) heating rate. An ultra thin Pt wire (diameter = 76 μm) is soldered onto two electrical leads, and a tunable voltage pulse can be passed through the wire. The Pt wire resistively heats, and thus so does the sample, with a controllable heating pulse. The resistance is monitored transiently through a feedback loop, and the transient temperature profile can be calculated knowing the

electrical properties of platinum. This setup can uniformly heat the sample, and the ignition and combustion can be studied on a small amount of material as a means to probe the intrinsic behavior. A heating model, which assumes the particles in contact with the Pt conductively heat (with some contact resistance), predicts that the first layer very rapidly adjusts (~1 μs characteristic time) to the changing temperature of the wire, and thus the particle temperature profile is essentially equal to the wire heating rate. The heat transfer through the remainder of the powder (~25 μm) will then be governed by the self-propagating exothermic reaction. The heated wire setup was used to examine the ignition and combustion of nanoscale thermites through a series of experiments.

4.3.3.1 Wire / Photomultiplier Tube (PMT)

The ignition of and combustion behavior of nanoparticles and thermites is studied by rapidly heating a sample on the wire, and collecting the optical emission using a photomultiplier tube (PMT). The PMT collects the incoming light, and converts the signal to a digital format which is read by an oscilloscope. Using filters, this setup can be used in order to isolate specific wavelengths and study atomic emission, however, the more common application is to collect the broadband emission. The voltage pulse used to heat the wire is used as a trigger for the PMT, and ignition is said to have occurred at the onset of optical emission. The temperature of the wire is calculated, and an example of the data output is shown in Figure 4.8. The ignition temperature is reported to be at the onset of optical emission, and the burning time is taken to be the full-width at half maximum (FWHM) of the optical emission.

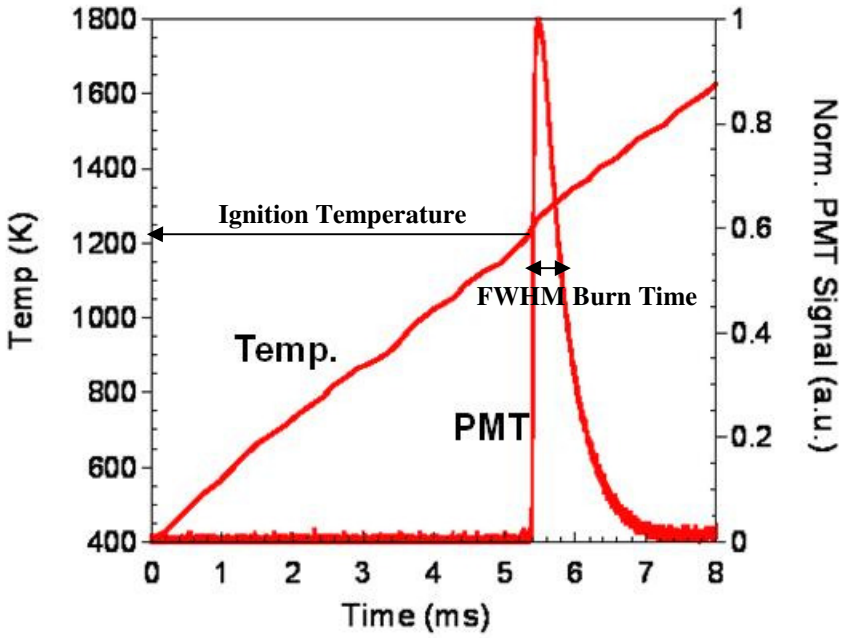

Figure 4.8 Typical data from the heated wire/photomultiplier tube (PMT) experiment of an Al/CuO thermite. The temperature is calculated by monitoring the voltage and resistance, and using the well known properties of Pt. The ignition temperature is reported at the onset of optical emission, and the burn time is measured from the full-width at half-max of the optical emission.

4.3.3.2 Wire / Mass Spectrometry

The fast heating wire system can also be inserted into a mass spectrometer to look at the transient species evolution. The mass spectrometer is triggered off of the voltage pulse used to heat the wire, and an electron gun serves to ionize species which occur during the reaction. Charged species are accelerated upwards via an electric field to a detector, and species with different mass to charge ratios will arrive at different points in time, thus providing a correlation between arrival time and m/z ratio. The acquisition rate is in some way limited by how fast the system can collect and read out the data, and currently the system can record spectra a frequency of 10,000 Hz, or 1 spectrum per 100 μs. An example of the Al/CuO thermite reaction is shown in Figure 4.9. Each spectrum in the vertical direction represents a time step of 100 μs.

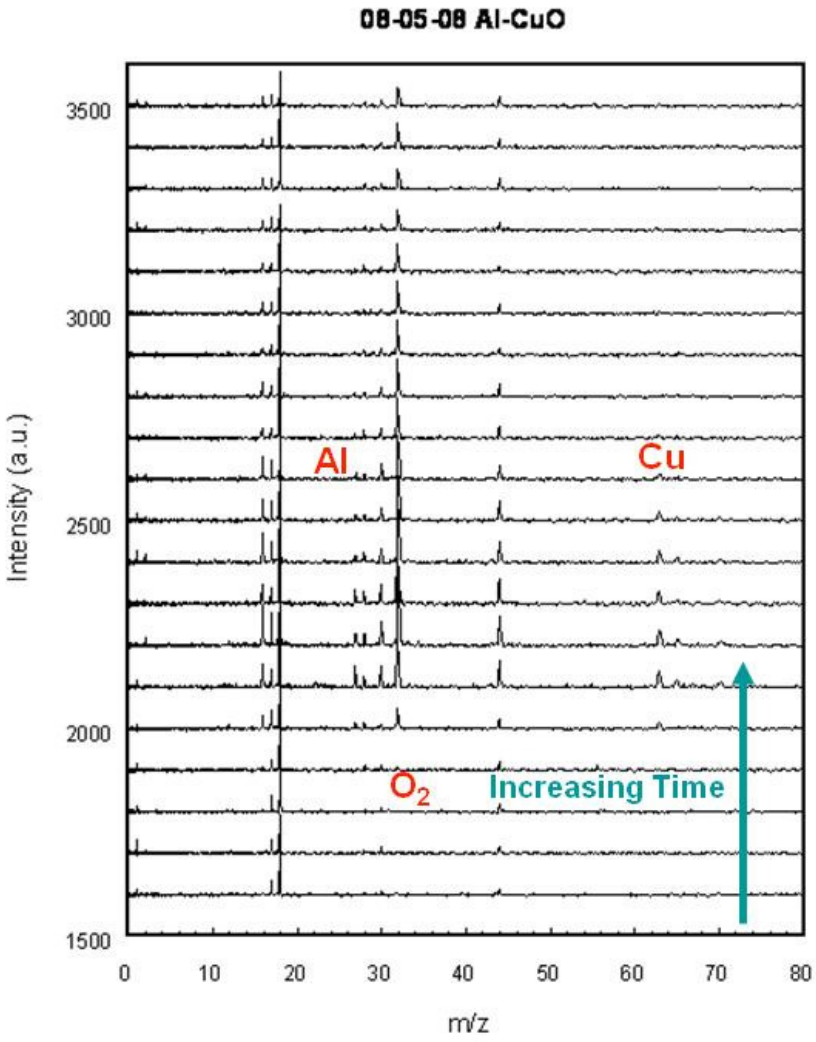

Figure 4.9 Typical data reported from the fast heated wire/ Mass spectrometer experiment. The system collects a spectrum every 100 μsec, and thus can measure the species evolution during the ignition and combustion of thermites on the wire.

This technique provides very useful and in-situ measurements for studying gaseous species produced during condensed phase reactions. However, some caution must be made until the technical and scientific understanding of the data is improved upon. For example, it is not quite clear what to call "ignition" in this data, as it could correspond to the point where O_2 or CO_2 is released, or could be the first spectrum where Al or Cu is detected. The burning time could also be subject to interpretation. Also, the combustion occurs under vacuum and thus some species may appear volatile which otherwise would not be able to vaporize. These issues

are just some of the challenges which are currently being investigated. Some work has been done to record movies of the thermite burning on the wire using a very fast CCD camera. Coupling optical data with the transient species identification will further the understanding of the instrument, and allow for the distinguishing of the processes involved in the ignition and combustion mechanism.

4.3.3.3 Wire / Movies at Argonne National Lab

We applied for some beam time using the Advanced Photon Source (APS) at Argonne National Laboratory (ANL) to look at high resolution movies of the thermite burning on the wire. APS is a national synchrotron x-ray research facility funded by the US Department of Energy, and supplies high energy x-rays to be used for experimental research. The wire setup was driven to Chicago and set up in a hutch to study the thermite reaction using the available x-rays. One goal of the experiment was also to collect time-resolved x-ray diffraction data, but this did not work due to the sample rapidly leaving the imaging volume upon reaction. We did, however, manage to collect movies of the thermite burning on the wire, using the x-ray source and a CCD camera capable of x-ray imaging. The images are collected by a real-time phase contrast imaging technique, where small pulses of x-ray bunches are produced and an image is constructed based on local variations in the material. Further details on this technique can be found elsewhere.[129] The movies were captured at a frame rate of 135,780 frames per second, corresponding to a time resolution of 7.4 μs per image. The PMT setup was also brought in order to have simultaneous optical emission measurements, with the hopes of making correlations between the movies and the optical emission (i.e. the ignition and combustion). The results will be presented later on.

4.3.4 High Heating Microscopy Holder

A special heating holder (Protochips, Inc.) designed to be used inside an electron microscope was used in this work to investigate the samples in-situ. The holder is capable of heating a small amount of material from room temperature to a maximum of 1473 K at a rate of 10^6 K/s. The technology is largely in the design of the grids, which are specially fabricated for this application using lithographic techniques. A schematic of the device/grid is shown in Figure 4.10

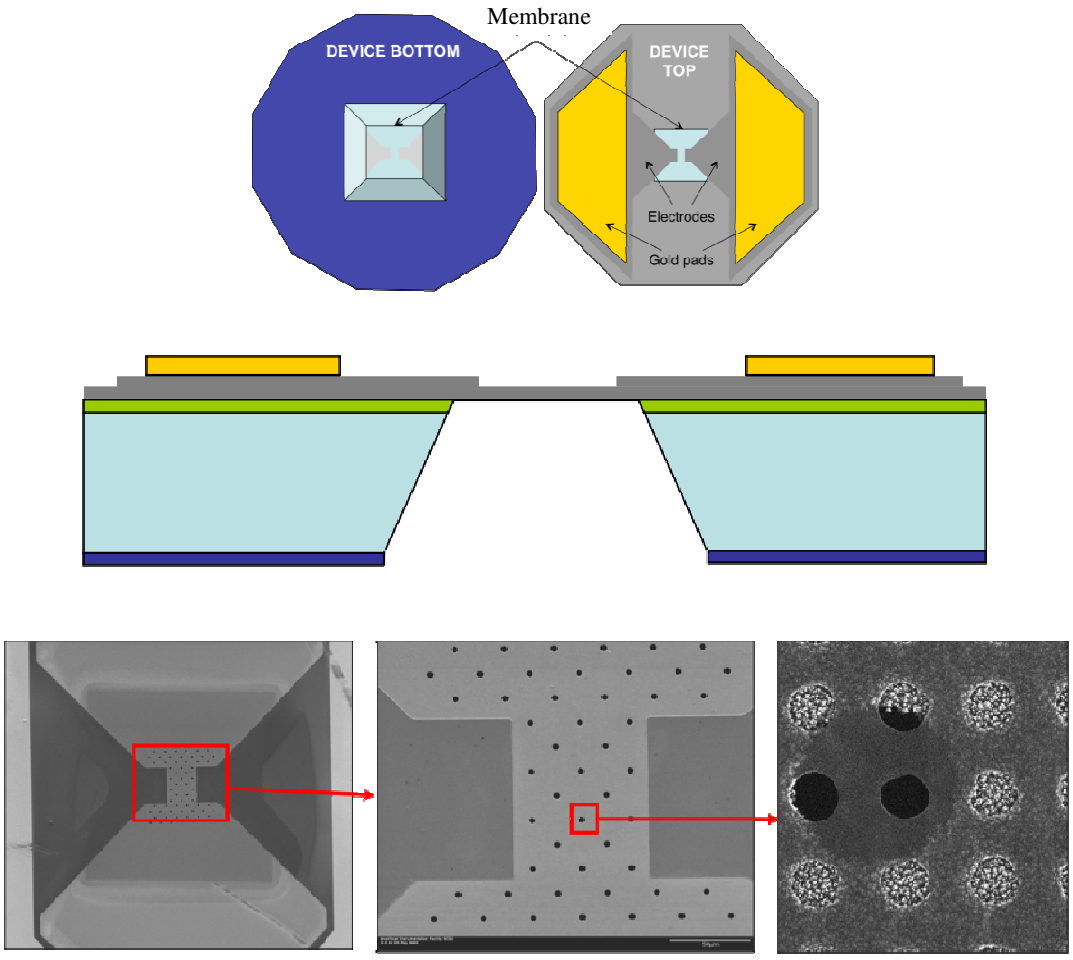

Figure 4.10 Schematic of the fabricated grids/devices used in the high-heating microscopy experiments. The grids can be observed in-situ in a scanning or transmission electron microscope, using a special holder with electrical feed throughs. The sample can be heated with a user-specified pulse, up to a maximum of 1473 K at a rate of 10^6 K/s.

Each fabricated device is calibrated using optical pyrometry, and then holes are punched through the device in an area of constant temperature. The device can then be used as-is in an SEM, or a very thin holy carbon film can be overlaid on top of the holes for TEM analysis (the thin carbon film stretches over the holes, and serves as a substrate for the sample over the holes, allowing the TEM beam to penetrate through the material). The temperature is ramped by supplying a given current pulse, which is uniquely specified for each device through a calibration file generated by the pyrometry measurements. The software interfaces to the power supply, and can heat the sample with a user-defined function. Based on the small thermal load of the substrate, it is speculated that the device will cool almost as quickly as it heats.

The heating rate was estimated by the supplier through a series of experiments inside a TEM. To do this, the temperature was held at an elevated constant value, and the image was then focused using the TEM beam. The device was then returned to room temperature. A camera was used to record a movie of the sample being heated, and the heating rate was estimated to be the maximum temperature divided by the time delay from the start of heating to when the image was in focus. This measurement worked because a TEM by default has a very poor depth-of-focus (contrary to an SEM), and thus must be highly focused in the Z direction in order to get a clear image. This instrument is really the first of its kind, and is particularly useful because the heating is tunable and can be performed in-situ in a microscope. Experimental results using this holder is a large focus of the work presented in Chapter 7.

4.4 Thermite Sample Preparation and Safety

Unless otherwise stated, all samples were prepared the same way. The fuel and oxidizer are weighed out and adding to a ceramic crucible. (Tip: place the ceramic crucibles on a wet Kimwipe, this helps reduce static). Approximately 10 mL of hexane is added, and the powders

are placed into an ultrasonicating bath with the water level ~2/3 up the sides of the crucible. The samples are then ultrasonicated for 30 minutes. During this time, the samples should be swirled by hand and moved around inside the bath to help the mixing. If the bath water becomes warm, add cold water. In some cases, material can get caked on the inner wall of the crucibles, so hexane can be added to remove the material. These are all small tips which will help to avoid batch to batch variations during the mixing.

After 30 minutes, the crucibles should be placed in a fume hood and the remaining hexane should be allowed to evaporate until the powders are completely dry. In some cases, this can be as little as a few hours, whereas in other cases the powders are left overnight. When practically no hexane is visible, it's likely safe to put the crucible into the furnace for ~5 minutes to rapidly dry the powders, however, this is generally not needed and makes little difference to the results. (Do NOT put the crucible in the furnace if there is a significant amount of hexane left, this is very dangerous). Once dry, the crucibles are brought to a plastic handling box. The material is then very gently broken up using a non-conductive spatula until the consistency is that of a loose powder. The material is then ready to be tested in the combustion cell.

It should be noted that several safety precautions should be taken when handling energetic materials. Electrostatic mats and wrist straps should be used to prevent accidental ignition. When handling energetic materials, always wear protective equipment, including a lab coat, safety goggles, gloves and a dust mask. Use an appropriate conductive spatula, so as to minimize the chance of spark ignition. As a rule of thumb, never face the open end of a crucible towards your face or any part body, and never weigh out more than 250 mg total. The highly sensitive material can accidentally be ignited, however, if handled safely, will not harm you as long as these precautions are taken. A plastic box has been built, where the bulk of handling the

energetic materials should take place. The most dangerous part of the handling is when the material must be broken up into a fine powder by a spatula. However, ignition has occurred by scraping material into the sample holder also.

4.5 Thermodynamic Equilibrium Calculations

Oftentimes it is necessary to use thermodynamic considerations to corroborate the experimental data, or in order to predict new and improved energetic formulations. Two equilibrium codes that were used in this work were NASA's Chemical Equilibrium with Applications (NASA CEA) code, and also the CHEETAH code from Lawrence Livermore National Laboratory (This software is export controlled). Thermodynamic equilibrium calculations fundamentally work by taking a given mixture composition, and perform iterative routines to minimize the free energy of the system while conserving the mass. The calculations only can consider the species located in the thermodynamic libraries, and thus will depend on the accuracy of the data. Some species, such as silver iodide (AgI), may also not be contained in the database, along with many alloying reactions, and thus the accuracy of the calculations should always be treated with some degree of skepticism.

Three types of calculations were often performed using NASA CEA in this work; constant temperature and pressure (TP), constant enthalpy and pressure combustion (HP), and constant energy and internal volume combustion (UV). The particular calculation was chosen depending on what was most appropriate. For looking at oxidizer decomposition, TP calculations were most appropriate. If we were looking at a thermite being combusted on a wire, then constant HP calculations are most appropriate, with the pressure being either atmospheric or under vacuum. For combustion inside the cell, UV calculations were used assuming a sample density of 0.00192 g/cc, calculated by assuming that 25 mg of sample is combusted in the 13 cc

cell. The calculations output the final pressure, temperature, and species distribution which have minimized the free energy of the system. A word of caution; these are equilibrium calculations and thus the results may be very different if trying to compare with in-situ measurements where the reaction is far from equilibrium. They should only be used to support experimental data, and not as results themselves.

Table 4.1 A summary of all experimental techniques relative to this work, along with some comments and criteria.

PHYSICAL CHARACTERIZATION				
Experiment	**Where Used**	**Sample Mass / Particle Size**	**What is Learned**	**Comments**
X-Ray Diffraction (XRD)	UMD, Chemistry	~1 mg	Crystalline species identification	-Similar crystal structures give the same pattern → Calculate peak width and lattice parameter to distinguish. -Only detects crystals, and not amorphous structures
X-Ray Photoelectron Spectroscopy (XPS)	UMD, Chemistry	~1 mg	Surface species analysis	-Only probes the first few nm of material near the surface. -Identifies species by knocking out inner core electrons, and measuring the kinetic energy of those emitted electrons. Can also look at Auger electrons if needed.
Scanning Electron Microscopy (SEM)	UMD, Kim Building	Picograms-milligrams / nanometers-millimeter diameter	High resolution image of surfaces	-Sample must be conductive or coated with a conductive material. -Secondary and Backscattered electron (SE/BSE) modes give high resolution images and elemental contrast, respectively.
Transmission Electron Microscopy (TEM)	UMD, Kim Building	Picograms / < 1 μm diameter	High resolution images of particles, Lattice structures/parameters	-Higher resolution images than SEM, and beam must be able to pass entirely through the sample. -Can determine atomic orientation and spacing.
Energy Dispersive X-Ray Spectrometry (EDS/EDX)	UMD, Kim Building on Su-70 SEM and JEOL FE-TEM	Same as SEM and TEM	Elemental Mapping and quantitative information	-Beam must be rastered in order to scan a region. -Detector is affixed above the sample and off to the side. -Spatial resolution loss based on beam energy and volumetric interactions. -Capable of quantitative analysis.
Electron Energy Loss Spectroscopy (EELS)	UMD, Kim Building on JEOL FE-TEM	Same as TEM	Elemental Mapping	-Detector situated below the sample. -Works by monitoring the energy loss through the sample. -Stronger signal and higher resolution than EDS.
Thermogravimetric Analysis (TGA)	UMD, Mech. E. NAWC	~10 mg – 1g, particle size independent	Weight loss / gain with μg resolution	-An ultra-sensitive scale to monitor the weight gain/loss in a gaseous environment. -Various gaseous environments.

	China Lake			-Slow heating rate, ~degrees per minute
Differential Scanning Calorimetry (DSC)	NAWC China Lake (UMD Mech E. has one also, may be others)	~10 mg – 1 g	Heat loss / flow from a sample	-Compares the heat loss / flow to a reference. -Can give quantitative information, such as enthalpies of latent processes. -Couples to a TGA to distinguish between latent processes and reaction/decomposition processes. -Slow heating rate, ~degrees per minute
IGNITION AND COMBUSTION CHARACTERIZATION				
Experiment	**Where Used**	**Sample Mass / Particle Size**	**What is Learned**	**Comments**
Combustion Cell	UMD, Zachariah Group	~25 mg	Relative Reactivity, Burning Time	-Pressurization rate → reactivity -FWHM of optical signal → burn time -Both relative measurements, and must be compared to other materials/systems
Burn Tube	UMD, Zachariah Group	~250 mg	Flame velocity	-Closed acrylic tubes used -Large sample mass → USE CAUTION
Wire / Photomultiplier Tube (T-Jump/PMT)	UMD, Zachariah Group	~Micrograms	Ignition Temperature, Burn Time	-Ignition T measured by onset of optical emission. -Filtering can allow for species identification on 1 or 2 PMTs. -Burn time measured by FWHM of optical system. -Does not need a condensed phase oxidizer -Can be operated in various gaseous environments. ~10^6 K/s heating rate.
Wire / Mass Spectrometry (T-Jump/MS)	UMD, Zachariah Group	~Micrograms	Ignition Temperature, Burn Time, Transient Species Identification	-Collects a spectrum once per 100 μs. -Plots intensity vs M/z ratio. -Detects the transient species evolution of condensed phase reactions between a fuel and oxidizer. ~10^6 K/s heating rate
Wire / Argonne Movies	Argonne National Lab, Advanced Photon Source	~Micrograms	High Resolution X-ray movies of nano-Al and thermites burning on the wire.	-Special CCD camera images the x-rays at a frame rate of 135,780 FPS (7.4 μs / image). -Could be some heating of the sample by the x-ray beam. -Simultaneously collected the optical signal with a PMT and XRD detector. ~10^6 K/s heating rate.
High Heating Holder	UMD, Kim Building on loan from Protochips, Inc.	~Picograms	Before and after images and elemental maps of condensed phase reactions	-May be some reaction with the carbon film. -SEM in BSE mode gives a quick elemental map. -Tunable heating pulse provides rapid heating (and cooling) of the sample on a special substrate. ~10^6 K/s heating rate.
EQUILIBRIUM CALCULATIONS				
Equilibrium Calculations NASA CEA/CHEETAH	Software NASA CEA can be downloaded for free CHEETAH is export controlled	N/A	Thermodynamic equilibrium pressure, temperature, and species distribution	-Constant TP → Decomposition calculations -Constant HP → Unconfined burning -Constant UV → Confined burning -Only useful in conjunction with experimental results. -Always treat the calculations with skepticism, many transient processes occur far from equilibrium conditions.

Chapter 5: Enhanced Reactivity of Nano-B/Al/CuO MICs

Relevant Experimental Techniques:

a) Combustion cell without optical measurements, Section 4.3.1

-Measure the pressurization rate (reactivity) of the mixtures

b) CHEETAH Equilibrium Codes, Section 4.4

-Predict the adiabatic flame temperature and species distribution

c) Thermogravimetric Analysis, Section 4.2.1

-Measure the "active content" of aluminum and boron which have an oxide shell.

5.1 Overview

This work was an investigation of using nano-sized boron in energetic thermite formulations. Nanoboron is attractive because of its mass and energy density, but researchers have generally been unable to get it to burn well. The primary experimental technique used in this work to measure reactivity was the combustion cell, and this work was done before the optical port was added, so only the pressurization rate is reported.

Boron was found to perform poorly as a fuel mixed with CuO. However, an enhancement to the reactivity was observed when nano-sized boron was added as the minor component to a more reactive Al/CuO thermite. Since the boron was the minor component, the speculation was that the primary reaction was somehow allowing the boron to be ignited on the same timescale as the Al/CuO. A phenomenological heat transfer model was developed in this work based largely on the considerations in Mohan et al.,[7] which referred to a heat-transfer modeling work conducted by Filippov and Rosner.[6] The findings were that the nanoboron could be heated above its melting temperature very fast through energy transport from the gaseous surroundings to the particle. Once ignited, it could participate in the reaction, and led to an

increase in the reactivity (the pressurization rate) via the formation of gaseous products, such as BO, BO_2, B_2O_3, etc. The major result from this work was that a practical use for nano-sized boron was found, and also some speculations on how to overcome its limitations were proposed. In particular, rapidly removing the shell and melting the boron core were necessary to ensure fast reaction.

5.2 Introduction and Relevant Literature Review

Traditionally, aluminum has been used as the fuel in nanocomposite thermites due to a combination of its high energy release and its abundance. However, thermodynamically boron is an attractive alternative since it has higher heating values on both a mass and volumetric basis. Table 5.1 shows the heating values of some metals which could be potential candidates. Other than beryllium, which is not practical due to its toxicity, boron shows higher heating values than all of the other metals.

Table 5.1 Heating values per mass and volume for various metals.

Metal	ΔH per unit Mass (Kcal/g)	ΔH per unit Volume (Kcal/cc)
Boron	-14.12	-33.19
Beryllium	-15.88	-29.38
Aluminum	-7.41	-20.01
Titanium	-4.71	-21.20
Vanadium	-3.64	-21.69
Magnesium	-5.91	-10.28
Nickel	-0.98	-8.72

When exposed to air, aluminum and boron form an oxide shell around the elemental core of fuel. The shell is typically only a few nanometers thick and, on a supermicron level, is an

insignificant amount of the particle mass. However, as the particle size transitions into the nanometer regime, the shell becomes a larger portion of the total mass and can play a critical role in the combustion process. Though the heating values clearly suggest that boron should outperform aluminum, the burning mechanisms of these two materials are speculated to be quite different when one takes into consideration the core-shell structure.

Different theories have been suggested to explain the burning of an aluminum particle with its elemental core and oxide shell. Initially, Glassman[25, 130] proposed that metal combustion is similar to droplet combustion, and therefore a D^2 model could be employed to describe the burn time. He further suggested that the ignition and combustion processes would be governed by the melting and boiling points of the metal and metal oxide. Price[131] suggested two possible mechanisms for the breakdown of the aluminum oxide shell and ignition of aluminum particles. The first mechanism involves the very different melting temperature of aluminum oxide (2327 K) and pure aluminum (930 K). As a result, upon particle heating, the elemental core melts and the molten aluminum expands. This induces thermal stresses in the oxide shell, leading to cracks that expose molten aluminum to the oxidizing species. The other possibility is that the oxide layer undergoes melting itself, which would require much higher temperatures for ignition.

More recently, Trunov et al[15] studied the effects of phase transformations in the oxide shell upon heating. They used thermogravimetric analysis and X-ray diffraction to study the oxidation of aluminum particles with various sizes and morphologies, and found that aluminum combustion can be explained by a four stage process. During the first stage, the thickness of the initial amorphous oxide shell increases until it reaches a critical value of about 5nm. The next stage involves the transformation of the oxide layer into denser γ-Al_2O_3, exposing some of the core aluminum. In the third stage, the γ-Al_2O_3 layer grows and partially transforms into θ-Al_2O_3

and δ-Al_2O_3. Finally, stage four involves the transformation of the shell into stable α-Al_2O_3. In recent work by our group on nanoaluminum, Rai et al[48] found that aluminum melting was necessary for fast reaction, and was due to the counter diffusion of aluminum metal out rather than oxidizer to the core. This results in the formation under some conditions of a hollow alumina product. Olsen et al[132] also showed the formation of a hollow product in combustion studies of micron-sized particles.

In boron, a different observation is made during particle heating. Similar to aluminum, a boron particle has an oxide shell (B_2O_3) which surrounds the elemental boron core. The oxide layer, however, melts at a much lower temperature (722 K) than the core (2375K), rendering a different burning scenario than aluminum. Upon heating, the oxide shell will melt before the solid core, thus leading to a diffusion-controlled process through the molten shell. The pioneering work of Macek and Semple[114] suggested that boron combustion always happens in a two-step process, separated by a dark period. The first step involves the removal of the oxide layer, while the second step involves the burning of a bare boron particle in air. Ulas *et al.*[115] also support that the combustion of boron particles is defined by a two-stage process. Again, the first stage of boron combustion was considered as the removal of the oxide layer. This process is a slow, kinetic and/or diffusion controlled process, which constitutes a significant portion of the overall burning time of the particle. After removal of the oxide layer, the second stage begins with the combustion of the pure boron.

Contradicting theories about the treatment of diffusion through the molten B_2O_3 layer have been proposed, with Glassman[25] suggesting that elemental boron dissolves into the molten B_2O_3 layer and diffuses outward to the $B_2O_{3(L)}$/gas interface, while King[133-136] suggested that O_2 dissolves into the molten layer and inwards to the $B/B_2O_{3(L)}$ interface. This argument has been

more recently addressed in a review article by Yeh and Kuo[137], where they report that the diffusion of boron into the molten $B_2O_{3(L)}$ dominates the diffusion process. They also report the formation of a polymeric vitreous $(BO)_n$ complex in the reaction between dissolved boron and molten B_2O_3. These results were used to develop a reaction mechanism for boron combustion.

Aluminum and boron differ in their combustion mechanisms primarily due to the inherent properties of the pure material and their oxides. Based upon Glassman's Criterion[25], aluminum will combust in a vapor phase in an oxygen environment since its oxide's volatization temperature is higher than the boiling point of pure aluminum. On the other hand, boron will not combust in the vapor phase since the boiling point of pure boron is significantly higher than the volatilization temperature of its oxide. In fact, since boron oxide melts at a much lower temperature than pure boron, it covers the particle and creates a substantial diffusive barrier between the oxidizer and pure fuel.

Despite the great potential of boron as a fuel, it has rarely achieved its potential in systems that require fast and complete combustion. Ulas *et al.*[115] suggest there are two major reason for this; 1) the ignition of boron particles is significantly delayed due to the presence of an oxide layer on the particle surface, and 2) the energy release is during the combustion process of boron particles in hydrogen containing gases is significantly lowered due to the formation of HBO_2. Yetter[138] adds to these issues the idea of an energy trap. Hydrogen containing species can accelerate the gas-phase combustion process. Unfortunately they promote the formation of HBO_2, which is thermodynamically favored over gaseous B_2O_3 as the temperature is lowered, which can result in the boron being "trapped" as HBO_2 and therefore not releasing all of its available energy. The energy trap arises from the fact that from an energetic standpoint, the best product of boron combustion is liquid boron oxide. Even in non-hydrogen containing

environments, the quickest way to remove the oxide layer and combust the pure boron material is at temperatures above the B_2O_3 boiling point of 2338 K. However, combustion at these temperatures would result in the formation of B_2O_3(g) whose heat of formation is approximately one third of the liquid form. Furthermore, in early studies Macek[139] showed that boron particles had burn times up to four times longer than similar sized aluminum in similar environments.

Most recently, an effort has been made to address the issue of oxide layer removal. Difluoroamino-based oxidizers have been developed, and have rejuvenated the hopes for boron combustion. With fluorine as an oxidizing agent, an increase in gas-phase combustion products can be realized; a desired effect for energetic materials. Ulas *et al.*[115] combusted single boron particles in fluorine-containing environments by injecting particles into the post flame region of a multi-diffusion flat-flame burner. Their results show the disappearance of the apparent "two-step" combustion process in the presence of fluorine, along with decreased burning times. This is a major result for boron combustion since the removal of the oxide layer adds significantly to the overall burning time, and if the oxide layer can be removed more efficiently, then boron might be able to be practically used in energetic formulations.

The primary work on boron particle burning has been studied with particle sizes in the micron range, and few works have investigated the use of nanoboron in composite systems. In separate works, Hunt et al.[140] and Park et al.[44] have shown decreasing activation energies with decreasing particle sizes, leading to increased reactivity. A lower activation energy should also imply a lower ignition temperature, and this was indeed corroborated by various authors such as Parr[141] and Bazyn[72]. When nanoaluminum is used in place of its micron-sized counterpart in composite systems, an increase of 1000 in the reactivity has been reported[1], therefore, we wanted to investigate the performance of nanoboron in such systems. It will be demonstrated

from constant-volume combustion experiments that nanoboron, while very unreactive itself, can be used to enhance the reactivity of nanoaluminum-based MICs. We develop a heat transfer model for boron particles surrounded by an aluminum thermite reaction, and propose that the aluminum reaction augments the burning of the boron by providing a high-temperature environment for fast ignition and combustion of the boron.

5.3 Experimental

5.3.1 Sample Preparation

For this work, stoichiometric samples (MICs) were prepared with the fuel being composites of boron and aluminum, and the oxidizer always being copper oxide. We will refer to the samples in terms of the molar percentage of boron in the fuel. For example, a 30%B sample means that 30% of the fuel atoms are boron, 70% are aluminum, and the corresponding amount of copper oxide is added to make the overall mixture stoichiometric assuming complete conversion to Al_2O_3 and B_2O_3. The aluminum used was obtained from the Argonide Corporation, and designated as "50 nm ALEX" by the supplier. ALEX is a nano-sized aluminum formed from the electroexplosion of an aluminum wire[142]. The nanoboron utilized in this study was termed SB99 and was obtained from the SB Boron Corporation. The average primary particle diameter is given to be 62 nm[82]. A second boron sample designated as SB95 was also obtained from the SB Boron Corporation. SB95 is an amorphous boron powder with particles sizes ranging up to 700 nm, as measured by a Fisher Sub-Sieve Sizer (FSSS). The oxidizer was copper (II) oxide nanopowder purchased from Sigma Aldrich, and had an average primary particle diameter and surface area specified by the supplier to be <50 nm and 29 m^2/g, respectively. Thermogravimetric Analysis (TGA) was performed (using a 50/50 Ar/O_2 environment and a heating rate of 5 K/min up to 1200 C) on both the aluminum and SB99 boron

samples to determine the amount of elemental metal (active content or activity) in the particles. TGA showed the aluminum to be 82% active, while the SB99 boron was found to be 72% active by mass. The SB95 active content was 96%, specified by the supplier. A summary of the materials used is given below in Table 5.2.

Table 5.2 A summary of nanopowders used in this work, including average primary particle diameter and active amount by mass.

Fuel	Source	Avg primary particle diameter	Measured by	Active Content	Measured by
Al	ALEX	50 nm	TEM	82%	TGA
B	SB-99	62 nm	Reference 23	72%	TGA
B	SB-95	700 nm	FSSS	96%	Supplier
Oxidizer					
CuO	Sigma-Aldrich	<50 nm	Sigma-Aldrich		

5.3.2 Measurement of Reactivity

In this work, we use the pressurization rate inside a small combustion cell as a measurement of the reactivity. A fixed mass (25 mg) of the sample powder was placed inside a constant-volume (~13 cc) pressure cell. Pressure signals of various samples are shown in Figure 5.1 as an example of the kind of typical data obtained for the combustion tests. We show two "slow" reactions (90% and 70%B) along with two "fast" reactions (50% and 30%B), and the reader should note that the time scale is very different. Decreasing the time scale causes a noisier signal, but is necessary in order to capture the first peak with finer time resolution. Another thing to point out in the signal is shock waves "ringing" off the walls, seen in the data as oscillatory behavior of the signal after the first peak. In all of these pressure traces, the first oscillation can be seen around 120 μs after the first major peak (this is most obvious in the 70%B trace). This corresponds to the approximate time it takes for a pressure wave to reflect off the

wall directly opposite the sensor. In the two "fast" pressure traces, there are some new peaks (i.e. around 50 μs). These could be caused by some secondary burning within the system, and we should not rule this out as a possibility. However, it may also be simply an artifact of the geometry and/or ejection of the powder after the pressure wave reflects off other walls of the cell or the sample holder.

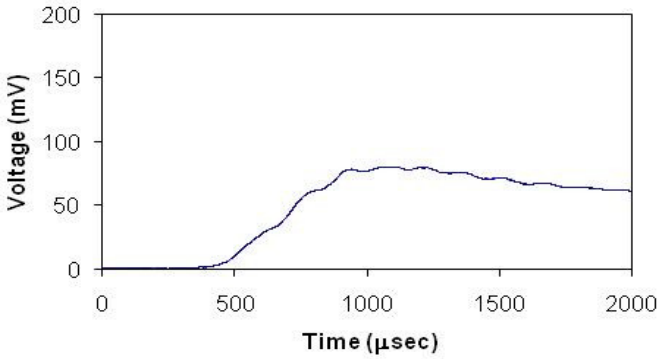

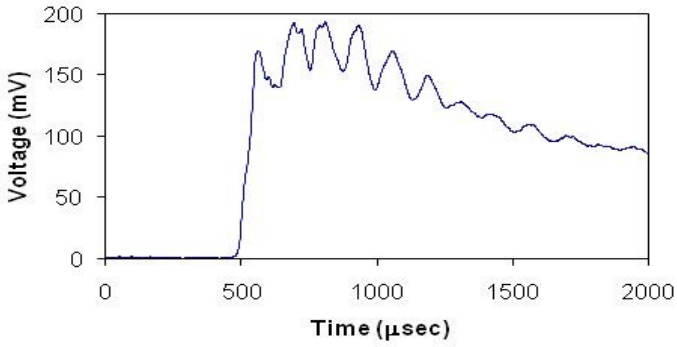

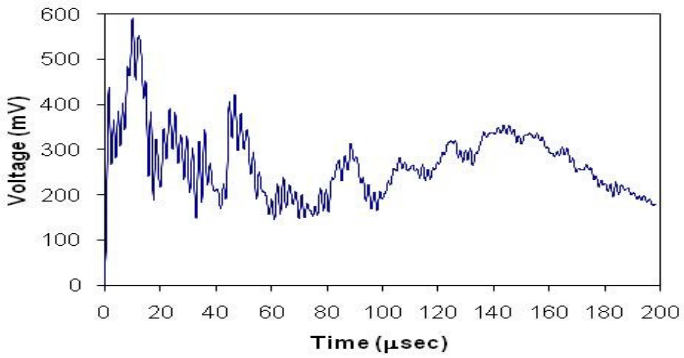

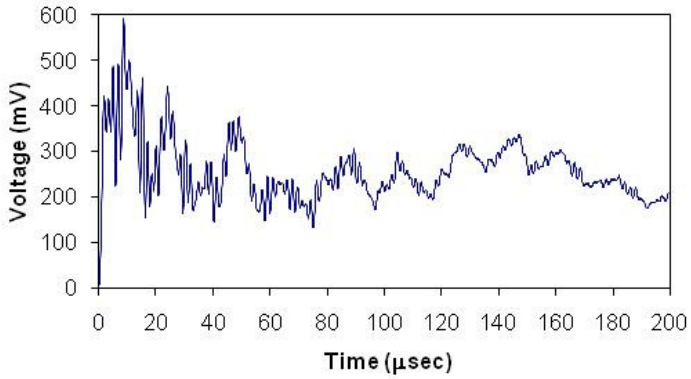

Figure 5.1 From top to bottom: Pressure traces for 90% (slowest), 70%, 50%, and 30% (fastest) B.

5.4 Results and Discussion

Shown in Figure 5.2 is the pressurization rate as a function of %B in an Al / B / CuO mixture for both 62 nm and 700 nm boron, along with data from a MIC of Al / CuO for comparison. It can be seen that, when compared to pure Al / CuO, an enhancement in reactivity is achieved for the cases where nanoboron is added as the minor component of the fuel (<50% by mol). It is also clear that a MIC comprised of boron as the primary fuel is quite ineffective and considerably underperforms an aluminum-based MIC. It can also be seen that, not only is 700 nm boron less reactive than its nano-counterpart, but there is no enhancement effect when added to nanoaluminum in any amount.

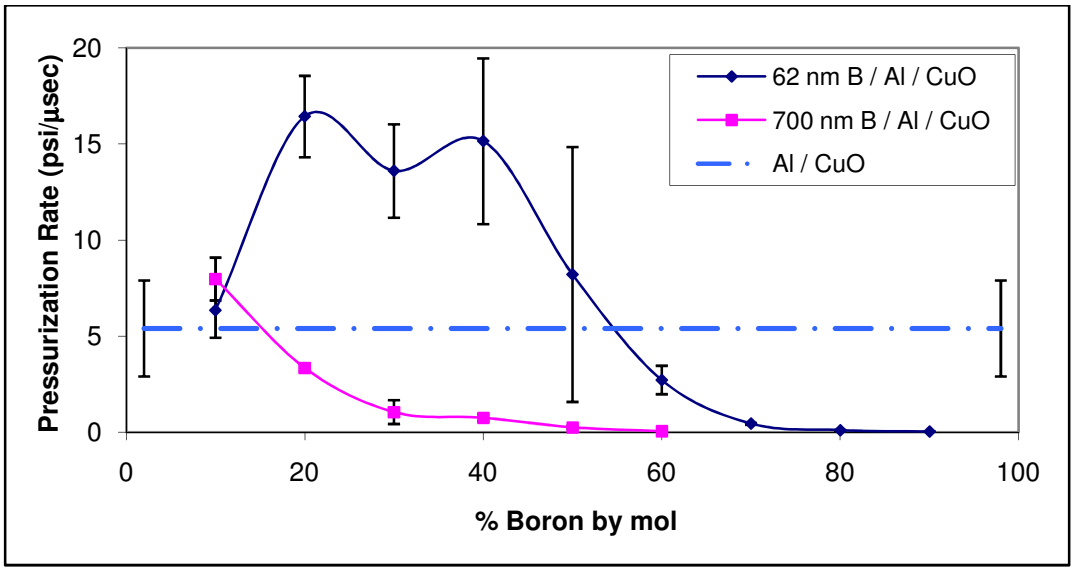

Figure 5.2 Experimental pressurization rate as a function of %Boron in an Al / B / CuO MIC for both nano and micron-sized boron. The horizontal line is Al / CuO data, included for comparison. Error bars represent the standard deviation of the experimental data.

Given that the data suggests that an enhancement in MIC burning occurs only when boron is the minor component, it is reasonable to speculate that the primary reaction (Al / CuO) is allowing for efficient ignition and combustion of the boron. The enhancement begins at <50%B by mol, and so we sought an explanation as to why this point was important. In order to examine this, an appropriate thermodynamic calculation is to look at the adiabatic flame temperature assuming that the aluminum reacts with the copper oxide, while the boron is acting as an inert material. The CHEETAH code (using the JCZS product library[143] as recommended by Sanders et al.[98]) was used to calculate the adiabatic flame temperature for the various mixtures (assuming the boron to be inert) and the results are shown in Figure 5.3. From Figure 5.3 we see that the mixtures with <50%B can reach temperatures higher than 2350 K, which is above the boiling point of B_2O_3 (2338 K) and the melting point of B (2350 K). Given that the experiment also showed an enhancement in this regime, it suggests that the primary reaction (Al

/ CuO) provides the energy necessary to remove the oxide shell and/or melt the boron, and thus enable it to participate in the combustion and enhance the reactivity. The removal of the oxide shell was discussed earlier as being necessary, while the melting of a nanoparticle can increase its reactivity significantly by allowing the fuel to become more mobile, as was seen by Rai et al.[48] for nanoaluminum.

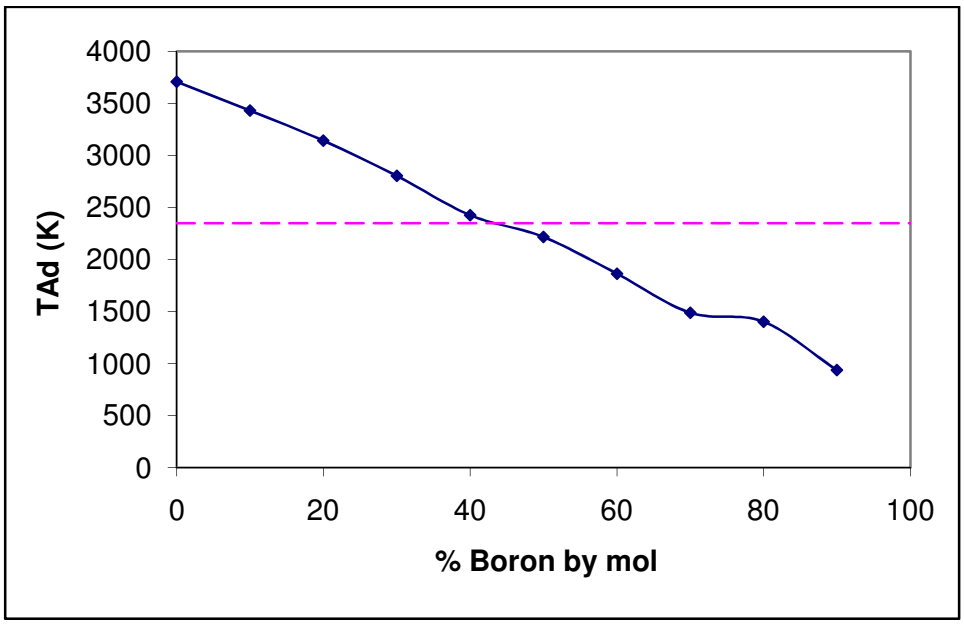

Figure 5.3 Adiabatic flame temperature calculations for Al / B / CuO mixture. B is considered inert in these calculations. The dotted line is 2350 K, the melting temperature of boron and above the boiling point of B_2O_3.

The experimentally measured rise times are shown in Figure 5.4, and include the 62 nm and 700 nm boron along with the 17 μs rise time for the Al / CuO reaction. Clearly, addition of the smaller boron decreases the rise time below that of Al / CuO when added as the minor component, while the larger boron only slows the reaction down. The data indicates that the 62 nm boron is participating in the combustion, and so an appropriate calculation should compare the timescale of the Al / CuO reaction (17 μs) to the timescale of heating a boron particle up to the surrounding temperature so that it can combust. A heat transfer model is developed to

investigate these time scales when the surrounding temperature is above 2350 K, the point where the experimental enhancement is observed.

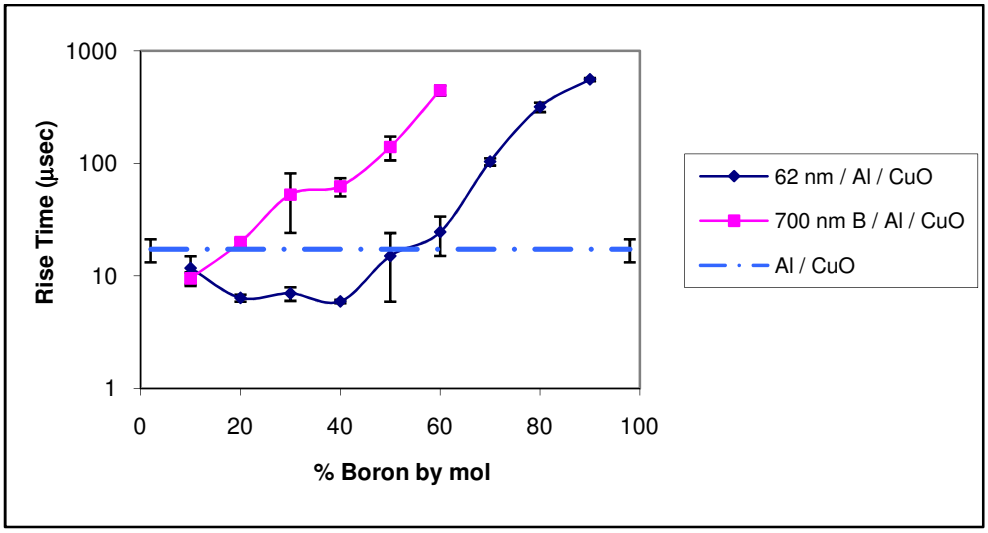

Figure 5.4 Experimental rise times as a function of %B in an Al / B / CuO MIC for both nano and micron-sized boron. The horizontal line is Al / CuO data, included for comparison. Error bars represent the standard deviation of the experimental data.

5.4.1 Phenomenological Heat Transfer Model

Here we develop a simple heat transfer model for a boron particle in a high temperature (>2350 K) environment. Several assumptions are made to simplify the problem:

1) The Al and CuO particles are evenly distributed about single boron particles.
2) The B_2O_3 shell thickness is 3.1 nm and 4.5 nm for the 62 nm and 700 nm particles, respectively. This is calculated by using the particle size, active content by mass, and bulk densities of B and B_2O_3 (2.34 g/cm^3 and 2.46 g/cm^3, respectively).
3) The convective term only considers energy transferred through collisions with gas molecules.

4) Interparticle radiation was found to make little difference to the model results, and thus was not included.

With the above assumptions in place, heat is convectively transferred to the particle by the gaseous species present during the Al / CuO reaction. The convection term can be written as the product of the heat transfer coefficient, h, the particle surface area, and the temperature difference between the surrounding environment and the particle.

$$\dot{q}_{conv} = hA(T - T_P) \tag{5.1}$$

The heat transfer coefficient for a solid sphere in a gaseous environment can be written in terms of the particle Nusselt number, Nu, the thermal conductivity of the gas, k_G, and the particle diameter as:

$$h = \frac{Nuk_G}{d_P} \tag{5.2}$$

For particles with diameters much greater than the mean free path of the gas, the Nusselt number approaches a constant value of 2. However, the particle sizes in this work are comparable to the mean free path, and thus are in a transitional regime between continuum and free-molecular heat transfer. In this regime, the Nusselt number is a function of the particle Knudsen number[6]. The adiabatic flame temperature and the experimental peak to peak pressure rise, shown in Figure 5.5, are used to estimate the mean free path, and thus the particle Knudsen numbers. The corresponding Nusselt numbers are then obtained from Figure 4 in Fillippov et al.[6] , and a polynomial fit is applied to write the Nusselt number as a function of temperature for the range of adiabatic flame temperatures achieved in the mixtures. This gives a range of Nusselt numbers from 0.06 to 0.13 for the 62 nm boron, and 0.34 to 0.54 for the 700 nm boron.

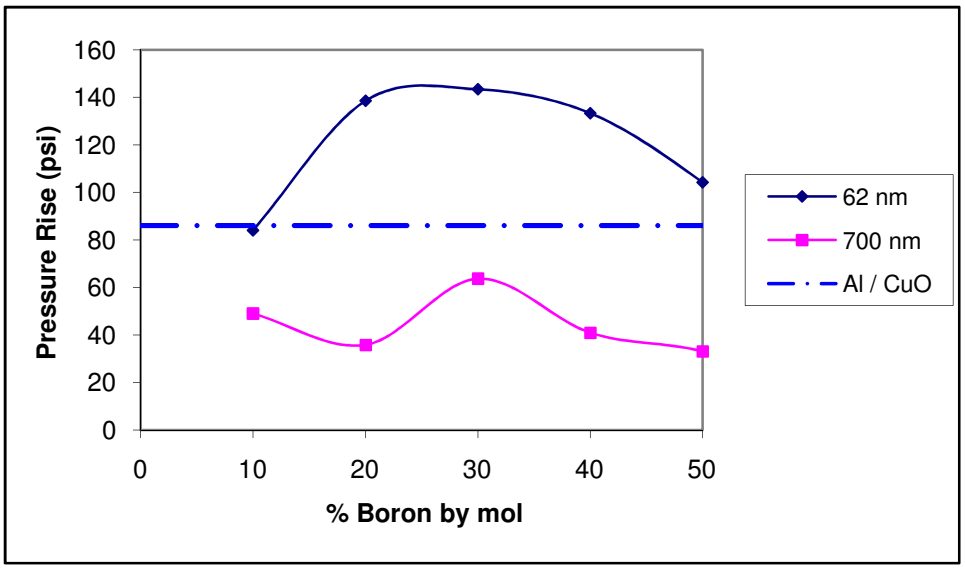

Figure 5.5 Experimentally measured pressure rise in the region where an enhanced reactivity is observed (<50%B by mol).

The thermal conductivity also changes as a function of the gas temperature and composition. The CHEETAH calculations (assuming B to be inert) were used to obtain the equilibrium species distribution. Since only nitrogen, oxygen and copper are in the product vapor an effective thermal conductivity is obtained as a molar average. For oxygen and nitrogen, the thermal conductivity as a function of temperature is given in Incropera and DeWitt[144] up to 3000 K, and we extrapolate it to 3500 K. For copper, the thermal conductivity can be estimated as a function of temperature using kinetic theory for a monatomic gas in terms of the atomic mass (m) and diameter (σ):

$$k(T) = \left(\frac{k_B T}{\pi^3 m \sigma^4} \right)^{1/2} \tag{5.3}$$

The convection term has now been completely formulated as a function of temperature and particle properties. To calculate the total heating time, we calculate three individual processes.

1) Sensible heating from room temperature to the surrounding temperature (Eq 5.5)

2) Time to evaporate the initial B_2O_3 shell (constant Tp = 2338 K) (Eq 5.6)

3) Time to melt the boron (constant Tp = 2350 K) (Eq 5.7)

(Note: The time to melt the B_2O_3 shell is insignificant).

We have included radiation heat loss by assuming the boron particles transfer energy to the pressure cell wall at 300 K (T_{Wall}). Here, ε is the emissivity of B_2O_3 (assumed to be 1), σ_B is the Stefan-Boltzmann constant, and A is the particle surface area.

$$\dot{q}_{Rad} = \varepsilon \sigma_B A(T_P^{\,4} - T_{Wall}^{\,4}) \tag{5.4}$$

The individual heating times for the above three cases can be obtained by integration of Equations 5.5-5.7, respectively:

$$\frac{dT_P}{dt} = \frac{(\dot{q}_{conv} - \dot{q}_{Rad})}{m \cdot C_P} \tag{5.5}$$

$$\frac{dm}{dt} = \frac{(\dot{q}_{conv} - \dot{q}_{Rad})}{H_{Vap,B_2O_3}} \tag{5.6}$$

$$\frac{dm}{dt} = \frac{(\dot{q}_{conv} - \dot{q}_{Rad})}{H_{Fus,B}} \tag{5.7}$$

Here T_P is the particle temperature, m is the particle mass, C_P is the heat capacity, $H_{Vap,\ B2O3}$ is the latent heat of vaporization of B_2O_3 at 2338 K (5.19 MJ/kg), and $H_{Fus,B}$ is the latent heat of fusion for boron at 2350 K (4.64 MJ/kg). The heat capacity used was weighted (since both B and B_2O_3 are present in the particle), and was calculated as a function of particle temperature using the Shomate approximation of the coefficients in the NIST-JANAF thermochemical tables[145].

Equations 5.5-5.7 were numerically integrated, and the results of the model are shown for 62 nm boron and 700 nm boron in Figures 5.6 and 5.7, respectively. The calculations indicate that the total time to heat the 62 nm boron up to the surrounding temperature is faster than 17 μs, the Al / CuO time scale, at temperatures above 2370 K while for the 700 nm boron, the time always lags and does not become faster until the surrounding temperature is above 2800 K. It also is evident that the removal of the oxide shell alone cannot explain why 700 nm boron does not enhance the reactivity, since it is removed almost as quickly as in the case of 62 nm boron. However, we see that the sensible heating time for the micronboron is significantly longer than for the nanoboron, and we also see that the time required to melt the micron boron is over an order of magnitude longer than for the nanoboron. Thus, from the experimental and model results, it's reasonable to conclude that for boron to enhance the reactivity, the particles must be heated, have their oxide shell removed, and be melted on a timescale shorter than that for the thermite reaction in order to participate in the combustion and enhance the reactivity.

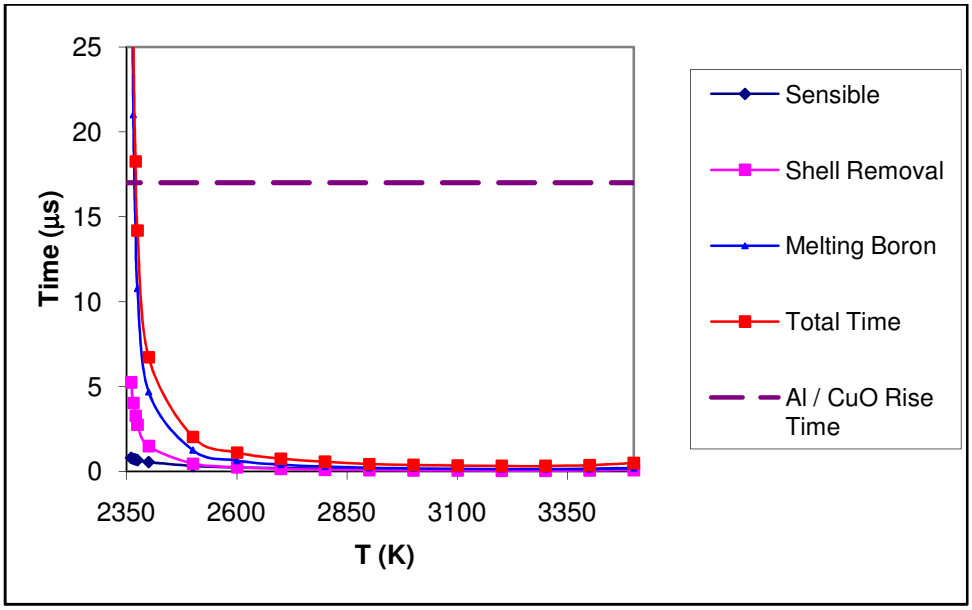

Figure 5.6 Model predictions of the timescales as a function of surrounding temperature for a 62 nm boron particle.

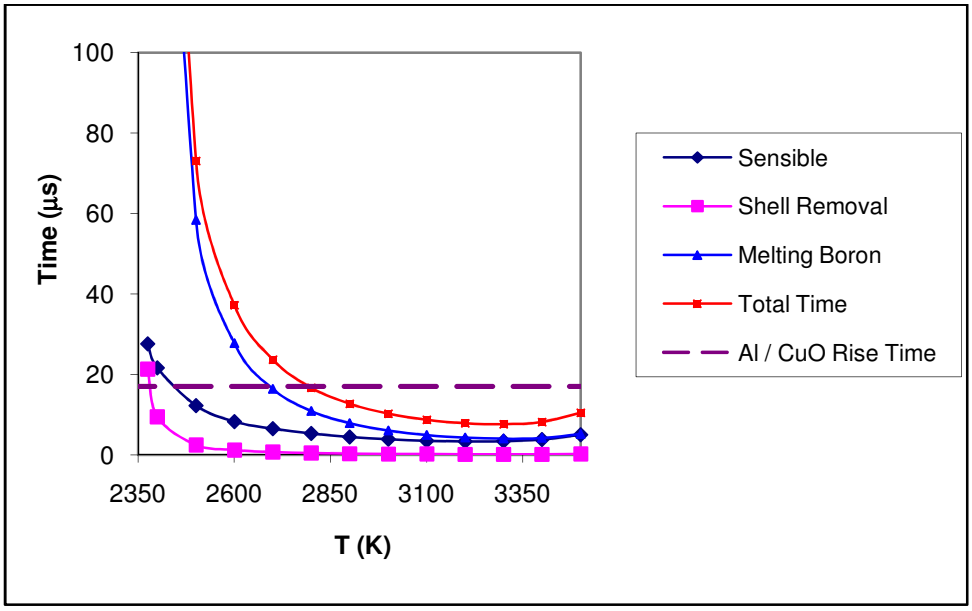

Figure 5.7 Model predictions of the timescales as a function of surrounding temperature for a 700 nm boron particle.

Boron's ability to enhance the reactivity is most likely due to the increased gas production when boron is present as a fuel. If the boron is able to participate in the combustion, it should oxidize to gaseous B_2O_3, along with sub-oxides such as BO and BO_2. As a result, the absolute pressure rise could be higher than that observed for Al / CuO, where the temperature is below the Al_2O_3 boiling point and thus the oxide product is molten. To investigate this, CHEETAH calculations were again performed, but now the boron was assumed to be reactive. The adiabatic temperature and gas species distribution as a function of %B are shown in Figure 5.8, and the formation of a significant amount of boron oxide species (BO, BO_2, B_2O_3) in the products can be seen. The calculation predicts the total gas production to increase relative to an Al / CuO mixture, where copper is the only major gas product. The increase in gaseous products increases the total pressure, and this was consistent with the experimental data (Figure 5.5).

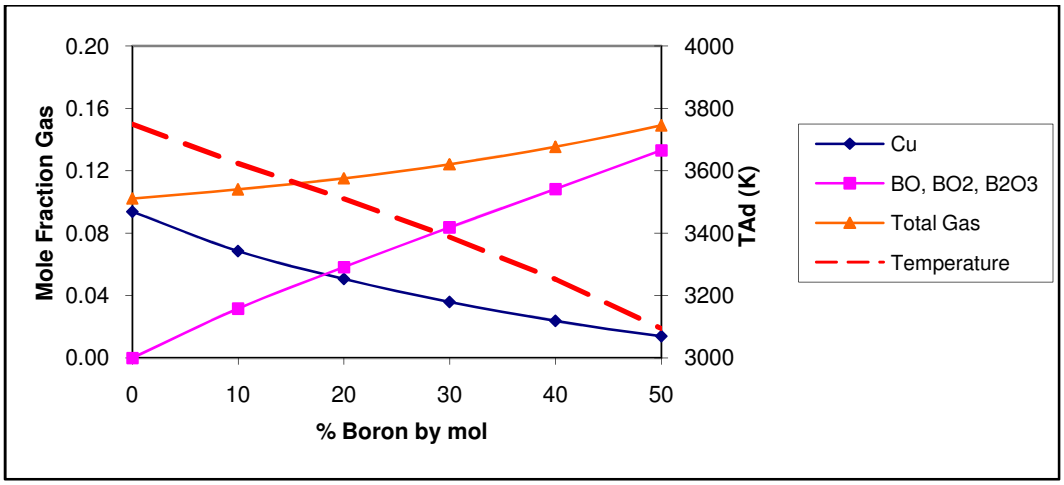

Figure 5.8 Adiabatic temperature and equilibrium gas species composition assuming boron to be reactive.

Not only does gas production affect the pressure rise, it can also affect the rise time. This is because the mode of energy propagation through a loose powder MIC is speculated to be primarily via convection of gaseous intermediate species[104]. Other experimental works[98] show a correlation between the peak reactivity and the peak gas production, but this does not necessarily correspond to the maximum temperature. In this work, the pressure rise time does become faster (see Figure 5.4) for the cases where the enhancement was seen. This is likely a result of the increased gas production aiding in the convective energy propagation through the loose powder.

A major assumption in our model was that the convective heat transfer to the particle only happened through collisions with gaseous species. However, additionally there could be condensation of intermediate gaseous species, such as copper, onto the particles. This heat of condensation would enhance the heat transfer to the particles, and decrease the time to heat the boron even further than predicted by the model. However, a layer of condensed material on the particles would serve as a barrier to oxidation much like the B_2O_3 does if it is not removed. The complexities of that effect are beyond the scope of this investigation.

5.5 Main Conclusions of Work

It has been demonstrated from constant-volume combustion studies that the addition of nanoboron to a MIC of Al / CuO can enhance the reactivity when the boron is <50 mol% of the fuel, while an enhancement was not observed when micronboron was used instead. Thermodynamic calculations assuming the boron to be inert showed that the aluminum reaction with CuO was able to raise the mixture temperature above 2350 K, above the boiling point of B_2O_3 and melting point of boron. This led to the development of a phenomenological heat transfer model which investigated the sensible and latent heating time for boron particles surrounded by a high-temperature environment. The model shows the heating time becomes faster than the Al / CuO reaction time, 17 μs, at temperatures above 2370 K for the nanoboron and above 2800 K for the larger boron. The heating time for the micronboron severely lags because of the very large time to melt the boron. From the experimental and model results, we speculate that not only is the sensible heating and removal of the oxide shell necessary for fast reaction, the melting of the boron is also critical.

Chapter 6: Simultaneous Pressure and Optical Measurements of Nanoaluminum Thermites: Investigating the Reaction Mechanism

Relevant Experimental Techniques:

a) Combustion cell with optical measurements, Section 4.3.1

-Measure the pressurization rate (reactivity) of the mixtures

-Measure the optical emission (burn time) of the thermites

b) CHEETAH Equilibrium Code, Section 4.4

-Predict the adiabatic flame temperature and species distribution

c) NASA CEA Equilibrium Code, Section 4.4

-Predict the decomposition behavior of metal oxides at a constant temperature and pressure.

d) Fast heated wire / Mass spectrometry, Section 4.3.3.2

-Only discussed briefly, but showed evidence of O_2 being released before anything else during fast heating, a major concept in this work.

6.1 Overview

This work was purely an investigation of the reaction mechanism in various nanocomposite thermites. The combustion cell was modified to allow for simultaneous collection of the optical emission along with the pressure signal. Up until this study, it was commonplace for researchers to try and explain experimental trends in pressure by using thermodynamic equilibrium predictions. The problem, however, is that no one has ever verified the extent of reaction within the very fast timescale of the pressure rise, and thus whether equilibrium calculations were even appropriate to use. In conventional thinking, as a fuel and oxidizer burns to produce a gas, the temperature and pressure should rise concurrently as further reaction leads to more generation of products. In nanocomposite thermites, however, it will be shown that the pressure and optical signals (temperature) peak at very different timescales, with

the pressure rising much faster than the optical emission in certain systems. If the optical signal can indeed correlate with the temperature, the results suggest that the pressurization is actually occurring at a low temperature, and thus must arise from a non-equilibrium process.

Around the time of this work, some results from the mass spectrometer system found that the emergence of O_2 occurs before other species indicative of reaction (i.e. Cu). This work expanded on these findings, and provided an alternate explanation for the pressurization; that it arises from the evolution of O_2 gas during the thermal decomposition of the metal oxides. Conceptually, the aluminum fuel ignites in some way with the oxidizer and energy is liberated from the reaction. This energy is utilized to further decompose the oxidizer on a timescale much faster than the aluminum burning (depending on the oxidizer). The decomposition pressurizes the system with gaseous oxidizing species, and the aluminum continues to burn in the pressurized, gaseous oxidizing environment.

One of the major findings of this work is the idea that the pressurization and optical emission can occur on different timescales, depending on the system, and this work provides an explanation as to how this is possible. If the oxidizer cannot be decomposed rapidly, then the burning is slow, as it is rate-limited by the oxidizer. This is experimentally seen as a concurrent pressure and optical signal. However, if the oxidizer can decompose rapidly to release oxidizing gases, then the thermite reaches a limit where the burning (optical emission) becomes rate-limited by the aluminum. This is experimentally seen as a fast pressure rise followed by a prolonged optical signal. The gas production mechanism will be oxidizer-dependent, i.e. MoO_3 sublimates, CuO decomposes, etc., and this work suggests that an oxidizer should not be selected based on its ability to produce equilibrium gas, but should be selected based on its ability to produce intermediate gaseous species via rapid decomposition or sublimation.

6.2 Introduction and Relevant Literature Review

A variety of metal oxides have been used in nano-Al based thermites, including, but not limited to, CuO, WO_3, MoO_3, Bi_2O_3 and Fe_2O_3. The burning of these thermites is highly sensitive to the choice of oxidizer, however, the reactivity typically does not scale with common parameters such as energy density or adiabatic flame temperature. Thus, the reaction mechanisms likely differ from system to systems. Certain oxidizers can melt upon heating (Bi_2O_3, WO_3), some decompose to suboxides and release O_2 gas (CuO, Fe_2O_3), and others sublimate (MoO_3). Understanding these phase change processes is likely a critical part to understanding the kinetics of the reaction, since the O_2 must be liberated from the metal oxide in order to react with the aluminum fuel.

A variety of experimental methods have been used to investigate the reactivity of these thermites, in an effort to understand the mechanisms involved during the reaction. These including thermal analysis,[73, 74] combustion in a shock tube,[63] flame propagation in open channels[51, 91-96] and tubes,[98-100] heated filament studies,[74] and constant-volume pressure cells.[50, 52, 96, 101-103] The pressure signal and/or optical emission are can be collected to investigate the reactivity of these materials. The pressurization rate has been shown to correlate with flame propagation velocities,[89] and is typically reported as a relative measurement of reactivity. Other authors[98, 100] have shown a correlation between the peak pressure and propagation velocity. Recently, authors[98-100] have used an instrumented burn tube to collect the optical and pressure signals simultaneously.

If the reaction is self-propagating, there are three phenomena occurring simultaneously; ignition of the material, reaction between the fuel and oxidizer, and energy propagation. None of these phenomena themselves are well understood at the nanoscale or with practical (>10^6 K/s)

heating rates. Nanoaluminum has been shown to have a much lower ignition temperature than micron-sized aluminum. While both micron-sized particles and nanoparticle have a naturally formed oxide shell surrounding the elemental core, in the nanoparticle the oxide shell can account for a relatively large portion of the particles mass. Upon heating, the aluminum core melts at a much lower temperature than the oxide shell (933 K vs. 2327 K) and can expand, inducing stresses on the oxide shell. The response of the shell to this expansion may be different for a nanoparticle vs a large particle, leading to a lower ignition temperature. Some authors argue that a decomposition or phase change in the shell occurs, thus allowing aluminum to diffuse outwards,[15, 48, 61],while other authors argue that the rapid expansion of the core induces enough stress to completely shatter the shell and unload the aluminum as small liquid clusters.[109-111] The burning mechanism of aluminum thereafter will be quite different depending on what mechanism of ignition happens.

The burning mechanism of very small aluminum particles is not well understood. For combustion-type applications, the heating rate of nanoparticles will be high (10^6-10^8 K/s). Experiments should be designed to reproduce these heating rates, and one such experimental technique which accomplishes this is a shock tube. Bazyn et al.[71, 72] studied the combustion of nanoaluminum at elevated temperatures and pressures in a shock tube. The authors combust aluminum at varying temperatures, pressures and oxygen mole fractions, and use three-color pyrometry to measure the particle temperature. The authors show that the ambient temperature plays a significant roll on the aluminum combustion, indicating that heat losses are much more important for nanoparticles than for larger sized particles. The same authors[26] show that a transition from a diffusion to a kinetic-limited mechanism begins to occur below a critical

particle size, ~10 μm. For a kinetic-limited mechanism, the flame sits closer to, if not on, the particle surface and the flame temperature is limited by the boiling point of aluminum.

The third phenomena occurring in the reaction mechanism of a self-propagating MIC is energy propagation, and authors[97, 98] have shown that the dominant mode of energy propagation through a loose powder is convection. As a result, MICs often exhibit an optimal reactivity which correlates with gas production instead of temperature. For example, Sanders et al.[98] found that Al/CuO has a peak reactivity for an equivalence ratio very near stoichiometric. The authors use equilibrium calculations to show that a stoichiometric mixture produces the maximum amount of Cu gas, and any deviation from this mixture will lower the temperature, hindering the gas production, and hence the convective mode of energy propagation. Conversely, other mixtures often exhibit enhanced reactivity for slightly fuel-rich mixtures. The same authors show that an Al/Bi_2O_3 thermite has a greater propagation velocity and peak pressure for an equivalence ratio of 1.3 compared to an equivalence ratio of 1.0, even though the calculated adiabatic flame temperature is a few hundred degrees lower at the fuel rich condition. Also, Al/MoO_3 shows an optimal reactivity for an equivalence ratio around 1.2-1.4. The enhancement is attributed to enhanced gas production for fuel-rich conditions, as it correlates to thermodynamic equilibrium calculations.

Both Sanders et al.[98] and Malchi et al.[100] show that the peak pressure correlates with the flame propagation velocity. In the two works, an instrumented burn tube is used to simultaneously collect the pressure and optical signals. The authors use equilibrium calculations to show correlations between the predicted equilibrium gas and the experimental trends in pressure. From Figure 9 in Malchi et al.,[100] it appears that the optical signal reaches its peak on the same time scale as the pressure does, ~10 μs.

6.3 Thermochemistry of Mixtures

Recent mass spectrometry work by our group[146] had indicated that oxygen release from the metal oxide decomposition is important in the reaction mechanism of thermites, in particular for CuO and Fe_2O_3. The current work expands on this idea to investigate the burning of nanoaluminum composites in a constant-volume pressure cell. The pressure and optical signals are collected simultaneously to have two different measurements of reactivity. The oxides studied are CuO, Fe_2O_3, and SnO_2. These particular oxidizers have adiabatic flame temperatures at or above the boiling point of the metal in the metal oxide, and the gas is predicted to be almost entirely comprised of this metal at equilibrium. These oxidizers also decompose to suboxides and gaseous oxidizers, which will be discussed in more detail later. The calculated equilibrium for stoichiometric mixtures of these oxidizers with aluminum is shown in Table 6.1. The CHEETAH 4.0 code was used with the JCZS product library,[143] as recommended by Sanders et al.[98] The mixture density was assumed to be 0.00192 g/cc, since we always react 25 mg of material in our 13 cc cell. The experimental pressurization rate is also given for comparison.

Table 6.1 Calculated temperature and gas production for stoichiometric mixtures of various metal oxides with nanoaluminum.

Metal Oxide	Boiling Point Metal (K)	Tad (Cheetah UV) (K)	Moles Gas / kg reactant	Contribution of Metal to the Total Gas	Experimental Pressurization Rate (psi/μsec)
CuO	2837	2967	3.5	97%	11.1
SnO2	2533	2573	2.2	94%	7.7
Fe2O3	3023	2834	0.52	98%	0.017
WO3	5933	3447	0.13	<0.01%	0.028

We will start by investigating the simultaneous pressure and optical signals for the three oxidizers mentioned above. We will then go on to perturb the system by adding increasing amounts of WO_3 in place of the metal oxide. We chose WO_3 because, when added as the minor component, the adiabatic temperature remains relatively unchanged. Also, WO_3 is predicted to produce very little equilibrium gas and also does not decompose to O_2 or any significant gaseous oxidizing species until >2800 K. All blends are stoichiometric and are referred to in terms of the molar %WO_3 in the oxidizer. For example, a 40%WO_3 mixture means that 40% of the oxidizer molecules are WO_3, 60% are the other oxidizer, and the corresponding amount of aluminum is added to make the overall mixture stoichiometric assuming complete conversion to Al_2O_3.

6.4 Experimental

The aluminum used in this study was 50 nm ALEX, purchased from the Argonide Corporation. The aluminum was found to be 70% active by mass, as measured in a TGA. All other materials were purchased from Sigma Aldrich, and have average particle diameters <100 nm as specified by the supplier. Thermites were prepared by the standard mixing technique. (Section 4.4).

A fixed mass (25 mg) of the powder was weighed out and placed in a small (13 cc free volume) combustion cell. The sample sits in a bowl-shaped sample holder, and a nichrome coil contacts the top of the powder so the reaction propagates downwards and into the holder upon ignition. Two ports (located on the sides of the cell) were utilized to collect the pressure and optical signal simultaneously. In one port a lens tube assembly, containing a plano-convex lens (f=50 mm), collected light and imaged onto an optical fiber coupled to a high speed Si photo detector (1 ns rise time, model DET10A, Thorlabs). In the second port a piezo-electric pressure sensor was employed, the details for which can be found in Prakash et al.[101].

The powder is ignited by manually increasing the voltage and current until the sample ignited. This is done as rapidly as possible to avoid significant heating of the powder. The data collection was triggered by the rising optical signal. There is always a ~60 μs delay between the onset of the optical emission and the onset of the pressure signal. This is due to the time delay between the optical triggering and when the pressure wave arrives at the sensor, a few centimeters away. The pressure data was thus shifted in time for the analysis so that the onset of the pressure and light are shown to occur simultaneously.

6.5 Results and Discussion

We first show the simultaneous pressure and optical signals for pure Al/CuO, Al/SnO_2, and Al/Fe_2O_3 in Figure 6.1. Also included is pure Al/WO_3 for comparison. Note that the axes for each plot have all been adjusted to fill the plot area. From Figure 6.1, we can immediately see that CuO and SnO_2 exhibit a pressure peak well before the optical signal reaches its peak. In the case of Fe_2O_3 and WO_3, the pressure and optical signals occur concurrently.

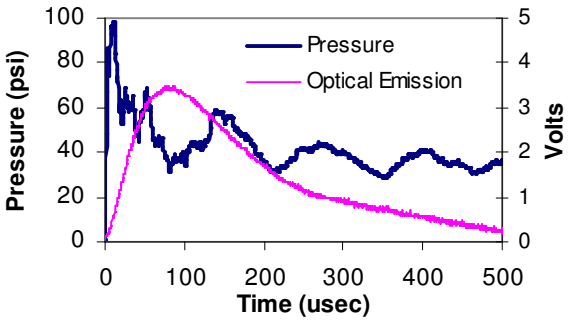

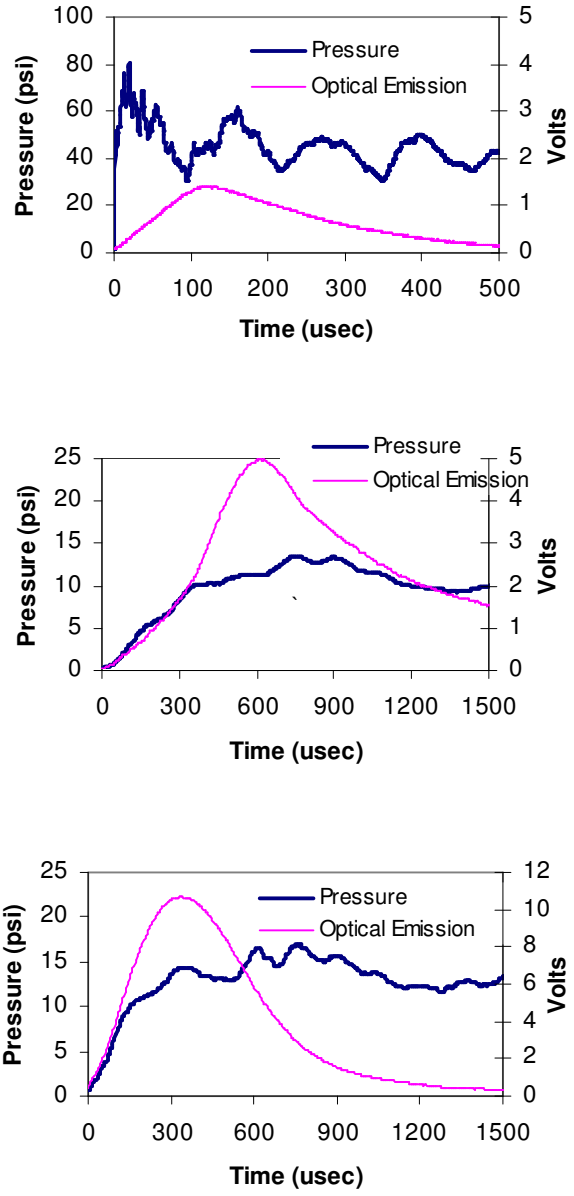

Figure 6.1 Simultaneous optical and pressure signals from top to bottom: Al/CuO, Al/SnO_2, and Al/Fe_2O_3. Also shown is Al/WO_3 (bottom).

It is important to take a moment to discuss our interpretation of the optical signal and the various considerations which may complicate the analysis. First of all, an accurate measurement of temperature is for such a large sample is greatly complicated by the fact that the viewing area is optically thick and thus the measurement would be biased to the outermost, or coolest, region

of the reaction. Also, we have no reason to believe that the flame region would be spatially homogeneous. It is possible that the optical signal could be measuring the emission from large chunks of material which ignite later in time, however, we do not believe this to be the case since we do see actual evidence of this occasionally (i.e. a "bump" in the optical signal after the peak). The experimental data shown in Figure 6.1 is for a sample mass of 25 mg. In order to determine whether the sample mass had any effect on the optical signal, we also repeated this for a sample mass of 10mg. In this case we see a decrease in the pressure signal (as expected) but no change in the optical signal. The relative intensities of the optical signal are qualitatively consistent with what would be expected based on adiabatic flame temperature calculations (i.e. Al/WO_3 is the hottest/brightest and Al/SnO_2 is the coolest/weakest, with Al/CuO and Al/Fe_2O_3 being in between). Optical emission generally signifies a combustion event is occurring, and the intensity is highly sensitive to the temperature of radiating particles (~T^4). Therefore, we will simply use the optical measurement as a relative measurement of the system temperature, and we assume that the FWHM of the optical signal is capturing the burn time of the average sized particles in the system.

Now that the optical emission has been discussed, we see from Figure 6.1 that for the Al/CuO and Al/SnO_2 systems, the pressurization is happening well before the system temperature is at its peak value. These systems have adiabatic flame temperatures near the boiling point of the metal (Cu and Sn), and so the vaporization of the metal should not occur until the temperature is near its hottest point. This is clearly not the case for these two systems, and thus the pressure rise is likely caused by something else.

An alternate explanation is that the pressure rise is attributed to the decomposition of the oxidizer. We have recently investigated this idea for the Al/Fe_2O_3 and Al/CuO thermite system

using fast-heating wire experiments coupled with mass spectrometry. Upon rapid heating, a significant O_2 signal emerges first, followed by other species indicative of the reaction, i.e. Al_2O_3, Cu, Fe. The O_2 signal is a product of the thermal decomposition of the metal oxide in the case of both CuO and Fe_2O_3. An enhancement in the O_2 release (relative to the pure oxidizer) is seen for the thermite, indicating that some energy from the reaction further decomposes the oxidizer.

To illustrate this we use NASA's CEA code to show the decomposition behavior of the metal oxides in Figure 6.2, where the equilibrium species distribution is plotted as a function of temperature (Constant TP with P = 1 atm). The markers indicate the point where no oxygen-containing species remain in the condensed phase (i.e. Cu_2O(L) or Fe_3O_4(L), decomposition products of CuO and Fe_2O_3).

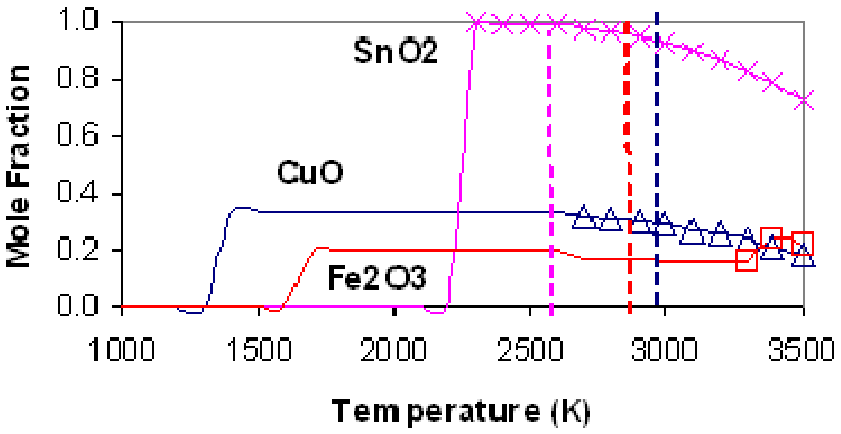

Figure 6.2 Gas release from oxidizer decomposition as a function of temperature. The gas is O_2 for all oxidizers, and includes SnO(g) for the SnO_2. The markers indicate the points where no oxygen remains in the condensed phase. The vertical line shows the adiabatic temperature for reference, from left to right; SnO_2, Fe_2O_3, CuO, and WO_3. Constant TP calculations assuming P=1atm for all runs. Note that WO_3 is not included since it does not decompose to O_2 upon its decomposition (>2800 K).

For all three oxidizers, we see the emergence of O_2 when the temperature reaches a certain value and the metal oxide decomposes to a suboxide and O_2. In the case of SnO_2 a significant amount of SnO gas is also formed during decomposition, therefore, we have lumped the O_2 and SnO together into one quantity, since both are gaseous decomposition products and are likely important in oxidizing the aluminum. Note that we do not include WO_3 in Figure 6.2 because WO_3 does not thermally decompose into significant amounts of O_2. Instead, the calculations show the emergence of other oxide species (i.e. WO_2, WO_3, $(WO_3)_x$).

From Figure 6.2 we see an interesting observation: CuO and SnO_2 fully decompose to gaseous oxidizing species at temperatures *below* their adiabatic flame temperatures. In contrast, Fe_2O_3 does not fully decompose until >3200 K, several hundred degrees above its adiabatic temperature. From the experimental data and the arguments above, it is reasonable to speculate that the decomposition of CuO and SnO_2 is what leads to the first pressure spike, followed by a much longer optical trace as the aluminum continues to burn. In the case of Fe_2O_3, the oxidizer cannot efficiently decompose, and therefore the decomposition may in fact be the rate limiting step. We must emphasize that we are not implying that the oxidizer has completely decomposed within the pressure rise time (we have no way to prove that it has not either). Instead we are simply using the thermodynamic calculations to suggest that CuO and SnO_2 may decompose more efficiently than Fe_2O_3 because of the nature of the adiabatic and decomposition temperatures, whereas this is not the case for Fe_2O_3. The extent of decomposition or decomposition pathway under such high heating rates is not something we can currently measure within the pressure rise time. That being said, we now turn to the experimental results where WO_3 is added.

The experimental pressurization rate is shown as a function of WO_3 for the three systems in Figure 6.3. For both the CuO and SnO_2 systems, the optimum reactivity occurs when no WO_3 is added, and drops significantly when even a small amount of WO_3 is introduced. For the Fe_2O_3, we see a significant enhancement and peak reactivity when the mixture is 80% WO_3. Clearly something in the blended Fe_2O_3/WO_3 system is enhancing the pressurization rate above either system alone.

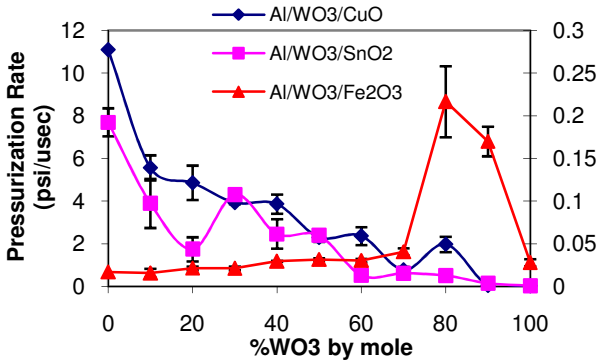

Figure 6.3 Experimental pressurization rate as a function of the molar % of WO_3 in the oxidizer. The $Al/WO_3/Fe_2O_3$ data is plotted on the secondary axis.

In order to show whether the trends in experimental pressurization rate could be explained by oxidizer decomposition, we seek some way to estimate the gaseous oxidizer (O_2 and SnO) release rate. Since knowledge of these rates is not well known, we assume the oxidizer decomposition and gas release rate are proportional to the number of moles of the decomposing species in the mixture (CuO, SnO_2, or Fe_2O_3). Because WO_3 does not show any decomposition products and gas release until >2800 K, we are fairly certain that WO_3 does not contribute to the initial pressure rise, at least in the CuO and SnO_2 systems. We chose to use pressurization rate rather than peak pressure as a measure of kinetics, since a peak pressure analysis can most easily be correlated only if one can assume complete decomposition of the oxidizer. The pressurization

rate and predicted oxidizer release rate are plotted for the three systems in Figure 6.4. The values have been normalized by the maximum.

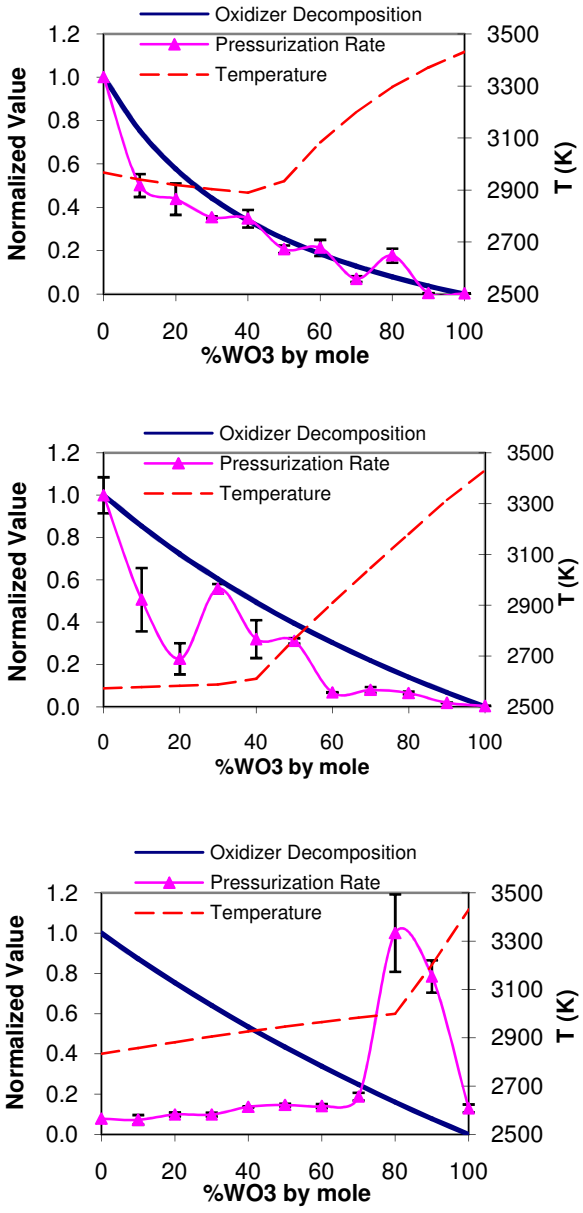

Figure 6.4 Gas release prediction and experimental pressurization rate (both normalized by the maximum value), along with the adiabatic temperature. Systems from top to bottom are Al/WO_3/CuO, Al/WO_3/SnO_2, and Al/WO_3/Fe_2O_3.

We see that the pressurization rate does indeed correlate with the predicted oxidizer release rate for the CuO and SnO_2 systems, but not for Fe_2O_3. This is further support that the pressurization rate is attributed to the oxidizer decomposition for the CuO and SnO_2. For the Fe_2O_3 system, the predicted oxygen release does not correlate with the trend in pressurization rate at all. We see a constant value of the pressurization rate up until about 70%WO_3, followed by a sharp jump to a peak at 80%, and then a decrease from 90-100% WO_3. One explanation for this behavior could be that the formation of Fe gas causes this peak, however, this does not explain why the pressurization rate is constant over such a wide range (0-70%). As WO_3 is added, we would expect the amount of Fe gas to change and affect the pressurization rate, but this was not observed. A more likely explanation is that the temperature reaches a high enough value to decompose the Fe_2O_3 efficiently. As discussed previously and shown in Figure 6.2, the adiabatic flame temperature of Al/Fe_2O_3 is lower than the point where Fe_2O_3 can fully decompose. As WO_3 is added the adiabatic temperature increases, and it's likely that at 80 and 90% WO_3, the temperature becomes high enough to efficiently decompose the $Fe2O_3$. To corroborate this idea, the raw data is shown for 70% and 80%WO_3 in the Al/WO_3/Fe_2O_3 system in Figure 6.5. What can be seen is that for 80%WO_3, the first pressure peak occurs well before the optical peak, while this is not the case for 70%. This is consistent with the idea that the system temperature reaches a point where the Fe_2O_3 can decompose efficiently, leading to a fast pressure spike relative to the burning.

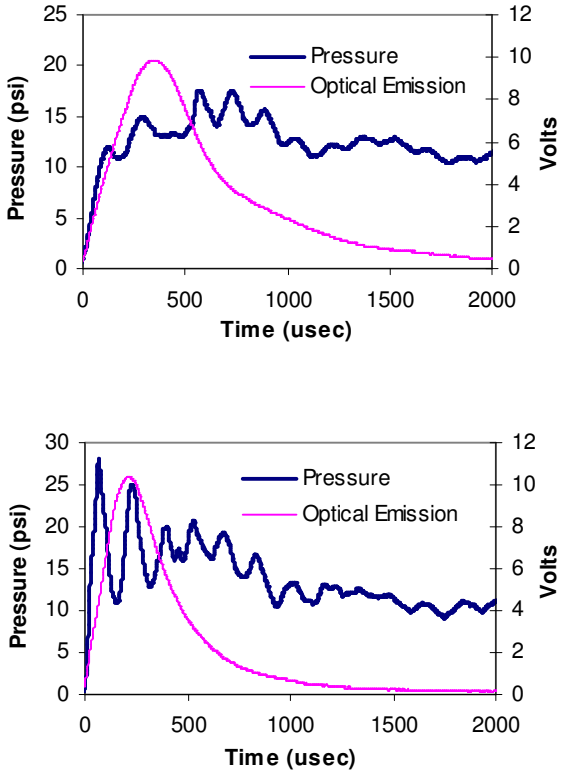

Figure 6.5 Raw data for the 70% (top) and 80% (bottom) WO_3 mixtures of Al/WO_3/Fe_2O_3. Note how the first major pressure peak occurs earlier than the optical peak for the 80% WO_3 mixture.

We can use the results and discussion thus far to make some speculations about the reaction mechanism. For systems where the adiabatic flame temperature is high enough and heat transfer is not limiting, when the fuel begins to burn, the oxidizer can decompose and pressurize the system faster than the reaction timescale. The fuel then continues to burn over a longer period, as can be seen in Figure 6.1 for the CuO and SnO_2. Systems such as these would thus be rate limited by the mechanism by which the aluminum burns in a gaseous oxidizing environment. For an oxidizer such as Fe_2O_3, the adiabatic flame temperature is below the point where the oxidizer can fully decompose and thus the oxidizer cannot decompose efficiently. The burning mechanism in this case is rate limited by the oxidizer decomposition and oxygen release.

The fact that the optical and pressure signals occur concurrently for Fe_2O_3 supports this argument, and indicates that the two are tightly coupled.

To further test these ideas, we can also look at the trends in the optical signals. We assume the burning time to be the full width half max of the optical signal. This is plotted for the three systems in Figure 6.6. The only system which shows a decrease in the burning time as the temperature increases (see Figure 6.4 for temperature) is the Fe_2O_3 system. For the other two systems, this is not the case. Instead, we see that the burning time does not change over a very wide range of added WO_3 (0-80%), even when WO_3 becomes the major component and the temperature increases. Also noteworthy is that the burning time is nearly identical for CuO and SnO_2, 185usec and 210usec, respectively. This supports our speculation that the burning is rate limited by the aluminum in these two systems, since the aluminum is the only common factor between the two systems. If we compare these burning times to those reported by Bazyn et al.[72] for the combustion of nanoaluminum in a shock tube, we see that our values compare reasonably well. This similarity suggests that the burning of a MIC may resemble the combustion of aluminum in a pressurized, oxygenated environment if the oxidizer can decompose efficiently relative to the timescale of the aluminum burning. This behavior was observed for CuO and SnO_2 over almost the entire range of WO_3, and was also seen for the Fe_2O_3 when enough WO_3 is added (80-90%).

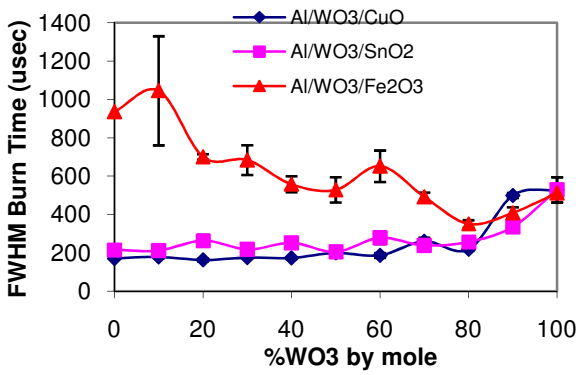

Figure 6.6 Experimental FWHM burn time for the three systems as a function of %WO_3.

As mentioned previously, the pressurization rate has been shown to correlate with the flame propagation velocity. However, this correlation is not quantitative. For example, Al/CuO has a pressurization rate on the order of 10 psi/µsec with a flame velocity of 550 m/s, while Al/Fe_2O_3 has a pressurization rate of 0.02 psi/µs with a flame velocity of 25 m/s (velocities are from unpublished data of burning in an acrylic burn tube and measuring the 2-point velocity with photodiodes). We can also look at the difference in burning times measured in this work, 170 and 936 µs for Al/CuO and Al/Fe_2O_3, respectively. The pressurization rates are different by a factor of 500, the burning times a factor of 5, and the flame velocities a factor of 20. It is evident that neither the pressurization rate nor the burning time alone can quantitatively predict the flame propagation velocity.

In this work, the difference between Al/CuO and Al/Fe_2O_3 was shown to be related to the ability of the oxidizers to release oxygen relative to the bulk of the aluminum burning. For Al/Fe_2O_3, both occur at the same time and so the pressurization rate should be directly related to the flame velocity. For Al/CuO however, predicting the propagation velocity is more complicated. In this case the system is speculated to pressurize quickly via the release of O_2 gas,

followed by the burning of aluminum over a longer time scale. If this is happening, then one would not expect the pressurization rate alone to predict the propagation velocity. Instead, the velocity would be more limited by the aluminum burning. As mentioned in the introduction, convection is considered to be primarily responsible for energy transport through the material. If O_2 gas is being released quickly, then it would contribute largely to the convection. If we consider a self-propagating flame to be a series of ignition sites, then upon ignition, the first layer would begin to burn and transfer energy forward. The subsequent unreacted layer will only need to be heated to the ignition point before the flame can continue propagating. To complicate this further, nanoparticles have small characteristic flow relaxation times, meaning that they can be easily swept up and carried forward by the gas. This itself may be an important phenomenon to include in modeling such a system. If a pressure rise is happening fast relative to the burning, it's possible that the O_2 can pick up unreacted particles and carry them forward, leading to a faster flame velocity than would be predicted by simply looking at the aluminum burning time.

6.6 Main Conclusions of Work

The reaction mechanism of aluminum-based MICs was investigated by simultaneously collecting the pressure and optical signals from combustion in a constant-volume pressure cell. Three oxidizers were studied, CuO, SnO_2, and Fe_2O_3, and were chosen based on their ability to decompose and release O_2 (and SnO for the SnO_2). WO_3 was blended with the three oxidizers as a means to perturb the system gas release, while keeping the system temperature relatively constant when added as the minor component. The results suggest that CuO and SnO_2 decompose to release gaseous oxidizers, leading to a rapid pressurization followed by a longer burn time which is rate-limited by the aluminum. For the Fe_2O_3, the experimental data show that the optical and pressure signals occur concurrently. The reaction mechanism in this case is

speculated to be rate-limited by the oxidizer decomposition. The results suggest that if oxidizer decomposition is fast relative to the reaction timescale, then the burning of an aluminum-based MIC may resemble the burning of aluminum in a pressurized, oxygenated environment.

Chapter 7: Reactive Sintering: An Import Component in the Combustion of Nanocomposite Thermites

Relevant Experimental Techniques

a) Fast heated wire / Photomultiplier Tube, Section 4.3.3.1

-Measure the ignition temperature of thermites rapidly heated

b) Scanning/Transmission Electron Microscopy with Energy Dispersive X-Ray Spectroscopy, Sections 4.1.3.1 - 4.1.3.3

-High resolution image and elemental linescan/mapping of reacted products

c) Fast heated wire / Movies at ANL, Section 4.3.3.3

-Collect high resolution movies of the oxidizers and thermites burning on the wire.

d) High Heating Microscopy Holder, section 4.3.4

-In-situ rapid heating of oxidizers and thermite inside an electron microscope

-Probing condensed-phase reactions

e) Other, Wet Chemical synthesis of copper oxide

-Performed by Dr. Chunwei Wu to make ultrafine (6 nm) CuO particles

7.1 Overview

The following work is a compilation of experiments which utilize very rapid heating rates, which mimics a combusting environment. At the time of this writing, very little progress had been made to develop experimental techniques which can rapidly and uniformly heat a small amount of material, so as to study the intrinsic reaction mechanism. The two experimental techniques which accomplish fast and uniform heating are shock tubes (Section 3.3.1.3) and filament heating (Section 3.3.1.4). Both of these techniques are set up to monitor the optical

emission, to which ignition and burning times are assigned. The filament also is used to measure transient species evolution in a mass spectrometer (Section 4.3.3.2), and has recently led to new discoveries about the mechanisms involved in the reaction.

This work investigates the reaction mechanisms in thermites in ways never seen before. The starting point for discussion will be that the ignition temperatures experimentally seen in thermites are always well above the melting point of aluminum, and much closer to melting or decomposition temperatures for the metal oxide. Thus, the ignition is inherently controlled by some process that the metal oxide undergoes once a critical temperature is achieved. A unique heating holder was used to heat samples inside an electron microscope, and at a rate of 10^6 K/s. The before and after images are compared, and reveal some new information. The heated filament was brought to the Advanced Photon Source, and high resolution image sequences were captured of the thermites burning on the wire.

Across the board, we saw evidence that large morphological changes occurred early in the burning. Entire aggregates of small primary particles were found to have completely sintered into a single, nearly spherical particle. Also, this metal product was often found to be in surface contact with an Al_2O_3 product. These observations led us to describe the reaction as a "Reactive Sintering Mechanism." In such a mechanism, the fuel and oxidizer begin reacting at an interface. The heat generated during the reaction gets preferentially conducted to neighboring particles in the aggregates, and serves to rapidly melt/decompose the aggregate. As material is melted, it is rapidly delivered to the interface where the condensed phase reaction continues. During this process, some of the O_2 or other volatile species can escape and pressurize the system, and the remainder of the aluminum can continue to burn heterogeneously with the gasified oxidizer. This result adds to the findings of Chapter 6, where we indicated that the fast pressure rise

occurred from some "partial reaction," followed by the remainder of the optical emission. The current work adds an explanation as to what the partial reaction is.

Since significant sintering was observed to occur in all systems studied, we speculate that it should be a very important consideration for development of new and improved architectures for thermites. A model is presented to show that two adjacent particles will sinter into one if the heating is significantly fast. In fact, the sintering timescale could rival or overtake a characteristic reaction timescale. In other words, agglomerated nanoparticles may not maintain their high surface to volume ratios during the bulk of the burn, and may in fact form much larger spherical particles very early after ignition. If this is the case, it challenges the assumption that decreasing the particle size will necessarily lead to an enhancement in reactivity, a result which would significantly impact the energetics community.

7.2 Introduction and Relevant Literature Review

Using nanoparticles in thermite formulations greatly reduces mass diffusion lengths between the fuel and oxidizer, and also increases the interfacial contact and homogeneity of mixing. Upon ignition, these materials give rise to a self-propagating reaction with a characteristically high temperature, and low to moderate gas production. Since the discovery of the high reactivity of nanocomposite thermites, research efforts have increased to understand the ignition and combustion mechanism, so that improvements in safety and performance can be achieved.

Despite the amount of experimental results available in the literature, the ignition and combustion mechanism remains poorly understood. A major problem has been designing experimental techniques which can probe the intrinsic reaction while replicating the environment

these materials are subject to, during the self-heating in the freely propagating reaction. This means very rapid and uniform heating, speculated to be somewhere in the range of $4x10^4$ K/s to upwards of 10^8 K/s (an ad-hoc calculation assuming thermites can reach an ignition temperature of ~1000 K in 10 μs, which is an experimentally observed pressure rise time).[10, 147] Furthermore, in order to understand the thermite mechanism, the ignition and combustion mechanism of nano-Al itself must first be well understood.

It is well known that nano-Al forms an oxide shell when exposed to air. This shell is amorphous and uniform,[11] and typically has a thickness of 2-3 nm.[15] The oxide shell can occupy a relatively large portion of the particle's mass, and in some cases can even exceed 50 Wt%.[16] The interaction between the low melting point core (933 K) and the high melting point shell (2327 K) is speculated to be critical in understanding why the ignition temperature of nanoaluminum is experimentally observed to occur close to the melting temperature of Al, and not near the melting temperature of the Al_2O_3 shell, as is seen for large aluminum.[62] Two schools of thought have prevailed for rapidly heated nano-Al: one suggests that the melting and volumetric expansion is enough to completely rupture the oxide shell, followed by the ejection of small clusters of molten aluminum at high velocities,[110,111,109] while the other suggests that the melting and expansion of the core causes the shell to crack and/or break down via phase transitions, exposing the aluminum core and rendering a diffusion-based mechanism.[15,48,112,8, 148] It has also been shown through molecular dynamics simulations that built in electric fields in the oxide shell can greatly enhance the diffusion rate of aluminum through the shell,[112] thus allowing for enhanced reactivity. Understanding the mechanism of ignition is a crucial prerequisite in understanding the mechanism of combustion.

Only a few works have examined the combustion of nano-Al at very high heating rates. One experimental technique which accomplishes the appropriate heating is a shock tube, and Bazyn et. al. have conducted several experiments of nano-Al burning in varying environments inside a shock tube.[71,72,26] The authors use pyrometry to measure the combustion temperature of the particles as a function of pressure and gas composition, and suggest that the burning cannot be modeled by a "droplet burning" model, but instead large heat losses characteristic of nanoparticles cause the flame to sit much closer, if not directly on the particle surface. This suggests that heterogeneous reactions between the gas and the particle are prominent in the combustion mechanism. The authors have also investigated the ignition and combustion of nanocomposite Al/Fe_2O_3 and Al/MoO_3 using the same technique, and measured the ignition temperatures in an inert environment to be 1400 and 1800 K, respectively.[63] It should be noted that these ignition temperatures are significantly higher than the melting temperature of Al, which in some cases has been experimentally observed to be very close to when nano-Al ignites in a gaseous oxidizing environment.[62] The authors also measure the combustion temperatures of the composites to be in the range of 2750 – 3350 K (close to the boiling point of Al), and find that combusting in an oxygenated environment can raise the temperature several hundred degrees, indicating some degree of reaction with the gas.

Besides the aforementioned shock tube experiments, there have been limited other studies of the ignition and combustion of nanocomposite materials which:

a) Avoid the negative effects of studying a bulk sample such as packing density, mixing, differences in heating, etc.
b) Probe intrinsic properties
c) Uniformly and rapidly heat the samples

These considerations have led to the development of temperature jump (T-Jump) techniques, which can ramp the temperature of a small amount of sample very quickly. In these experiments a thin wire or filament is supplied a tunable voltage pulse and rapidly heats (~10^6 K/s) through resistive heating. The ignition and combustion event can be monitored optically,[74,113] or in a mass spectrometer[149] to probe transient species evolution. Chowdhury et al.[113] used this setup to examine the ignition delay in a nano-Al/CuO composite as a function of aluminum oxide shell thickness. The authors concluded that the diffusion of Al through the oxide shell was responsible for the delay, since an increasing delay time was measured with increasing oxide shell thickness. This work raised questions about what is actually the appropriate temperature to report for ignition, especially when a delay is present in a rapidly heated environment. If some mass transfer rate limiting step (i.e. diffusion of Al through Al_2O_3) occurs in a very rapidly heated environment, then the apparent ignition temperatures could possibly be higher than what would be measured using an experimental apparatus which slowly heats the sample.

One other phenomenon which has received little attention in nanoparticle combustion studies and will be a topic of discussion in this work is the sintering of adjacent particles. This directly impacts the question of size dependence to reactivity, and what is the "effective" particle size of the reacting material. Commercially available nanoparticles are almost always highly agglomerated, and the "size" specified by a supplier oftentimes is the average size of the primary particles within these aggregates. Surface tension forces will of course drive the particles to coalesce if the temperature is sufficiently high to make the particles liquid-like.[123, 124] In a reacting thermite, nanoparticles can be heated and sintered by heat transfer from the surroundings, as well as from the energy liberated during an exothermic chemical reaction. The

latter is referred to as reactive sintering, and is a phenomenon which, for example, has been shown to be important in Al/Ni reacting systems.[125, 126]

The key point we will have to consider is whether the kinetic timescale for sintering[31] is compatible with reactive timescales we observe experimentally. If it is, then this consideration might change the manner in which one considers the effect of particle size on reactivity. It will also raise two very important questions:

1) Do nanoparticles maintain their high surface area morphology during combustion, and if not, then what is the appropriate "size" to report?
2) Is there an advantage of using agglomerated nanoparticles below a certain critical size?

The current work is a compilation of various experiments of both nano-Al and nano-Al thermites subjected to rapidly heated conditions. Several different types of thermite systems were tested both on a rapidly heated Pt wire, and within electron microscopes equipped with a rapid heating holder.

7.3 Experimental

In this work several thermite systems are compared to determine whether there are mechanistic similarities. Not all systems were studied using each experimental technique, largely due to time constraints on borrowed equipment or facility usage. The particular thermite studied in each case, therefore, was selected based on what would give the clearest representation of the steps involved in the nanocomposite thermite reaction for the particular experimental technique. The nano-Al used in this work is termed "50 nm ALEX," and was purchased from the Argonide Corporation. The primary particle size is specified by the supplier to be 50 nm,

and the elemental portion of the particles was found to be 70% by mass, as measured using thermo gravimetric analysis (TGA). A representative image of the nano-Al is shown in Figure 7.1. The primary particles are largely spherical in nature, and are highly agglomerated.

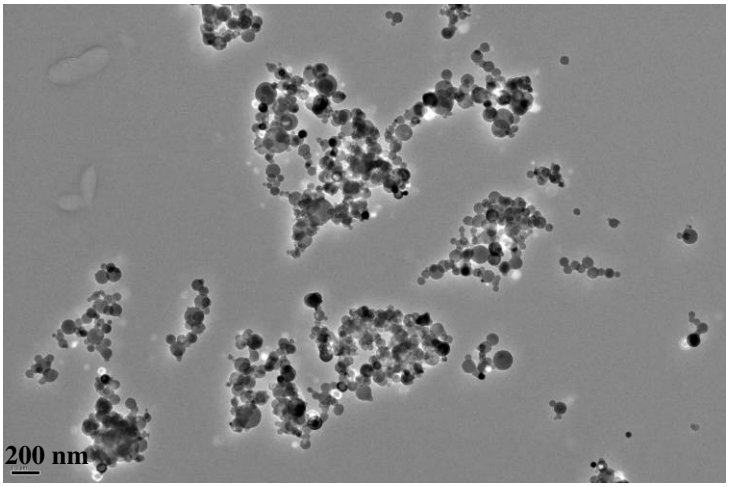

Figure 7.1 Representative transmission electron microscope image of "ALEX" nano-Al. The particles have an average primary diameter of 50nm as specified by the supplier. A native passivating oxide shell with a thickness of 2-5nm is also present, though it cannot be resolved at this magnification.

One of the samples of CuO, which we will term “6nm CuO”, was synthesized by a wet chemical technique (using copper nitrate and sodium hydroxide), and the primary particle diameter was found by electron microscopy to be ~6 nm. A representative image of the as-prepared material is shown in Figure 7.2. The particles are spherical and relatively monodisperse, with varying degrees of aggregation.

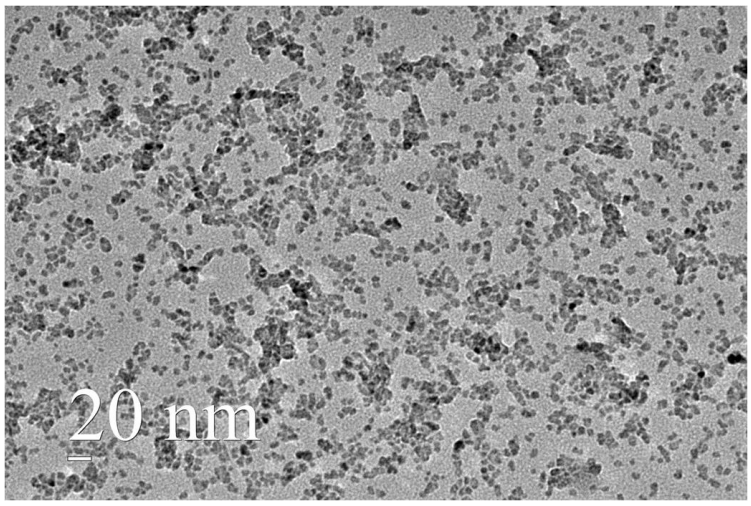

Figure 7.2 Representative TEM image of the as-prepared CuO. The primary particle size is ~6nm, as measured by TEM. The particles are spherical with varying amounts of agglomeration. A higher resolution image of the CuO can be seen in Figure 7.4c.

All other oxidizers were purchased from Sigma Aldrich, and also were spherical and agglomerated. These include Bi_2O_3 (90-210nm), WO_3 (<100nm), Fe_2O_3 (<50nm), and CuO (<50nm) with the sizes specified by the supplier. Table 7.1 provides a summary of the materials used.

Table 7.1 A summary of the materials used in this work. The sizes were all as-specified by the supplier except for the synthesized 6nmCuO, where the size was measured by TEM.

Material	Source	Size (primary particle)
Nano-Al (70% Al, 30% Al_2O_3 measured by TGA)	Argonide Corp	50 nm
6nmCuO	Prepared by wet chemical synthesis	6 nm (TEM)
CuO	Sigma Aldrich	<50 nm
Fe_2O_3	Sigma Aldrich	<50 nm
WO_3	Sigma Aldrich	<100 nm
Bi_2O_3	Sigma Aldrich	90-210 nm

To prepare thermites, stoichiometric amounts of the nano-Al and oxidizer were weighed and added to either a ceramic crucible or glass vial along with a few milliliters of hexane. The samples were then sealed and placed into a sonicating bath, followed by ultrasonication for ~30 minutes to ensure intimate mixing. For the wire experiments, the hexane/sample mixture was directly pipetted onto the wire, and the hexane was allowed to evaporate before testing. To prepare the grids for microscopy, the hexane was allowed to evaporate and then a small amount of ethanol was added to pipette the sample onto the grid. Ethanol was simply chosen based on experience that it evaporated easier from the microscopy grids.

Three separate experiments were conducted in this work, and as previously mentioned, not all samples were run for each experiment. The first used a temperature jump (T-Jump) setup to investigate the ignition temperature of the thermite sample rapidly heated on an ultra thin wire in air. The wire is made of Pt, with a diameter of 76 μm, and through utilization of a tunable voltage pulse, can be resistively heated to a maximum temperature of ~1800 K at a rate of approximately $5x10^5$ K/s.[113, 149] A photomultiplier tube (PMT) is used to monitor the optical emission, and ignition is said to have occurred at the onset of the emission.

Secondly, a specially designed heating holder (Aduro holder, Protochips, Inc.) was used to heat samples with a tunable heating pulse in-situ inside an electron microscope, from room temperature up to a maximum of 1473 K and at a rate as fast as ~10^6 K/s. The holder can be held at the desired temperature for a user-specified amount of time before being shut off. The specially fabricated grids are small thermal loads, and thus once the voltage is turned off, very rapidly cool to room temperature. Pure nano-Al, Al/6nmCuO, and Al/WO_3 thermites were rapidly heated using this holder inside an electron microscope (transmission or scanning, TEM or SEM), and the before and after images were compared to draw conclusions about the

mechanism. Finally, x-ray phase contrast imaging experiments were performed at the Advanced Photon Source (APS). We took the T-Jump system to APS, where a coherent x-ray beam was used to view the thermites rapidly heated on the Pt wire in real time at a frame rate of 135,780 Hz (7.4 μs per frame). The per-frame exposure time was actually much shorter ~500 ns, and was controlled by the pulse width of the synchrotron bunch structure. The high coherence of the undulator x-ray source at APS means that the relative phase of the x-rays (and not simply differential x-ray absorption) contributes to image contrast, making this technique extremely sensitive to gradients in electron density.[129] In addition, the PMT setup was used simultaneously used to monitor the optical emission, thus providing a correlation between the images and the emission of light. The various systems studied, along with which experimental techniques were used, are summarized in Table 7.2.

Table 7.2 Summary of the thermite systems studied by several different high heating experimental techniques. TEM and SEM are transmission and scanning electron microscope, respectively.

Material or Thermite	T-Jump/PMT setup for ignition Temp	T-Jump/Movie at ANL	High Heating TEM (JEOL JEM 2100 LaB6 TEM)	High Heating SEM (Hitachi SU-70 SEM)
Nano-Al	No	Yes	Yes	No
Nano-Al /6nm CuO	Yes	No	Yes	No
Nano-Al/CuO	Yes	Yes	No	No
Nano-Al/Fe_2O_3	Yes	Yes	No	No
Nano-Al/WO_3	Yes	No	No	Yes
Nano-Al/Bi_2O_3	Yes	No	No	No
CuO	N/A	Yes	No	Yes
Fe_2O_3	N/A	Yes	No	No

7.4 Results and Discussion

7.4.1 T-Jump/PMT Ignition Temperature

The ignition temperature, defined as the onset of optical emission during the rapid heating of the sample on the wire in air, is summarized for various thermite systems in Table 7.3. Also included in the table is the melting point of the oxidizer. The "melting" of an oxidizer is not a very clear terminology, and generally involves some form of thermal decomposition to a suboxide. Upon melting/decomposing, certain oxidizers can release gaseous O_2, or other gaseous oxidizing species. For example, CuO and Fe_2O_3 decompose to Cu_2O and Fe_3O_4 when heated, coupled with the release of O_2 gas. We have recently argued, through temporally resolved mass spectrometry, that the O_2 release for these particular oxidizers plays an important role in the ignition and combustion process.[146] Upon rapid heating, a critical partial pressure of gaseous oxygen may be reached, which facilitates the ignition of the aluminum fuel. This idea could be extended to oxidizers such as WO_3, SnO_2 and MoO_3, which can produce other gaseous oxidizing species, such as WO_2, SnO, and MoO_3 vapor.

Table 7.3 A comparison of the ignition temperature measured for various thermites and the melting temperature of the metal oxide. The ignition temperature was measured using the rapidly heated Pt wire experiment and monitoring the onset of optical emission via a photomultiplier tube.

Thermite	Ignition Temperature (K) +/- 40 K	Oxidizer Melting Temperature (Bulk values) (K)
Al / CuO	1217	1599
Al / WO_3	1292	1746
Al / Fe_2O_3	1508	1735
Al / Bi_2O_3	1067	1098

What can be seen in Table 7.3 is that the experimentally measured ignition temperatures are all above the melting temperature of aluminum (933 K), which is approximately where nano-Al is experimentally observed to ignite for lower heating rate experiments.[62] In other words, at

high heating rates it's not sufficient for only the aluminum to have melted, but the oxidizer must also have reached a temperature closer to its melting point. In some cases, ignition is seen to occur very close to the melting temperature of the metal oxide, while in other cases, the ignition temperature is significantly below the melting temperature of the bulk material. In all samples, there is a distribution of particle sizes, and thus a range of melting temperatures. Also, the melting/decomposition mechanism varies between the oxidizers. Certain metal oxides (Bi_2O_3 and WO_3) melt, whereas others (CuO and Fe_2O_3) decompose to a suboxide before melting, and this transition can release O_2. The decomposition can begin to occur below the bulk melting temperature, and in fact the decomposition temperature is much closer to the experimentally measured ignition temperatures. In any case, the results suggest that the melting or decomposition of the metal oxide plays a role in the ignition mechanism at high heating rates. For further investigation, we can now turn to the results of the high heating microscopy experiments.

7.4.2 High-Heating Microscopy

For the following discussion, all heating pulses used the maximum heating rate of 10^6 K/s, and the sample always starts at room temperature. At this heating rate the system takes approximately 1 ms to heat the sample to 1000 K. The sample is then "held" at the maximum temperature for a user-specified amount of time (1 ms is the minimum) before the electronics can turn off the voltage. The sample then rapidly cools by a rate governed by heat transfer, and since the substrate is a very small thermal load, this rate is expected to be comparable in magnitude to the heating rate. The parameters which are varied in the following section are the maximum temperature, along with the amount of time the sample is held before the voltage shuts off and

quenches the heating. All images are taken at room temperature, and are compared before and after being heated.

Before investigating the thermite systems, a sample of nano-Al with no oxidizer was prepared and investigated in-situ with a Transmission Electron Microscope (TEM, JEOL JEM 2100 Lab6). The results are presented in Figure 7.3. The nano-Al was first given a heating pulse to 1273 K, held for 1 ms, and turned off. Practically no morphological changes in the particle could be observed visually, aside from evidence of aluminum crystallization (Figure 7.3b). Typical burning times for nanoaluminum in rapidly heated oxygenated environments are on the order of several hundred microseconds,[72] so the observation of no change on a timescale of 1 ms was unexpected. Next, a second heating pulse was employed up to the maximum temperature of 1473 K, and this time the sample was held for 10 ms before the pulse was turned off (Figure 7.3c). In this case there was some obvious deformation of several particles, and visual evidence of the aluminum core diffusing out. We note that the changes are not very dramatic, and the particles maintain their shapes for the most part. Clearly no sign of violent "spallating" were observed, as has been suggested by the "Melt Dispersion Mechanism".[110,111,109] Finally, the particles were given a heating pulse from room temperature to 1473 K, and this time were held for 1 s before the pulse was shut off (Figure 7.3d). In this case a dramatic change was observed in all particles. It was clear that the aluminum had melted and either evaporated or possibly reacted with the underlying thin carbon film to form Al_4C_3. We do want to point out, however, that the structure of the oxide shell is still visible, indicating that the aluminum core had in some way migrated outwards through the shell during the heating.

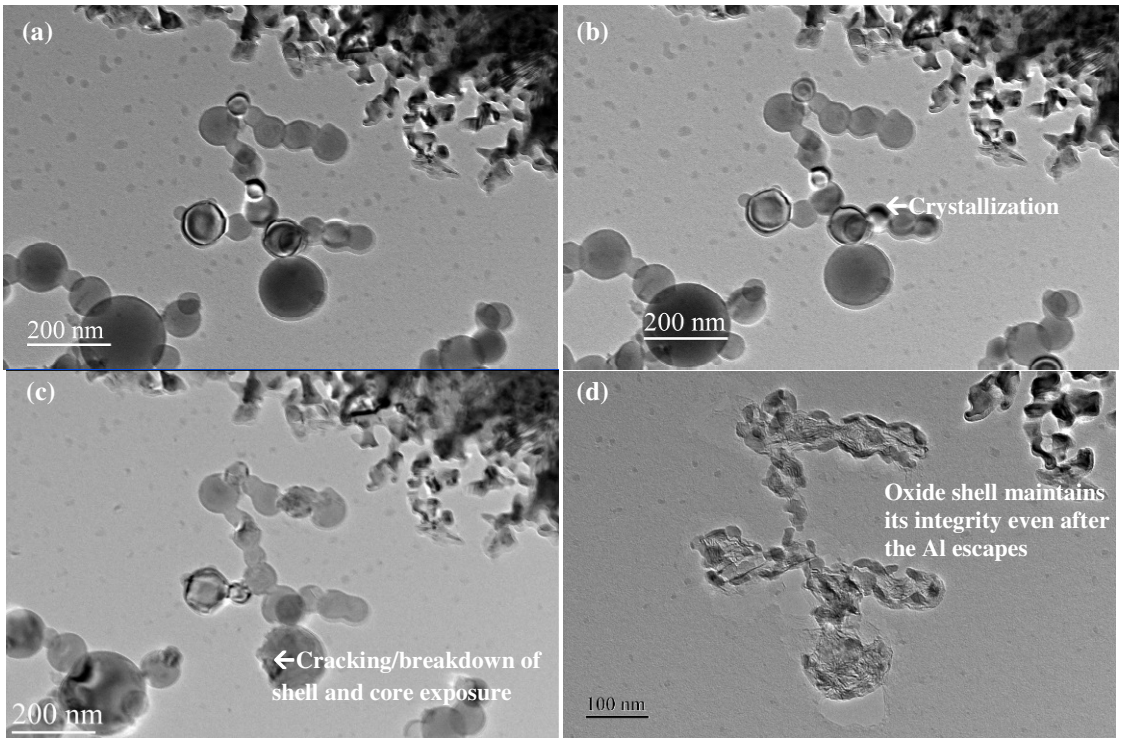

Figure 7.3 Nano-Al rapidly heated (10^6 K/s) via a special holder inside a transmission electron microscope. The heating pulses used in figures a-d are as follows: (a) unheated, (b) 300-1273 K, held for 1 ms, off, (c) 300-1473 K, held for 10 ms, off, (d) 300-1473 K, held for 1 s, off. Notice how the oxide shell remains mostly intact, implying that the aluminum has melted and diffused through the shell to escape. There is a possibility that the molten aluminum reacts with the carbon film in (d).

Next we turn to thermites. The first system looked at was nano-Al/6nmCuO in the TEM. This particular system was chosen primarily because the small monodisperse nature of the CuO made it easy to visually distinguish from the larger, polydisperse nano-Al. At the time of this study, the holder had not yet been modified for use with in-situ elemental analysis, so the sample was removed and the product was confirmed via elemental analysis in a separate microscope. The heating pulse used for this sample was to the maximum temperature of 1473 K, held for 10 ms, and then turned off. This particular pulse was chosen primarily because of the observations from Figure 7.3, showing that no obvious morphological changes occurred at the lesser heating pulse. The before and after heating images are shown in Figure 7.4, and clearly show that all particles have undergone a dramatic morphological change. The very fine 6 nm particles, which

were the CuO, have all formed a much larger and nearly spherical copper product. The aluminum particles are significantly deformed and the oxide product is found to be in contact with the copper. The results suggest that a large amount of sintering had occurred, however, it could not be distinguished at what point the sintering had occurred, and thus whether sintering precedes reaction or vice versa.

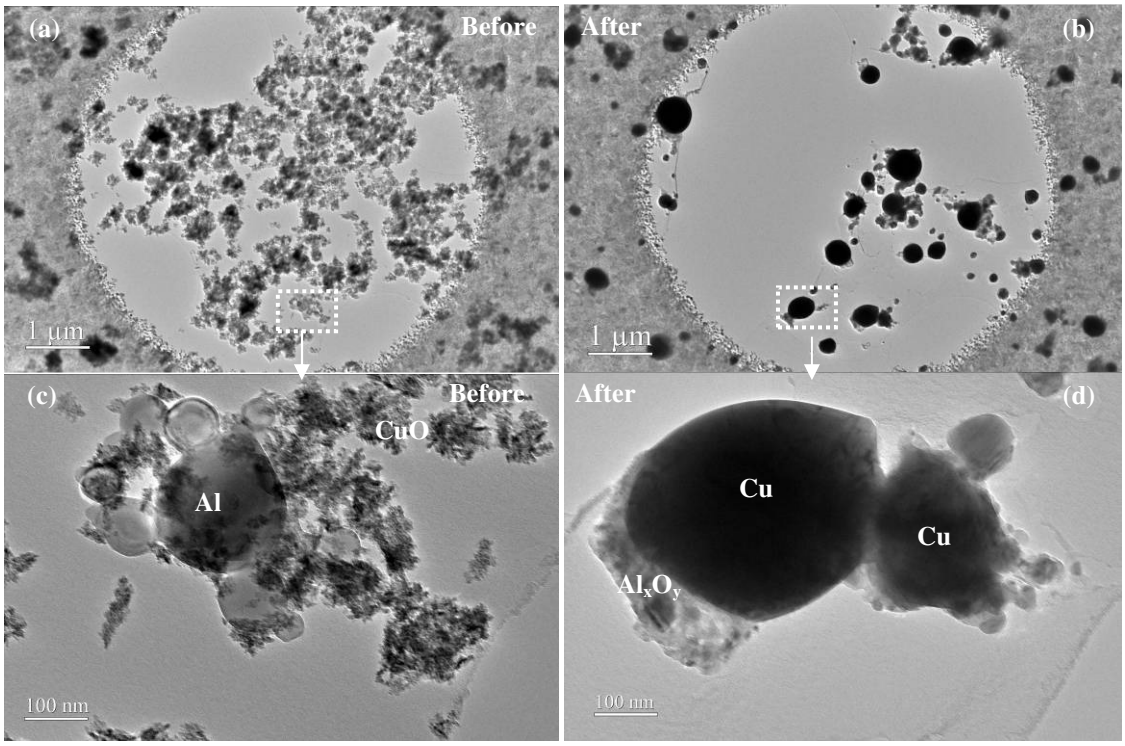

Figure 7.4 Before (left) and after (right) images of Al/6nmCuO reacted in-situ in a TEM. Images (c) and (d) are higher magnification images of the boxed regions in (a) and (b). The products were separately confirmed by elemental analysis in a separate microscope. The results suggest a reactive sintering mechanism has occurred to produce the observed morphology.

To provide a more qualitative understanding of how the Al/CuO formed the morphology shown in Figure 7.4, two samples of pure CuO were prepared and studied with a high resolution SEM. In this case, commercially available CuO (Sigma-Aldrich) was used, simply because the particle sizes are polydisperse and thus it gives a more representative picture of what occurs. At the time of this experiment, the sample holder had been modified for in-situ use with an SEM,

therefore allowing for simultaneous elemental analysis. Both samples were given a heating pulse at the maximum rate of 10^6 K/s and held for 1 ms before being shut off, however, one sample was heated to 1250 K while the other was heated to the maximum temperature of 1473 K. Before and after images are shown in Figure 7.5. The sample heated to 1250 K showed only mild amounts of sintering, while the sample heated to 1473 K showed a dramatic morphological change.

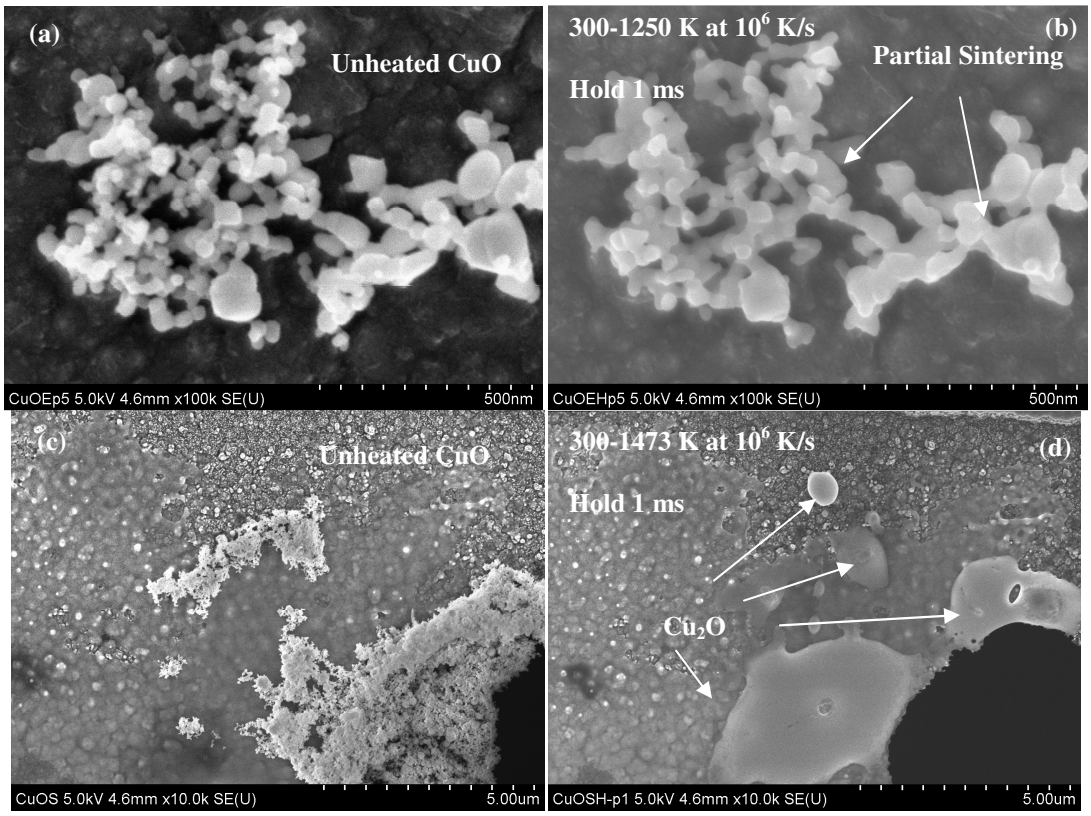

Figure 7.5 Images of CuO before (a/c) and after (b/d) rapid heating. The top sample was heated to 1250 K while the bottom sample was heated to the maximum of 1473 K. While a small amount of sintering is seen when the sample is heated to 1250 K, the changes are subtle compared to changes observed when heated to 1473 K. Note that the complete sintering of even micron-sized agglomerates occurs very quickly, in this case in a sub 1 ms timescale.

Agglomerates which were several microns in size had completely sintered into much larger "pools" of Cu_2O, confirmed by elemental analysis. CuO can decompose according to the mechanism:

$$4CuO\ (cr) \rightarrow 2Cu_2O\ (cr, L) + O_2$$

The melting temperature of bulk Cu_2O is 1517 K, however, with a wide range of particle sizes present, there will also be a range of melting temperatures. Once melting occurs, the kinetics of sintering are dramatically accelerated, and this point will be revisited later in this work. Another consideration worth mentioning is that sintering is an exothermic event, and this could also serve to self-accelerate the process, causing the particle temperature to rise, and for very small particles (<10 nm), by as much as a few hundred degrees.[124]

In any case, from these results it is quite clear that the highly agglomerated nanoparticles have sintered into particles with much larger characteristic lengthscales, and on a timescale faster than 1 ms. The sample was next given a series of subsequent heating pulses, however, the morphology remained unchanged. Comparing these results to the nano-Al/CuO thermite (Figure 7.4), we do not observe the formation of spherical copper particles from heating of the pure CuO. This comparison confirms that the exothermic reaction is indeed occurring to further reduce the Cu_2O and produce the spherical Cu product. In order to render the morphology seen in Figure 7.4, we propose that the Al and Cu_2O (or CuO) have come into surface contact and a heterogeneous reaction ensues. The heat liberated by the reaction serves to further drive the sintering process as energy is conducted through the aggregates. As material is melted during this process, capillary/surface tension forces serve to rapidly bring the constituents together, thus rapidly delivering oxidizer to the fuel. The results suggest that a reactive sintering mechanism

could be occurring for the nano-Al/CuO thermite. However, it cannot be resolved whether the sintering preceded the reaction, or vice versa.

Next we turn to a nano-Al/WO_3 sample studied in an SEM in order to determine whether similarities exist between different thermites. An SEM has the advantage of constructing a backscattered electron (BSE) image, which is well known to introduce contrast based on atomic weight (Higher weight → brighter in image). Aluminum and WO_3 can thus be easily distinguished in BSE image, and this is one reason WO_3 was chosen. The nano-Al/WO_3 was given a heating pulse to 1473 K, held for 1 ms, and turned off. The maximum temperature was chosen in an effort to heat as close to the experimentally measured ignition temperature as possible (1523 K for nano-Al/WO_3, as seen in Table 7.3). A shortened heating pulse was chosen to minimize film stability issues that were seen in the nano-Al/6nmCuO, and to also minimize any effects which may have been induced by additional heating from the holder. Typical burning times measured using the T-Jump setup for nano-Al/WO_3 are on the order of 1-2 ms, so this pulse was very appropriate to probe the intrinsic behavior during the ignition process. The rapid quenching of the sample holder allows for the "freezing" of the reaction shortly after ignition.

The before and after images of nano-Al/WO_3, along with the corresponding BSE images, are shown in Figure 7.6. The bright areas in the BSE image correspond to W-containing species, while the dark spots correspond to Al species (separately confirmed by elemental analysis). Unlike the nano-Al/CuO results, the selected area has both the thermite along with the pure oxidizer within the picture, thus allowing for a direct comparison between the two subjected to an identical heating pulse.

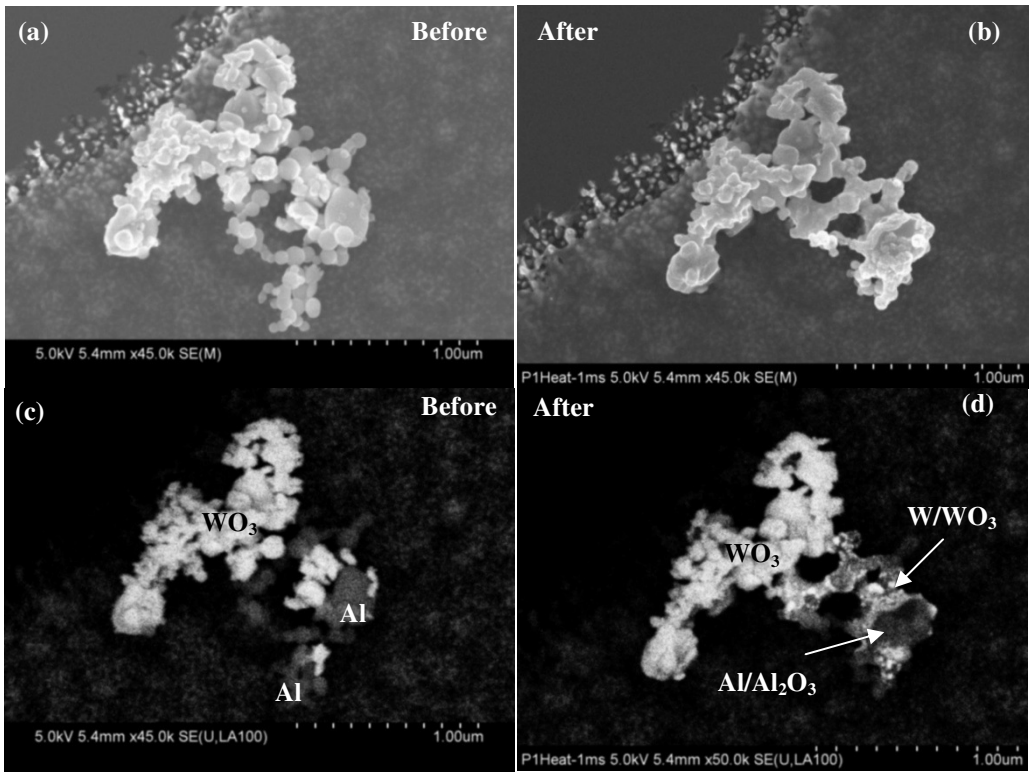

Figure 7.6 Secondary electron (a, b) and backscattered electron (c, d) images of a nano-Al/WO_3 thermite sample before (a/c) and after (b/d) heating from 300-1473 K at 10^6 K/s, held for 1 ms, off. The labeled species were separately confirmed using energy dispersive x-ray spectroscopy (EDS). Note that significant morphological changes only occurred in regions where the fuel and oxidizer were closely mixed, indicating that a reactive sintering mechanism again drove the melting/fusion of adjacent particles. The WO_3 not in close proximity to Al did not undergo much change, likely because the pulse was not hot enough to melt the WO_3 (MP 1746 K).

The results show that two very different types of behavior can be seen; for fuel and oxidizer in close proximity significant sintering has occurred and the products are found to be in surface contact, while WO_3 which was isolated from the fuel shows practically no morphological changes other than minor amounts of sintering. These observations suggest that the heating pulse alone had not been sufficient to melt the WO_3 (T_{melt} = 1746 K), however, in the areas where the fuel and oxidizer had been intimately mixed, the exothermic reaction had been vigorous enough to further melt the adjacent particles. Consistent with what was seen for nano-Al/6nmCuO, the results imply that a reactive sintering mechanism has occurred. The exothermic reaction leads to further melting of adjacent material, and capillary/surface tension forces cause

the newly melted material to rapidly migrate towards the interface where the reaction is occurring.

The sample was given a second identical heating pulse for an additional 1 ms. The image/BSE image pair after the second heating pulse can be seen in Figure 7.7. It should be noted that a large portion of the un-melted WO_3 broke away from the particle, and cannot be seen since this particular image was taken at a higher magnification to emphasize the structure.

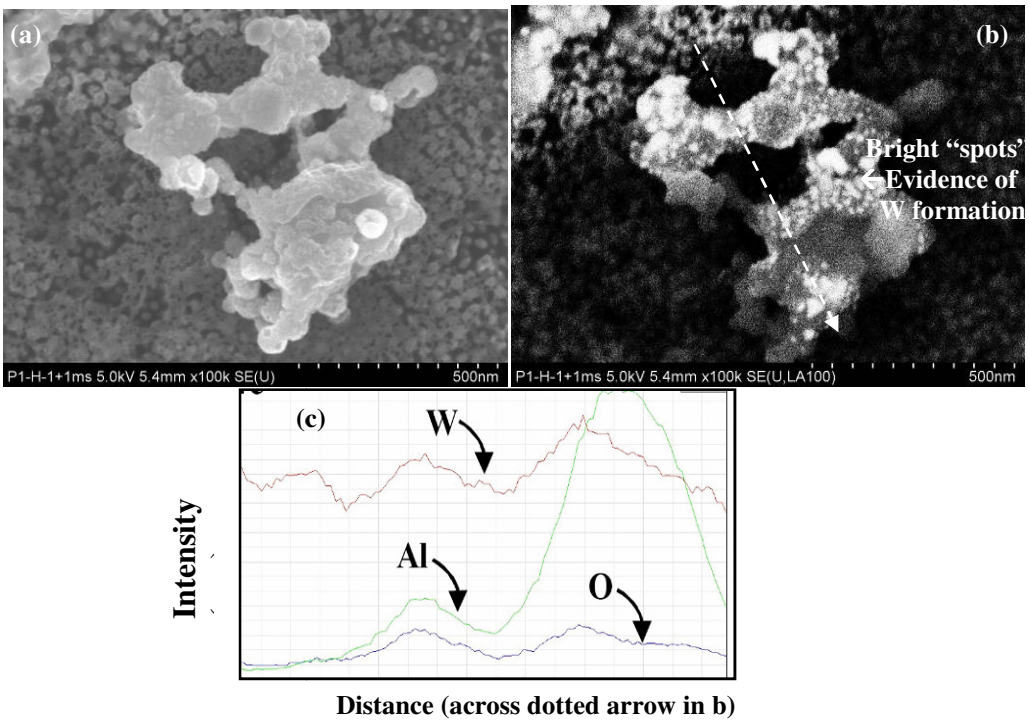

Figure 7.7 Nano-Al/WO_3 image/BSE pair (a/b) from Figure 7.6, but after a second identical heating pulse. Note the formation of small white spots in (b), indicating the formation of solid tungsten as the reaction proceeds. The W, Al, and O intensity are plotted as a function of position across the dotted arrow in (b). This linescan indicates that interdiffusion of Al/WO_3 has occurred, indicative of condensed phase reactions at an interface.

Also shown in Figure 7.7c is an elemental linescan plotting the intensity of W, O, and Al as a function of position across the particles (white line marked in Figure 7.7b). The concentration profile indicates that there is some overlap between the species, implying that

inter-mixing of the constituents may occur near the interface, an indicator that a condensed-phase reaction mechanism is happening. In addition, the BSE image (7.8b) shows the emergence of several small bright "spots", when compared to Figure 7.6d. The spots are likely small clusters of solid tungsten which form during the heterogeneous reaction, and the second heating pulse is allowing for a further extent of reaction. The tungsten which forms is, not surprisingly, solid due to its high melting point (3680 K). As a comparison, the Cu product previously discussed (Figure 7.4) has a low melting temperature (1356 K). Even if both thermites had reacted by similar mechanisms, the observed morphology may differ depending on the ability of the product to form larger spherical particles within the timescale of the heating pulse.

All of the results from the heating microscopy studies show large morphological changes, with evidence suggesting significant sintering of adjacent particles. The thermites showed different behavior relative to the pure materials, and the changes were most dramatic where the fuel and oxidizer were in close proximity, suggesting that the exothermic reaction can further drive the sintering process. The results also show the aluminum to be in surface contact with the product, suggesting that the constituents may have come into surface contact and reacted via a condensed-phase mechanism at the interface. Unfortunately, from these experiments we cannot pinpoint exactly at what point sintering occurred, and thus how it may be important to the ignition mechanism. In one extreme, a critical temperature may be achieved where condensed phase species begin to rapidly sinter, bringing fuel and oxidizer particles into surface contact and reacting at the interface. In another extreme, an alternate mechanism of ignition (i.e. O_2 release from the oxidizer and heterogeneous reaction at the Al surface) may occur, and large thermal gradients from the exothermic reaction drive the sintering of neighboring particles into the observed morphologies. What is also missing in the microscopy experiments is a more accurate

timescale of the very fast processes. The minimum amount of time the sample could be held with the holder is 1 ms, and even that may be too fast to capture the processes of interest. The next section investigates the burning of thermites on a rapidly heated wire, and will place a more accurate timestamp on the sintering processes.

7.4.3 Real-Time Phase Contrast Imaging

In this section, high resolution image sequences of samples rapidly heated on the wire are presented. The images are created by a real time x-ray phase contrast technique, which provides much better structural resolution than traditional x-ray radiography. These experiments were performed using synchrotron x-rays from the Advanced Photon Source. The same T-Jump wire as discussed earlier was used to ramp the temperature of the samples from room temperature to ~1800 K at approximately $5x10^5$ K/s. Simultaneous optical emission was monitored for the thermites using a photomultiplier tube (PMT). As a preliminary test, rapidly heated nano-Al was investigated, however, no morphological changes were seen to occur other than a small volumetric change as the material slowly melted. Thermites and the pure oxidizers, on the other hand, showed very dramatic behavior that was imaged with ~7.4 μs time resolution.

Figure 7.8 is an image sequence of the nano-Al/CuO thermite being heated on the wire. The images labeled as t = 0 μs correspond to the first image where a morphological change can be visually seen.

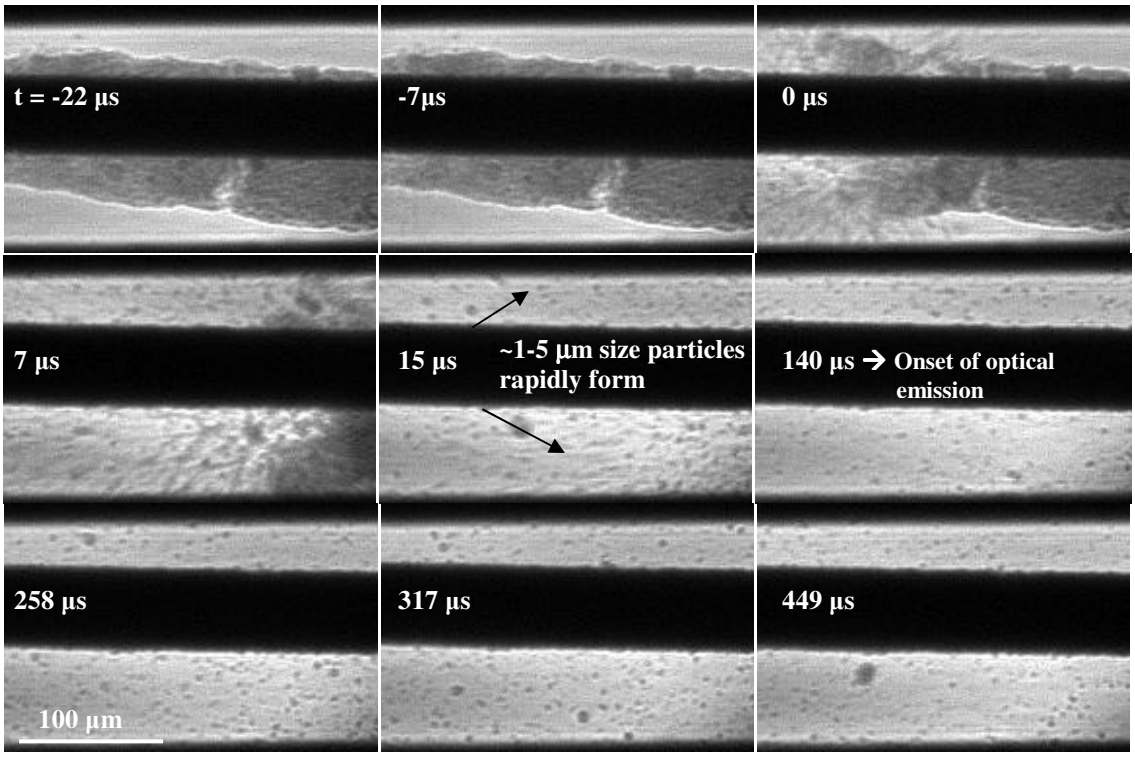

Figure 7.8 Series of snapshots of nano-Al/CuO thermite reacted on the wire (dark area in images). Spherical particles with diameters on the order of a few microns were observed to form very early, and well before the onset of optical emission. The results are qualitatively consistent to the observations in Figure 7.4, and suggest the formation of large spherical particles in this case is also attributed to a reactive sintering mechanism.

The particles are seen to blow off the wire, through a propagation process that moves from left to right along the wire. This behavior has been observed in previous work, and is presumably due to the evolution of O_2 gas from the CuO.[150] The onset of optical emission, as measured by the PMT, is labeled in the figure, and is more commonly referred to as the "ignition temperature" when using this setup. What can be seen in Figure 7.8 is that larger particles form rapidly in time, and well before the onset of the optical emission. The exact shape or size distribution of the particles is not something which can accurately be measured due to the limited spatial resolution of the x-ray phase contrast imaging technique (~2 µm), but many of the particle sizes appear to be on the order of micrometers. Another important observation is that the results appear to be consistent with the microscopy results of Figure 7.4, where it was shown that

sintering of agglomerated nanoparticles led to the formation of larger, nearly spherical particles (~1 μm in some case). While the experimental technique used in Figure 7.8 does not spatially resolve the intricacies that an electron microscope can, the qualitative similarities lead us to believe that the mechanisms are similar, and thus in this case a reactive sintering mechanism also occurs to form larger nearly spherical particles early in the burning.

As a comparison, pure CuO was also heated with the same pulse, and the image sequence is shown in Figure 7.9. The material was observed to volumetrically shrink, followed by evidence of "bubbling" over the next several milliseconds of heating. These results can be compared to the microscopy results (Figure 7.5), where large agglomerates of nanoparticles rapidly formed "pools" of Cu_2O once a critical temperature as achieved. On the wire, the CuO (cr) likely decomposes into molten Cu_2O, and simultaneously evolves O_2 gas. The wire heating alone is insufficient to rapidly decompose the Cu_2O (L), and thus a large amount of oxygen remains trapped in the condensed phase. The O_2 which was released (or continues to be released via Cu_2O decomposition) is trapped inside the melt and forms pockets of gas as it migrates out through the matrix, experimentally seen as the formation of bubbles within the material.

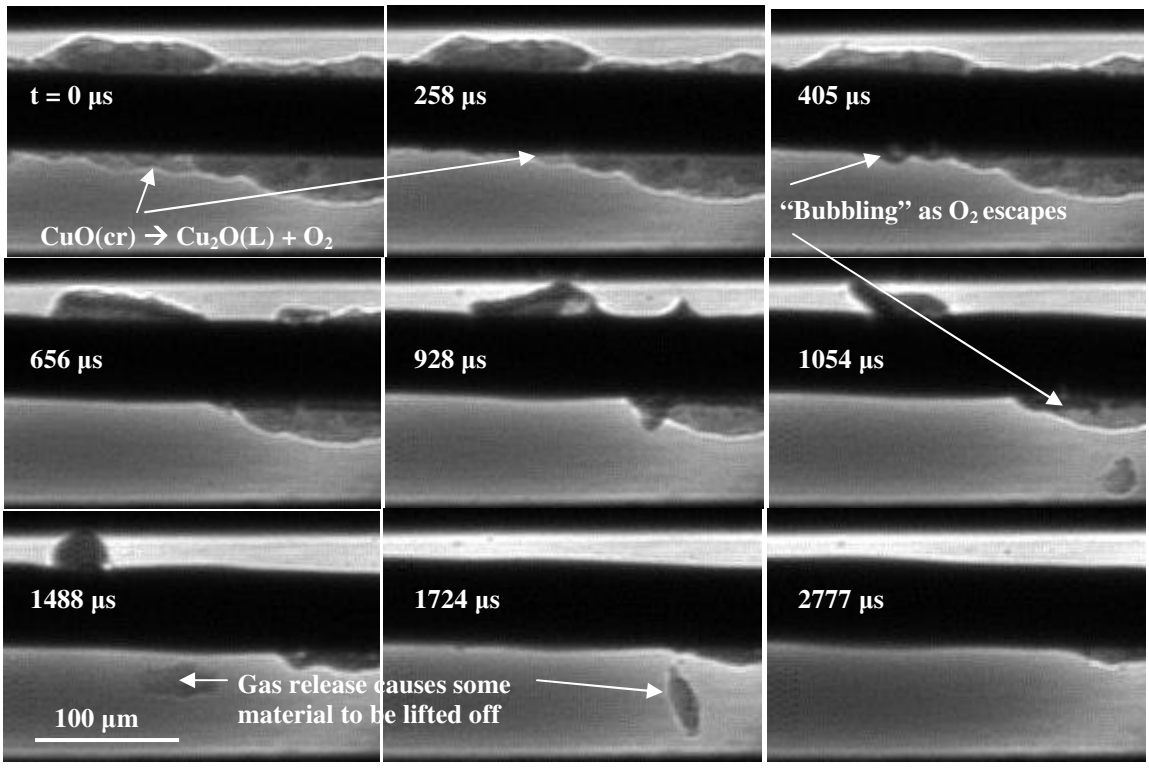

Figure 7.9 Series of snapshots nanosized CuO heated on the wire. The video shows signs of "bubbling" indicating that pockets of O_2 are trapped within molten Cu_2O. The gas release causes some material to be lifted off the wire. Overall, the material is removed from the wire much slower than was observed for the thermite.

It is evident from these results that the CuO is indeed releasing gaseous O_2, and thus is serving as a gas generator. In the presence of nano-Al, an exothermic reaction can serve to greatly accelerate the oxidizer decomposition. What cannot be resolved is whether the nano-Al reacts with the released O_2 gas, or whether it reacts with the Cu_2O (L). In fact, it could be a combination of both. Since reaction under vacuum was clearly observed for nano-Al/CuO (Figure 7.4), it would lead us to believe that at least some amount of reaction proceeds in the condensed phase, since a large amount of O_2 gas should escape into the high vacuum and thus not participate in the reaction.

Based on the experimental evidence and discussion thus far, it's plausible to speculate that what happens for the nano-Al/CuO thermite is that the sample is heated to a critical

temperature where CuO can start decomposing/melting. If there is no exothermic reaction, a Cu_2O melt is formed, and thus only a portion of O_2 is released. With added Al, however, an exothermic reaction can initiate presumably at the interface between Al and Cu_2O (L) (or possibly O_2). Modeling this interfacial reaction is beyond the scope of this work, however, it should be noted that built-in electric fields[112] could potentially play an important role to accelerate the kinetics if the fuel and oxidizer are brought in very close proximity. The energy liberated serves to rapidly melt/decompose adjacent particles of CuO into Cu_2O (L). As molten Cu_2O is produced during this process, capillary/surface tension forces cause the material to rapidly be delivered towards the interface where it continues to react. Experimentally, this is consistent with the observations that many micron-sized particles form during the thermite reaction, and not for the pure CuO. As the reactive sintering mechanism occurs, a significant amount of O_2 gas which did not participate in the reaction may be released, either during the CuO decomposition to Cu_2O or during the Cu_2O decomposition to Cu. The gas released serves to convectively propagate the energy and support a fast self-propagating reaction. Once latent processes and decomposition are complete, some amount of unreacted aluminum continues to burn in a gaseous oxidizing environment, and this is where the temperature can be seen to rise, experimentally seen as a delayed optical signal relative to the phase changes.

As a direct comparison, a nano-Al/Fe_2O_3 thermite was also studied using the setup. In a previous work,[147] we argued that Fe_2O_3 does not decompose very efficiently due to the fact that it forms FeO (L), which does not completely dissociate until a temperature (~3300 K) even exceeding the adiabatic flame temperature (~3100 K). Therefore, it traps a significant amount of oxidizer in the suboxides it produces, even in the presence of a hot exothermic reaction. The image sequence of the thermite rapidly heated on the wire is shown in Figure 7.10. What can be

seen is that much larger spherical particles are formed, and some even appear to be hollow. Hollow particles indicate that some gaseous O_2 is released into a molten Fe_xO_y matrix and thus forms "bubbles," analogous with what was seen for pure CuO in the absence of an exothermic reaction (Figure 7.9). The gas release is not nearly as rapid for the nano-Fe_2O_3 thermite as it is for the nano-Al/CuO thermite, and this is likely attributed to high dissociation temperatures of the suboxides of Fe_xO_y produced. Directly comparing the image sequences for the two thermite (Figures 7.8 and 7.10), it appears as though a more intense gas release is visually seen as the formation of much finer particles.

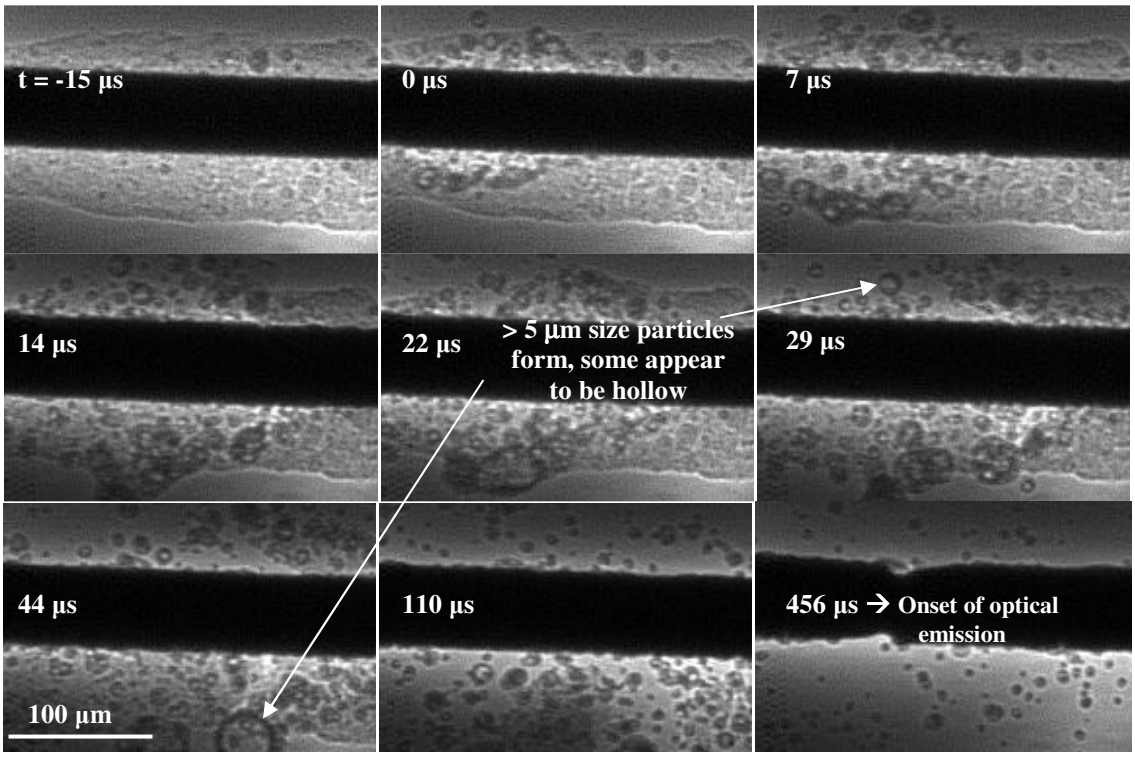

Figure 7.10 Series of snapshots of nano-Al/Fe_2O_3 thermite reacted on the wire. Note the formation of micron-sized spherical particles, in this case much larger than was observed for the nano-Al/CuO thermite (see Figure 7.8). Some particles appear to be hollow in this case. The formation of spherical particles occurs well before the onset of optical emission was measured.

Although the spatial resolution of the x-ray image sequences is clearly inferior to an electron microscope, the image sequences provide an estimate of the time resolution of the

sintering processes. The approximate timescale for larger particle formation (sintering) can be visually approximated for the thermites from the image sequences. Using Figures 7.8 and 7.10, the sintering time is roughly estimated as the difference in time between the first visual evidence of a reaction (t = 0 μs) and when most of the material appears to exist off of the wire as larger particles. This is a very rough approximation, but it's interesting when compared to other measured quantities. The sintering timescale is tabulated in Table 7.4, along with the apparent ignition point (onset of optical emission) and the FWHM burning time for comparison. The apparent sintering time for the nano-Al/CuO is on par with the pressure rise time of 10.4 μs experimentally measured during combustion experiments in a previous work.[147] In this previous work, we had argued that the pressure rise was evidence of some partial reaction, followed by a prolonged burning in a gaseous oxidizing environment, experimentally seen as a prolonged optical signal. What can be added based on the results of the current work is an explanation for the mechanism of the "partial reaction." The sintering timescale appears to have some relevance, at least for the nano-Al/CuO thermite, and thus the next section will be a discussion of this timescale.

Table 7.4 Various timescales estimated from the movies of the thermites rapidly heated on the wire. Note that in all cases, larger spherical particles form on a faster timescale than when ignition occurs, and much faster than the measured burning times.

Thermite	Approximate time to form larger spherical particles μs	Onset of Optical Emission (Ignition Point) μs	FWHM Burn Time μs
Al / Fe_2O_3	~44	456	1900
Al / CuO	~15	140	960

7.5 Characteristic Reaction and Sintering Times

Up to this point, we have shown that sintering is indeed occurring, however, we have only really discussed it in the context of a reactive sintering mechanism. That is, the exothermic reaction initiates, and this causes rapid melting/fusion of adjacent particles. In all cases, the maximum temperatures experimentally achieved were close to or just above the decomposition temperature. In some practical applications, however, it's possible that the heating can occur even more vigorously and to higher temperatures. Therefore, it may be possible that a large amount of sintering can be thermally activated on timescales even faster than the reaction. If this occurs, then the size and morphology of the particles may be drastically altered from their initial states, and this may be a critical consideration in applications where nanoparticles are being investigated in energetic applications. Specifically, two examples where the kinetic timescale of the sintering event may be particularly important are:

1) Self-heating by convection of intermediate gases in a self-propagating thermite
2) Addition of nanoparticles to a high explosive, where the ambient temperature may rapidly rise to high temperatures (i.e. ~3000 K behind a shock front)

The following section presents a simple estimate of the timescale for sintering of nanoparticles convectively heated by a hot gas, which, should be relevant to the two cases above. Since we are ignoring the local heat of reaction in this analysis, the results may be considered an overestimate of the characteristic sintering time.

7.5.1 Reaction Time Scale

An estimate of the reaction timescale depends on the particular combustion system and configuration, and for the following analysis, we limit ourselves to our own studies. In a

previous work using a combustion bomb,[147] we showed that the pressure rise occurred on the order of 10 μs, whereas the FWHM burning time was approximately 200 μs. Since we are interested in seeing whether sintering is occurring to affect the combustion process, we choose a characteristic reaction time that is a small fraction (5%) of the optically-measured burning time. This leads to a characteristic reaction time of 10 μs, which is coincidentally also the pressure rise time. We ignore particle size effects on burn time for simplicity.

7.5.2 Sintering Time Scale

To estimate an appropriate sintering timescale, two separate calculations must be included:

1) Time to heat and completely melt nanoparticles
2) Fusion of adjacent particles into a single particle, i.e. the "sintering" process

In a thermite system, there are actually three materials present; aluminum, an aluminum oxide shell, and the metal oxide. The metal oxide could sinter with other metal oxide particles, or the aluminum may sinter with neighboring aluminum (in which case it likely does not occur until the melting of the Al_2O_3 shell occurs). Given that most of the experimental evidence and discussion have focused on the oxidizer, the calculations focus on sintering time of two identical particles of CuO.

To calculate the heating timescale, an approach from a previous work is followed.[151] For simplicity, particles are not treated as agglomerates, but instead as single spheres surrounded by a hot gas, and with radiation losses assumed to be negligible. A lump-capacitance model of heating is assumed, which assumes that the heat transfer within the particle is fast relative to the heat transfer between the gas and solid interface, and therefore the particle temperature is

uniform throughout at any instance in time. The particle temperature profile is thus governed by the heat transfer from the surrounding gas to the particle, and the rate can be written as:

$$\frac{dT_p}{dt} = \frac{hA}{\rho V C_p}(T_{gas} - T_p) \tag{7.1}$$

Where T_p, A, V, C_p refer to the temperature, surface area, volume, and temperature-dependent heat capacity (calculated with fitting parameters available on the NIST webbook) of the particle, t is time, and T_{gas} is the gas temperature. h is the heat transfer coefficient, defined in terms of the Nusselt number (Nu), thermal conductivity of the gas and particle diameter (d_p) as:

$$h = \frac{Nuk_g}{d_p} \tag{7.2}$$

The Nusselt number of the particles is estimated from the modeling results of Filippov et al.[6] for a large gas to particle temperature ratio and accommodation coefficient of 0.3.

For the heating calculation, the gas temperature was assumed to be fixed at 1700 K, just above the melting temperature of CuO (1599 K). This temperature is chosen so as to provide a source of heat to melt the particles (i.e. above the chosen melting point). It should be noted that it is not known what temperature the surrounding gas will be, and in fact it may even be as high as the adiabatic flame temperature (~3000 K). Since the experimental results tabulated in Table 7.4 suggested that apparent sintering occurs before the onset of optical emission was detected, it is more likely that the gas temperature is well below the adiabatic flame temperature. In any case, the use of 1700 K is a conservative choice, and any increase in the temperature will result in a decrease the sintering time.

To calculate the timescale of the actual fusion process (τ_{fus}), the approach laid out in Mukherjee et al. is followed.[31] Below the melting point, particles can fuse via solid state grain boundary diffusion, whereas above the melting point surface tension forces dominate and the timescale can be estimated by a viscous flow mechanism.[127] Preliminary calculations suggest that the timescale becomes orders of magnitude faster once the melting temperature is reached and the mechanism changes. Therefore, we make the assumption that no morphological changes occur until the particle has been completely melted. Once this occurs, the fusion time can be approximated by:

$$\tau_{fus} = \frac{\mu d_{eff}}{2\sigma_l} \tag{7.3}$$

where d_{eff} is the instantaneous effective particle diameter (~$2d_p$) , μ is the size dependent liquid viscosity calculated by an empirical fit[128] (~100 mPa*s), and σ_l is the surface tension of the liquid (~0.7 J/m^2) [152].

Equation (1) was numerically integrated in two steps; time to sensibly heat CuO from room temperature to the melting point, followed by the time to melt the particle at a constant temperature of 1599 K. The latent heat of fusion of Cu_2O (112 kJ/mol, ICT database) was used, since this is what CuO decomposes to as it melts. The heating time is reported as the sum of these two times. Equation (3) was used to calculate the subsequent fusion time at 1599 K. The heating time is compared with the fusion timescale in Figure 7.11, and as a function of particle diameter. The total sintering time is the sum of the time to heat, melt, and fuse two identical particles with initial diameter d_p.

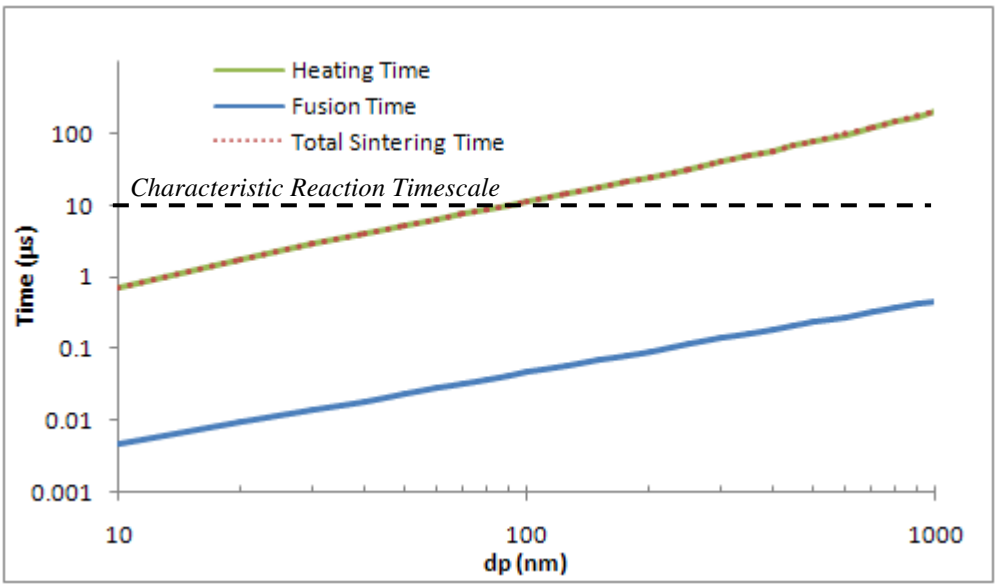

Figure 7.11 Model predictions of the total time to sinter CuO nanoparticles in air at 1700 K relative to a characteristic reaction timescale. The total sintering time is assumed to be the sum of two components depicted in the figure; the heating (sensible and latent) time of nanoparticles to the melting temperature, along with the time to fuse the particles calculated by a viscous flow mechanism. The timescale of fusion is found to be much faster than the heating time, therefore, the calculation of the total sintering time can be reduced simply to a calculation of the time it takes to heat and melt nanoparticles. The results show the sintering and reaction timescales are comparable, indicative of a reactive sintering mechanism.

From Figure 7.11, it can be seen that the actual fusion of particles happens on a much faster timescale than the heating time of the particles. In other words, if melting can be achieved then a calculation of the "sintering timescale" of particles can be reduced to a calculation of the time it takes to heat and melt the particles. Most important, however, is that sintering time is comparable to the characteristic reaction timescale. Thus, it is reasonable to expect that sintering processes and their effects (heat release, wetting, change in size, etc.) directly participate in the reaction dynamics of nanothermite mixtures. The reaction rate is therefore coupled to the sintering rate, and this correlation supports that a reactive sintering mechanism is occurring. In a real self-propagating thermite, the reaction may occur in two steps: reactive sintering which rapidly decomposes the oxidizer and pressurizes the system, followed by the combustion of the remaining aluminum in a pressurized, oxygenate environment. These results are consistent with

the findings in our previous work,[147] but further expand on how a two step mechanism may be possible.

The calculation can be extended to the addition of nano-Al (or thermites) to a high explosive, where temperatures are expected to exceed 3000 K, well above the melting point of the oxide shell in aluminum. The model predicts sintering times that are orders of magnitude smaller than some experimentally measured reaction times scales, and suggest that, depending on the particular heating environment, significant sintering may precede much of the combustion. If nanoparticles are indeed sintering into larger particle much faster than the characteristic reaction timescale, then this would entirely change our conceptual understanding of how reactivity should scale with particle size. In several examples, authors have experimentally shown a very low diameter dependence on nanoparticle burning times,[153, 154] even though the burning time has traditionally been speculated to scale directly with diameter according to a "d^1" law. In many works, however, the designation of particle size is somewhat ambiguous, as nanoparticles are often found to be highly aggregated. If early sintering occurs, then instead of classifying the particle dimensions in terms of the average primary particle diameter or the exposed surface area, it may perhaps be more appropriate to calculate the average volume of an aggregate and report the size of an equivalent-volume sphere. Also, experimental techniques which utilize slow heating rates may give different results than high heating experiments. For example, if the reaction of nano-Al in a gas is being studied using thermogravimetric analysis, the intense heat losses may prevent the particle from ever reaching the melting point of Al_2O_3, and thus the particles may maintain their morphologies during the oxidation and display strong size dependence. If, however, nano-Al is shocked to a very high temperature at a high heating rate,

the thermal heating alone may serve to melt and sinter particles early, and thus a size-dependence may not be observed.

When one collectively looks at all the experimental results along with the predictions of the model, it should become quite clear that particle sintering is an important phenomenon to consider for energetic applications involving agglomerated nanoparticles. In the thermites, it's suggested that the sintering is directly coupled to the reaction by a reactive sintering mechanism. However, particle sintering can also be thermally activated in situations where the heat transfer is vigorous to rapidly raise the temperature above the melting point, and thus the particles become fluid-like. The results strongly challenge questions about the conception that shrinking the particle size will necessarily lead to an enhancement in reactivity.

7.6 Main Conclusions From This Study

This reaction mechanism of nano-Al based thermites using several high heating techniques was investigated. First, thermites were rapidly heated on an ultra thin Pt wire, and the optical emission was monitored to determine the ignition temperature. It was found that the four nano-Al based thermites (CuO, Fe_2O_3, WO_3, Bi_2O_3) ignited above the melting temperature of Al, and closer to the melting/decomposition temperature of the metal oxide.

High heating microscopy experiments were conducted for pure nano-Al and CuO, along with nano-Al/6nmCuO and nano-Al/WO_3 thermites. For nano-Al, the results indicate a significant heating pulse was required before large morphological changes were observed. For the thermites, both systems showed evidence that a reactive sintering mechanism involving condensed phase reactions had occurred. The results showed very different behavior for the pure

metal oxide than what was seen in region where the fuel and oxidizer were in close proximity, suggesting the exothermic reaction largely drives the observed morphological changes.

High resolution image sequences of a thermite of nano-Al/CuO heated on the wire was next collected using a phase-contrast imaging technique, along with images of just the pure oxidizer. The results are consistent with the microscopy experiment in that larger, more spherical particles indicative of reactive sintering were observed. In addition, the images showed the timescale of sintering was much faster than the onset of optical emission, indicating some reaction precedes thermal runaway. It was shown that the CuO is indeed the gas generator, and it is suggested that in the presence of an exothermic reaction, some amount of the oxidizer rapidly decomposes to release gas. A nano-Al/Fe_2O_3 was also viewed on the wire, and exhibited much larger particle formation, along with evidence of oxygen being trapped and bubbling out over a longer timescale. The results show qualitative differences between thermites with an oxidizer which can rapidly decompose (CuO) versus one which does not (Fe_2O_3).

Finally, the sintering timescale of CuO nanoparticles is estimated via a simplistic model and compared with a characteristic reaction timescale. The results show that the sintering time is comparable to an experimentally measured pressure rise time, suggesting that a reactive sintering mechanism occurs early and rapidly pressurizes the system. The model was also extended for nano-Al heated by hot gases behind a shock front, and show that in some cases sintering may occur orders of magnitude faster than the reaction.

All of the results suggest a reactive sintering mechanism is occurring early during the burning of nanocomposite thermites, and the model results suggest that convective heating can activate sintering processes on fast timescales, with or without an exothermic reaction. Large

morphological changes accompany sintering, thus greatly changing the particle size and morphology. Overall, the results and discussion within this paper provide insight into a new mechanism for nanocomposite thermites which can occur on fast timescales. A reactive sintering mechanism is seen to occur, and suggests that we must re-think our understanding of critical parameters in nanocomposite thermites, such as particle size, morphology, interfacial contact, stoichiometry, etc.

Chapter 8: Antimicrobial Energetic Systems: $Al/AgIO_3$ and Al/Ag_2O

Relevant Experimental Techniques

a) Combustion cell with optical measurements, Section 4.3.1

-Measure the pressurization rate (reactivity) of the mixtures

-Measure the optical emission (burn time) of the thermites

b) NASA CEA Equilibrium Code, Section 4.4

-Predict the decomposition behavior and adiabatic flame temperature of the systems

c) Simultaneous DSC-TGA, Section 4.2.2

-Measure the decomposition behavior of $AgIO_3$ and quantify the enthalpies of melting and decomposition at low heating rates

d) Fast heated wire / Mass spectrometry, Section 4.3.3.2

-Study the decomposition mechanism of $AgIO_3$ at high heating rates and compare with DSC-TGA experiment.

e) Fast heated wire / Photomultiplier Tube, Section 4.3.3.1

-Measure the ignition temperature of thermites rapidly heated

f) Burn Tube, Section 4.3.2

-Performed at China Lake, measured the flame velocity of $Al/AgIO_3$

g) Scanning/Transmission Electron Microscopy with Energy Dispersive X-Ray Spectroscopy, Sections 4.1.3.1 - 4.1.3.3

-High resolution image and elemental linescan/mapping of reacted products

h) X-Ray Diffraction, Section 4.1.1

-Crystalline species identification of the reacted product to confirm the formation of elemental silver and silver iodide

i) X-Ray Photoelectron Spectroscopy, Section 4.1.2

-Confirm whether the silver and silver iodide products are surface-exposed

This chapter investigates the use of silver-based oxidizers in thermite systems. Silver is long known to be able to destroy bacteria, even at room temperature. This is particularly useful because certain strains of harmful biological spores (i.e. Anthrax) are very heat-resistant, and thus the short live high temperature reaction may not be sufficient to destroy the deadly spores. Therefore, researchers have begun looking at new types of oxidizers which are energetic, but also produce a useful product which can continue killing the spores even when the exothermic reaction completes. Elemental silver is a very good biocidal agent, but other forms of silver may work just as well, if not better.

This chapter is broken down into two different works. Section 8.1 first investigates the use of silver iodate ($AgIO_3$), which was synthesized by Dr. Curtis Johnson, and this was a joint work between UMD and NAWC-China Lake. This work really showed the full picture of how we take an unknown thermite system such as $Al/AgIO_3$ and characterize the ignition, combustion, and post-reaction products using a variety of experimental techniques. One main conclusion of this work was that the primary reaction product was found to be AgI. While AgI may itself be an excellent biocidal agent, there has not been a lot of work to determine its potency relative to elemental silver. This led us to then go on and synthesize the oxidizer Ag_2O using a wet chemical technique, and is the topic of Section 8.2. Ag_2O has a great potential to yield large amounts of elemental silver when reacted with aluminum, and thus was an interesting oxidizer to investigate. We found that it performed poorly itself, but when mixed with $AgIO_3$ and CuO, it performed quite well. In both systems, a significant amount of Ag_2O could be added before the reactivity dropped off to about 50% of its performance. We performed XRD and XPS to characterize the product, and showed that some surface-exposed silver was produced. However, TEM showed that the reacted product indicated a reactive sintering mechanism had

occurred. This results in particles that had an Al_2O_3 product in direct contact with the produced silver, and in fact, the silver had in some way mixed with copper in the ternary systems. Both of these considerations will greatly reduce the surface exposure of the produced silver.

8.1 Ignition and Combustion Characteristics of Nanoscale Al/$AgIO_3$: A Potential Energetic Biocidal System

8.1.1 Overview

This work investigates the ignition and reaction of Al/$AgIO_3$ thermites for potential use in biocidal applications. Rapid-heating wire experiments were performed to measure the ignition temperature and investigate the thermal decomposition of the oxidizer using a T-Jump/TOF Mass Spectrometer, and an optical emission setup. Combustion experiments inside a constant-volume pressure cell were also carried out, and the relative performance was compared with other thermite systems. The ignition temperature in air at atmospheric pressure was found to be 1215 +/- 40 K. The $AgIO_3$ was found to significantly outperform CuO and Fe_2O_3 oxidizers in pressurization tests, and this is attributed to the enhanced gas release as the $AgIO_3$ thermally decomposes to release iodine in addition to oxygen. The reacted product was collected to investigate the final state of the products. Transmission electron microscopy and x-ray diffraction were performed to show that the major Ag product species was AgI, and not elemental Ag and I_2. The AgI was found to be surface exposed to the environment, and exists primarily as agglomerated spherical nanoparticles, and is found in some cases to coat the Al_2O_3 after the reaction.

8.1.2 Introduction and Relevant Literature Review

Interest in neutralizing biological-based weapons has posed a challenge to the use of traditional energetic materials which produce a very short lived thermal event. It has recently been proposed that a new class of energetic material, which offers both a thermal event coupled with a long lasting biocidal character, could be useful in mitigating biological materials. What really matters then is how much biocidal agent can be produced by the energetic, along with what chemical form it presents itself in the final product. The latter point is particularly relevant, since it is quite possible to have a biocidal product which either ends up to have a low surface area and thus minimal efficiency, or worse yet, be wrapped up within the matrix of one of the products of reaction and thus not exposed to the environment.

An ideal energetic system designed for neutralization of biological agents should possess the following characteristics.

1. High thermal release with minimal overpressure.
2. Produces a species which is effective against the biological agent, is non-toxic to humans, and also is chemically and thermally stable to keep it active for sustained periods of time.

For the thermal release component, "reactive materials," particularly those comprising thermite chemistry produce a very high energy release per unit volume or mass. Furthermore, since the products of combustion tend to be primarily in the condensed phase, some of the issues associated with high blast overpressures are minimized. For the biocidal component, a variety of materials could potentially be used, one of which is the subject of this work.

The highly insoluble salt, silver iodate ($AgIO_3$), has been considered recently for its potential use in thermite-based biocidal applications.[116] Silver exhibits biocidal properties in

many forms.[117] Morones et al.[118] have investigated nano-sized silver, and showed it to be effective at killing bacteria, especially when the particle size was very small (<10 nm). Smetana et al.[119] also investigated the biocidal activity of several silver/silver-based samples with and without coatings and concluded that small, irregular surfaces are necessary for high biocidal activity. The authors claim that silver ions are the actual biocidal species, and having silver oxide surfaces on the nanoparticles can serve to facilitate the transport of silver ions, and thus improve the effectiveness. Silver bromide nanoparticle/polymer composites have been reported to exhibit potent, long lasting antibacterial activity,[120] and silver iodide is used as an antiseptic[121]. Iodine is also a widely known and used biocide.[122]

This work investigates the burning of Al/$AgIO_3$ nanothermites, which are commonly classified as metastable intermolecular composites (MICs).[89] As discussed previously, we are concerned with both the combustion performance along with the final state of the products. Rapid-heating wire experiments and constant-volume combustion tests were performed in order to investigate the burning and report the ignition temperature. The reacted products were examined using x-ray diffraction and electron microscopy to determine the composition and morphology.

In discussing the performance of the Al/$AgIO_3$ system in this work, it will often be helpful to make comparisons to two other common thermite systems, Al/CuO and Al/Fe_2O_3. CuO is generally considered to be a relatively good oxidizer, while Fe_2O_3 is a relatively poor one, and we discussed some possible reasons for this in a recent work.[147] It's necessary to include this data to provide the reader with some context for the measurements presented in this paper, in particular the combustion studies performed inside a pressure cell. The measurements we make are often relative in nature, and so we must show comparisons with materials tested

under the exact same experimental conditions to give the reader some idea of the relative performance.

Some thermodynamic equilibrium calculations of the thermites studied in this work are summarized in Table 8.1.1. Data for the Fe_2O_3 and CuO thermites are taken from Fisher and Grubelich,[155] with gas production based on adiabatic reaction at atmospheric pressure and do not take into account the presence of an oxide shell on the Al. The Al/$AgIO_3$ equilibrium data was calculated using the NASA CEA software for constant enthalpy and pressure, and also did not include an oxide shell (including 30 Wt% Al_2O_3 gives 3625 K for the adiabatic reaction temperature, only a slight difference). The list of gaseous species is certainly incomplete, and we have only listed the major gas species predicted to occur during the thermite reaction. There are several other minor gases which are predicted to form, including but not limited to Al, Al_2O, AlO, AgI, Cu_2, etc. Also, there are also some species which may not be contained in the thermodynamic database used by the CEA software, and so the adiabatic flame temperature listed for Al/$AgIO_3$ should be considered as an approximate value. With these points in mind, we can see in Table 8.1.1 that the Al/$AgIO_3$ thermite has a higher adiabatic flame temperature and also has the potential to produce more gas than the two metal oxide thermites. It can be seen in the case of the metal oxides that the adiabatic reaction temperature is limited by the metal boiling points, whereas for the $AgIO_3$, the adiabatic reaction temperature is limited by dissociation of Al_2O_3. The high adiabatic flame temperature, along with the gas release capabilities indicate that $AgIO_3$ should perform very well in burning tests, and this will be experimentally verified.

Table 8.1.1 Constant enthalpy and pressure thermodynamic equilibrium calculations of stoichiometric thermite systems. Data for Fe_2O_3 and CuO is taken from Fisher and Grubelich, 1998. The $AgIO_3$ calculation was done using NASA's CEA equilibrium software with a constant enthalpy and pressure.

Thermite Reaction	mmol gas/g	Major Gas species	Adiabatic Temperature K	Comment
$2\ Al + Fe_2O_3 \rightarrow Al_2O_3 + 2\ Fe$	1.4	Fe	3135	b.p. of Fe
$2\ Al + 3\ CuO \rightarrow Al_2O_3 + 3\ Cu$	5.4	Cu	2843	b.p. of Cu
$2\ Al + AgIO_3 \rightarrow Al_2O_3 + Ag + I$	~8.9	Ag + I + Al_2O_3[a]	3681[b]	b.p. of Al_2O_3

[a] Al_2O_3 involves dissociation into several gaseous products (AlO, Al_2O, O, O_2, etc.), rather than molecular Al_2O_3. [b] The product libraries do not contain some volatile species such as AlOI or AgI, and this may slightly affect the value.

8.1.2 Experimental

8.1.2.1 Sample Preparation

The nanoaluminum samples used in this work were purchased from the Argonide Corporation (designated as "50 nm ALEX") and from NanoTechnologies (80 nm size). TGA showed the aluminum to be 70% (50 nm Al) and 72% (80 nm Al) elemental by mass, and only this portion is considered when determining the equivalence ratio. The CuO and Fe_2O_3 (<100 nm as specified by the supplier) used in the pressure cell and wire studies were purchased from Sigma Aldrich, and a second CuO sample (45 nm average particle size as determined by surface area analysis) was provided by Technanogy. Micron-sized silver iodate was purchased from City Chemical, and had a specific surface area of 0.9 m^2/g, corresponding to a particle size of 1.2 μm, based on uniform spherical particles. A larger sized (5-400 μm) silver iodate, obtained from Baker & Adamson, was sieved (-60 mesh) and ball-milled to reduce the size to 900 nm, based on specific surface area (this sample was only used in thermal analysis experiments). Nanoscale silver iodate was prepared by precipitation from aqueous solutions of silver nitrate and potassium

iodate or sodium iodate, using a modification of a literature method[156]. A solution of 30.97 g of $AgNO_3$ in 125 mL of water was added over 45 seconds to a solution of 39.58 g of KIO_3 (1.4% molar excess) in 950 mL of water, with rapid mechanical stirring. The resulting mixture was stirred for 5 minutes, then filtered and washed with water, water/acetone mixture, acetone, and ether. After air drying on the fritted funnel, the product was further dried in an oven at 403 K for 10 hours. Surface area analysis by nitrogen adsorption gave a specific surface area of 6.95 m^2/g, which would correspond to a particle size of 156 nm for uniform spherical particles. A similar preparation using sodium iodate reagent produced a powder with a specific surface area of 4.0 m^2/g, corresponding to a spherical particle size of 270 nm. However, the actual particle morphology consists of thin platelets, roughly 1 μm in diameter. Silver iodide was purchased from Sigma Aldrich, and the size was not specified by the supplier.

Thermite samples were prepared by weighing the aluminum and oxidizer components (stoichiometric), then adding ~10 mL of hexane. The samples were then ultrasonicated in a sonic bath for 30 minutes to ensure intimate mixing. For the wire tests, a micropipette was used to coat the wire with the hexane/thermite mixture, and the hexane allowed to evaporate. For the pressure cell tests, the hexane/thermite mixture was first evaporated at room temperature and finally at 373 K for a few minutes to drive off any remaining hexane. The dry powder was then gently broken up with a spatula to remove any large clumps, and until the consistency was that of a loose powder.

We must note that the degree of mixing achieved in each sample was not studied in this work. A scanning electron micrograph of an Al/$AgIO_3$ nanocomposite powder is presented in a reference (Johnson, et al, 2008), and shows that mixing is limited by clumping of both ingredients. The $AgIO_3$ has a platelet-like morphology, and could potentially mix differently

than spherical nanoparticles under the same amount of ultrasonication. Ideally, all of the oxidizers studied would have exactly the same morphology so that there was no difference in the homogeneity or mixing of the materials, but this was not the case. We chose a 30 minute sonication time primarily from past experience that this amount of time gave the best reproducible conditions. If the time is too short, the mixing is poor and batch to batch variations occur, whereas too long of a sonication time caused some material to stick to the vial walls.

8.1.2.2 Fast-Heated Wire Tests

Measuring the ignition temperature in nanocomposite materials is complicated by the fact that the ignition mechanism is likely dependent on the heating rate. It is not uncommon for the reported ignition temperature to be several hundred degrees different depending on what experimental technique was used to heat the particles. As discussed in a review article by Dreizin[157], an appropriate experiment would be one that heats the sample uniformly and with high heating rates.

In a recently-developed temperature-jump/time-of-flight mass spectrometer (T-Jump/TOFMS) system,[149] we coat a thin platinum wire (76 μm diameter) with a very small amount of sample (<0.03 mg). The wire is then rapidly joule heated using a tunable voltage pulse to achieve heating rates up to ~$5x10^5$ K/s and a maximum temperature of ~1800 K. By simultaneously monitoring the transient resistivity of the wire, the temporal temperature distribution can be calculated. To investigate the decomposition and combustion processes, the coated platinum wire is inserted into the high vacuum region of the mass spectrometer close to the ionization region. The wire is rapidly heated and the gaseous product species are ionized using an electron gun. Sampling of the product species by the mass spectrometer occurs

simultaneously to the sample heating so that time resolved mass spectra can be obtained at a rate of 10,000 Hz. The TOFMS system was originally designed to determine elemental composition in a single particle,[158] and thus is highly sensitive to the mass (~femtograms). A more detailed description of the modified experimental setup is given elsewhere.[149]

To determine the ignition temperature, the wire is heated in air at atmospheric pressure and the optical emission is monitored by a photomultiplier tube. Ignition is said to have occurred when the optical signal reaches 2% of its maximum value. Three shots are performed for each sample, and the average value is taken to be the ignition temperature. The uncertainty in the ignition temperature is estimated to be 40 K, based on several factors, including the length of the wire, contact resistance, etc.

8.1.2.3 Pressure Cell Combustion Tests

A fixed mass (25 mg) of the loose thermite powder is placed in a constant-volume pressure cell[101, 151, 154] and ignited by resistive heating of a nichrome wire. A piezoelectric pressure transducer is attached to one port of the cell, while a lens tube assembly is attached to the other to collect the light and focus it onto a photodiode. The transient optical and pressure signals are captured simultaneously using a digital oscilloscope. The pressurization rate is calculated by dividing the maximum pressure by the rise time of the pressure signal, and is reported as a relative measurement of the reactivity. The pressurization rate has been used to report reactivity since it has been shown to correlate with flame propagation velocities[89], another commonly used measurement of reactivity. The burn time of the thermite is taken to be the Full-Width at Half-Maximum (FWHM) of the optical signal.

We must stress that both the pressurization rate and luminosity measurements should only be thought of in terms of relative performance at the current time. As mentioned, the pressurization rate has been shown to experimentally correlate with flame propagation rates, and thus is considered to be somehow proportional to the reaction rate. We recently argued that the luminosity could be used as a measurement of burning time, but this assumption was only based on experiments that showed the optical signal to be independent of the sample mass, and also since optical emission has long been used to measure particle burning times. Until some controlled experiments can be carried out on materials with well-defined characteristics, both of these measurements should be treated with some skepticism for now and are only used to show relative comparisons between the $AgIO_3$ system and other more common thermites.

8.1.2.4 Thermal Analysis, Surface Area Analysis, and High-Speed Video

Simultaneous differential scanning calorimetry and thermogravimetric analysis (DSC-TGA) was conducted on a TA Instruments Q600 SDT. The $AgIO_3$ sample was the ball-milled Baker & Adamson material (900 nm). A 4.28 mg sample was heated from room temperature to 1073 K at 5 K/min under a flow of nitrogen gas. Following the suggestion of a reviewer, a second experiment was conducted at a higher heating rate, 50 K/min, using a 5.72 mg sample. This sample was also held at 1073 K for 30 min. Surface area analysis was conducted on a Quantachrome Autosorb 1C surface analyzer, using low temperature nitrogen adsorption. High-speed digital video imaging was conducted with a Vision Research Phantom v9.1 camera.

8.1.2.5 Post Reaction Analysis

The reacted product was collected after combustion in the pressure cell by scraping the product off of the sample holder and into a ceramic crucible with some hexane. The crucible

was sonicated for several minutes, and a pipette was used to dropper the sample onto a grid (Au mesh/Carbon film) for analysis in a high resolution transmission electron microscope (TEM, JEOL JEM 2100 FEG). The TEM is equipped with an energy dispersive x-ray spectrometer (EDS, Oxford INCA 250) , which can be operated in scanning mode to perform 1D elemental line scans and 2D elemental maps of the sample. The dry powdered product was collected and prepared for x-ray diffraction (XRD, Bruker C2 Discover with GADDS, operating at 40 kV and 40 mA with unfiltered Cu κα radiation, λ = 1.5406 Å) analysis to determine any crystal structures which may form during the reaction.

8.1.2.6 Thermodynamic Properties

Thermodynamic data involving reactions of $AgIO_3$ and AgI were obtained from the data base of the Facility for the Analysis of Chemical Thermodynamics at the website http://www.crct.polymtl.ca/reacweb.htm. The data base is supported by the Center for Research in Computational Thermochemistry at Ecole Polytechnique in Montreal, Canada.

8.1.3 Results and Discussion

The experimental results presented in this work were conducted at both the University of Maryland and at China Lake. The results were combined in this paper, and for that reason, different materials and mixing parameters have been used depending on the experiment. A table summarizing all of the experiments, along with the materials and equivalence ratios used is shown in Table 8.1.2. We expect only subtle differences between using different aluminum and CuO suppliers, and the slight variance in equivalence ratio was done in order to compare the maximum performance in the open powder burning experiments. As previously discussed, the pressurization rate is a relative measurement, so the equivalence ratio was kept constant to make

a direct comparison between systems. Optimizing the equivalence ratio for each oxidizer would have altered the values slightly, but the generalized trend would still exist.

Table 8.1.2 A table of all experiments carried out, along with the equivalence ratio and particle sizes/sources.

Experiment	Sample Studied	Equivalence Ratio	Fuel, size	Oxidizer, size
Fast heated wire	Al/Fe_2O_3	1.0	ALEX, 50 nm	Sigma-Aldrich, <100 nm
	Al/CuO	1.0	ALEX, 50 nm	Sigma-Aldrich, <50 nm
	$Al/AgIO_3$	1.0	ALEX, 50 nm	Synthesized, 270 nm
	$AgIO_3$	N/A	N/A	Synthesized, 270 nm
	AgI	N/A	N/A	Sigma-Aldrich, not given
Simultaneous TGA/DSC	$AgIO_3$ (Fig 1)	N/A	N/A	City Chemical Ball-Milled, ~900 nm
Pressure Cell	Al/Fe_2O_3	1.0	ALEX, 50 nm	Sigma-Aldrich, <100 nm
	Al/CuO	1.0	ALEX, 50 nm	Sigma-Aldrich, <50 nm
	$Al/AgIO_3$	1.0	ALEX, 50 nm	Synthesized, 270 nm
XRD SEM/TEM/ EDS	$Al/AgIO_3$ (From Cell Fig 5-7)	1.0	ALEX, 50 nm	Synthesized, 270 nm
	$Al/AgIO_3$ (From Plate Fig 8)	1.25	NanoTech., 80 nm	Synthesized, 270 nm
Powder Burn (Fig 4)	$Al/AgIO_3$	1.12	NanoTech, 80 nm	Synthesized, 270 nm
	$Al/AgIO_3$	1.06		Baker & Adamson, 1200 nm
	Al/CuO	1.27		Technanogy, 45 nm

8.1.3.1 Combustion Characterization

The ignition temperature of stoichiometric $Al/AgIO_3$ in air and at atmospheric pressure measured using the hot wire setup at a heating rate of $5x10^5$ K/s was found to be 1215 +/- 40 K. In comparison and for the sake of discussion, the ignition temperatures of Al/CuO and Al/Fe_2O_3 under the same conditions are 1220 +/- 40 K and 1510 +/- 40 K, respectively. For both CuO and Fe_2O_3 (Sigma Aldrich), we have studied the oxidizer thermal decomposition using the T-Jump/TOFMS with and without the aluminum fuel. The results show that O_2 release occurs

prior to evidence of reaction (Al, Cu, Fe species), indicating that the thermite ignition mechanism involves some degree of thermal decomposition of the oxidizer to a suboxide and O_2 gas.

Constant temperature and pressure (TP) equilibrium calculations using NASA's CEA software show that CuO decomposes to Cu_2O and O_2, and Fe_2O_3 decomposes to Fe_3O_4 and O_2 under atmospheric conditions at approximately 1400 K and 1700 K, respectively. It should be noted that the decomposition can start occurring at lower temperatures, but at the reported values a large increase in the decomposition was seen to occur in the NASA CEA calculations. It should also be noted, and will be shown later, that the decomposition mechanism may change at high heating rates, so the decomposition temperatures are only listed for the sake of discussion. These calculated temperatures are consistent with the experimental ignition temperatures within ~200 K, and the difference could easily be attributed to the wide range of particle sizes and thus melting/decomposition temperatures within the sample, or to inaccuracies in the calculation. Combining the experimental results with the thermodynamic calculations, it is reasonable to speculate that the ignition of Al requires a critical partial pressure of O_2 to be reached in order to overcome heat losses and facilitate the ignition of the fuel.

Stern[159] indicates that under atmospheric conditions, $AgIO_3$ decomposes to AgI and O_2 around 678 K and includes a few references supporting this. We investigated the thermal behavior of $AgIO_3$ in more detail by both slow heating (DSC-TGA) and fast heating (hot wire mass spectrometry) experiments. Figure 8.1.1 shows DSC-TGA analysis of the 900 nm $AgIO_3$. Three endotherms are observed in the temperature range of 670-840 K, attributed to melting of $AgIO_3$ near 692 K, followed by decomposition to AgI around 740 K, and melting of AgI at 827 K. The sample exhibited an 18% weight loss during the second endotherm, consistent with the

17% calculated weight loss for conversion of $AgIO_3$ to AgI. Visually, heating of $AgIO_3$ in air resulted in melting, followed by gas evolution and a color change from colorless to a yellow liquid (AgI is yellow). The third endotherm temperature matches the literature value for the melting point of AgI (831 K).[160] Further heating of the sample above the melting point of AgI resulted in an increasing rate of weight loss until the experiment ended on reaching 1073 K (where the total weight loss was 66%). This higher temperature weight loss appears to be due to evaporation of the AgI product (b.p. 1779 K[160]). Holding the sample at 1073 K for 30 min resulted in a total weight loss of 84%, confirming that both Ag and I are lost from the sample at this temperature. Integration of the endotherms gives approximate enthalpies for fusion of $AgIO_3$ (25 kJ/mol), decomposition to AgI (60 kJ/mol), and fusion of AgI (4 kJ/mol). The literature value for the heat of fusion of AgI is considerably higher at 9.4 kJ/mol,[160] indicating that some of the AgI was probably in liquid form prior to the endotherm. The calculated enthalpy of decomposition of solid $AgIO_3$ to solid AgI, 116 kJ/mol, is similar to the observed total of 85 kJ/mol for fusion and decomposition of $AgIO_3$. In a second DSC-TGA experiment conducted at 50 K/min the three minima for the endotherms shifted to 706 K, 807 K, and 833 K. The endotherm for the $AgIO_3$ decomposition had by far the largest shift to higher temperature, about 67 K, for the ten-fold increase in heating rate.

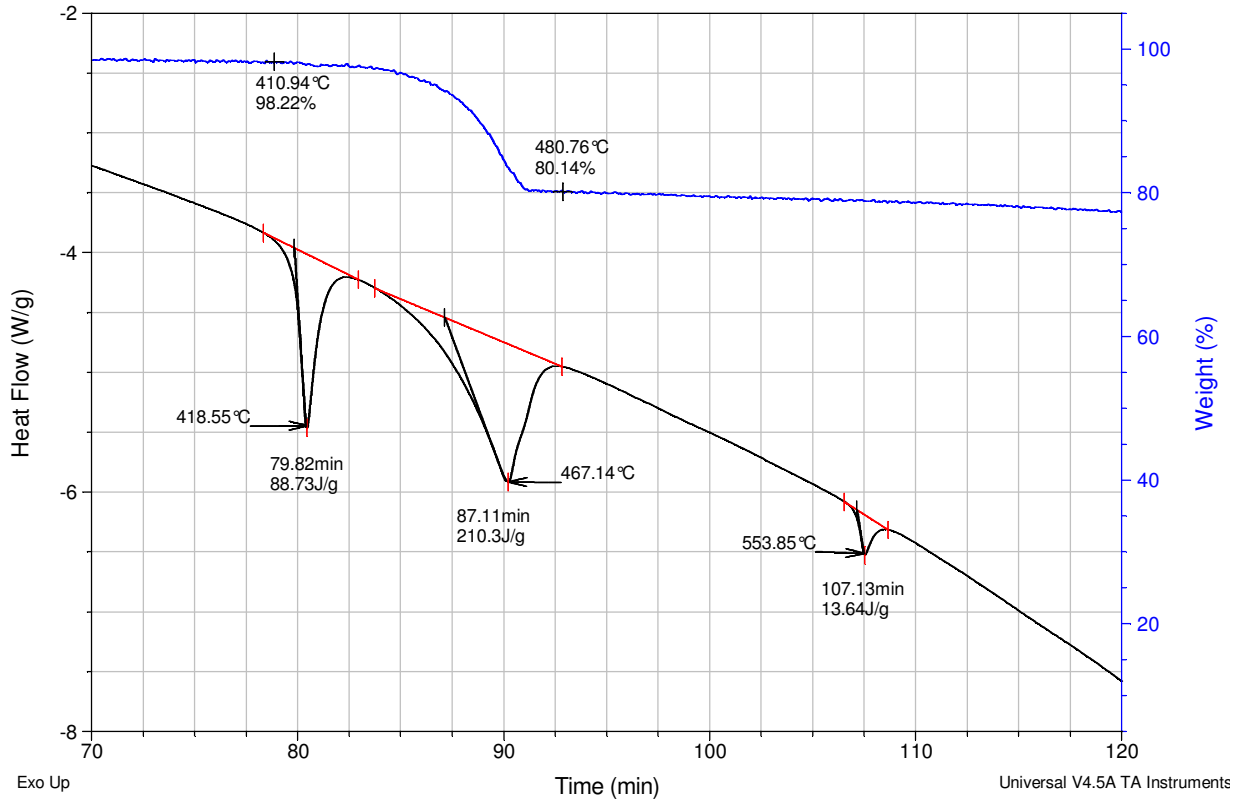

Figure 8.1.1 Thermal analysis by DSC-TGA of $AgIO_3$ heated under nitrogen at 5 K/min. The $AgIO_3$ was commercial micron sized $AgIO_3$ ball milled down to a particle size of around 900 nm. This experiment was run at NAWC China Lake by Curtis Johnson.

Thermal decomposition of the 270 nm $AgIO_3$ at high heating rates was investigated by conducting the hot wire experiment using the T-Jump/TOFMS. From the experimental results, we detect the release of O_2, O and I, above 1150 K, which is about 350-400 K higher than the temperature observed in the DSC-TGA experiments. The release profile is plotted along with the wire temperature in Figure 8.1.2. We do not detect any silver or silver iodide (AgI) gas formation. These results indicate that at high heating rates, the decomposition mechanism has completely changed from what was observed in the DSC-TGA experiment. A possible mechanism involving the release of iodine and oxygen could involve the formation of the known compound Ag_5IO_6, analogous to the decomposition of $Ba(IO_3)_2$, which forms $Ba_5(IO_6)_2$. [161]

Iodine has also been reported in the thermal decomposition of $NaIO_3$, where about 28% of the salt decomposes to Na_2O, I_2, and O_2, with the rest decomposing to NaI and O_2. [162]

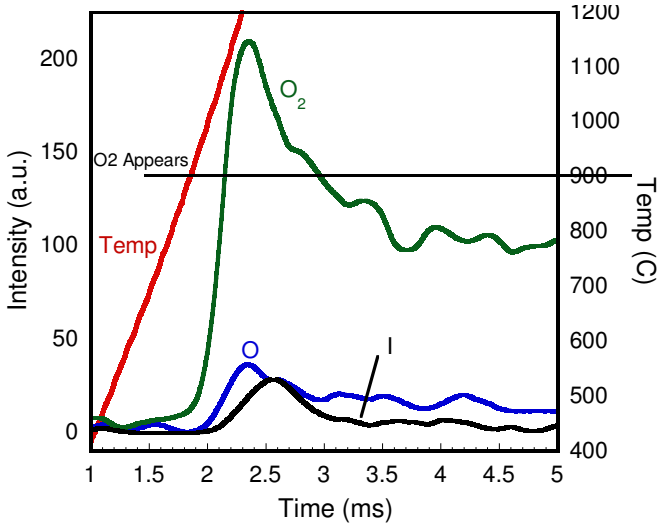

Figure 8.1.2 Transient gas release profile as determined by rapidly heating $AgIO_3$ in the mass spectrometer. The material is the synthesized 270 nm $AgIO_3$.

In order to further examine the decomposition mechanism, AgI was also tested on the wire. In this case we see a small AgI signal with a relatively large Ag and I signal occurring concurrently. This sort of behavior is consistent with the AgI being evaporated and then being cracked by the electron beam into elemental Ag and I, otherwise we would expect to see the emergence of Ag and I at different temperatures corresponding to their individual vaporization temperatures. In any case, the AgI results showed a very different spectrum than the $AgIO_3$. The results imply that AgI is not an intermediate product in the decomposition of $AgIO_3$ at high heating rates, and would therefore suggest that the decomposition mechanism is more likely analogous to that observed for $Ba(IO_3)_2$. It also suggests that thermal analysis techniques may not necessarily be accurate in predicting decomposition behavior under very intense heating rates.

The experimental ignition temperature of $Al/AgIO_3$ (1215 K) is well above the point where $AgIO_3$ is found to decompose and release oxygen using slow heating thermal analysis (~740 K). However, it does correlate with the O_2 release temperature experimentally seen in the mass spectrometer (1173 K) at high heating rates. While the decomposition mechanism is evidently different at high heating rates, we see experimentally that the release of O_2 is an important part of the ignition mechanism, consistent with CuO and Fe_2O_3. Analogous to these systems, we may speculate that the ignition in the $Al/AgIO_3$ thermite may be dependent on the thermal decomposition of $AgIO_3$ to provide a critical partial pressure of O_2 to ignite the aluminum.

Next we record a video of the thermite sample heated on the wire in vacuum and at atmospheric conditions. At atmospheric conditions, we see a violent reaction and evidence of the unreacted powder being lifted off the wire. A series of snapshots of the powder burning on the wire is shown in Figure 8.1.3. What can be seen is that the unreacted powder can be propelled away from the wire prior to any luminescence/burning. Nanoparticles have very fast characteristic flow relaxation times, meaning that they can easily be picked up and swept forward by gas. If the oxidizer is thermally decomposing to release O_2 or other gases such as Iodine, the hot decomposition gases could be responsible for a large part of the convective heat transfer, while also propelling the unreacted powder forward. This behavior could lead to propagation rates that occur much faster than the characteristic burning time of the fuel particles.

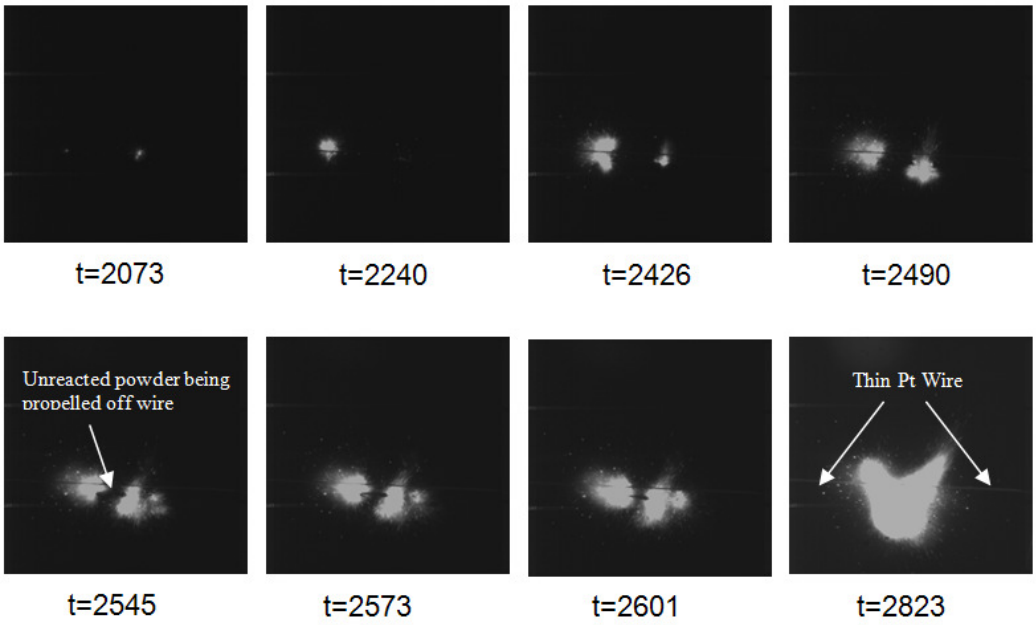

Figure 8.1.3 Sequential snapshots of Al/$AgIO_3$ burning in air. The wire can only faintly be seen, and remains stationary throughout the burning. The thermite is Al (ALEX) and $AgIO_3$ (270nm), with an equivalence ratio of 1.0.

In the mass spectrometer (10^{-7} torr), the thermite showed visual signs of burning but it was clearly less violent than at atmospheric conditions. We also collected the time-resolved mass spectra, and found the data to be similar to the pure $AgIO_3$ (O_2, I, and O release), but the rise times of these signals were faster. The heat liberated during the reaction seems only to be further decomposing the oxidizer. While the Al/$AgIO_3$ thermite does show visual signs of reacting under vacuum, one must be careful about interpreting the results. The mean free path of gas molecules under vacuum is orders of magnitude higher than in air, and so some oxygen may simply escape from the thermite before it reacts with the aluminum. Also, the interparticle heat transfer may be hindered due to the lack of interstitial air to rapidly conduct/convect heat to adjacent particles. Therefore, it's possible that the temperature does not reach the adiabatic flame temperature, and thus species such as Ag vapor may not be seen in this system, but may exist for larger samples reacted at atmospheric pressures.

Combustion cell tests were used to evaluate $Al/AgIO_3$ relative performance against other thermites under atmospheric conditions. The experimentally measured pressure and optical data is tabulated for $Al/AgIO_3$ along with a relatively slow (Al/Fe_2O_3) and fast (Al/CuO) thermite for comparison in Table 8.1.3. Clearly the $Al/AgIO_3$ system significantly outperforms both other oxidizers in terms of relative performance, achieving a much higher peak pressure and pressurization rate. Combining the mass spectrometer results with the thermodynamic predictions, the improved performance is likely a combination of higher reaction temperatures and enhanced gas release during the oxidizer decomposition.

Table 8.1.3 Pressure cell data for $Al/AgIO_3$ along with a relatively slow (Al/Fe_2O_3) and fast (Al/CuO) thermite (CuO and Fe_2O_3 from Sigma Aldrich).

	Al/Fe_2O_3	**Al/CuO**	**$Al/AgIO_3$**
Pressure Rise (psi)	13.4	116	296
Pressure Rise Time (μs)	800	13	5.3
Pressurization Rate (psi/μs)	0.017	9.0	57
FWHM Burn Time (μs)	936	192	172

We have recently argued that the initial pressure spike for a fast-burning MIC (i.e. Al/CuO) is mainly attributed to the oxidizer decomposition, since the decomposition happens at a temperature well below the adiabatic flame temperature.[154] As the aluminum is ignited and begins to burn, we argued that the energy liberated by the reaction further causes the oxidizer to thermally decompose and release gas, thus pressurizing the system, followed by the remainder of the aluminum burning. In the pressure cell tests, this is experimentally seen as a fast pressure spike followed by an optical emission signal over a much longer timescale. We proposed that the burning mechanism in such a system is similar to the burning of aluminum in a pressurized, oxygenated environment. For the $Al/AgIO_3$ thermite, we see the same characteristic behavior; a fast initial pressure spike followed by a longer optical burning time.

In comparing the pressure cell data for Al/CuO and Al/$AgIO_3$ (Table 8.1.3), one sees that both thermites have approximately the same burning time, but very different pressurization behavior. If both systems were thermally decomposing and releasing oxygen, followed by the remainder of the aluminum burning, then we would expect similar times since the burning would be rate-limited by the aluminum in both cases. The large difference in pressurization is likely attributed to the decomposition products of the two oxidizers. $AgIO_3$ can release significantly more gas upon thermal decomposition, i.e. O_2, O, I. If the temperature was able to quickly approach the adiabatic flame temperature listed in Table 8.1.1, some amount of Ag could also be vaporized and thus contribute to the pressure.

Combustion tests were also conducted on loose powder samples placed along a line on a supporting aluminum pan. Propagation rates were determined by high speed video imaging, with the results presented in Figure 8.1.4. Combustion proceeded steadily across the samples, giving propagation rates of 630 m/s for a sample composed of 80 nm Al/270 nm $AgIO_3$, 600 m/s for 80 nm Al/1.2 μm $AgIO_3$, and 340 m/s for 80 nm Al/45 nm CuO (Technanogy). The propagation rate for Al/CuO (where the equivalence ratio was 1.27) is similar to the ~500 m/s reported in an open tray burn test[98]. As with the combustion cell tests, the $AgIO_3$ oxidizer gave a higher reactivity compared to CuO. Surprisingly, the micron-sized $AgIO_3$ thermite had nearly the same propagation rate as the nanothermite. If the characteristic heating/decomposition time of the oxidizer is much faster than the characteristic reaction time of the aluminum, then this behavior might be expected. However, further work would be required to verify this. The combustion tests and the measured high propagation rate of the micron $AgIO_3$ thermite are consistent with a mechanism where the $AgIO_3$ rapidly decomposes and releases Iodine and also oxygen, which then reacts with Al.

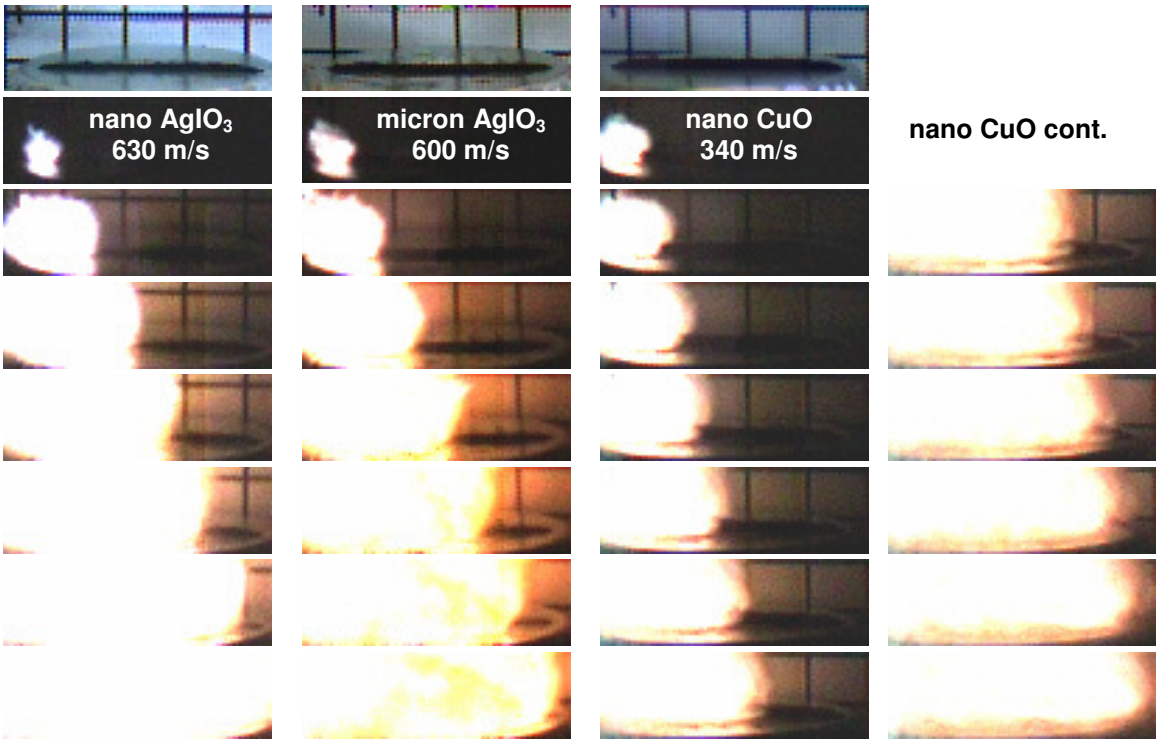

Figure 8.1.4 Video images of the combustion of three thermite samples in air. These videos were taken at NAWC China Lake by Curtis Johnson. The images at the top show the samples prior to combustion, with a 45 mg line of powder placed on an aluminum support. A grid directly behind the sample has a spacing of 10.8 mm between lines. Samples were ignited by a spark from a wire attached to a tesla coil (tip of wire visible in the upper left corner of the top images). Images were recorded at 10 µs intervals, using a 2 µs exposure. The Al in this study is 80 nm from NanoTechnologies. The CuO in this study is 45 nm from Technanogy. Each sample was fuel-rich in this study with equivalency ratios of 1.12 for the nano $AgIO_3$ material, 1.06 for the micron $AgIO_3$ material, and 1.27 for the CuO material.

8.1.3.2 Post Combustion Characterization

In biocidal applications, the nature and dispersion of the product may supersede the importance of the actual combustion performance. A representative TEM image along with the elemental maps of Al, O, I, and Ag is shown in Figure 8.1.5 for products from the pressure cell test. (Unfortunately, the image quality was limited by instability of the material under the electron beam, where prolonged exposure induced morphological changes. This behavior is somewhat common when trying to image species such as iodine, which can readily

ionize/vaporize under an intense electron beam). We see particles that contain Al and O, and other particles which contain both Ag and I. In several cases, we see particles that appear to contain all four elements. Two such particles are shown in Figure 8.1.6 along with an elemental linescan coupled with elemental analysis. The results show the formation of a core-shell structure of Al_2O_3 surrounded by Ag and I. (In the next section we confirm via X-Ray diffraction that this is actually AgI). Conceptually, this core shell structure could form since Al_2O_3 has a relatively high boiling/decomposition point (~4000 K). Either the Al_2O_3 never exists in the gas phase, or upon cooling, will be the first species to condense. The Ag and I then somehow recombine, either through gas phase recombination reactions or heterogeneous surface reactions, and coat the Al_2O_3 surface before solidifying. The actual mechanism or extent of coating is beyond the scope of the work, but it is important to mention that we do see that the biocidal agent is exposed to the environment post-reaction, and is not trapped (i.e. as the core in core-shell structure).

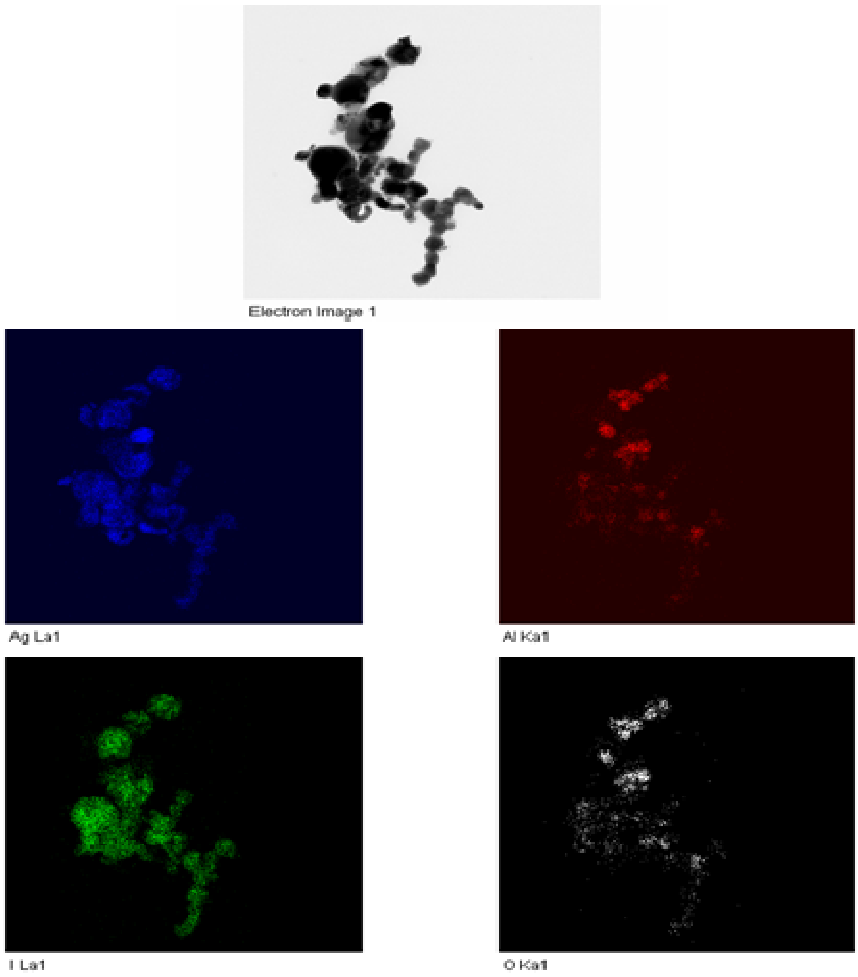

Figure 8.1.5 Representative TEM image and 2D elemental maps (using EDX) of Ag, Al, I, and O after reaction inside the combustion cell. Higher resolution images could not be achieved due to beam interactions and morphological changes in the sample with prolonged beam exposure. The thermite was Al (ALEX) and synthesized $AgIO_3$ (270 nm) with an equivalence ratio of 1.0.

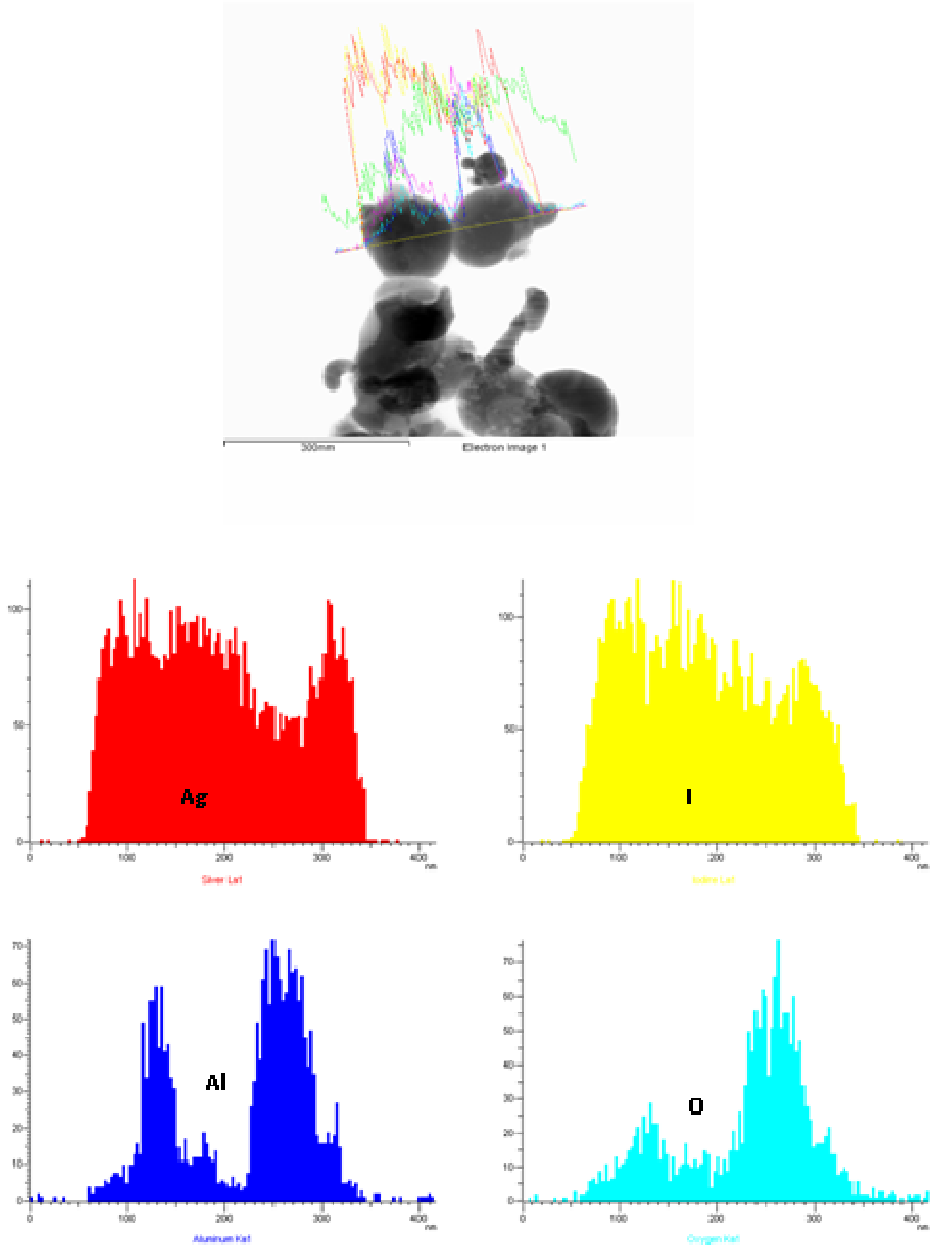

Figure 8.1.6 TEM image and 1D elemental linescan (using EDX) across two adjacent particles of Al/$AgIO_3$ reacted in the pressure cell. Note the presence of an Al/O core surrounded by AgI in each particle. The extra (green) line shown in the image was Carbon from the film. The thermite was Al (ALEX) and synthesized $AgIO_3$ (270 nm) with an equivalence ratio of 1.0.

The XRD patterns for pure $AgIO_3$, along with unreacted and reacted Al/$AgIO_3$ thermites are shown in Figure 8.1.7. What we see is the disappearance of Al and $AgIO_3$ spectra, and the emergence of AgI in the product. Most of the peaks in the XRD pattern match well with γ-AgI,

which is the dominant polymorph obtained when AgI is rapidly cooled from its melting point[163]. The presence of a lesser amount of the β polymorph of AgI is indicated by the peak near 2θ = 22. The alumina that forms exhibits only weak peaks in the XRD pattern. The peak at 2θ = 67, along with the shoulder at 45.5 degrees, are likely due to δ-Al_2O_3, which is commonly observed when molten Al_2O_3 rapidly crystallizes, such as in the synthesis of nanophase alumina by arc plasma[164]. Elemental silver was not detected by XRD, so it appears that the biocidal reaction product of Al/$AgIO_3$ is almost entirely AgI.

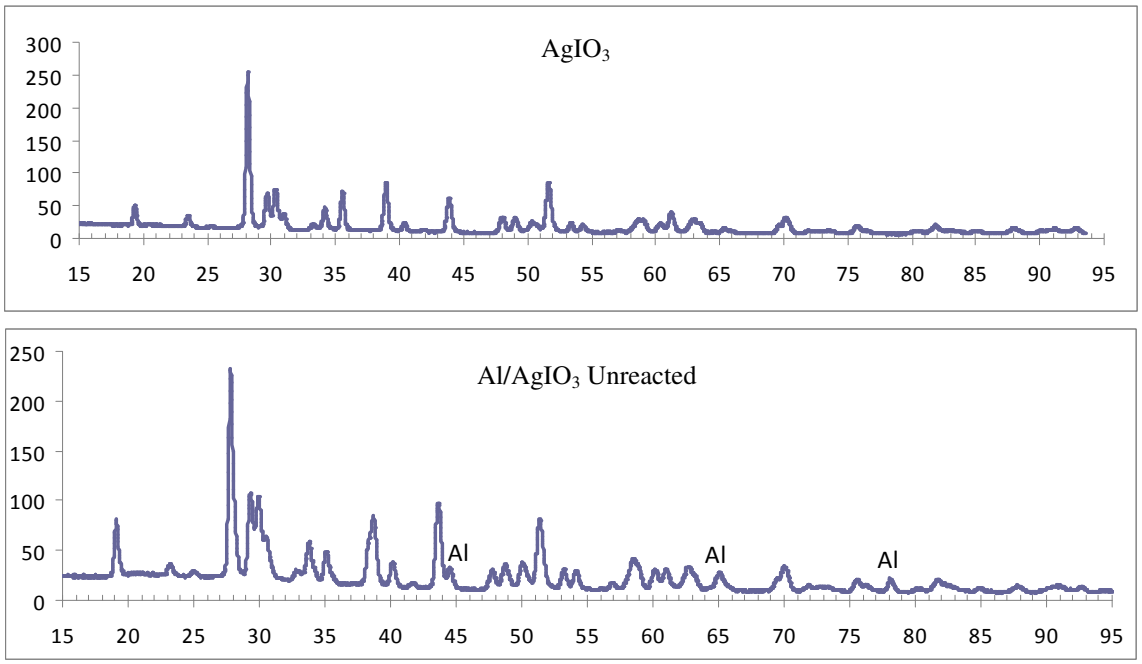

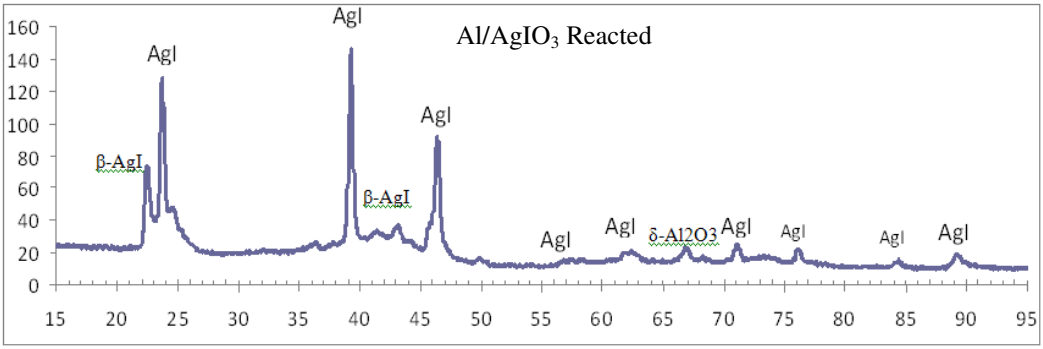

Figure 8.1.7 XRD patterns (Intensity vs 2θ) for pure $AgIO_3$, along with the thermite before and after reaction in the pressure cell. The major detectable reaction product is AgI. Unless otherwise noted, the AgI peaks are γ-AgI. The thermite was Al (ALEX) and synthesized $AgIO_3$ (270 nm) with an equivalence ratio of 1.0.

Segregated AgI and aluminum oxide products have also been identified in an experiment conducted to quench the hot products from the thermite reaction. A 20 mg sample was placed at the center of one copper plate, and a second plate was placed parallel to and 10 mm above the first plate. The sample was initiated with a spark. Residue collected on the top plate at a point directly above the original sample consists mainly of micron-scale globular structures, as shown in micrographs a, b, and d in Figure 8.1.8. This deposit is highly enriched in Al (and O), based on the overall atomic ratio of 10 Al per Ag in this region, vs. a ratio of 2.5 in the thermite. Elemental mapping indicates that all of the micron-scale features are predominantly aluminum oxide. Spot EDX analysis shows that some of the submicron particles are highly enriched in Ag (Ag:I ratio approximately 5:1), as marked in micrograph d. Overall, the Ag:I ratio was 4:3 in this region, and an elemental map of iodine showed essentially uniform occurrence, except in the area of the large aluminum oxide particle in the upper left corner of micrograph b. This large smooth particle may have cooled slower than the smaller aluminum oxide deposits, resulting in less condensation of AgI on the surface. Residue from a region 10 mm away from the center of the top plate is shown in the micrograph in Figure 8.1.8c. This area contains rather sparse deposits identified mainly as micron-sized aluminum oxide spherical particles, ≤100 nanometer

AgI particles, and some micron-sized islands of elemental Ag. In this region the Al/Ag ratio is 1.6. The center region would be the hottest region during the reaction, where molten aluminum oxide deposited (m.p. 2327 K). This region is depleted of Ag and I, probably by transport of the vapor to cooler regions. Both regions analyzed contain nearly stoichiometric Ag and I, consistent with the observation of AgI as the predominant Ag product by XRD analysis. However, small amounts of elemental silver deposits were also observed, including nanoparticulates.

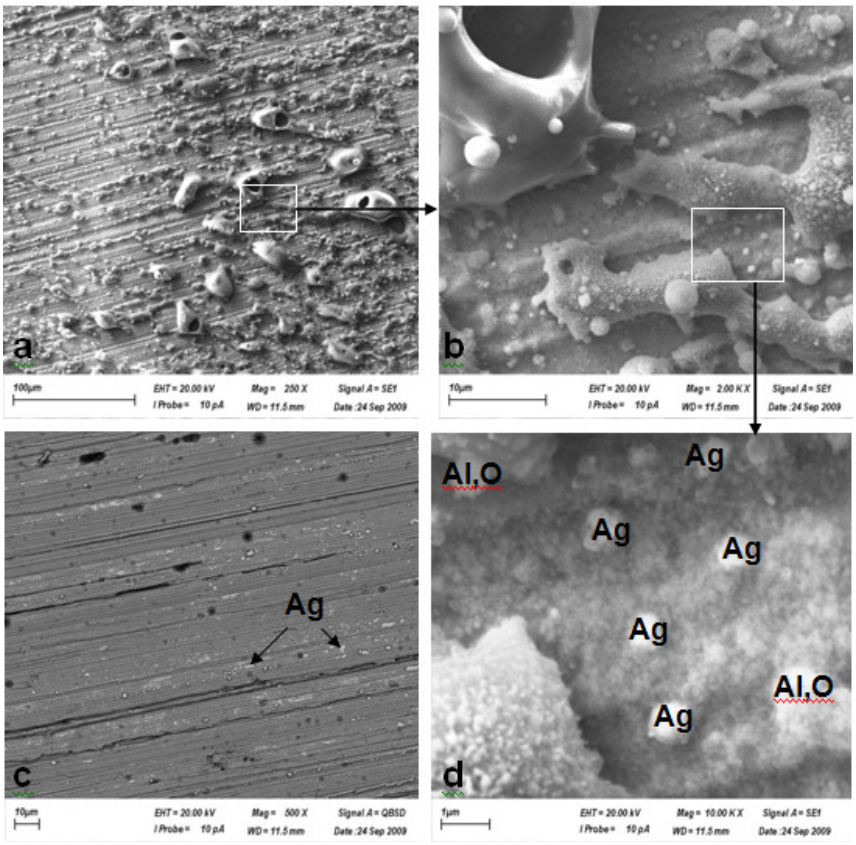

Figure 8.1.8 Scanning electron micrographs of reaction products from spark initiated nano Al/$AgIO_3$ (20 mg) deposited on a copper plate. These images were taken at NAWC China Lake by Curtis Johnson. Micrographs a, b, and d (taken at different magnifications) show the region of the copper plate that was positioned 10 mm directly above the sample. Micrograph c shows a region of the copper plate that was 10 mm distant from the spot of the top micrograph. Micrograph c was taken in the quantum backscatter mode, where the light elements (Al, O) appear as dark spots in the image, while the heavy elements (Ag, I) appear as light spots. Small islands of elemental Ag (essentially free of iodine) are marked in micrograph c. The nearly horizontal lines result from abrasive polishing of the copper plate. The Al was from Nanotechnologies, and the $AgIO_3$ was synthesized (270 nm).

From the post reaction analysis, we do see that high surface area nanoparticles of the biocidal elements are formed. Furthermore, both Ag and I are surface exposed; i.e. not trapped within the interior of a particle.

8.1.4 Main Conclusions of Work

$AgIO_3$ was investigated as an oxidizer in nanoaluminum-based thermites, in particular for systems designed for biocidal activity. The ignition temperature of the $Al/AgIO_3$ was determined to be 1215 +/- 40 K for rapid heating on a wire. Mass spectrometry showed that the $AgIO_3$ decomposed into O_2, O, and I. High speed imaging showed that the reaction proceeded violently in air, with ejection of powder radially away from the wire. Pressure cell tests showed that the $Al/AgIO_3$ significantly outperformed Al/CuO in pressurization rate, while both systems show nearly the same burning time. This suggests that the burning mechanisms are similar and rate-limited by the aluminum. The pressurization enhancement is likely attributed to the enhanced gas release as $AgIO_3$ decomposes, along with the higher energy content and reaction temperature of this system. Post-reaction analysis was performed, and XRD showed primarily AgI as the crystalline reaction product. Electron microscopy with elemental analysis indicated that the silver iodide products were generally spherical and agglomerated, with the AgI covering some of the surfaces of aluminum oxide to form core-shell particles.

8.2 Synthesis and Reactivity of Nano-Ag_2O as an Oxidizer for High Yield Antimicrobial Energetic Systems

8.2.1 Overview

This work investigates Ag_2O as a potential oxidizer in energetic thermite systems designed to produce a high yield of elemental silver, which has been long shown to exhibit excellent biocidal activity. Ag_2O was synthesized by a wet chemical technique, and its performance in nanoaluminum-based thermite systems was examined using a constant volume combustion cell. The Ag_2O itself was found to be a poor oxidizer, but performed well when blended with both $AgIO_3$ and CuO. In the Al/$AgIO_3$/Ag_2O system, the reactivity dropped off relatively linearly as the mass loading of Ag_2O increased, followed by a sharp drop around 40 Wt% Ag_2O, and indicating a shift in the reaction mechanism. In the blended Al/CuO/Ag_2O, we found that the system reactivity remains relatively unchanged even when the mass loading of Ag_2O exceeded 50 Wt%, and at 77 Wt% the reactivity had only dropped by about a factor of 2. In other words, a large amount of the initial mass can be converted into biocidal silver with little loss of performance. The reacted products were collected and examined using with x-ray diffraction (XRD) and x-ray photoelectron spectroscopy (XPS) to confirm the formation of elemental silver. The XPS data indicates that a thin oxide shell is present on the silver, a desirable effect for the enhanced transport of potent Ag^+ ions to the environment.

8.2.2 Introduction and Relevant Literature Review

This work investigates Ag_2O as a potential oxidizer in energetic thermite systems designed for antimicrobial activity. A comparison of several silver-based oxidizers is shown below in Table 8.2.1, along with the theoretically predicted maximum amount of elemental silver

produced per gram of mixture. Note that the values of produced silver are given as a theoretical maximum, and will actually be lower if any recombination can occur (as is the case for $AgIO_3$, where the product is largely AgI).[165] As can be seen, not only does Ag_2O have the highest yield of elemental silver (86% conversion by mass) out of any other silver-based oxidizer, it will also not suffer from recombination reactions like many of the other species. Therefore, if the silver oxide can be fully reduced during the reaction, then the residual product will primarily be composed of large amounts of antimicrobial silver.

Table 8.2.1 Various silver-containing oxidizers and the maximum calculated silver production in stoichiometric thermite mixtures with aluminum. Note that the calculations assume no recombination (i.e. Ag + $0.5I_2$ → AgI) and therefore may overestimate the mass production of silver depending on the extent of recombination.

Oxidizer	Stoichiometric Reaction (assuming no recombination)	grams Ag produced (max) / gram thermite
Ag_2O	$2Al + 3Ag_2O \rightarrow Al_2O_3 + 6Ag$	0.86
AgO	$2Al + 3AgO \rightarrow Al_2O_3 + 3Ag$	0.76
Ag_2SO_4	$8Al + 3Ag_2SO_4 \rightarrow 4Al_2O_3 + 6Ag + 3S$	0.56
$AgNO_3$	$2Al + AgNO_3 \rightarrow Al_2O_3 + Ag + 0.5N_2$	0.48
$AgClO_4$	$8Al + 3AgClO_4 \rightarrow 4Al_2O_3 + 3Ag + 1.5Cl_2$	0.39
$AgIO_3$	$2Al + AgIO_3 \rightarrow Al_2O_3 + Ag + 0.5I_2$	0.32

In this work we have synthesized <20nm Ag_2O by a wet chemical process, and we investigate the use of Ag_2O as an oxidizer in energetic thermite systems. The aluminum and Ag_2O mixture, along with aluminum and blends of Ag_2O with both $AgIO_3$ and CuO are also investigated for the combustion characteristics as a function of Ag_2O loading. Ex-situ x-ray diffraction and x-ray photoelectron spectroscopy are used to characterize the products and show that surface-exposed elemental silver is produced.

8.2.3 Experimental

8.2.3.1 Materials

The nanoaluminum, termed "50nm ALEX," was purchased from the Argonide Corporation, has an average particle diameter of 50nm as specified by the supplier, and TGA showed the aluminum to be 70% elemental by mass. The copper oxide used in this work was purchased from Sigma Aldrich, and has an average particle diameter of <50nm as specified by the supplier. The nanoscale $AgIO_3$ was synthesized at the Naval Air Warfare Center Weapons Division (NAWCWD) by precipitation from aqueous solutions of silver nitrate and potassium iodate or sodium iodate, using a modification of a literature method.[156] The morphology of the as-produced $AgIO_3$ was thin platelets, with the specific surface area measured to be 4.0 m^2/g, corresponding to a spherical particle diameter of 270 nm. More information on the method and characterization can be found in a separate work[165].

The nano-scale Ag_2O was synthesized through a wet chemical technique. A 0.005 M silver nitrate ($AgNO_3$, >99% purity, Sigma Aldrich) aqueous solution was prepared, and 80 mL was heated to 60 ^{0}C. 20 mL of a 0.025 M sodium hydroxide (NaOH, >98%, anhydrous, Sigma Aldrich) aqueous solution was added drop-wise, while the solution was constantly stirred with a magnetic stir bar, until the solution had the consistency of a grey-yellow colloidal suspension. The reaction of silver nitrate with sodium hydroxide produces silver hydroxide via the following mechanism:

$$AgNO_3 + NaOH \rightarrow AgOH + Na^+ + NO_3^-$$

However, the intermediate AgOH is very thermodynamically unstable, and ultimately produces Ag_2O through the following recombination process:

$$2AgOH \rightarrow Ag_2O + H_2O \ (pK = 2.875)$$

The solution was kept at 60 ^{0}C for two hours to ensure complete reaction. The particles were then collected in 3-4 cycles of a centrifuge/re-dispersion washing process using ethanol, and the solution was allowed to dry leaving behind the brown Ag_2O particles. A transmission electron microscope image of the as-produced Ag_2O is shown below in Figure 8.2.1. As can be seen, the majority of the primary particles are spherical with diameters <20nm, and the particles are highly agglomerated. To confirm the product to be Ag_2O, we run X-Ray Diffraction (XRD, Bruker C2 Discover with GADDS, operating at 40 kV and 40 mA with unfiltered Cu κα radiation, λ = 1.5406 Å). The XRD data for the as-prepared sample is shown in Figure 8.2.2, and confirms the material to be Ag_2O.

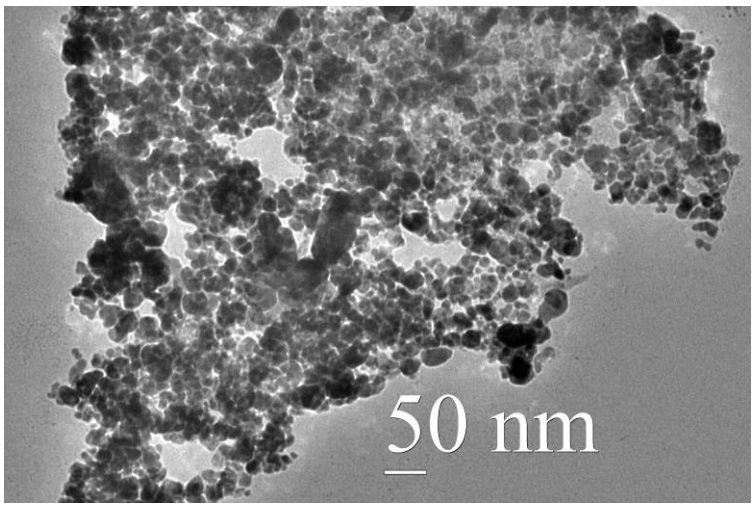

Figure 8.2.1 Transmission electron microscope image of the as-produced Ag_2O nanoparticles. The particles are primarily spherical and highly agglomerated. The primary particles are generally <20 nm in diameter.

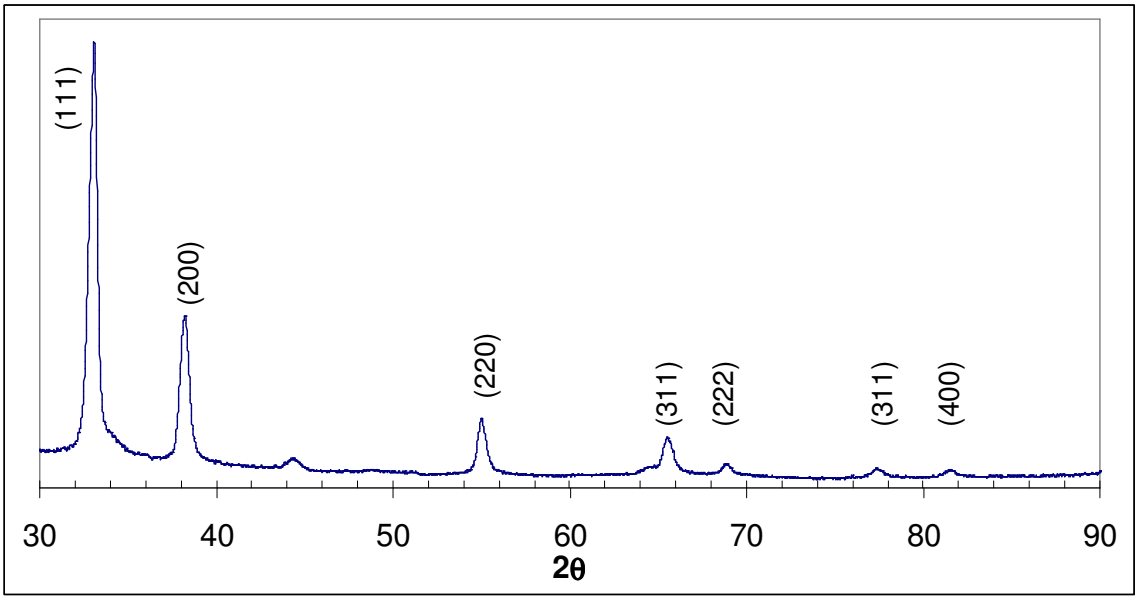

Figure 8.2.2 X-Ray Diffraction of the as-produced nanoparticles. The labeled peaks confirm the production of Ag_2O.

The thermite samples were prepared by adding the powders to a ceramic crucible with ~10mL of hexane and ultrasonicating for 30 minutes to ensure substantial mixing. The hexane was then allowed to evaporate overnight until the samples were completely dry. The loose powder was then very gently broken up using a spatula until the samples had the consistency of a homogeneous loose-powder. All samples are prepared stoichiometrically assuming complete conversion to Al_2O_3. For the blended $Al/AgIO_3/Ag_2O$ and $Al/CuO/Ag_2O$ systems, the samples are labeled in terms of the Wt% of Ag_2O in the overall mixture. Caution should be used when handling these mixtures, and especially attention to ESD to prevent accidental ignition.

8.2.3.2 Measurement of Reactivity

A fixed mass of 25 mg is loaded into a sample holder and combusted inside a pressure cell. The cell was originally designed to measure the transient pressure signal,[101] and was later modified to simultaneously collect the optical emission though a series of lenses coupled to a

photodiode.[147] The transient optical emission and pressure signals are captured during the burning via an oscilloscope, and both can be used to draw conclusions about the combustion behavior. The pressurization rate (peak to peak pressure divided by the pressure rise time) is calculated and is used as a measurement of the system reactivity,[89] and the burn time is taken to be the full width of the optical signal at half maximum. The assignment of pressurization rate to reactivity and optical emission to burn time is somewhat arbitrary, so the results are often presented as relative trends which conclusions can be inferred from. The pressurization rate for the ternary systems has thus been normalized to the measurement for the corresponding binary system (Al/$AgIO_3$ or Al/CuO. The burning times for the ternary systems will be shown, but the discussion will focus on the trends in the data instead of the absolute values.

8.2.3.3 Post-Reaction Analysis

The reacted sample was collected after combustion in the pressure cell, and was analyzed using various techniques. X-ray diffraction (XRD, Bruker C2 Discover with GADDS, operating at 40 kV and 40 mA with unfiltered Cu Kα radiation, λ = 1.5406 Å) was used to determine the crystalline species produced during the reaction. Transmission electron microscopy (TEM, JEOL 2100F) coupled with energy dispersive x-ray spectroscopy (EDS, Oxford INCA 250) was used to analyze the product and determine the morphology and location of the silver in the product. X-ray photoelectron spectroscopy (XPS) data was collected using a Kratos Axis 165 system operating in hybrid mode, with monochromatic aluminum x-rays (1486.5 eV). Survey spectra and high resolution spectra were collected with pass energies of 160 eV and 20 eV respectively. Samples were mounted on double sided carbon tape, charge neutralization was require to minimize sample charging, all peaks were calibrated to the adventitious hydrocarbon peak at 284.8 eV.

8.2.4 Results and Discussion

8.2.4.1 Combustion Performance

The pressure cell results for the thermite systems alone are shown in Table 8.2.2. The $AgIO_3$ significantly outperforms both oxidizers, and we have recently argued that this is largely attributed to iodine gas release during the decomposition of the oxidizer.[165] The Al/Ag_2O system performed very poorly in pressurization rate when compared to a relatively common and reactive thermite, Al/CuO. The reason for this is somewhat of an anomaly when one looks at the thermodynamic predictions of both systems.

Table 8.2.2 Experimental results for the three thermite systems used in this work. All oxidizers were mixed with nanoaluminum with an equivalence ratio of 1.

	Al/$AgIO_3$	**Al/CuO**	**Al/Ag_2O**
Pressure Rise (psi)	296	116	10.0
Pressure Rise Time (μs)	5.3	13	1459
Pressurization Rate (psi/μs)	57	9.0	0.002
FWHM Burn Time (μs)	172	192	1381

T

Table 8.2.3 is a side-by-side comparison of thermodynamic equilibrium predictions for Al/CuO and Al/Ag_2O thermites. The calculations are constant HP equilibrium calculations assuming phase changes.[155] Both systems are predicted to produce a relatively large amount of equilibrium gas (mostly comprised of the metal Cu or Ag), and both systems are comparable in terms of the density. However, the Al/Ag_2O system barely burns while the Al/CuO system reacts violently.

Table 8.2.3 A comparison of thermodynamic equilibrium predictions of Al/CuO and Al/Ag_2O thermites. Calculations are from Fischer and Grubelich[155] and assume constant HP with phase changes taken into account.

Reaction	ρ_{TMD} g/cm^3	T_{AD} K	moles gas per 100 g	Primary gas at equilibrium
$2Al + 3CuO \rightarrow Al_2O_3(L) + 3Cu(L,g)$	5.109	2843	0.5400	Cu
$2Al + 3Ag_2O \rightarrow Al_2O_3(L) + 6Ag(L,g)$	6.386	2436	0.4298	Ag

We have recently argued that the oxidizer decomposition is primarily responsible for pressurizing the system if oxidizer can be decomposed efficiently and on a timescale faster than the burn time of the fuel.[147] If this is the case, the system is rate limited by the aluminum and resembles burning in a pressurized, oxygenated environment. According to the ICT Database of Thermochemical Values, Ag_2O has an enthalpy of formation of -31 kJ/mol and a decomposition temperature of 523 ^{0}K. In comparison, CuO has an enthalpy of formation of -156 kJ/mol, and calculations using NASA CEA predict it to start decomposing ~1100 ^{0}K at atmospheric pressure. From these considerations we would expect Ag_2O would also release its oxygen efficiently and pressurize the system fast relative to the burning, yet the experimental data suggests otherwise.

From Table 8.2.3, the only thing that stands out between the two thermite systems is the adiabatic flame temperature difference. These temperatures are 2843 ^{0}K and 2436 ^{0}K for Al/CuO and Al/Ag_2O, respectively. While everything else seems similar for the two systems, it's possible that the lower adiabatic flame temperature of Al/Ag_2O leads to something mechanistically different in its burning. We note that this temperature is much closer to the melting temperature of Al_2O_3 (2327 ^{0}K). Upon ignition, the flame self-propagates through the powder. It is possible that the melting of Al_2O_3 is important to ensure fast reaction of the nanoaluminum for two reasons:

1) Nanoaluminum is naturally passivated by a few nm thick Al_2O_3 shell,[11,15] and the melting of this shell may be important for a fast diffusion-type reaction mechanism.[15,48,112]

2) The reaction may involve reactions at the aluminum particle surface. If the temperature is too low so that the oxide product is solid instead of molten, it

provides a substantial diffusion barrier between the fuel and oxidizer which increases in thickness as the reaction proceeds.

Obviously a definitive explanation of the relative performance differences between Ag_2O and CuO would require study beyond the scope of this paper. The reacted Al/Ag_2O was collected and examined using XRD, the results of which are shown in Figure 8.2.3. It can be seen that there is some residual Ag_2O detected in the product, and this may indicate that the oxidizer is not fully decomposed during the reaction.

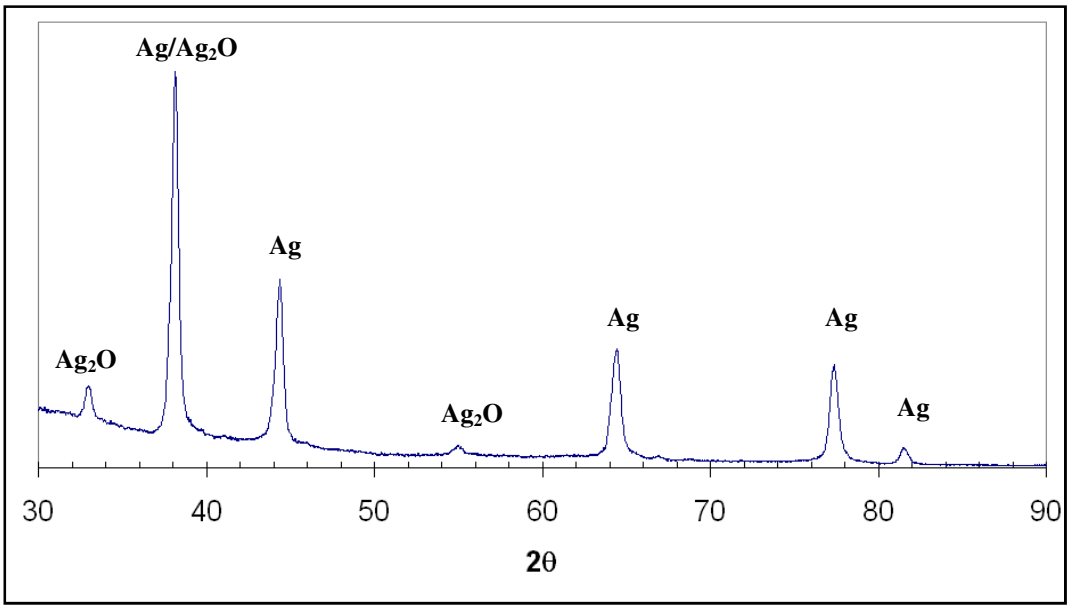

Figure 8.2.3 X-Ray diffraction of reacted Al/Ag_2O. Note the presence of Ag_2O even after the reaction, indicating that some of the oxidizer was not fully decomposed.

Next we look at ternary thermite systems consisting of nano-Al and blends of Ag_2O with both $AgIO_3$ and CuO. $AgIO_3$ was chosen because it performs very well in combustion tests, and also because its product AgI is likely biocidal in nature. The CuO was chosen because it is a relatively good oxidizer, but also the high boiling point of Cu (2840 ^{0}K) relative to Ag (2436

^{0}K). From a design standpoint, this is an important consideration due to the possible formation of core-shell structures governed by the relevant vaporization temperatures. For example, Bi_2O_3 may be a poor choice due to the low boiling point (1833 ^{0}K) of bismuth compared to the boiling point of silver. Upon cooling, a significant amount of Bi may heterogeneously condense onto Ag, rendering an undesirable Al core/Bi shell morphology. Alternatively, CuO is a better candidate due to the higher boiling point of copper. If heterogeneous condensation were indeed occurring, then at least in this case we would expect the silver to condense onto copper, an acceptable morphology since the silver would still be exposed to the environment.

The pressurization rates of the ternary systems are presented in Figure 8.2.4. As mentioned, the data has been normalized by the pure Al/$AgIO_3$ and the Al/CuO in order to keep the discussion in terms of relative performance. For the Al/$AgIO_3$/Ag_2O system, the pressurization rate drops steadily as Ag_2O is added. Around 40 Wt% Ag_2O, there is a very sudden and sharp drop in the pressurization rate, likely indicating a change in the reaction mechanism. For the Al/CuO/Ag_2O system, we see that the pressurization behavior remains relatively unchanged until >60 Wt% Ag_2O, and even then does not exhibit a sharp drop off in reactivity like was seen for the $AgIO_3$ system. Even at 77 Wt% Ag_2O, the pressurization rate has only dropped by a factor of two, and this is likely an insignificant tradeoff when the primary goal is to have a reactive system which can produce a high yield of elemental silver.

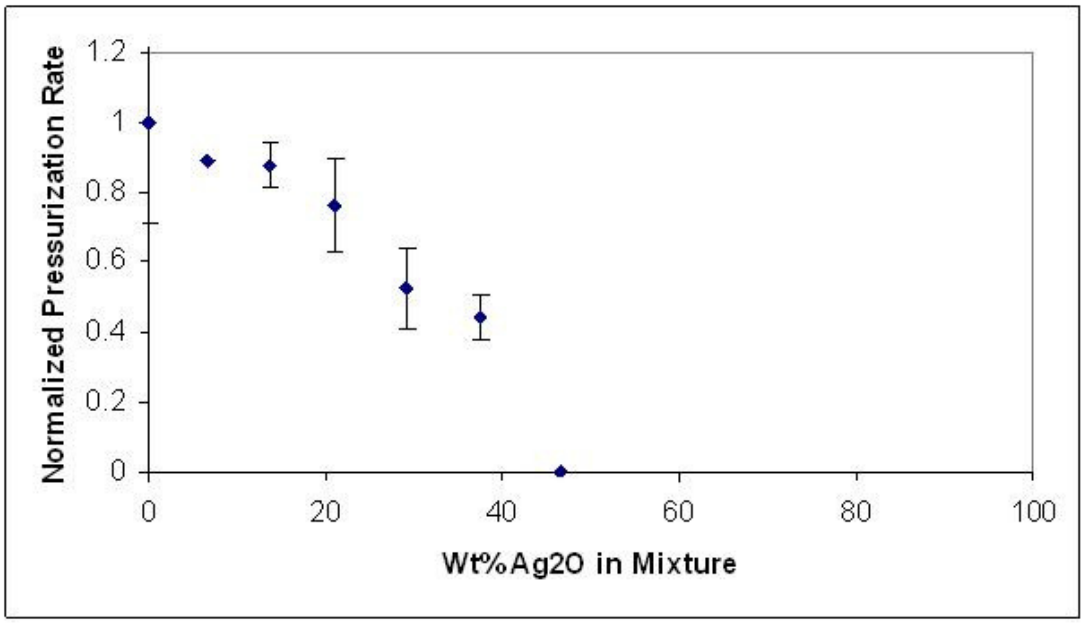

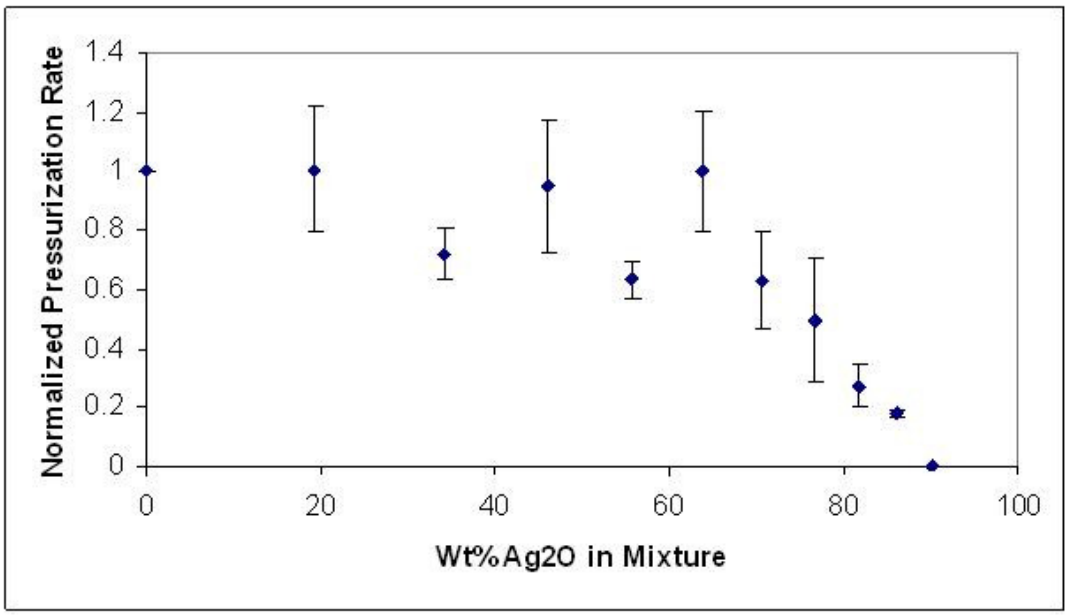

Figure 8.2.4 Experimental results for the Al/$AgIO_3$/Ag_2O (top) and Al/CuO/Ag_2O systems (bottom). Values have been normalized by pure Al/$AgIO_3$ and pure Al/CuO for the top and bottom, respectively. All mixtures are stoichiometric with an equivalence ratio of 1 assuming complete reaction to Al_2O_3.

Next we look at the measured burning times, which are taken to be the full width half max of the optical emission. This is shown for the two systems as a function of mass loading of Ag_2O in Figure 8.2.5. What can be seen is that the burn time stays relatively constant as Ag_2O is added to both systems. Above 40% in the Al/$AgIO_3$/Ag_2O system there is a sudden and sharp

increase in the burning time, and this is also the point where the pressurization rate was found to decrease suddenly. For the Al/CuO/Ag_2O system the burn time remains relatively constant over the entire range of added Ag_2O, and does not increase suddenly until the oxidizer is solely Ag_2O (90 Wt% Ag_2O in the mixture).

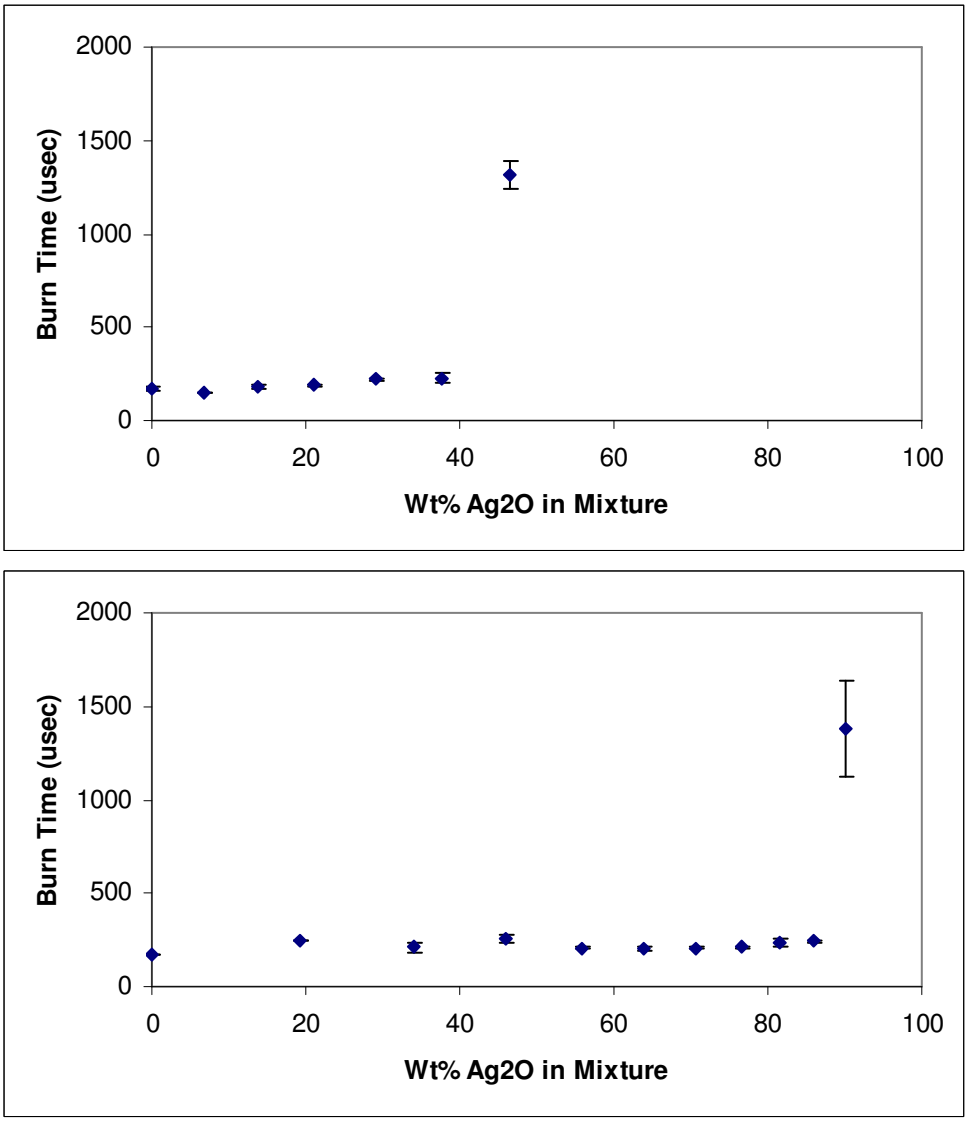

Figure 8.2.5 Burn time (full width half max of optical signal) as a function of Ag_2O mass loading for Al/$AgIO_3$/Ag_2O (top) and Al/CuO/Ag_2O (bottom).

Several of the species which may be of interest (i.e. AgI and AgO) are currently not contained within the thermodynamic product library of the NASA CEA code, and therefore

equilibrium calculations are not included. We can, however, make some speculations based on both the pressurization and burn time correlations. If the oxidizer decomposition is leading to the pressurization rate as we have recently suggested,[147] then the trends in pressurization rate start to make sense. For the $Al/AgIO_3/Ag_2O$ system, as Ag_2O is added, less $AgIO_3$ is available to decompose and pressurize the system. In addition, the flame temperature decreases as Ag_2O is added and the reactivity may suddenly drop if a temperature-sensitive reaction can no longer happen, i.e. the dissociation of AgI into Ag and I above 2650 ^{0}K.[165] In the $Al/CuO/Ag_2O$, virtually no change in the pressurization rate was observed as Ag_2O was added up to over 60 Wt%. As previously discussed, it was somewhat of an anomaly that Ag_2O did not perform well compared to CuO (see Table 8.2.3 and discussion). From thermodynamic considerations, it should readily decompose to release O_2 gas, similar to what is seen for CuO. It was therefore speculated that the adiabatic flame temperature of Al/Ag_2O being very close to the melting temperature of Al_2O_3 could be an important factor limiting the burning, if melting of Al_2O_3 was necessary for fast reaction.

Based on the pressurization trends in the ternary $Al/Ag_2O/CuO$ system, it can be seen that even a small amount of CuO could lead to a greatly enhanced reactivity relative to the binary Al/Ag_2O system. A small amount of CuO may, therefore, raise the temperature above the melting point of Al_2O_3 and thus facilitate fast reaction of the aluminum. The fact that no relative change in pressurization occurs over a range of added Ag_2O suggests that the Ag_2O and CuO behave by comparable mechanisms, i.e. decomposition and O_2 gas release. This idea can be corroborated by also looking at the relative trend in burn times, where practically no change was seen over the entire range of the ternary system, and only increased significantly for the binary Al/Ag_2O system. A constant burn time is indicative of a system which is rate limited by the fuel,

since the fuel is the only common component. We have recently argued that this behavior can be expected if a partial exothermic reaction is sufficient to rapidly decompose the oxidizer, and thus allow the aluminum to burn in a pressurized, oxygenated environment.[147]

8.2.4.2 Post-Reaction Analysis

The reacted product was collected for each sample and studied using XRD to determine the crystalline product species. The diffraction patterns for the $Al/AgIO_3/Ag_2O$ system are shown in Figure 8.2.6. As can be seen, the strongest peak of Ag at $2\theta = 38.15$ ° from the (111) plane increases with the mass loading of Ag_2O, while the strongest peak of AgI at $2\theta = 23.81$ ° from (111) plane decreases. Above 40% the relative intensity of both peaks drops off, and this behavior is likely due to the change in mechanism, experimentally seen as the sharp drop-off in reactivity from the pressure cell data.

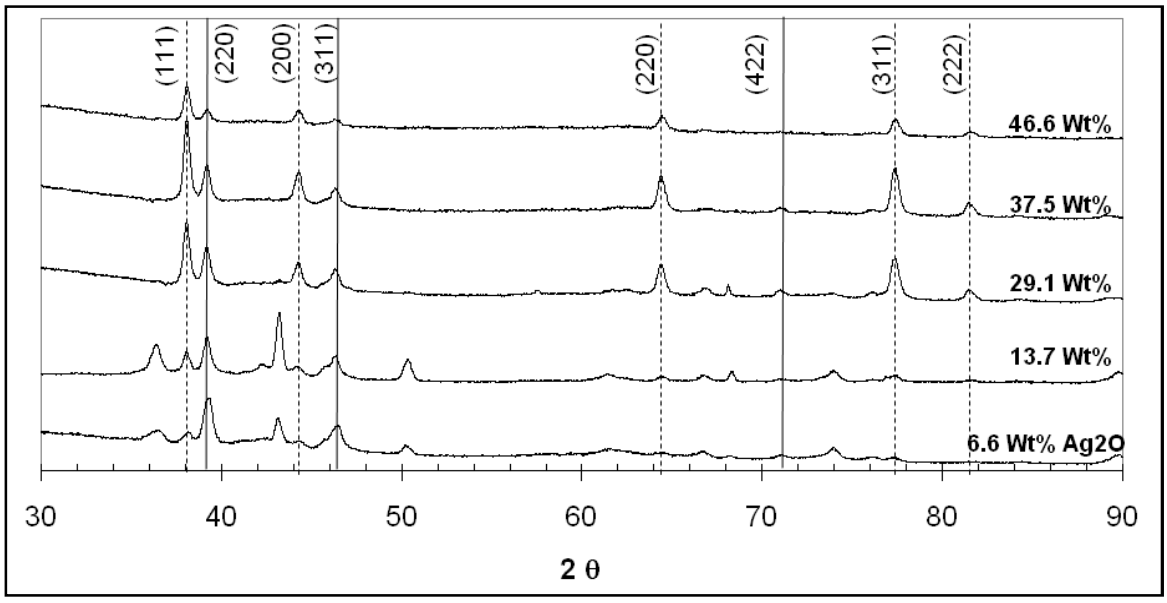

Figure 8.2.6 X-Ray diffraction of the reacted $Al/AgIO_3/Ag_2O$ samples collected after combustion in the pressure cell. The dotted vertical lines are Ag peaks, while the bold lines are AgI. XRD confirms the formation of elemental silver, along with decreasing amounts of AgI as the Ag_2O mass loading increases. Above 46.6 Wt%, a drop in the intensity of both Ag and AgI is observed, indicating a shift in the reaction mechanism, and experimentally supported by a sudden drop in the pressurization rate and increase in burn time.

The XRD data for the Al/CuO/Ag_2O system is shown in Figure 8.2.7. The Ag peaks are all present, however, only trace amounts of crystalline Cu were detected in the product relative to the amount of Ag which was formed. It's possible that some of the reduced copper can reoxidize with the air in the pressure cell to form an amorphous product, whereas the silver does not readily re-oxidize. It can also be seen that no apparent trend in the intensity of the Ag peaks was observed with increased mass loading of Ag_2O. While this could simply be due to differing sample sizes used in the XRD, it's a somewhat curious observation.

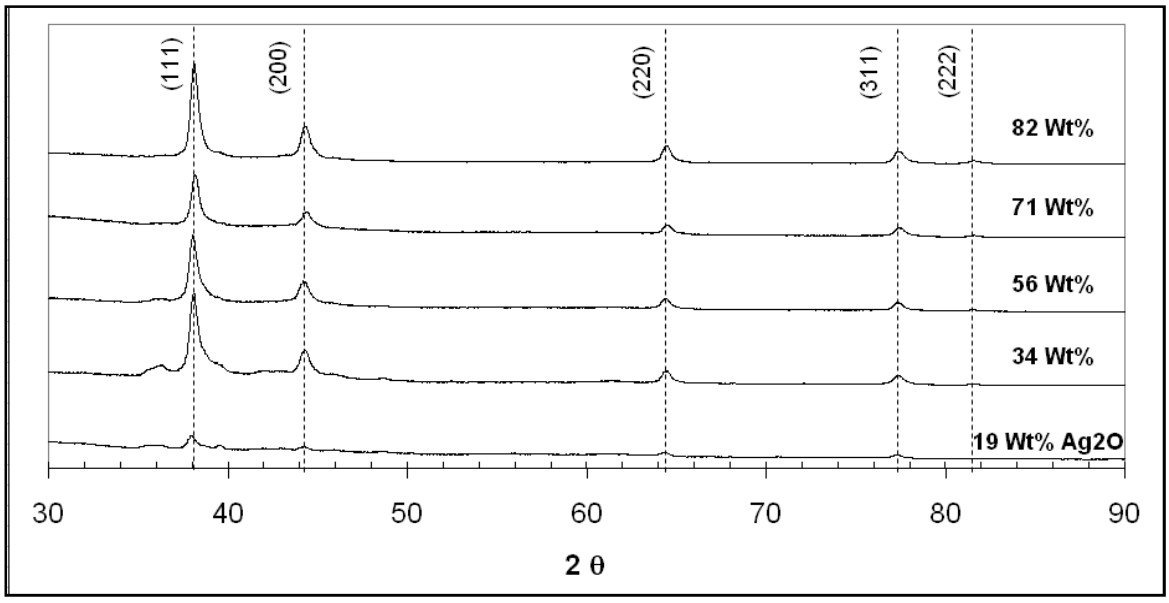

Figure 8.2.7 X-Ray diffraction of the reacted Al/CuO/Ag_2O samples collected after combustion in the pressure cell. XRD confirms the formation of elemental silver.

XPS data for silver Ag 3d and Ag MNN were collected for both ternary systems. Data was collected for various Wt% of Ag_2O in each system, however, only one set of results will be presented from each system. The data selected is for mixtures with a large Wt% of added Ag_2O, but before a significant drop in reactivity was measured. This corresponded to 29 Wt% Ag_2O for the Al/Ag_2O/$AgIO_3$ system, and 77 Wt% for the Al/Ag_2O/CuO thermite. A comparison of the

spectra before (a,b) and after (c,d) combustion for 29 Wt% Ag_2O in $Al/Ag_2O/AgIO_3$ and 77 Wt% Ag_2O in $Al/Ag_2O/CuO$ are shown in Figures 8.2.8 and 8.2.9, respectively.

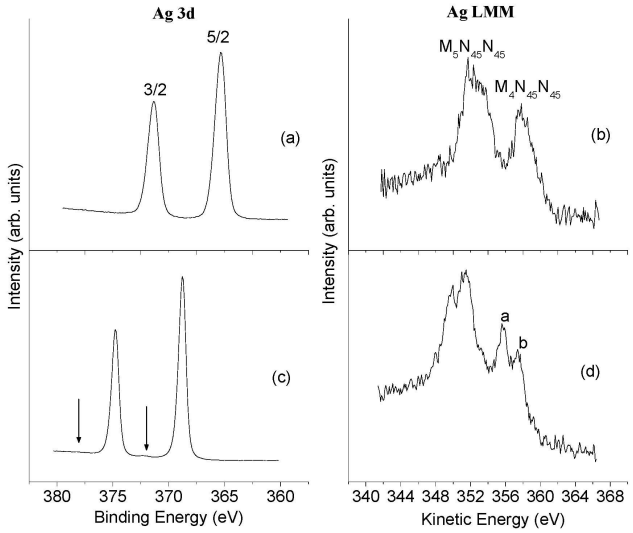

Figure 8.2.8 Ag 3d core level and Ag MNN Auger spectra for the $AgIO_3$ starting material (a,b) as compared to the spectra from the product of combustion (c,d) for an $Al/Ag_2O/AgIO_3$ mixture with 29 Wt% Ag_2O.

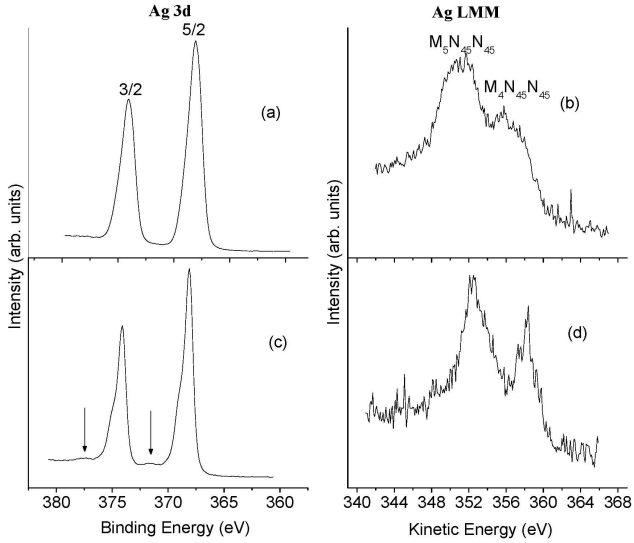

Figure 8.2.9 Ag 3d core level and Ag MNN Auger spectra for the Ag_2O starting material (a,b) as compared to the product of combustion (c,d) for an $Al/Ag_2O/CuO$ mixture with 77 Wt% CuO.

Due to very small shifts in binding energy in the Ag 3d region, less than 0.4 eV between Ag, Ag_2O and AgO, it is not possible to discern oxidation state changes based on BE shifts alone.

However, the Auger transition exhibits considerable shifts, this two electron hole final state being more sensitive to surrounding environment. Even more convenient is to compare Auger parameters which have the added benefit of being independent of sample charging and work function. The modified Auger parameter, α' can be obtained through XPS measurements and is defined as:

$$\alpha' = \text{KE(Auger)} - \text{KE(photoelectron)} + h\nu$$

where KE(Auger) is the kinetic energy of an auger transition, KE(photoelectron) is the kinetic energy of a core level photoelectron, and $h\nu$ is the photoexitation energy.

While the BE shift alones are subtle, the Ag 3d and Auger spectra after combustion are significantly different from that of the starting material for both samples. The Ag 3d peaks show a significant narrowing of the FWHM, the appearance of a second peak and low intensity plasmon loss peaks associated with the Ag 3d5/2 and 3/2 spin-orbit-split components. The presence of the plasmon peaks which are separated from the most intense Ag 3d 5/2 an 3/2 by ~3.5 eV to higher binding energy[166] (labeled with an arrows in the figure) and the narrowed FWHM are characteristic of metal formation. The appearance of the additional peak at 368.9 eV could be due to the formation of some silver aluminum alloy, as it is in good agreement with literature values, 368.8-369.0 eV.[167] Another possibility is small metallic clusters of silver dispersed on the alumina have also been reported to lead to increases in the Ag 3d binding energy compared to bulk Ag.[168] The Auger parameter of 726.3 eV calculated using the most intense Ag 3d5/2 peak and the Ag $M_4N_{45}N_{45}$ transition is also consistent with the formation of metallic silver.

In Figure 8.2.8, the Ag spectra from the combusted sample differ significantly from both the $AgIO_3$ and Ag_2O starting materials. The Ag 3d 5/2 for the reacted sample has a FWHM of 0.79 eV and Plasmon loss peaks again both these features are consistent with metal formation. For the MNN Auger peaks shown in Figure 8.2.8 (d) both $M_4N_{45}N_{45}$ transition (~356 eV) and $M_5N_{45}N_{45}$ transition (~349 eV) seem to be split into two, Auger parameters were calculated using both peaks for the $M_4N_{45}N_{45}$ transition, labeled a and b in Figure 8.2.8 and energies reported in Table 8.2.4. The binding energy position for the 5/2 peak of 368.8 eV is surprisingly high for pure metallic silver or silver iodide as expected and seen in the x-ray diffraction. Based on the Auger parameter values and XRD results we believe this binding energy to be erroneously high due to differential charging between the hydrocarbon used as the calibration point and the silver. We assign the Auger parameter calculated using peak b (α'= 726.2 eV) to be due to metallic silver and peak a (α'=724.5 eV) to be due to silver iodide, their values compared to literature values in Table 8.2.4.

Table 8.2.4 Modified Auger parameters (α').

	Ag 3d Binding Energy (eV)	Ag $M_4N_5N_5$ Kinetic Energy (eV)	α' (eV)
Ag	368.1-368.3*	357.9-358.3	726.0-726.6
AgI	368.0*	356.1*	724.1*
Ag_2O	368.1* 368.0#	356.6*, 356.6#	724.4*, 724.3#
$AgIO_3$	367.9#	355.8	723.7
40% Ag_2O ($AgIO_3$)	368.8#	357.4#a, 355.7#b	726.2#a, 724.5#b
70% Ag_2O (CuO)	368.1#, 368.9#	358.2#	726.3#, 727.1#

*Taken From Moulder[167]
This work
[a] For AgI
[b] For Ag

While XPS does indicate elemental silver is present and surface exposed, it does not quantify the amount, nor does it discern microstructural behavior post reaction. Therefore, some

of the reacted product was collected and investigated with a TEM. The $Al/Ag_2O/AgIO_3$ is not included, since EDS could not easily distinguish between elemental Ag and AgI. Also, significant morphological changes were induced by the electron beam, thus making imaging and elemental analysis nearly impossible. Since AgI is considered a biocidal species itself, identifying its relative position to Ag is of less importance than looking at a non-biocidal species, such as Cu relative to Ag. Therefore, only results for $Al/Ag_2O/CuO$ are shown. The sample chosen to investigate was 64 Wt% Ag_2O, which corresponds to the maximum amount of Ag_2O which resulted in no loss to the reactivity (see Figure 8.2.4). A TEM image, along with corresponding elemental maps is shown in Figure 8.2.10.

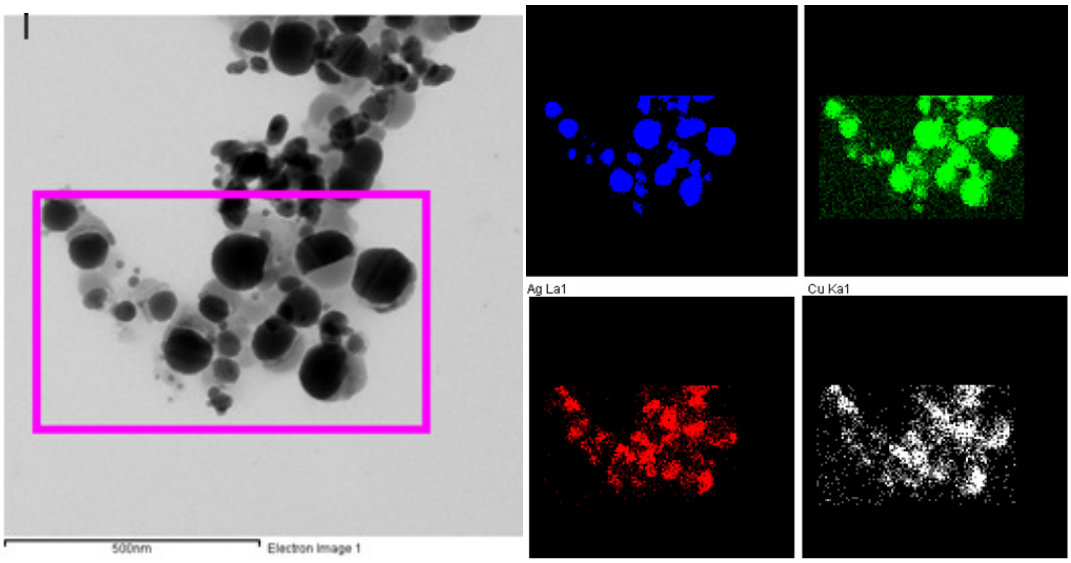

Figure 8.2.10 Elemental map of the reacted product of Al-CuO-Ag_2O at 64 Wt% Ag_2O. Note the Al_2O_3 is in surface contact with a product of what appears to be a mixture of both Ag and Cu. The results support a reactive sintering mechanism has occurred, however, this morphology will largely reduce the surface exposure of elemental silver.

What can clearly be seen is that the produced Ag/Cu is in surface contact with a product containing Al and O, most likely Al_2O_3 though this cannot be directly measured. The Ag and Cu positions are found to almost entirely overlap. It's not likely that alloying reactions between the

two have occurred, since no new XRD peaks were observed, so it is speculated that the morphology is a matrix of elemental silver and Cu which has intermixed. What can also be seen is that the large aggregated nanoparticles (<20 nm diameter, see Figure 8.2.4) have completely sintered in to characteristically larger and more uniform structures in surface contact. To further characterize the observed morphologies, an elemental linescan was performed and is shown in Figure 8.2.11.

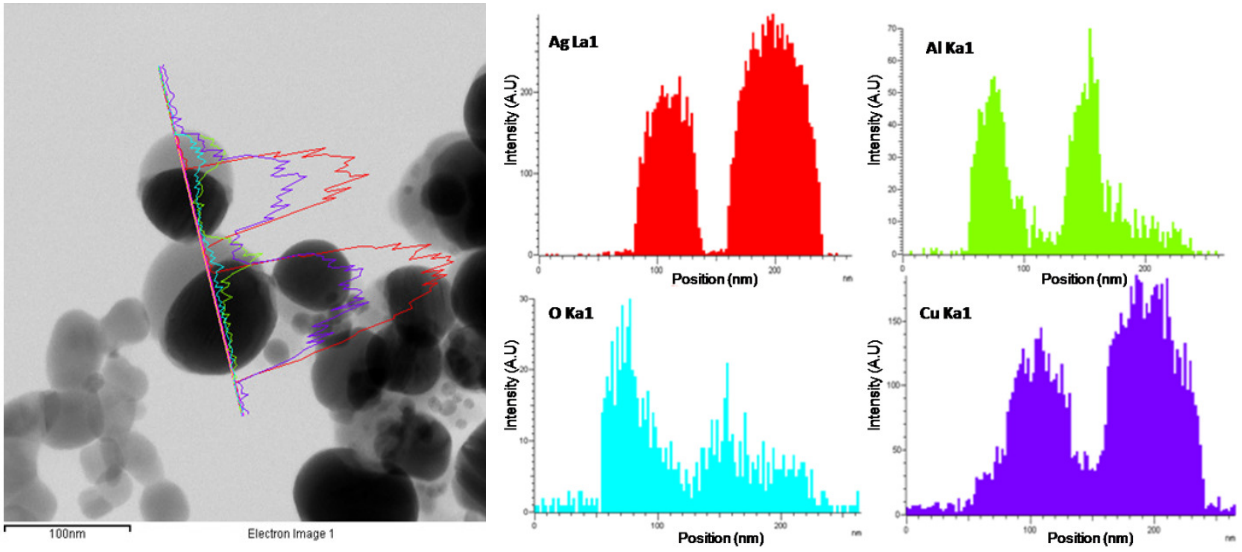

Figure 8.2.11: Image and elemental linescan across two particles showing the bright/dark morphology characteristic in the product. The sample was the same as Figure 8.2.10. The linescan indicates that an Ag/Cu matrix is in surface contact with Al and O (assumed to be Al_2O_3). It is speculated the morphology is the result of a reactive sintering mechanism.

The linescan shows that the lighter material corresponds to Al and O, whereas the dark material is a mix of both Ag and Cu. It is very clear that the fuel and oxidizer have come into surface contact during the reaction to produce the product. The results suggest that a reactive sintering mechanism had occurred. In a reactive sintering mechanism, the reaction occurs at the interface between fuel and oxidizer. As energy is liberated from the exothermic reaction, material is further melted and rapidly delivered to the interface where it continues to react. In

this case, the molten Ag and Cu produced during the reaction are perhaps miscible, and this could explain the coexistence.

Although the TEM results are interesting from a mechanistic point of view, the implications are quite negative for biocidal applications. If the fuel and oxidizer create a product which is in surface contact, then a large amount of the produced Ag will not be exposed to the environment post reaction. While CuO ternary systems can help to increase the reactivity of Ag_2O up to very high mass loadings of Ag_2O, the Ag/Cu matrix which forms also will greatly reduce the exposed surface area. If a reactive sintering mechanism (or simply thermal sintering) is indeed occurring, the elemental silver will not maintain the high surface to volume ratio characteristic of the initial Ag_2O, and will form much larger structures. While all of these points will lead to reduced overall surface area of the produced Ag, the real question for ternary systems will be whether the enhanced reactivity and high-yield of elemental Ag outweighs the negative effects, and only experimental testing can resolve whether the biodical performance is overall improved.

8.2.5 Main Conclusions of Work

Ultrafine Ag_2O powder was synthesized by a wet chemical technique and mixed with nano-Al to form energetic thermite systems designed to produce high yields of antimicrobial silver as a combustion product. The loose powders were combusted in a constant volume pressure cell, where both the transient pressure and optical emission are monitored to investigate performance. While Ag_2O itself performs poorly in terms of pressurization rate and burn time, the Ag_2O performed well when combined with two more reactive oxidizers, $AgIO_3$ and CuO. The pressurization rate dropped off fairly linearly as the mss loading of Ag_2O increased in the

$Al/AgIO_3/Ag_2O$ system, followed by a sharp drop off above 40 Wt%. The pressurization rate remained virtually unchanged as the Ag_2O loading was increased in an $Al/CuO/Ag_2O$ system, and had only dropped by about a factor of two when the loading was 77 Wt%. In other words, the yield of elemental silver produced during the reaction can be dramatically increased with little loss in combustion performance. The burn times remain relatively constant, indicating the burning to be rate limited by the aluminum. Ex-situ x-ray diffraction (XRD), x-ray photoelectron spectroscopy (XPS), and transmission electron microscopy (TEM) were performed to characterize select formulations. XRD confirms the production of crystalline silver, and XPS also detected elemental silver, indicating some amount of the silver was surface-exposed. TEM, however, showed large amounts of the silver product was in surface contact with Al_2O_3, and also was trapped within a matrix of Cu for the $Al/Ag_2O/CuO$ ternary system. It is speculated that a reactive sintering mechanism occurs, and large amounts of the product are sintered into characteristically larger particles. High-yields of elemental silver can thus be produced in highly reactive ternary formulations, however, the TEM results suggest several factors which could potentially decrease the biocidal efficacy, due to the formation of undesired morphologies which ultimately prevent the silver from being exposed to the environment.

Chapter 9: Summary of Results and Recommendations for Future Work

9.1 Main Contributions of this Work

This work has been an investigation of nanoscale thermites from both a mechanistic and a practical standpoint. We began by investigating nanoboron in nanocomposite thermite formulations. Boron is attractive mainly due to its high energy density on both a mass and volumetric basis. However, the kinetics of boron oxidation had always been found to be slow, and this has largely been attributed to the removal of its low-melting oxide shell. Nano-sized boron was mixed with CuO and tested in the pressure cell, and the results suggested that it was a very poor fuel in these systems. The boron was next mixed into a reactive thermite, Al/CuO, and the pressurization rate was measured as a function of boron loading. It was seen that the reactivity (pressurization rate) could be enhanced in an Al/CuO thermite when boron was added as the minor component (< 50 mol % of the fuel). It was also seen that no enhancement occurred when micron-sized boron was used. To explain the enhancement, it was speculated that the primary reaction (i.e. the Al/CuO) was facilitating the ignition of the boron. Adiabatic flame temperature calculations were performed, and it was seen that the primary reaction could raise the temperature above the boiling point of B_2O_3 and the melting point of B. Therefore, one or both of these criteria had to be met for boron to be ignited and enhance the reactivity. A heat transfer model was developed to investigate the heating time of boron in a gas. It was found that, for both nano and micron-sized boron, the B_2O_3 shell could rapidly be removed. The big difference, however, was in the time it took to melt the boron. The predicted melting time was compared to the experimental reaction time (the pressure rise time of 10 μs). It was found that nanoboron could be heated and melted faster than 10 μs at the temperatures of interest, whereas

micron-sized boron could not be. Thus, we concluded that rapid melting of the fuel was necessary for fast reaction of boron. Once ignited, the boron could participate in the reaction and form gaseous products (i.e. BO, BO_2, B_2O_3). This is experimentally seen as an increase in the pressurization rate when nanoboron was the minor component.

Next, the pressure cell was modified so that the optical and pressure signals could be measured simultaneously, and this was the focus of Chapter 6. From preliminary results, it immediately became obvious that different thermites yielded very different simultaneous pressure/optical behavior. For "slow" thermites such as Al/Fe_2O_3, the pressure and optical signal were shown to rise concurrently. There was nothing unordinary about this behavior: As the reaction produced gaseous products, the temperature in the system simultaneously rose, experimentally seen as a rising optical signal. However, for "fast" thermites such as Al/CuO and Al/SnO_2, it was seen that the pressure reaches its peak on a very fast timescale (~10 μs), and the optical emission follows with a longer timescale, peaking in around 100 μs and lasting approximately twice that amount of time. This behavior suggested that the pressure rise was attributed to some low-temperature, and non-equilibrium, process. Of the various possibilities to produce gas, the one that was most likely was that the oxidizer can decompose to a sub-oxide and release gas. For example, CuO can decompose to Cu_2O and O_2 at a low temperature relative to the adiabatic temperature. These ideas were investigated using equilibrium codes, and mass spectrometry measurements performed by our group have since corroborated these claims.

Our interpretation of "fast" thermites was that some "partial reaction" occurred and led to the rapid release of intermediate gas (O_2 for CuO, SnO + O_2 for SnO_2). The aluminum then continues to burn in the pressurized, oxygenated environment. To investigate these ideas using the pressure cell, a non-gas producer (WO_3) was added to perturb the gas release. The idea was

that if the pressurization rate could indeed be attributed to oxidizer decomposition, then the trend in pressurization rate should scale with the moles of decomposing oxidizer (the CuO or SnO_2). For both "fast" oxidizers, this was experimentally seen to occur. In the case of Fe_2O_3, which we argued could not decompose efficiently to release its O_2, a trend between pressurization rate and moles of Fe_2O_3 was not observed. The burning times (FWHM of optical signal) were also measured for the oxidizers as WO_3 was added. For the "slow" Al/WO_3/Fe_2O_3, there was a linear trend in the burn time as WO_3 was added, a result which suggested the burning was in some way rate-limited by the release of the O_2 from the oxidizer. For both "fast" thermites, the burn time was approximately 200 μs, and did not change until a large amount of WO_3 was added. The fact that the burn time was the same between the two thermites, and also as WO_3 was added, suggested that the burning was rate-limited by the only common component between the two systems, the aluminum. Shock tube measurements of aluminum burning in pressurized air performed by a separate group also reported burning times of ~200 μs.[72] Thus, we concluded that if O_2 can rapidly be released from the oxidizer, the bulk of aluminum burns as though it's in a pressurized, oxygenated environment. From a modeling standpoint, this finding is significant and may be used to make simplifying assumptions of the burning mechanism.

The idea that the pressurization arises from something other than equilibrium gas production is a very important result. Up until this point, researchers had been making measurements of the pressure/pressurization, and oftentimes used equilibrium calculations to explain the trends. For example, several researchers used equilibrium calculations to correlate pressure measurements in the Al/CuO system with the production of copper gas.[98, 100] This had never been verified, and our work served to provide an alternate explanation of the origins of gas release. The results of this work also strongly caution the use of using equilibrium gas and

temperature predictions to explain trends in the pressure/pressurization, since the origin of the gas release/pressurization is not from the generation of equilibrium gases, but instead comes from the generation of intermediate gases. This work was largely mechanistic in nature, but the results are useful from a practical standpoint also. One implication is that instead of selecting oxidizers based on their ability to produce equilibrium gas, we should search for oxidizers which can efficiently release oxygen and produce high amounts of equilibrium gas.

In Chapter 7, we looked at the mechanism of nanoaluminum and nanocomposite thermites using several high heating rate techniques, an area which is generally lacking in the literature. This research was made possible through the development of heating holders which could accomplish heating rates on the order of 10^6 K/s. Rapid heating microscopy results showed that a diffusion mechanism was occurring for nanoaluminum, and a "Melt Dispersion Mechanism" was not. Microscopy of the thermites showed evidence that the constituents had reacted at an interface, and in the condensed phase to produce highly sintered products of characteristically larger length scales. We argued that the fuel and oxidizer had thus reacted via a "Reactive Sintering Mechanism." This result showed that large amounts of sintering occurred during the burn, and raised important questions about whether the reaction precedes sintering, or vice versa. From a practical standpoint, if sintering occurs faster than the reaction proceeds, then the nano-architectures will be lost early in the burning. If this happens, then it really questions the potential of using nanoparticles at all below a certain size.

Thermites were also viewed reacting on the wire, and using a phase contrast imaging technique at the Advanced Photon Source of Argonne National Lab. It was seen in the movies of the thermites burning that larger, more spherical, particles formed very early during the burn, and well before the onset of optical emission. This result suggested that sintering does indeed

precede much of the burning. A heating model was used to investigate the characteristic sintering time, assumed to be the time it takes to heat, melt, and fuse two adjacent particles as a function of temperature and diameter. The model results suggested that once particles melt, the fusion into a single particle occurs very fast. The sintering time, therefore, is more closely related to the time it takes to heat and melt the particles. For CuO heated at 1700 K, the sintering time was seen to be approximately equal to the pressure rise time of 10 μs. Thus, we concluded that the fast pressure rise (i.e. the "partial reaction" mentioned above) was due to the reactive sintering component. It is suggested that constituents come into surface contact and react at the interface. The exothermic reaction serves to rapidly melt/sinter particles in the aggregated chains, and they continue to react at the interface, while simultaneously releasing gas. The aluminum can then continue to burn in a gaseous, pressurized environment. This mechanism explains how the apparent two-step combustion (fast pressure rise → slow optical emission) occurs for "fast" thermites such as Al/CuO and Al/SnO_2.

In Chapter 8, we investigated two oxidizers ($AgIO_3$ and Ag_2O) which have the ability to produce biocidal species at equilibrium. The goal was to have a reactive system which produces elemental silver, or forms of silver, so as to have an energetic event coupled with a long-lasting biocidal event. The $AgIO_3$ sample was first investigated, and several experimental techniques were used to fully characterize the reaction and analyze the products of combustion. Using mass spectrometry, the $AgIO_3$ was found to behave mechanistically differently during thermal decomposition at high heating rates vs slow, a result which should raise questions about using thermal analysis to predict decomposition pathways. $AgIO_3$ decomposed to O_2 and iodine, which were speculated to enhance the pressurization rate, experimentally observed in the pressure cell. The product was found through various techniques to be AgI, and not elemental

Ag and I_2. The biocidal efficacy of AgI was something which was not well understood at the time of the writing. The formation of AgI from $AgIO_3$ led us to investigate other Ag-based systems, in particular Ag_2O due to its ability to produce high-yields of elemental silver. The reactivity of Ag_2O was found to be poor on its own, however, ternary systems of Ag_2O with $AgIO_3$ or CuO were quite reactive, and it was found that large amounts of Ag_2O could be added before the pressurization rate significantly dropped off. We suggested that Ag_2O burns poorly because its adiabatic flame temperature was close to the melting point of Al_2O_3, perhaps hindering mass transport of Al through the shell. The reacted product of Al/Ag_2O/CuO was found to contain Ag, with some amount of it surface-exposed. However, the Ag and Cu product were seen in TEM to have formed into some matrix with each other, and this matrix was largely in surface contact with the Al_2O_3 product. The results suggested that a reactive sintering mechanism had occurred, and in this example would have a negative impact because it affects the surface exposure of Ag.

9.2 Recommendations for Future Work

Based on the results of this work, it is suggested that interfacial contact will be one of the most important considerations when designing improved inorganic energetic formulations. It has been seen that rods and wires burn well, along with sheet-like morphologies. Also, the mixing solvent and procedure affect the results, as does changing parameters such as equivalence ratio. All of these considerations may inherently change the relative fuel/oxidizer contact area. In a self-propagating thermite, it must be kept in mind that some gas will have to escape in order to convectively propagate the energy. Therefore, if the oxidizer is encapsulated it may hinder the convective propagation even if it releases gas. There are several other examples which could be

envisioned, and in the end the best system may maximize interfacial contact, but will allow convective gases to escape.

In Chapter 7 large amounts of a condensed-phase reactions and sintering were observed to occur. This is of particular importance if time and money is to be spent on the creation of novel architectures. If sintering occurs faster than the reaction, then the morphologies will be significantly impacted early, and thus will not maintain the architectures during combustion. A reactive sintering mechanism implies that a large amount of condensed phase reaction occurs, and thus on the oxidizer size we should search for oxidizers which conduct O_2 ions efficiently, such as Bi_2O_3. In fact, Bi_2O_3 is somewhat of an ideal oxidizer, since its fast ion conductivity leads to fast reaction in the condensed phase, whereas the gas produced is bismuth. This is an important consideration if the condensed phase reaction is actually faster than heterogeneous reactions, as is evidenced by these results. The goal, therefore, is to keep O_2 in the condensed phase to keep it in close proximity to the Al, but it must readily transport and give up during the reaction O_2, else the reaction rate will be hindered.

The work done by Prakash[169] is a very interesting concept that is worth continued investigation. In this work, a core-shell oxidizer of a highly reactive $KMnO_4$ core surrounded by a less reactive Fe_2O_3 shell was synthesized. This is currently being repeated using a CuO shell by Dr. Chunwei Wu, and these sorts of novel oxidizers could potentially rejuvenate the excitement of thermites. Through using coatings or other synthesis techniques, new types of safer and better-performing oxidizers can improve at least the PV component of the burning.

Another work which should be more carefully looked at is done by Apperson.[53] In this, the authors saw enhanced reactivity between nanoparticles, rods, and wires of the same material.

The improved reactivity of using rods and wires may likely be explained by improvements in the interfacial contact area and thus heterogeneous reactions in these systems. Different shapes of CuO can easily be synthesized using a 1 step mechanism,[170] and it would be interesting to characterize these various shapes of oxidizer in the combustion tests of the wire and pressure cell. Also, we were unable to produce different sizes of oxidizers using spray pyrolysis, but if this can be done then it is a strong piece of the puzzle. If the sintering timescale of metal oxides is very fast relative to the reaction timescale, then the size really should not matter, for the fuel will simply sinter into much larger particles early in the reaction. Perhaps using rods and wires can serve to minimize the sintering, another concept which would be interesting to investigate.

For biocidal applications, I_2O_5 should be further investigated as an oxidizer. It is water-soluble itself, though there is some suspicion that it forms HIO_3 upon addition to water. With our aerosol techniques, water-soluble oxidizers are easy to work with and we can play all sorts of tricks such as making the materials porous to see whether this has a positive effect on reactivity. I_2O_5 shares a similarity with Bi_2O_3, in that the vaporization of I_2 occurs at a low temperature. This should greatly enhance energy transport through the material.

On the fuel side, I worry about the potential of nanoaluminum, once thought to be great. We are seeing that there seems to be a minimum burning time reachable in the thermites, ~200 μs. Even with ~1000 K increase in the adiabatic flame temperature (i.e. Al/SnO_2 and $Al/AgIO_3$), the measured burning time is practically the same. This is an anomaly to combustion, where the reactivity should scale exponentially with temperature. Some of Bazyn's shock tube results[71] show that it's very hard to get a nanoparticle of aluminum to heat up and support a lifted off diffusion flame. This is very likely going to be true in thermites also, where a large amount of the enthalpy is used to sensibly heat the condensed phase species, or vaporize some of the metal.

If a lifted off diffusion flame cannot be achieved, then the reaction will occur via heterogeneous gas/liquid reactions, or condensed phase liquid/liquid reactions. Both of these processes are slower than homogeneous gas/gas reactions, and would cripple the energy release rate. Furthermore, as the reaction occurs, a larger and larger diffusion barrier would form between the fuel and oxidizer, so the reaction rate itself likely drops as the particle burns. Also, if the environment was hot enough to melt the Al_2O_3, sintering times become very fast for nanoparticles and thus I would expect these large aggregated structures to sinter into much larger particles well before the burning is complete. This idea would need much experimental support, but I cannot see how it would not happen once viscous diffusion can occur and the sintering timescale approaches the picosecond regime.

I would recommend looking at magnesium as a fuel, though the group has tried and been unsuccessful in synthesizing nano-sized Mg in the past. I think a good place to start would be investigating large Magnesium particles as an additive to a nano-Al thermite, even ~micron sized particles. We saw an enhancement in using 5-20 micron aluminum hydride, so I would not be surprised if the size didn't matter all that much. Magnesium has always been somewhat interesting to me, because it has a reasonable energy density, but more importantly boils at a low temperature. I think it could thus support a lifted off diffusion flame much easier than aluminum, and thus may be able to burn much faster for a comparably sized particle.

Appendix: Pressure Cell Operation

Part A: Sample Preparation

Step 1: Weigh out materials and add to a ceramic crucible

Step 2: Add ~10 mL of hexane (about ¾ full) and place crucible in sonicating bath. Ultrasonicate for 30 minutes, and swirl the crucibles every 5-10 minutes.

Tips:
-The white plastic piece can be used to hold up to 4 crucibles in place.
-The bath water level should come about half to three quarters up the crucible.
-If the bath water gets warm, replace with cold water.
-There are certain spots where the sonic waves are most intense. Try and keep the crucibles on those spots.

Step 3: Allow powder to dry overnight in fume hood. If you want to accelerate the drying process, after the powder has settled on the bottom of the crucible, dump the hexane into a beaker and allow it to evaporate in the hood. If you do this, the powders will be ready within an hour or two.

Step 4: After the powder is dry, very gently break it in the plastic handling box in the lab. Try and break up all large clumps so that the powder appears homogeneous, but be careful during this step.

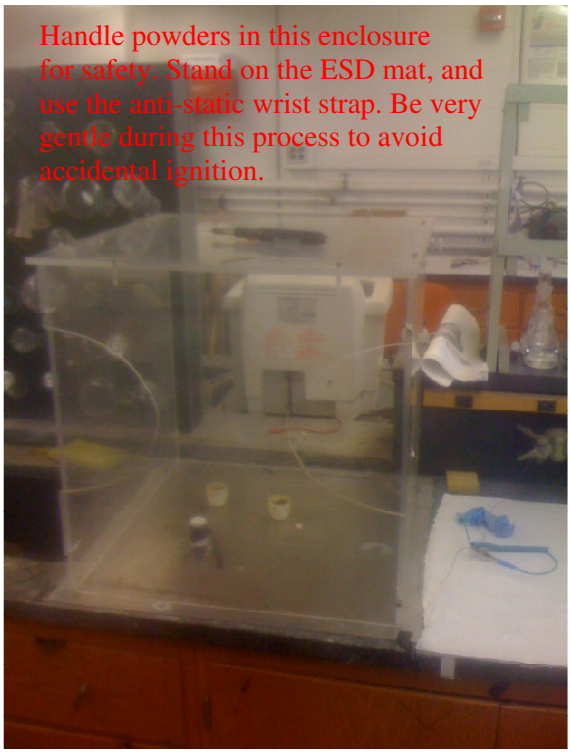
Handle powders in this enclosure for safety. Stand on the ESD mat, and use the anti-static wrist strap. Be very gentle during this process to avoid accidental ignition.

Part B: Operating the Pressure Cell

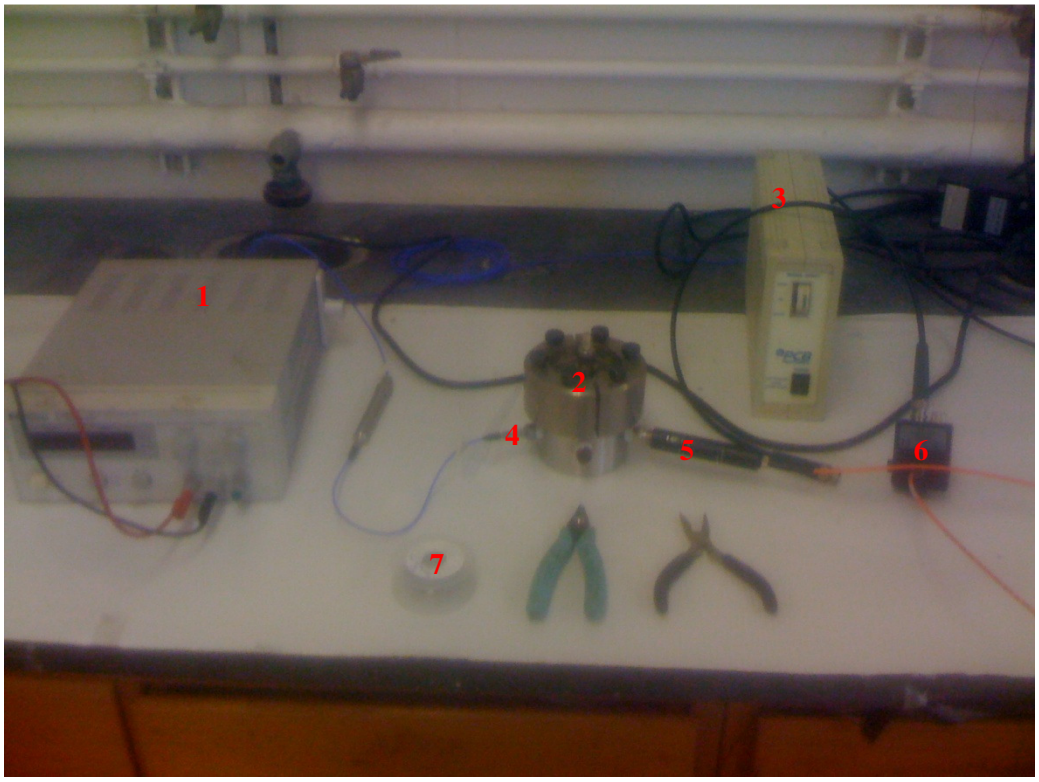

Components:

1) DC Power Supply- Hewlitt Packard, HPE3610A, 0-9 V, 0-3 A
2) Stainless Steel Pressure Cell, custom built, 13 cc free volume
3) Signal Conditioner- Piezotronics, 482A21, in series with pressure transducer
4) Piezoelectric Pressure Sensor, PCB 113A
5) Lens Tube Assembly- PCX lens (f = 5 cm) → Neutral Density Filter (OD 2) → PCX lens (f = 5 cm) → optical fiber, all components available from Thorlabs
6) Si-based photodetector, Thorlabs, model DET10A, connected to lens tube assembly by fiber-optic
7) Nichrome Wire, Ted Pella, Inc.

Pieces 3 and 6 are directly connected to channels 1 and 2 of an oscilloscope for data collection.

Step 1: Loading the sample

-Open pressure cell.
-Clean cell with Kimwipes and alcohol as needed.
-Weigh 25 mg (or desired amount) of sample, and add to sample holder.
-Drop sample holder base into the cell.
-Use curved tweezers to lower the sample holder into the cell.

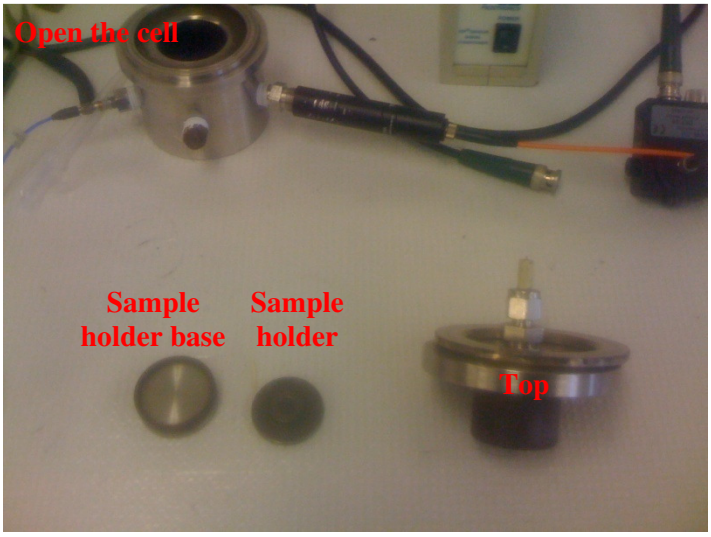

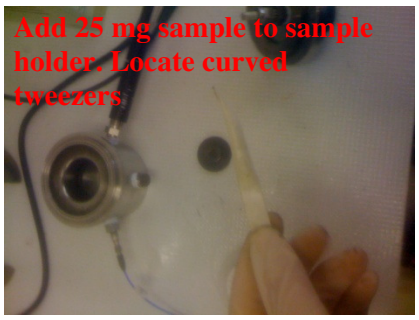

Step 2: We need to use the nichrome wire as an ignition source. The wire attaches to the underside of the piece labeled “top” above, and onto a copper wire stud which sticks out from the center.

-Cut off ~10 cm of NiCr (nichrome) wire.
-Make a small loop, and wrap the loop around the small copper piece several times.
-If needed, lightly pinch the wrapped piece with pliers to clamp the nichrome to the copper stud.
-Use a plastic pipette, and coil the remaining wire around it 3-4 times.
-Cut off the remaining wire so that the end is just past where the base ends. The point is for end of the nichrome wire to make contact with the inner wall of the pressure cell when sealed.

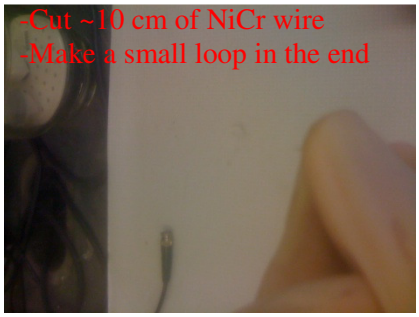

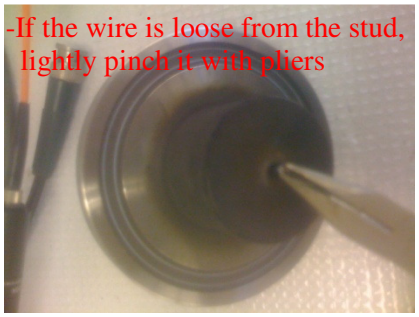

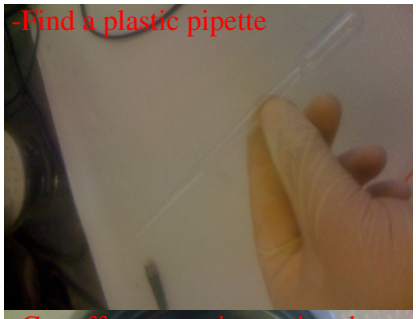

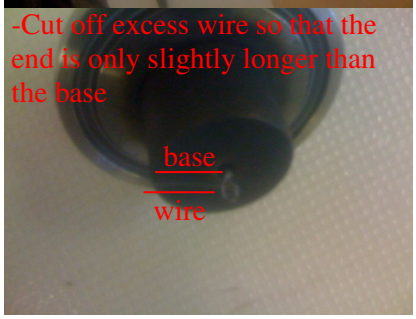

Step 3: Close the cell and test for continuity

-Place “ring” onto top piece if it was removed.
-Lower top piece onto cell.
-Seal the cell (Use an adjustable wrench to tighten 1/2 turn past finger tight).
-Attach one banana wire to the very top, other to the base.
-Test for continuity. If you increase the voltage dial and the green indicator lights up in the lower position, you have continuity. If not, open cell and try again.

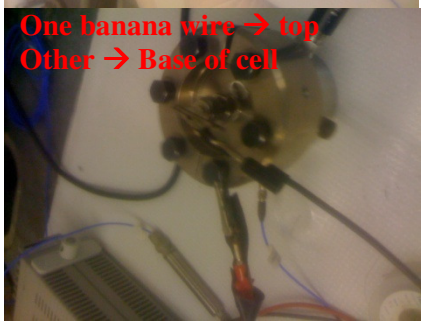

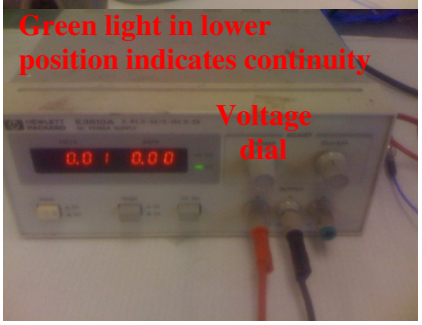

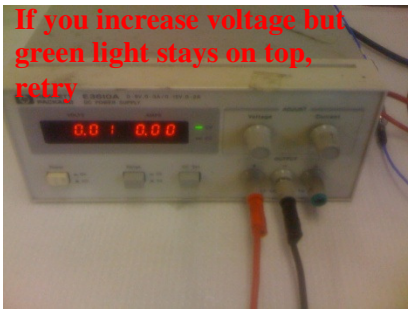

Step 4: Setting up the oscilloscope

The following assumes the pressure signal is connected to channel 1, and the optical signal connected to channel 2.

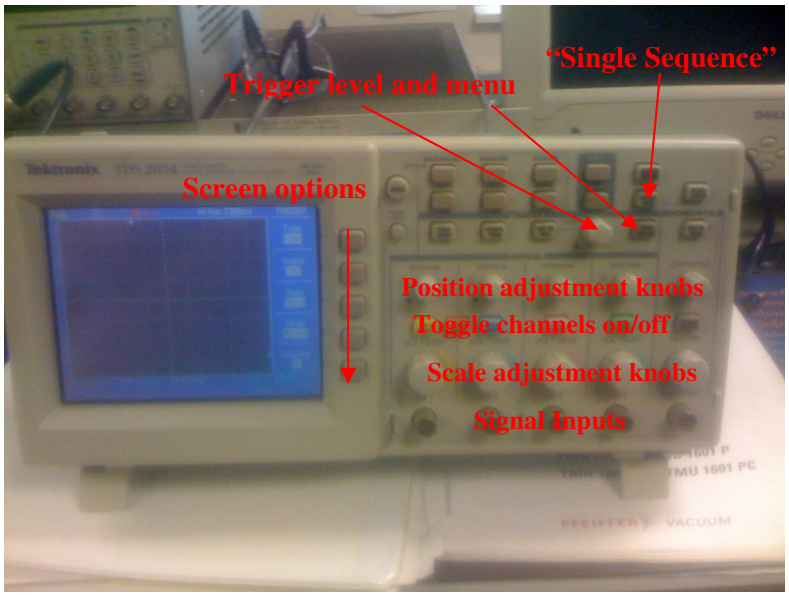

The position and scale settings vary from thermite to thermite. For a "fast" thermite (i.e. Al/CuO), a starting point is to use 100 mV per division for the pressure and optical signal, 100 µs /division for the time scale. Data collection triggers off a rising optical signal (Ch2), with the trigger level set slightly above the background. Adjust the scales as needed. The trigger settings, from top to bottom, should read: Type: edge, Source: Ch2, Slope: Rising, Mode: Normal, Coupling: DC.

Once this is all set, press the "Single Sequence" button and a green "Ready" will appear at the top of the screen.

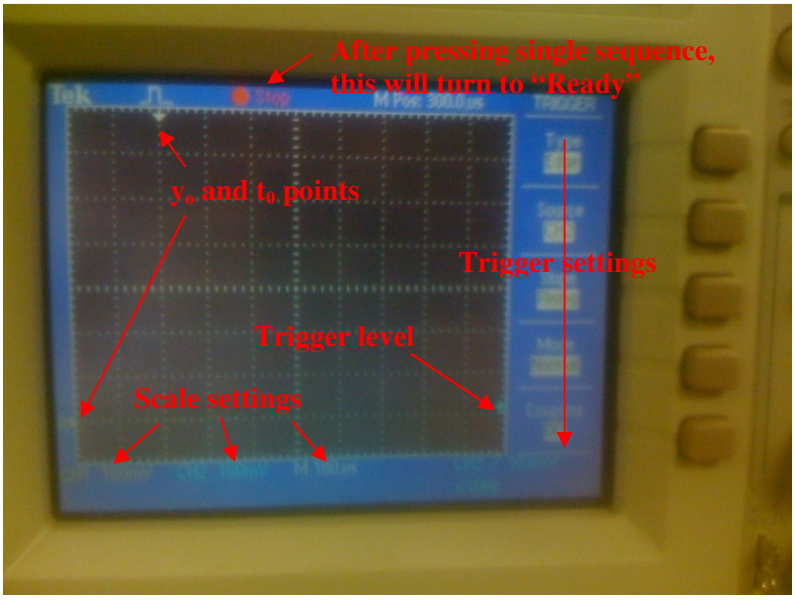

Part C: Collecting and Analyzing the Data

Step 1: Collecting the data

-To ignite the sample, spin both the voltage and current knobs on the power supply simultaneously and as quickly as possible. The signals should show up on the screen if there were no problems, and the green "Ready" will turn into a red "Stop." Note: If the trigger level is too low, this can accidentally trigger.

Now open "Instrument Manager" (Start→Programs→Wavestar for Oscilloscopes→Instrument Manager).

-Note: You may have to set the date back on the computer if the software has expired.
-Check to see if the software is communicating with the oscilloscope. If it is not, the words "not responding" will appear.
-Click and then select stop, then start. You may need to reset the oscilloscope scope and check connections.
-Repeat until the unit shows as "responding."
-You may then close the instrument manager.

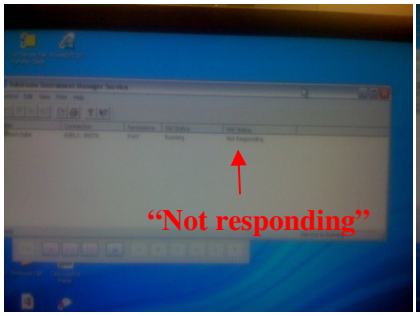

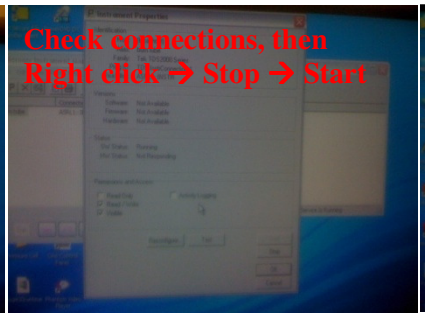

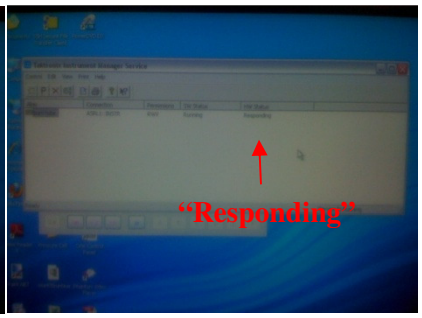

-Open the Wavestar Program (Start→Programs→Wavestar for Oscilloscopes→Wavestar for Oscilloscopes).
-For each sample, save two waveform tabulars and one YT sheet (File → New → Waveform tabular)
-From the dropdown list on the left, copy the Ch1 data (Pressure) to waveform tabular 1 (Hold right click, drag and drop).
-Copy Ch2 data (Optical signal) to waveform tabular 2.
-Copy both Ch1 and Ch2 to the YT sheet.
-Save the entire workbook ("Save Workbook As").

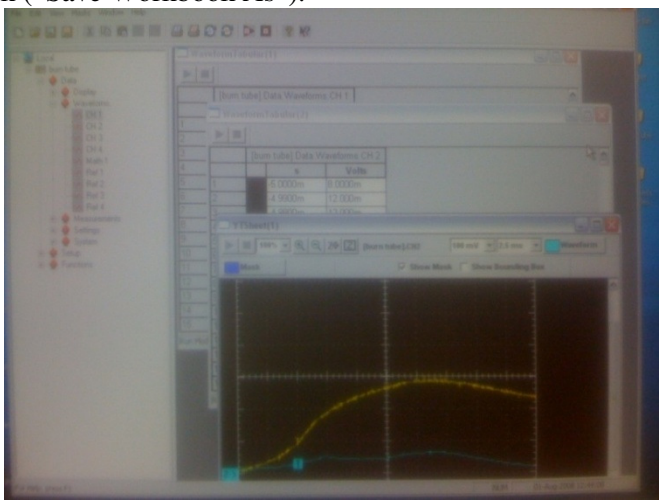

Step 2: Processing the data

The following is simply my suggestion, and a user may want to do things differently. However, make sure whatever you do is repeatable and consistent.

-Copy and paste the two waveform tabulars into Excel.
-Convert voltage to psi (1 mV =0.237 psi).
-Smooth the data by averaging 5 adjacent points.
-Use a peak find function to calculate Vmax and Pmax.
-Calculate 5% of Vmax and Pmax, calculate 50% of Vmax.
-Use the cursor to find the times corresponding to:
→ 5% Pmax, 5% Vmax
→ 50% Vmax (2 points)
→ Pmax and Vmax
-The pressurization rate is then Pmax / time difference between 5% Pmax and Pmax.
-The "burn time" is then the time between the two values of 50% Vmax (Full Width Half Max).
-Shift the data so that the onset of voltage and pressure overlap, (Delta V, Delta P, t0, and Delta T do this in my example below).
-Plot the smoothed and shifted simultaneous pressure/optical signals.

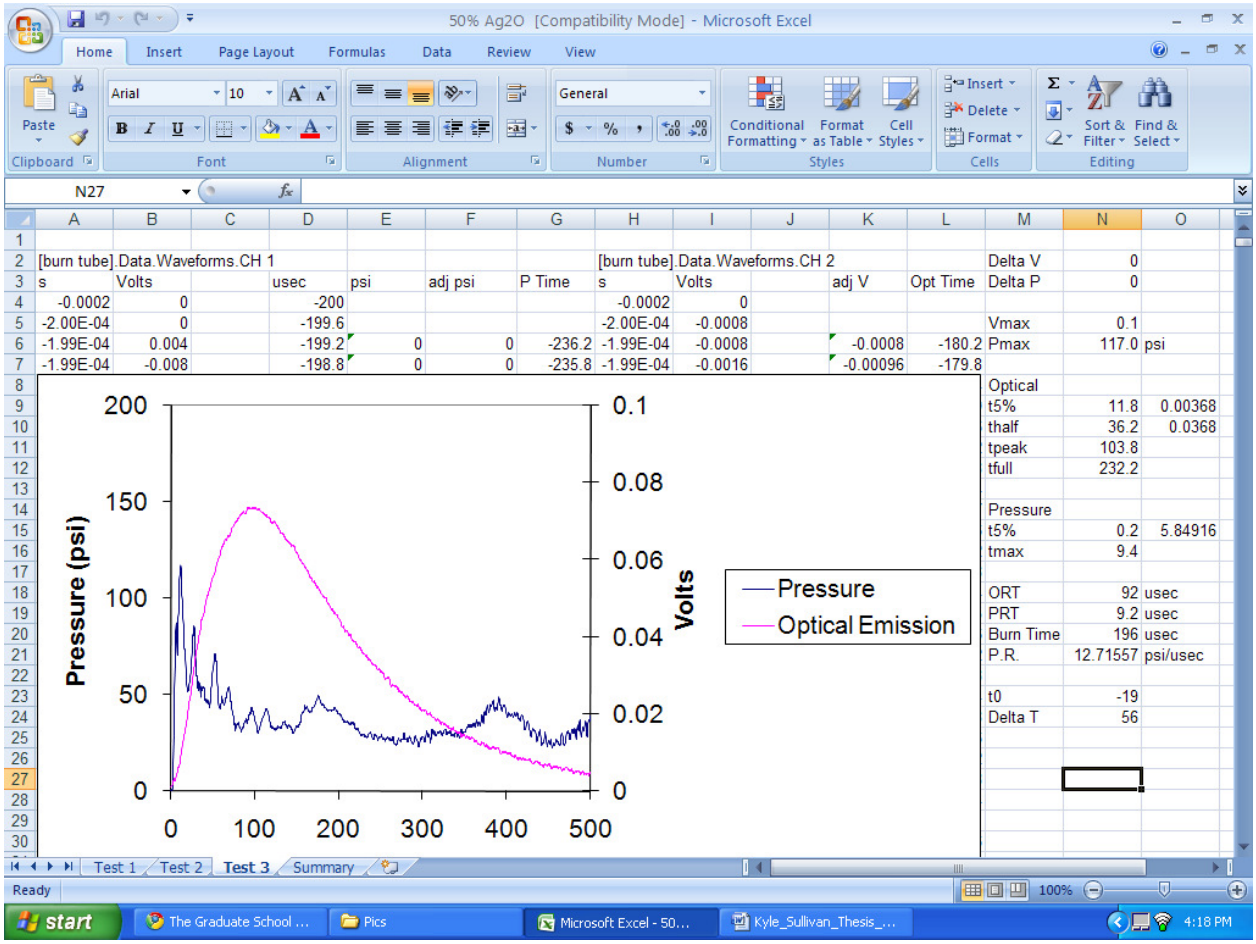

	A	B	C	D	E	F	G	H	I	J	K	L	M	N	O
1															
2	[burn tube].Data.Waveforms.CH 1							[burn tube].Data.Waveforms.CH 2					Delta V	0	
3	s	Volts		usec	psi	adj psi	P Time	s	Volts		adj V	Opt Time	Delta P	0	
4	-0.0002	0		-200				-0.0002	0						
5	-2.00E-04	0		-199.6				-2.00E-04	-0.0008				Vmax	0.1	
6	-1.99E-04	0.004		-199.2	0	0	-236.2	-1.99E-04	-0.0008		-0.0008	-180.2	Pmax	117.0	psi
7	-1.99E-04	-0.008		-198.8	0	0	-235.8	-1.99E-04	-0.0016		-0.00096	-179.8			
8													Optical		
9													t5%	11.8	0.00368
10													thalf	36.2	0.0368
11													tpeak	103.8	
12													tfull	232.2	
13															
14													Pressure		
15													t5%	0.2	5.84916
16													tmax	9.4	
17															
18													ORT	92	usec
19													PRT	9.2	usec
20													Burn Time	196	usec
21													P.R.	12.71557	psi/usec
22															
23													t0	-19	
24													Delta T	56	
25															
26															
27															
28															
29															
30															

List Of References

1. C. E. Aumann; G. L. Skofronick; J. A. Martin, *Journal of Vacuum Science & Technology, B: Microelectronics and Nanometer Structures* **1995,** 13, (3), 1178-83.
2. D. E. Wilson; K. K. Kim in: *Combustion of Consolidated and Confined Metastable Intermolecular Composites*, 43rd AIAA Sciences Metting and Exhibit, Reno, NV, January 10-13, 2005; Reno, NV, 2005.
3. Fischer; Grubelich in: *32nd AIAA/ASME/SAE/ASEE Joint Propulsion Conference* Lake Buena Vista, FL, 1996; Lake Buena Vista, FL, 1996.
4. P. Buffat; J. P. Borel, *Physical Review A* **1976,** 13, (6), 2287-2298.
5. S. K. Friedlander, *Smoke, Dust, and Haze Fundamentals of Aerosol Dynamics*. 2nd ed.; Oxford University Press, Inc.: New York, 2000.
6. A. V. Filippov; D. E. Rosner, *International Journal of Heat and Mass Transfer* **1999,** 43, (1), 127-138.
7. S. Mohan; M. A. Trunov; E. L. Dreizin, *Journal of Propulsion and Power* **2008,** 24, (2), 199-205.
8. T. Bazyn; H. Krier; N. Glumac, *Proceedings of the Combustion Institute* **2007,** 31, 2021-2028.
9. D. Mukherjee; C. G. Sonwane; M. R. Zachariah, *Journal of Chemical Physics* **2003,** 119, (6), 3391-3404.
10. K. S. Martirosyan; L. Z. Wang; A. Vicent; D. Luss, *Propellants Explosives Pyrotechnics* **2009,** 34, (6), 532-538.
11. L. P. H. Jeurgens; W. G. Sloof; F. D. Tichelaar; E. J. Mittemeijer, *Physical Review B: Condensed Matter and Materials Physics* **2000,** 62, (7), 4707-4719.
12. L. P. H. Jeurgens; W. G. Sloof; F. D. Tichelaar; E. J. Mittemeijer, *Thin Solid Films* **2002,** 418, (2), 89-101.
13. L. P. H. Jeurgens; W. G. Sloof; F. D. Tichelaar; E. J. Mittemeijer, *Journal of Applied Physics* **2002,** 92, (3), 1649-1656.
14. J. C. Sanchez-Lopez; A. R. Gonzalez-Elipe; A. Fernandez, *Journal of Materials Research* **1998,** 13, (3), 703-710.
15. M. A. Trunov; M. Schoenitz; X. Zhu; E. L. Dreizin, *Combustion and Flame* **2005,** 140, (4), 310-318.
16. J. J. Granier; M. L. Pantoya, *Combustion and Flame* **2004,** 138, (4), 373-383.
17. T. J. Foley; C. E. Johnson; K. T. Higa, *Chemistry of Materials* **2005,** 17, (16), 4086-4091.
18. Y. Gao Method for preparing nanoscale nickel-coated aluminum powder. 1009-8870 101041180, 20070428., 2007.
19. K. Park; A. Rai; M. R. Zachariah, *Journal of Nanoparticle Research* **2006,** 8, (3-4), 455-464.
20. R. J. Jouet; J. R. Carney; R. H. Granholm; H. W. Sandusky; A. D. Warren, *Materials Science and Technology* **2006,** 22, (4), 422-429.
21. R. J. Jouet; A. D. Warren; D. M. Rosenberg; V. J. Bellitto; K. Park; M. R. Zachariah, *Chemistry of Materials* **2005,** 17, (11), 2987-2996.
22. S. R. Turns, *An Introduction to Combustion*. Second ed.; McGraw-Hill Book Co.: Singapore, 2000.
23. M. W. Beckstead; B. R. Newbold; C. Waroquet, *CPIA Publication* **2000,** 701, (JANNAF 37th Combustion Subcommittee Meeting, 2000, Vol. 1), 485-504.
24. C. K. Law, *Combustion Science and Technology* **1973,** 7, (5), 197-212.
25. I. Glassman, *Combustion*. 3rd ed.; Academic Press: San Diego, CA, 1996.
26. T. Bazyn; H. Krier; N. Glumac, *Proceedings of the Combustion Institute* **2007,** 31, (Pt. 2), 2021-2028.
27. Y. F. Ivanov; M. N. Osmonoliev; V. S. Sedoi; V. A. Arkhipov; S. S. Bondarchuk; A. B. Vorozhtsov; A. G. Korotkikh; V. T. Kuznetsov, *Propellants, Explosives, Pyrotechnics* **2003,** 28, (6), 319-333.

28. W. Jiang; K. Yatsui, *IEEE Transactions on Plasma Science* **1998,** 26, (5), 1498-1501.
29. Y. S. Kwon; Y. H. Jung; N. A. Yavorovsky; A. P. Illyn; J. S. Kim, *Scripta Materialia* **2001,** 44, (8/9), 2247-2251.
30. R. Sarathi; T. K. Sindhu; S. R. Chakravarthy, *Materials Characterization* **2007,** 58, (2), 148-155.
31. F. Tepper, *International Journal of Powder Metallurgy (Princeton, New Jersey)* **1999,** 35, (7), 39-44.
32. F. Tepper, *Powder Metallurgy* **2000,** 43, (4), 320-322.
33. V. Y. Zelinskii; N. A. Yavorovskii; L. T. Proskurovskaya; V. I. Davydovich, *Fizika i Khimiya Obrabotki Materialov* **1984**, (1), 57-9.
34. R. L. Axelbaum, *Powder Metallurgy* **2000,** 43, (4), 323-325.
35. H. F. Calcote; W. Felder, *Symposium (International) on Combustion, [Proceedings]* **1992,** 24th, 1869-76.
36. C. E. Johnson; K. T. Higa, *Materials Research Society Symposium Proceedings* **1997,** 457, (Nanophase and Nanocomposite Materials II), 131-135.
37. D. E. Rosner, *Industrial & Engineering Chemistry Research* **2005,** 44, (16), 6045-6055.
38. K. L. Steffens; M. R. Zachariah; D. P. DuFaux; R. L. Axelbaum, *Chemistry of Materials* **1996,** 8, (8), 1871-1880.
39. M. S. Wooldridge, *Progress in Energy and Combustion Science* **1998,** 24, (1), 63-87.
40. Y. Champion, *Annales de Chimie (Cachan, France)* **2006,** 31, (3), 281-294.
41. C. G. Granqvist; R. A. Buhrman, *Journal of Applied Physics* **1976,** 47, (5), 2200-19.
42. A. W. Miziolek, *AMPTIAC Newsletter* **2002,** 6, (1), 43-48.
43. R. J. Munz; T. Addona; A. C. Da Cruz, *Pure and Applied Chemistry* **1999,** 71, (10), 1889-1897.
44. K. Park; D. Lee; A. Rai; D. Mukherjee; M. R. Zachariah, *Journal of Physical Chemistry B* **2005,** 109, (15), 7290-7299.
45. J. Phillips; W. L. Perry; W. J. Kroenke Manufacture of spherical metal nanoparticles by plasma heating of precursor aerosol for vapor condensation. 2001-17289
6689192, 20011213., 2004.
46. A. Pivkina; D. Ivanov; Y. Frolov; S. Mudretsova; A. Nickolskaya; J. Schoonman, *Journal of Thermal Analysis and Calorimetry* **2006,** 86, (3), 733-738.
47. J. A. Puszynski, *Proceedings of the International Pyrotechnics Seminar* **2002,** 29th, 191-202.
48. A. Rai; K. Park; L. Zhou; M. R. Zachariah, *Combustion Theory and Modelling* **2006,** 10, (5), 843-859.
49. R. Schefflan; S. Kovenklioglu; D. Kalyon; M. Mezger; M. Leng, *Journal of Energetic Materials* **2006,** 24, (2), 141-156.
50. K. Moore; M. L. Pantoya; S. F. Son, *Journal of Propulsion and Power* **2007,** 23, (1), 181-185.
51. D. Prentice; M. L. Pantoya; B. J. Clapsaddle, *Journal of Physical Chemistry B* **2005,** 109, (43), 20180-20185.
52. J. A. Puszynski; C. J. Bulian; J. J. Swiatkiewicz, *Materials Research Society Symposium Proceedings* **2006,** 896, (Multifunctional Energetic Materials), 147-158.
53. S. Apperson; R. V. Shende; S. Subramanian; D. Tappmeyer; S. Gangopadhyay; Z. Chen; K. Gangopadhyay; P. Redner; S. Nicholich; D. Kapoor, *Applied Physics Letters* **2007,** 91, (24), 243109/1-243109/3.
54. R. Shende; S. Subramanian; S. Hasan; S. Apperson; R. Thiruvengadathan; K. Gangopadhyay; S. Gangopadhyay; P. Redner; D. Kapoor; S. Nicolich; W. Balas, *Propellants, Explosives, Pyrotechnics* **2008,** 33, (2), 122-130.
55. H. Borchert; E. V. Shevchenko; A. Robert; I. Mekis; A. Kornowski; G. Gruebel; H. Weller, *Langmuir* **2005,** 21, (5), 1931-1936.
56. J. T. Mang; R. P. Hjelm; S. F. Son; P. D. Peterson; B. S. Jorgensen, *Journal of Materials Research* **2007,** 22, (7), 1907-1920.
57. M. A. Trunov; S. M. Umbrajkar; M. Schoenitz; J. T. Mang; E. L. Dreizin, *Journal of Physical Chemistry B* **2006,** 110, (26), 13094-13099.

58. C. E. Johnson; S. Fallis; A. P. Chafin; T. J. Groshens; K. T. Higa; I. M. K. Ismail; T. W. Hawkins, *Journal of Propulsion and Power* **2007,** 23, (4), 669-682.
59. Y. V. Kazakov; A. E. Medvedev; A. V. Fedorov; V. M. Fomin, *Archivum Combustionis* **1987,** 7, (1-2), 7-17.
60. V. I. Rozenband; N. I. Vaganova, *Combustion and Flame* **1992,** 88, (1), 113-18.
61. M. A. Trunov; M. Schoenitz; E. L. Dreizin, *Combustion Theory and Modelling* **2006,** 10, (4), 603-623.
62. M. A. Trunov; M. Schoenitz; E. L. Dreizin, *Propellants, Explosives, Pyrotechnics* **2005,** 30, (1), 36-43.
63. T. Bazyn; N. Glumac; H. Krier; T. S. Ward; M. Schoenitz; E. L. Dreizin, *Combustion Science and Technology* **2007,** 179, (3), 457-476.
64. D. E. G. Jones; P. Brousseau; R. C. Fouchard; A. M. Turcotte; Q. S. M. Kwok, *Journal of Thermal Analysis and Calorimetry* **2000,** 61, (3), 805-818.
65. M. M. Mench; K. K. Kuo; C. L. Yeh; Y. C. Lu, *Combustion Science and Technology* **1998,** 135, (1-6), 269-292.
66. B. Rufino; F. Boulc'h; M. V. Coulet; G. Lacroix; R. Denoyel, *Acta Materialia* **2007,** 55, (8), 2815-2827.
67. I. Levin; D. Brandon, *Journal of the American Ceramic Society* **1998,** 81, (8), 1995-2012.
68. R. K. Dwivedi; G. Gowda, *Journal of Materials Science Letters* **1985,** 4, (3), 331-4.
69. A. Rai; D. Lee; K. Park; M. R. Zachariah, *Journal of Physical Chemistry B* **2004,** 108, (39), 14793-14795.
70. R. Mahadevan; D. Lee; H. Sakurai; M. R. Zachariah, *Journal of Physical Chemistry A* **2002,** 106, (46), 11083-11092.
71. T. Bazyn; H. Krier; N. Glumac in: *Shock Tube Measurements of Combustion of Nano-Aluminum*, 44th AIAA Aerospace Sciences Meeting and Exhibit, Reno, Nevada, 2006; Reno, Nevada, 2006; pp 1-8.
72. T. Bazyn; H. Krier; N. Glumac, *Combustion and Flame* **2006,** 145, (4), 703-713.
73. S. M. Umbrajkar; M. Schoenitz; E. L. Dreizin, *Thermochimica Acta* **2006,** 451, (1-2), 34-43.
74. M. Schoenitz; S. Umbrajkar; E. L. Dreizin, *Journal of Propulsion and Power* **2007,** 23, (4), 683-687.
75. S. R. Ahmad; D. A. Russell; C. J. Leach, *Propellants, Explosives, Pyrotechnics* **2001,** 26, (5), 235-245.
76. A. N. Ali; S. F. Son; B. W. Asay; M. E. Decroix; M. Q. Brewster, *Combustion Science and Technology* **2003,** 175, (8), 1551-1571.
77. P. Dimitriou; V. Hlavacek; S. M. Valone; R. G. Behrens; G. P. Hansen; J. L. Margrave, *AIChE Journal* **1989,** 35, (7), 1085-96.
78. B. L. Fetherolf; P. M. Liiva; W. H. Hsieh; K. K. Kuo, *Proceedings of the International Pyrotechnics Seminar* **1991,** 16th, 675-90.
79. K. K. Kuo; J. U. Kim; B. L. Fetherolf; T. Torikai, *Combustion and Flame* **1993,** 95, (4), 351-61.
80. N. S. Zakharov; S. A. Kazarin, *Izvestiya Akademii Nauk SSSR, Seriya Fizicheskaya* **1991,** 55, (6), 1198-201.
81. M. L. Mileham; M. P. Kramer; A. E. Stiegman, *Journal of Physical Chemistry C* **2007,** 111, (45), 16883-16888.
82. S. Wang; Y. Yang; H. Yu; D. D. Dlott, *Propellants, Explosives, Pyrotechnics* **2005,** 30, (2), 148-155.
83. Y. Yang; Z. Sun; S. Wang; D. D. Dlott, *Journal of Physical Chemistry B* **2003,** 107, (19), 4485-4493.
84. M. A. Zamkov; R. W. Conner; D. D. Dlott, *Journal of Physical Chemistry C* **2007,** 111, (28), 10278-10284.
85. Y. L. Shoshin; M. A. Trunov; X. Zhu; M. Schoenitz; E. L. Dreizin, *Combustion and Flame* **2006,** 144, (4), 688-697.

86. S. Umbrajkar; M. A. Trunov; M. Schoenitz; E. L. Dreizin; R. Broad, *Propellants, Explosives, Pyrotechnics* **2007,** 32, (1), 32-41.
87. S. M. Umbrajkar; M. Schoenitz; E. L. Dreizin, *Propellants, Explosives, Pyrotechnics* **2006,** 31, (5), 382-389.
88. T. S. Ward; M. A. Trunov; M. Schoenitz; E. L. Dreizin, *International Journal of Heat and Mass Transfer* **2006,** 49, (25-26), 4943-4954.
89. S. F. Son; J. R. Busse; B. W. Asay; P. D. Peterson; J. T. Mang; B. Bockmon; M. L. Pantoya, *Proceedings of the International Pyrotechnics Seminar* **2002,** 29th, 203-212.
90. D. G. Tasker; B. W. Asay; J. C. King; V. E. Sanders; S. F. Son, *Journal of Applied Physics* **2006,** 99, (2), 023705/1-023705/7.
91. B. J. Clapsaddle; L. Zhao; A. E. Gash; J. H. Satcher, Jr.; K. J. Shea; M. L. Pantoya; R. L. Simpson, *Materials Research Society Symposium Proceedings* **2003,** 800, (Synthesis, Characterization and Properties of Energetic/Reactive Nanomaterials), 91-96.
92. Y.-S. Kwon; A. A. Gromov; A. P. Ilyin; E. M. Popenko; G.-H. Rim, *Combustion and Flame* **2003,** 133, (4), 385-391.
93. D. S. Moore; S. F. Son; B. W. Asay, *Propellants, Explosives, Pyrotechnics* **2004,** 29, (2), 106-111.
94. W. L. Perry; B. L. Smith; C. J. Bulian; J. R. Busse; C. S. Macomber; R. C. Dye; S. F. Son, *Propellants, Explosives, Pyrotechnics* **2004,** 29, (2), 99-105.
95. K. B. Plantier; M. L. Pantoya; A. E. Gash, *Combustion and Flame* **2005,** 140, (4), 299-309.
96. M. Schoenitz; T. S. Ward; E. L. Dreizin, *Proceedings of the Combustion Institute* **2005,** 30, (Pt. 2), 2071-2078.
97. S. F. Son; B. W. Asay; T. J. Foley; R. A. Yetter; M. H. Wu; G. A. Risha, *Journal of Propulsion and Power* **2007,** 23, (4), 715-721.
98. V. E. Sanders; B. W. Asay; T. J. Foley; B. C. Tappan; A. N. Pacheco; S. F. Son, *Journal of Propulsion and Power* **2007,** 23, (4), 707-714.
99. B. S. Bockmon; M. L. Pantoya; S. F. Son; B. W. Asay; J. T. Mang, *Journal of Applied Physics* **2005,** 98, (6), 064903/1-064903/7.
100. J. Y. Malchi; T. J. Foley; S. F. Son; R. A. Yetter, *Combustion, Science, and Technology* **2008,** 180, 1278-1294.
101. A. Prakash; A. V. McCormick; M. R. Zachariah, *Advanced Materials (Weinheim, Germany)* **2005,** 17, (7), 900-903.
102. J. A. Puszynski; C. J. Bulian; J. J. Swiatkiewicz, *Journal of Propulsion and Power* **2007,** 23, (4), 698-706.
103. W. L. Perry; B. C. Tappan; B. L. Reardon; V. E. Sanders; S. F. Son, *Journal of Applied Physics* **2007,** 101, (6), 064313/1-064313/5.
104. B. W. Asay; S. F. Son; J. R. Busse; D. M. Oschwald, *AIP Conference Proceedings* **2004,** 706, (Pt. 2, Shock Compression of Condensed Matter--2003, Part 2), 827-830.
105. S. F. Son; M. Q. Brewster, *Combustion Science and Technology* **1995,** 107, (1-3), 127-154.
106. A. P. Ershov, *Fizika Goreniya i Vzryva* **1997,** 33, (1), 98-106.
107. A. P. Ershov; A. L. Kupershtokh; D. A. Medvedev, *Fizika Goreniya i Vzryva* **2001,** 37, (2), 94-102.
108. K. C. Walter; D. R. Pesiri; D. E. Wilson, *Journal of Propulsion and Power* **2007,** 23, (4), 645-650.
109. V. I. Levitas, *Combustion and Flame* **2009,** 156, (2), 543-546.
110. V. I. Levitas; B. W. Asay; S. F. Son; M. Pantoya, *Journal of Applied Physics* **2007,** 101, (8).
111. V. I. Levitas; M. L. Pantoya; B. Dikici, *Applied Physics Letters* **2008,** 92, (1), 011921/1-011921/3.
112. B. J. Henz; T. Hawa; M. R. Zachariah, *Journal of Applied Physics* 107, (2).
113. S. Chowdhury; K. Sullivan; N. Piekiel; L. Zhou; M. R. Zachariah, *Journal of Physical Chemistry C Letters*.

114. A. Macek; J. M. Semple, *Combustion Science and Technology* **1969,** 1, (3), 181-91.
115. A. Ulas; K. K. Kuo; C. Gotzmer, *Combustion and Flame* **2001,** 127, (1/2), 1935-1957.
116. C. E. Johnson; K. T. Higa; W. R. Albro in: *Nanothermites with Condensable Gas Products*, Proceedings of the International Pyrotechnics Seminar, 2008; 2008; pp 159-168.
117. E. J. Rentz, *Journal of Nutritional & Environmental Medicine (Abingdon)* **2003,** 13, (2), 109-118.
118. J. R. Morones; J. L. Elechiguerra; A. Camacho; K. Holt; J. B. Kouri; J. T. Ramirez; M. J. Yacaman, *Nanotechnology* **2005,** 16, (10), 2346-2353.
119. A. B. Smetana; K. J. Klabunde; G. R. Marchin; C. M. Sorensen, *Langmuir* **2008,** 24, (14), 7457-7464.
120. V. Sambhy; M. M. MacBride; B. R. Peterson; A. Sen, *Journal of the American Chemical Society* **2006,** 128, 9798-9808.
121. Merck, *The Merck Index*. 13 ed.; Merck & Co., Inc.: Whitehouse Station, NJ, 2001.
122. P. M. G. Klien; J. Woodhouse Methods and Processes for Iodine Disinfection 7,033,509, April 25, 2006.
123. T. Hawa; M. R. Zachariah, *Physical Review B* **2007,** 76, (5).
124. K. E. J. Lehtinen; M. R. Zachariah, *Journal of Aerosol Science* **2002,** 33, (2), 357-368.
125. B. J. Henz; T. Hawa; M. Zachariah, *Journal of Applied Physics* **2009,** 105, (12).
126. K. J. Blobaum; D. Van Heerden; A. J. Gavens; T. P. Weihs, *Acta Materialia* **2003,** 51, (13), 3871-3884.
127. P. Tandon; D. E. Rosner, *Journal of Colloid and Interface Science* **1999,** 213, (2), 273-286.
128. T. Iida; H. Sakai; Y. Kita; K. Murakami, *High Temperature Materials and Processes* **2000,** 19, (3-4), 153-164.
129. Y. J. Wang; X. Liu; K. S. Im; W. K. Lee; J. Wang; K. Fezzaa; D. L. S. Hung; J. R. Winkelman, *Nature Physics* **2008,** 4, (4), 305-309.
130. T. A. Brzustowski; I. Glassman, **1964**, (IAA Accession No. A65-10970), 33 pp.
131. E. W. Price, *Combustion of Metallized Propellants*. Progress in Astronautics and Aeronautics: 1983; Vol. AIAA 90.
132. S. E. Olsen; M. W. Beckstead, *Journal of Propulsion and Power* **1996,** 12, (4), 662-671.
133. M. K. King in: *CPIA Publication 529*, 26th JANNAF Combustion Meeting, 1989; 1989.
134. M. K. King, *Journal of Spacecraft and Rockets* **1982,** 19, (4), 294-306.
135. M. K. King, *Combustion Science and Technology* **1974,** 8, (5-6), 255-73.
136. M. K. King, *Combustion Science and Technology* **1972,** 5, (4), 155-64.
137. C. L. Yeh; K. K. Kuo, *Progress in Energy and Combustion Science* **1997,** 22, (6), 511-541.
138. R. A. Yetter; H. Rabitz; F. L. Dryer; R. C. Brown; C. E. Kolb, *Combustion and Flame* **1991,** 83, (1-2), 43-62.
139. A. Macek; J. M. Semple, *Symp. (Int.) Combust., [Proc.], 13th* **1971**, 859-68.
140. E. M. Hunt; M. L. Pantoya, *Journal of Applied Physics* **2005,** 98, (3), 034909/1-034909/8.
141. T. Parr; C. Johnson; D. Hanson-Parr; K. Higa; K. Wilson in: JANNAF Combustion Subcommittee Meeting, December, 2003; 2003.
142. J. Katz, Tepper, F., Ivanov, G.V., Lerner, M.I. and V. Davidovich in: *CPIA Publication 675*, JANNAF Propulsion Meeting, 1998; 1998.
143. M. L. Hobbs; M. R. Baer; B. C. McGee, *Propellants, Explosives, Pyrotechnics* **1999,** 24, (5), 269-279.
144. F. P. Incropera; D. P. DeWitt, *Fundamentals of Heat and Mass Transfer*. 3rd ed.; John Wiley and Sons, Inc.: 1990.
145. M. W. Chase, Jr., *J. Phys. Chem. Ref. Data Monograph 9* **1998**, 1-1951.
146. L. Zhou; N. Piekiel; S. Chowdhury; M. R. Zachariah, *J Phys Chem C* **2010**.
147. K. T. Sullivan; M. R. Zachariah, *In press- Journal of Propulsion and Power* **2010**.
148. S. Chowdhury; K. Sullivan; N. Piekiel; L. Zhou; M. R. Zachariah, *Journal of Physical Chemistry C* **2010,** 114, (20), 9191-9195.

149. L. Zhou; N. Piekiel; S. Chowdhury; M. R. Zachariah, *Rapid Communications in Mass Spectrometry* **2009,** 23, (1), 194-202.
150. L. Zhou; N. Piekiel; S. Chowdhury; D. Lee; M. R. Zachariah, *Journal of Applied Physics* **2009,** 106, (8).
151. K. T. Sullivan; G. Young; M. R. Zachariah, *Combustion and Flame* **2007**.
152. S. Y. Sun; L. Zhang; S. Jahanshahi, *Metallurgical and Materials Transactions B-Process Metallurgy and Materials Processing Science* **2003,** 34, (5), 517-523.
153. R. A. Yetter; G. A. Risha; S. F. Son, *Proceedings of the Combustion Institute* **2009,** 32, 1819-1838.
154. G. Young; K. Sullivan; M. R. Zachariah; K. Yu, *Combustion and Flame* **2009,** 156, (2), 322-333.
155. S. H. Fischer; M. C. Grubelich in: *Theoretical Energy Release of Thermites, Intermetallics, and Combustible Metals*, 24th International Pyrotechnics Seminar, Monterey, CA, 1998; Monterey, CA, 1998.
156. J. Sendroy, *J. Biol. Chem* **1937,** 120, 335-403.
157. E. L. Dreizin, *Progress in Energy and Combustion Science* **2009,** 35, (2), 141-167.
158. D. Lee; H. Sakurai; R. Mehadavan; M. R. Zachariah, *Abstracts of Papers of the American Chemical Society* **2003,** 225, 520-PHYS.
159. K. H. Stern, *High Temperature Properties and Thermal Decomposition of Inorganic Salts with Oxyanions*. CRC Press LLC: Boca Raton, FL, 2001.
160. D. R. Lide, *CRC Handbook of Chemistry and Physics*. 78 ed.; CRC Press: New York, 1998.
161. N. Wiberg; A. F. Holleman, *Inorganic Chemistry*. Academic Press: San Diego, CA, 2001; p 453.
162. L. Erdey; J. Simon; S. Gal, *Talanta* **1968,** 15, (7), 653-&.
163. G. Burley, *Am. Mineral* **1963,** 48, 1266-76.
164. P. M. Kumar; C. Balasubramanian; N. D. Sali; S. V. Bhoraskar; V. K. Rohatgi; S. Badrinarayanan, *Materials Science and Engineering B* **1999,** B63, 215-227.
165. K. T. Sullivan; C. E. Johnson; N. W. Piekiel; S. Chowdhury; C. Wu; M. R. Zachariah, *Submitted to Combustion Science and Technology* **2010**.
166. Y. Tachibana; K. Kusunoki; T. Watanabe; K. Hashimoto; H. Ohsaki, *Thin Solid Films* **2003,** 442, (1-2), 212-216.
167. J. F. Moulder; W. F. Stickle; P. E. Sobol; K. D. Bomben, *Handbook of X-ray Photoelectron Spectroscopy*. 5th ed.; Perkin-Elmer Co.: Eden Prairie, 1992.
168. J. A. Rodriguez; M. Kuhn; J. Hrbek, *Journal of Physical Chemistry* **1996,** 100, (46), 18240-18248.
169. A. Prakash; A. V. McCormick; M. R. Zachariah, *Nano Letters* **2005,** 5, (7), 1357-1360.
170. J. W. Zhu; H. P. Bi; Y. P. Wang; X. Wang; X. J. Yang; L. Lu, *Materials Chemistry and Physics* **2008,** 109, (1), 34-38.